PLANT EXTRACT-NANOPARTICLES HYBRID AS CORROSION INHIBITORS FOR AA2024 ALUMINIUM ALLOY

BY

Auwal KASIM, B.Eng.(ABU) 2000; M.Sc.(ABU) 2008

(PH.D/ENG/17733/2007-08)

A PH.D DISSERTATION SUBMITTED TO THE SCHOOL OF POSTGRADUATE STUDIES, AHMADU BELLO UNIVERSITY, ZARIA IN PARTIAL FULFILMENT OF THE REQUIREMENTS FOR THE AWARD OF A DOCTOR OF PHILOSOPHY DEGREE IN METALLURGICAL AND MATERIALS ENGINEERING.

DEPARTMENT OF METALLURGICAL AND MATERIALS ENGINEERING,

FACULTY OF ENGINEERING,

AHMADU BELLO UNIVERSITY, ZARIA,

NIGERIA.

MAY, 2013.

DECLARATION

I declare that the work in this Dissertation entitled "**PLANT EXTRACT-NANOPARTICLES HYBRID AS CORROSION INHIBITORS FOR AA2024 ALUMINIUM ALLOY"** has been carried out by me in the Department of Metallurgical and Materials Engineering, Ahmadu Bello University, Zaria, Nigeria. The information derived from the literature has been duly acknowledged in the text and a list of references provided. No part of this Dissertation was previously presented for another degree or diploma at this or any other Institution.

_____ _____

Auwal KASIM

(Ph.D/ENG/17733/2007-08) **Date**

CERTIFICATION

This Dissertation entitled "**PLANT EXTRACT-NANOPARTICLES HYBRID AS CORROSION INHIBITORS FOR AA2024 ALUMINIUM ALLOY"** by Auwal KASIM meets the regulations governing the award of the degree of Doctor of Philosophy in Metallurgical & Materials Engineering of the Ahmadu Bello University, Zaria, Nigeria and is approved for its contribution to knowledge and literary presentation.

Prof. S. A. Yaro	
Chairman, Supervisory Committee	Date
Dr. O. Aponbiede	
Member, Supervisory Committee	Date
Dr. T. Ause	
Member, Supervisory Committee	Date
Prof. S. A. Yaro	
Head of Department	Date
Prof. J. A. Adebayo	
Dean, School of Postgraduate Studies	Date

ACKNOWLEDGEMENTS

First, to almighty ALLAH, who makes it possible for me to see the light of this moment.

Then to my supervisors, Professor Shehu Aliyu Yaro, Dr. Ola Aponbiede and Dr. T. Ause, not only for their untiring effort towards guiding me, but also for making sure that the work was executed. I am also immensely thankful to Prof. I. A. Madugu, Dr Junaid Kabir, Dr Abubakar Isma'il and Dr I. A. Mohammed-Dabo for their concern.

I am profoundly indebted to the management of Ahmadu Bello University, Zaria under the acting Vice Chancellorship of Prof. J. U. Umoh, who chose Professor Shehu Aliyu Yaro to represent the University at the UNESCO team that visited the educational/research institutions of the Republic of South Africa. I am particularly grateful to Professor Shehu Aliyu Yaro for extending the benefits of his visit to us and again to Ahmadu Bello University, Zaria for ETF award.

I am especially grateful to Dr. Engr. (Mrs) Abimbola Patricia Idowu Popoola of the Department of Chemical and Metallurgical Engineering, Tswhane University of Technology, Pretoria, South Africa for giving me the opportunity to perform my bench work there. Worthy of mention, also, are Drs. Agbo and Johnson, Engr. Sunday Fayomi, Engr. Feyisayo & Family, Muhammad Auwal Ibrahim and Abdurrasheed for their immense support and keeping me homely in South Africa.

I would also like to appreciate the support given to me by the entire Departmental staff, most especially Dr. M. Abdulwahab, Engr. Umar Shehu, Engr. Jimoh Gaminana, Engr. Kamilu Bello, Engr. F. Asuke, Mal Yusuf, Mr. Zang David, Mr. Danladi and Mrs L. B. Dauda.

The immense contributions of my childhood friends were highly acknowledged. Specifically Dr. Sa'id Minjibir, Engr. Auwal Abdu, Arc. Sani Ahmed, Qs. Aminu Bashir, Qs. I. A. Wudil, Mujahid Kabir, Dr. Garba Dahiru, Dr Zaiyad Garba, Mal. Yaya, Rufa'i Ahmed, Mujtaba Ali Muhammad, the entire RUMFOBA class 90 and others too numerous to mention.

The integral part of my life (my parents, brothers and sisters) deserves special appreciation. Words alone could not express how grateful I am to my mother (Hajia Husainah), father (Mal. Kasim Adamu) and the entire family for their support in all ramifications. To my humble wife, Hajia Sa'adatu, daughters (Fa'izah and Asiyah) and the one(s) being expected, I pray Almighty Allah to shower his blessings on them, protect and guide them unto the right path; the path of those who earned the pleasure of Allah, not the one for those who earned his anger nor that of those who go astray.

DEDICATION

To the less-priviledged, victims of "man-made" or natural disasters and ***the loving memory of my father, Malam Kasim Adamu, may Jannatul Firdaus be his final abode.***

ABSTRACT

The influence of two plant extracts, *Parkia biglobosa* (African locust bean) and *Vitex doniana* (Black plum) on electrochemical corrosion behaviour of as-cast AA2024 aluminium alloy exposed to artificial sea water (3.5%NaCl solution) was investigated. The results of the ^{1}H NMR-based metabolomics of leave extracts of *Parkia biglobosa* (PBE) and *Vitex doniana* (VDE) revealed aromatic and other functional groups such as $-CH_3$, and R-OH which are attributes of a good inhibitor. The performances of these extracts were evaluated individually, synergistically and under the influence of Boehmite Nanoparticles in different amounts of 0.1, 0.2, 0.3, 0.4 and 0.5g. Parkia biglobosa extracts gave better Inhibition Efficiencies (IE%) than Vitex doniana extracts whether alone or in synergistic combinations; this could probably be due to the high density/concentration of aromatics and other functional groups as revealed by ^{1}H NMR-based spectrum. Comparison of the performances of the different extract-extract and extract-Nanoparticle systems were also made on the basis of Inhibition Efficiencies (IE%), determined from both chemical (Gravimetric-based Mass Loss) and electrochemical techniques (Linear Polarisation Resistance and Electrochemical Impedance Spectroscopy). Only PBE+VDE+Boehmite Nanoparticle synergistic system was found to compare favourably with Sodium chromate, the reference inhibitor against which the effectiveness of the different inhibitor systems (single, binary and ternary) was compared. An optimum IE% of 92.15% for PBE+VDE+Boehmite Nanoparticles system compared favourably with IE% of 92.57% for Sodium Chromate. The adsorbed films of Sodium Chromate and PBE+VDE+Boehmite Nanoparticles systems were found to be stable around -0.6V when evaluated by Chronopotentiometry. The synergism parameters were found to be greater

than unity, affirming synergy among the inhibitor molecules/ions. Kinetic and thermodynamic data generated suggested co-adsorption through a combination of both Physisorption and Chemisorption mode of interaction between the inhibitors and the substrates. The linearity of Langmuir adsorption Isotherms further supported adsorption proposition, while the El-Awady's adsorption Isotherms consolidated the Langmuir's model by calculating the number of active sites; obtained values greater than unity inferred that the inhibitor molecules occupied more than one site. SEM/EDX panorama of the inhibited samples revealed evidences of interference of corrosion products with the additive substances to form new phases, as revealed by X-Ray Diffractograms, which was a plausible mechanism for the action of the inhibitors, and not just adsorption or co-adsorption. Raman spectroscopic analyses were found to be particularly helpful when examining the surfaces of the substrates inhibited by the plant extracts. Variations in Raman shifts were indicative of surface interactions; due either to adsorption of organic molecules onto the alloy surfaces or release of certain metal ions into solution, leading to appearance of certain peaks. All the characterisation techniques, using SEM/EDX, XRD and Raman Spectroscopy, gave insights into the influence of the additive substances on the electrodes/substrates. This was achieved through morphological revelations, phase identifications and other thin corrosion products elucidation. IE% results obtained from Linear Polarisation Resistance, Electrochemical Impedance Spectroscopy and Gravimetric-based mass loss were compared using ANOVA statistical tool and found to be in good agreement. In conclusion, PBE+VDE+Boehmite Nanoparticles system could serve as an ecofriendly alternative to Sodium Chromate.

Table of Contents

Title Page I
Declaration II
Certification III
Acknowledgements IV
Dedication V
Abstract VI
List of Figures XII
List of Tables XVI
List of Appendices XX
Abbreviations and Symbols XXII
CHAPTER ONE 1
1.0 INTRODUCTION 1
1.1 General Background 1
1.2 Statement of Research Problems 5
1.3 Justification for the Research Work 5
1.4 Aims and Objectives 7
1.5 Scope and Limitations 8
1.6 Contribution to Knowledge 9
CHAPTER TWO 10
2.0 LITERATURE REVIEW 10

2.1 Methods of Approach to Corrosion Phenomena 11
2.2 Classification of Spontaneous Corrosion Reactions 11
2.3 Aluminium and its Alloys 12
2.4 Classification of Aluminium Alloys 14
2.5 Corrosion of Aluminium and its Alloys 14
2.6 Electrical Double Layer 17
2.7 Influence of Corrosion Product Deposits 18
2.8 Thermodynamics and Kinetics of Corrosion 21
2.8.1 Thermodynamics of Corrosion; Pourbaix (*E/pH* Equilibrium) Diagrams 21
2.8.2 Kinetics of Corrosion 22
2.9 Polarization 27
2.9.1 Activation Polarization 28
2.9.2 Concentration Polarization 29
2.9.3 Resistance Polarization 30
2.10 Corrosion Prevention and Control Techniques 32
2.11 Corrosion Inhibitors 32
2.11.1 Classification of Inhibitors 33
2.12 Role of Surface Modified Nanoparticles in Corrosion Inhibition 39
2.13 Synergism 40
2.14 Mechanism of Inhibition 41
2.15 Adsorption Isotherms 47
2.16 Background Information on the Substances Used as Inhibitors 49
2.16.1 Sodium Chromate (Na_2CrO_4) 49
2.16.2 *Parkia biglobosa* (African Locust Bean) Tree 49
2.16.3 *Vitex doniana* Sweet (Black Plum) Tree 49
2.16.4 Boehmite Nanoparticles [AlO(OH)] 50
2.17 Corrosion Measurement Techniques 50
2.17.1 Linear Polarisation Resistance (LPR) 53
2.17.2 Electrochemical Impedance Spectroscopy (EIS) 58
2.17.3 Chronopotentiometry 61
2.17.4 Gravimetric-based Mass Loss Method 62
2.18 Materials Characterisation 64
2.18.1 NMR-based Metabolomic Analysis of the Plant Extracts 64

2.18.2 X-Ray Fluorescence (XRF).....65
2.18.3 Scanning Electron Microscopy/Energy-Dispersive X-Ray Spectroscopy (SEM/EDS) 65
2.18.4 X-Ray Diffraction (XRD) 66
2.18.5 Raman Spectroscopy.....67
CHAPTER THREE 69
3.0 MATERIALS AND METHODS.....69
3.1 Primary Materials 69
3.2 Equipment, Apparatuses, Machines and Other Materials.....69
3.3 Methods 70
3.3.1 Extraction of Some Phytoconstituents from the Plants 70
3.3.2 NMR-Based Metabolomic Screening of the Plant Extracts.....71
3.3.3 Production of the Test Alloy 71
3.4 Preparation of Solutions for Corrosion Testing 72
3.5 Pre-Corrosion Materials Characterisation.....73
3.6 Sample Preparation for Corrosion Testing 73
3.6.1 Preparation of Samples for Gravimetric-Based Mass Loss 73
3.6.2 Preparation of Samples for Electrochemical Testing 74
3.7 Corrosion Testing 74
3.7.1 Electrochemical Techniques 74
3.7.2 Gravimetric-Based Mass Loss 79
3.8 Post-Corrosion Materials Characterisation 79
3.8.1 Scanning Electron Microscopy/ Energy Dispersive Spectrometry (SEM/EDS) 79
3.8.2 X-Ray Diffraction (XRD) 80
3.8.3 Raman Spectroscopy 80
CHAPTER FOUR 81
4.0 RESULTS 81
4.1 X-Ray Fluorescence result of the Cast Alloy (AA2024).....81
4.2 NMR Spectra of ethanolic leave extracts of *Parkia biglobosa* & *Vitex doniana.* 81
4.3 Corrosion Testing 83
4.3.1 Classical method.....83
4.3.2 Linear Polarisation Resistance 91
4.3.3 Electrochemical Impedance Spectroscopy (EIS) 98

4.3.4 Chronopotentiometric Analysis 105
4.4 Kinetics and Thermodynamics Consideration 112
4.5 Elucidation of Synergism 113
4.6 Adsorption Isotherms 114
4.6.1 Langmuir Adsorption Isotherm 114
4.6.2 El-Awady's Adsorption Isotherm 115
4.7 Characterisation 117
4.7.1 Scanning Electron Microscopy/Energy Dispersive X-Ray (SEM/EDXA) 117
4.7.2 XRD Results 122
4.7.3. Raman Spectroscopic Analysis 132
4.8 Analysis of Variance (ANOVA) 138
CHAPTER FIVE 140
5.0 DISCUSSION OF RESULTS 140
5.1 X-Ray Fluorescence Result of the Cast Alloy (AA2024) 140
5.2 Characterisation of the Extract by Nuclear Magnetic Resonance (NMR) 140
5.2.1 Parkia biglobosa. 140
5.2.2 Vitex doniana 141
5.3 Corrosion Testing 142
5.3.1 Classical methods 142
5.3.2 Linear Polarisation Resistance 149
5.3.3 Electrochemical Impedance Spectroscopy (EIS) 157
5.3.4 Chronopotentiometric Analysis 163
5.4 Effect of the Boehmite Nanoparticles on the Performance of the Plant Extracts 165
5.5 Kinetics and Thermodynamics Consideration 167
5.6 Elucidation of Synergism 169
5.7 Adsorption Isotherms 169
5.7.1 Langmuir Adsorption Isotherm 169
5.7.2 El-Awady's Adsorption Isotherm 170
5.8 Characterisation 171
5.8.1 Scanning Electron Microscopy/Energy Dispersive X-Ray (SEM/EDXA) 171
5.8.2 XRD Results 176
5.8.3. Raman Spectroscopic Analysis 184
5.9 Analysis of Variance (ANOVA) 189

CHAPTER SIX **191**
6.0 SUMMARY, CONCLUSIONS AND RECOMMENDATIONS 191
6.1 Summary 191
6.2 Conclusions 194
6.3 Recommendations 195
REFERENCES 197
APPENDICES 213

LIST OF FIGURES

Figure 1.1: World production of Aluminium, Copper and Zinc for the period 1900-2002 2

Figure 2.1: Equilibrium binary solid solubility as a function of temperature for alloying elements most frequently added to aluminum. 12

Figure 2.2: Schematic Electrical Double Layer. 17

Figure 2.3**:** Schematic of an idealized corrosion product deposit on a corroding surface. 20

Figure 2.4: Schematic showing a corrosion product deposit composed of interconnected tortuous pores. 21

Figure 2.5: Pourbaix diagram for the Aluminium-water system at 25°C showing nominal zones of immunity, passivity and corrosion. 23

Figure 2.6: Schematic activation free energy distribution. 29

Figure 2.7: Logarithmic plot of current density, ***i*,** overvoltage, **η,** for a polarized electrode. 31

Figure 2.8: Typical polarization curve showing Tafel plot/extrapolation. 56

Figure 2.9: Schematic of AC/DC impedance circuit. 60

Figure 2.10: A simplified polarization resistance model circuit 60

Figure 3.1: Schematic of linear polarisation experimental circuit. 76

Figure 3.2: A simplified instrumentation of the EIS experimental set-up. 78

Figure 3.3: Electrochemical equivalent circuit used to fit the impedance spectra. 78

Figure 4.1: Proton NMR Spectrum of Ethanolic Extract of *Parkia biglobosa (PBE)* leaves extracts. 81

Figure 4.2: Proton NMR spectrum of Ethanolic extract of *Vitex doniana(VDE)*. 82

Figure 4.3: Variation of corrosion rates with temperatures for the test sample in control (3.5%NaCl) solution. 83

Figure 4.4: Variation of Inhibition Efficiencies (IE%) with different amounts of Na_2CrO_4 at different temperatures. 84

Figure 4.5: Variation of Inhibition Efficiencies (IE%) with different concentrations of *Parkia biglobosa* extracts at different temperatures. 85

Figure 4.6: Variation of Inhibition Efficiencies (IE%) with different concentrations of *Parkia biglobosa* extracts and Boehmite Nanoparticles at different temperatures. 86

Figure 4.7: Variation of Inhibition Efficiencies (IE%) with different concentrations of *Vitex doniana* extracts at different temperatures. 87

Figure 4.8: Variation of Inhibition Efficiencies (IE%) with different concentrations of *Vitex doniana* extracts and Boehmite Nanoparticles at different temperatures. 88

Figure 4.9: Variation of Inhibition Efficiencies (IE%) with different concentrations of Parkia biglobosa and *Vitex doniana* extracts at different temperatures. 89

Figure 4.10: Variation of Inhibition Efficiencies (IE%) with different concentrations of *Parkia biglobosa*/*Vitex doniana* extracts and amounts of Boehmite Nanoparticles at different temperatures. 90

Figure 4.11: Polarisation curves for AA2024 containing different concentrations of Na_2CrO_4 at room temperature. 91

Figure 4.12: Polarisation curves for AA2024 containing different concentrations of PBE at room temperature. 92

Figure 4.13: Polarisation curves for AA2024 containing different concentrations of PBE+ Boehmite at room temperature. 93

Figure 4.14: Polarisation curves for AA2024 containing different concentrations of PBE+ VDE at room temperature. 94

Figure 4.15: Polarisation curves for AA2024 containing different concentrations of PBE+VDE+Boehmite at room temperature. 95

Figure 4.16: Polarisation curves for AA2024 containing different concentrations of VDE at room temperature. 96

Figure 4.17: Polarisation curves for AA2024 containing different concentrations of VDE+Boehmite at room temperature. 97

Figure 4.18: Nyquist diagram for AA2024 Aluminium Alloy Inhibited by Na_2CrO_4. 98

Figure 4.19: Nyquist diagram for AA2024 Aluminium Alloy Inhibited by PBE+VDE+NANO BOEHMITE system. 99

Figure 4.20: Nyquist diagram for AA2024 Aluminium Alloy Inhibited by PBE+VDE. 100

Figure 4.21: Nyquist diagram for AA2024 Aluminium Alloy Inhibited by PBE. 101

Figure 4.22: Nyquist diagram for AA2024 Aluminium Alloy Inhibited by PBE+Boehmite. 102

Figure 4.23: Nyquist diagram for AA2024 Aluminium Alloy Inhibited by VDE. 103

Figure 4.24: Nyquist diagram for AA2024 Aluminium Alloy Inhibited by VDE+Boehmite. 104

Figure 4.25: Chronopotentiograms of the test samples exposed to 3.5%NaCl+Na_2CrO_4 solution. 105

Figure 4.26: Chronopotentiograms of the test samples exposed to 3.5%NaCl+PBE solution. 106

Figure 4.27: Chronopotentiograms of the test samples exposed to 3.5%NaCl+PBE+ Boehmite solution. 107

Figure 4.28: Chronopotentiograms of the tests sample exposed to 3.5%NaCl +PBE+VDE solution. 108

Figure 4.29: Chronopotentiograms of the test samples exposed to 3.5%NaCl+ PBE+VDE+ BOEHMITE solution. 109

Figure 4.30: Chronopotentiograms of the test samples exposed to 3.5%NaCl+VDE solution. 110

Figure 4.31: Chronopotentiograms of the test samples exposed to 3.5%NaCl+VDE+ Boehmite solution. 111

Figure 4.32: Langmuir Adsorption Isotherms for the adsorption of PBE+VDE+NANO system onto the surfaces of AA2024 coupons in 3.5%NaCl solution. 114

Figure 4.33: El-Awady's Adsorption Isotherms for the adsorption of PBE+VDE+NANO system onto the surfaces of AA2024 coupons in 3.5%NaCl solution. 115

Figure 4.34: SEM Micrographs, with the corresponding EDX Spectrum, for the as-cast sample. 117

Figure 4.35: SEM Micrographs, with the corresponding EDX Spectrum, for the sample exposed to 3.5%NaCl solution. 118

Figure 4.36: SEM Micrographs, with the corresponding EDX Spectrum, for the sample in 3.5%NaCl+Na_2CrO_4 solution. 118

Figure 4.37: SEM Micrographs, with the corresponding EDX Spectrum, for the sample in 3.5%NaCl+PB Extracts solution. 119

Figure 4.38: SEM Micrographs, with the corresponding EDX Spectrum, for the sample in 3.5%NaCl + PB Extracts + Boehmite Nanoparticles solution. 119

Figure 4.39: SEM Micrographs, with the corresponding EDX Spectrum, for the sample in 3.5%NaCl with PB+VD Extracts + Boehmite Nanoparticles solution. 120

Figure 4.40: SEM Micrographs, with the corresponding EDX Spectrum, for the sample in 3.5%NaCl+VD Extracts solution. 120

Figure 4.41: SEM Micrographs, with the corresponding EDX Spectrum, for the sample in 3.5%NaCl + VD Extracts + Boehmite Nanoparticles solution. 121

Figure 4.42: SEM Micrographs, with the corresponding EDX Spectrum, for the sample in 3.5%NaCl+PB+VD Extract solution. 121

Figure 4.43: XRD pattern of the as-cast test sample. 123

Figure 4.44: XRD pattern of the test sample exposed to 3.5%NaCl solution. 124

Figure 4.45: XRD pattern of the test sample in 3.5%NaCl containing Sodium chromate solution. 125

Figure 4.46: XRD pattern of the test sample in 3.5%NaCl containing PB Extracts. 126

Figure 4.47: XRD pattern of the test sample in 3.5%NaCl containing PBE+Boehmite. 127

Figure 4.48: XRD pattern of the test sample in 3.5%NaCl containing PB+VD Extracts. 128

Figure 4.49: XRD pattern of the test sample in 3.5%NaCl containing PB+VD+Boehmite. 129

Figure 4.50: XRD pattern of the test sample in 3.5%NaCl containing VD Extracts. 130

Figure 4.51: XRD pattern of the test sample in 3.5%NaCl containing VD+Boehmite solution. 131

Figure 4.52: Raman Spectrum and the image of overall surface of the as-cast test alloy. 132

Figure 4.53: Raman Spectrum and the image of overall surface of the test alloy in 3.5%NaCl solution. 133

Figure 4.54: Raman spectrum and the image of overall surface of the test alloy in 3.5%NaCl and sodium chromate solution. 133

Figure 4.55: Raman spectrum and the image of overall surface of the test alloy in 3.5%NaCl and PBE solution. 134

Figure 4.56: Raman spectrum and the image of overall surface of the test alloy in 3.5%NaCl and PBE+Boehmite Nanoparticles Solution. 134

Figure 4.57: Raman spectrum and the image of overall surface of the test alloy in 3.5%NaCl and PBE+VDE solution. 135

Figure 4.58: Raman spectrum and the image of overall surface of the test alloy in 3.5%NaCl and PBE+VDE+Boehmite Nanoparticles Solution. 135

Figure 4.59: Raman spectrum and the image of overall surface of the test alloy in 3.5%NaCl and VD Extracts Solution. 136

Figure 4.60: Raman spectrum and the image of overall surface of the test alloy in 3.5%NaCl and VDE+Boehmite nanoparticles Solution. 136

LIST OF TABLES

Table 2.1: Classification of Wrought Aluminium & Aluminium Alloys. 13

Table 2.2: Corrosion inspection and plant condition monitoring techniques. 52

Table 2.3: In-plant monitoring techniques. 53

Table 3.1: Nominal compositions of the test alloy. 72

Table 3.2: Compositions of the solutions used in the corrosion tests. 73

Table 4.1: X-Ray Fluorescence (XRF) results of the test alloy under investigation. 81

Table 4.2: Polarisation parameters and the corresponding Inhibition Efficiencies (IE%) for the corrosion of AA2024 Aluminium Alloy in 3.5%NaCl containing different concentrations of $NaCr_2O_4$ at room temperature. 91

Table 4.3: Polarisation parameters and the corresponding Inhibition Efficiencies (IE%) for the corrosion of AA2024 Aluminium Alloy in 3.5%NaCl containing different concentrations of PBE at room temperature. 92

Table 4.4: Polarisation parameters and the corresponding Inhibition Efficiencies (IE%) for the corrosion of AA2024 Aluminium Alloy in 3.5%NaCl containing different concentrations of PBE+Boehmite at room temperature. 93

Table 4.5: Polarisation parameters and the corresponding Inhibition Efficiencies (IE%) for the corrosion of AA2024 Aluminium Alloy in 3.5%NaCl containing different concentrations of PBE+VDE at room temperature. 94

Table 4.6: Polarisation parameters and the corresponding Inhibition Efficiencies (IE%) for the corrosion of AA2024 Aluminium Alloy in 3.5%NaCl containing different concentrations of PBE+VDE+ Nano Boehmite at room temperature. 95

Table 4.7: Polarisation parameters and the corresponding Inhibition Efficiencies (IE%) for the corrosion of AA2024 Aluminium Alloy in 3.5%NaCl containing different concentrations VDE at room temperature. 96

Table 4.8: Polarisation parameters and the corresponding Inhibition Efficiencies (IE%) for the corrosion of AA2024 Aluminium Alloy in 3.5%NaCl containing different concentrations VDE + Boehmite Nanoparticles at room temperature. 97

Table 4.9: Parameters obtained from Nyquist diagram for the corrosion of AA2024 coupons inhibited by Na_2CrO_4 in 3.5%NaCl solution at room temperature. 98

Table 4.10: Parameters obtained from Nyquist diagram for the corrosion of AA2024 coupons inhibited by PBE+VDE+NANO BOEHMITE system in 3.5%NaCl solution at room temperature. 99

Table 4.11: Parameters obtained from Nyquist diagram for the corrosion of AA2024 coupons inhibited by PBE+VDE system in 3.5%NaCl solution at room temperature. 100

Table 4.12: Parameters obtained from Nyquist diagram for the corrosion of AA2024 coupons inhibited by PBE system in 3.5%NaCl solution at room temperature. 101

Table 4.13: Parameters obtained from Nyquist diagram for the corrosion of AA2024 coupons inhibited by PBE+ Boehmite nanoparticles system in 3.5%NaCl solution at room temperature. 102

Table 4.14: Parameters obtained from Nyquist diagram for the corrosion of AA2024 coupons inhibited by VDE system in 3.5%NaCl solution at room temperature. 103

Table 4.15: Parameters obtained from Nyquist diagram for the corrosion of AA2024 coupons inhibited by VDE+Boehmite Nanoparticles system in 3.5%NaCl solution at room temperature. 104

Table 4.16: Kinetic and thermodynamic parameters for the various inhibitor Systems at different temperatures. 112

Table 4.17: Synergism parameter (S_Θ) for different concentrations of investigated extracts-extracts (PBE+VDE) systems at different temperatures. 113

Table 4.18: Synergism parameter (S_Θ) for different concentrations of investigated extracts-nanoparticles (PBE+VDE+ Boehmite) systems at different temperatures. 113

Table 4.19: Calculated parameters from Langmuir and El-awady. 116

Table 4.20: Chemical/phases composition of the cast alloy as revealed by the XRD. 123

Table 4.21: Chemical/phases composition of the test sample exposed to 3.5% NaCl solution. 124

Table 4.22 : Chemical/phases composition of the test sample 125

Table 4.23: Chemical/phases composition of the test sample in 3.5%NaCl containing PB Extracts. 126

Table 4.24: Chemical/phases composition of the test sample in 3.5%NaCl containing PBE+Boehmite solution. 127

Table 4.25: Chemical/phases composition of the test sample in 3.5%NaCl containing PB+VD extracts. 128

Table 4.26: Chemical/phases composition of the test sample in 3.5%NaCl containing PB+VD+BOEHMITE. 129

Table 4.27: Chemical/phase composition of the test sample in 3.5%NaCl containing VD Extracts. 130

Table 4.28: Chemical/phases composition of the test sample in 3.5%NaCl containing VD+Boehmite. 131

Table 4.29: Summary of the Raman peak shifts (cm^{-1}) of the corrosion products formed on the AA2024 coupons in the different systems under investigation. 137

Table 4.30: Inhibition Efficiencies (IE%) obtained using LPR, EIS and Gravimetric-based mass loss (ML) for Sodium Chromate system at room temperature. 138

Table 4.31: ANOVA results generated for Sodium Chromate systems at room temperature and different concentrations. 138

Table 4.32: Inhibition Efficiencies (IE%) obtained using LPR, EIS and Gravimetric-based mass loss (ML) for PBE+VDE+Boehmite system at room temperature. 139

Table 4.33: ANOVA results generated for PBE+VDE+BOEHMITE systems at room temperature and different concentrations. 139

LIST OF APPENDICES

APPENDICES I: Expert High Score Programme and JCPDS Card used to obtain information on XRD Patterns and related information. 214

APPENDICES II: SEM/EDX Microanalysis Detailed Report. 281

APPENDICES III: Inhibition Efficiencies & Surface Coverage values for the Different Systems investigated at different Temperatures & Concentrations. 319

Table 1: Inhibition efficiencies and surface coverages obtained from the corrosion rates for different concentrations of *Parkia biglobosa* extracts in 3.5%NaCl solution at different temperatures. 319

Table 2: Inhibition efficiencies and surface coverages obtained from the corrosion rates for different concentrations of of *Vitex doniana* extracts in 3.5%NaCl solution at different temperature. 319

Table 3: Inhibition efficiencies and surface coverages obtained from the corrosion rates for different concentrations of Sodium chromate in 3.5%NaCl solution at different temperatures. 321

Table 4: Inhibition efficiencies and surface coverages obtained from the corrosion rates for different concentrations of *Parkia biglobosa* and *Vitex doniana* in 3.5%NaCl solution at different temperatures. 321

Table 5: Inhibition efficiencies and surface coverages obtained from the corrosion rates for different concentrations of *Parkia biglobosa, Vitex doniana* and Boehmite Nanoparticles in 3.5%NaCl solution at different temperatures. 322

Table 6: Inhibition efficiencies and surface coverages obtained from the corrosion rates for different concentrations of *Vitex doniana* and Boehmite Nanoparticles in 3.5%NaCl solution at different temperatures. 323

Table 7: Inhibition efficiencies and surface coverages obtained from the Corrosion rates for different concentrations of *Parkia biglobosa* + Boehmite Nanoparticles in 3.5%NaCl solution at different temperatures. 324

APPENDICES IV: Comparisms of room Temperature IE% values obtained from LPR, EIS and ML. 325

Table 8: Comparism of Room Temperature IE% Values for Sodium Chromate System 325

Table 9: Comparism of Room Temperature IE% Values for PBE+VDE +Boehmite Nanoparticles System 325

Table 10: Comparism of Room Temperature IE% Values for PBE+ VDE System 325

Table 11: Comparism of Room Temperature IE% Values for PBE System 326

Table 12: Comparism of Room Temperature IE% Values for PBE+Boehmite Nanoparticles System 326

Table 13: Comparism of Room Temperature IE% Values for VDE System 327
Table 14: Comparism of Room Temperature IE% Values for VDE+Boehmite Nanoparticles System 327

ABBREVIATIONS AND SYMBOLS

IE%	Inhibition Efficiency
OCP	Open Circuit Potential
Al	Aluminium
Cu	Copper
Mn	Manganese
Mg	Magnesium
Mo	Molybdenum
Fe	Iron
Cr	Chromium
C	Carbon
EDL	Electrical Double Layer
IMCs	Intermetallic Compounds
r	Reaction Rate
E	Potential drop
F	Faraday's constant
i	Electric Current
i_{corr}/j_{corr}	Current Density as Defined in the Text
i_o	Exchange Current Density
i_l	Limiting Diffusion Current Density
ΔG	Free Energy Change
ΔG^o	Standard Free Energy
ΔH	Enthalpy Change
ΔS_a	Entropy of Activation
ΔS^o	Standard Entropy
Q_{ads}	Heat of Adsorption
z	Charge on an electron
R	Gas constant
T	Absolute Temperature
Z'	Imaginary Impedance
Z	Real Impedance

E_a	Activation Energy
K	Adsorptional constant
θ	Surface Coverage
c	Inhibitor Concentration
η	Overvoltage/Overpotential/Polarisation
β	Tafel constant
□	Inhibition coefficient
r_o	Corrosion rate in Absence of Inhibitor
r_i	Corrosion rate in Presence of Inhibitor
ψ	Change in Surface Potential
δ	Constant of a Substituent R
ρ	Reaction Parameter/ Specimen Density as Defined in the Text
$P^n{}_{(w)}$	Vapour pressure of Water at Temperature T
$P_{(org)}$	Vapour Pressure of Pure organic Compound at Temperature T
C_s	Saturation Concentration of Organic Compound
σ	Interfacial Tension
y	Number of Active Sites
PBE	*Parkia Biglobosa* Extracts
VDE	*Vitex Doniana* Extracts
AC	Alternating Current
DC	Direct Current
EIS	Electrochemical Impedance Spectroscopy
LPR	Linear Polarisation Resistance
E_{corr}	Open Circuit Potential
R_p	Polarisation Resistance
R_s	Solution Resistance
C_{dl}	Capacitance of the Double Layer
R_{ct}	Charge Transfer Resistance
Δw	Mass Loss
CPR	Corrosion Penetration Rate
A	Sample Area
T	Immersion Time

Si	Silicon
Li	Lithium
Ni	Nickel
XRF	X-Ray Fluorescence
XRD	X-Ray Diffractometry
SEM	Scanning Electron Microscopy
EDS/EDX	Energy Dispersive X-Ray Spectroscopy
NMR	Nuclear Magnetic Resonance
RS	Raman Spectroscopy
$Z_{i(\max)}$	Maximum Cell Impedance
π	Phase Angle
CPE	Constant Phase Element
ICDD	International Centre for Diffraction Data
JCPDS	Joint Committee on Powder Diffraction Standard

CHAPTER ONE

1.0 INTRODUCTION

1.1 General Background

Systems are designed to meet performance goals where strength, weight, thermal, and electrical requirements are primary technology considerations while other important attributes such as corrosion resistance and environmental compatibility receive far less attention. Without an upfront analysis to mitigate corrosion, problems often occur after the system has been implemented into service. Correcting unanticipated corrosion during the operational phase of the lifecycle can be very costly. In some cases it may be impossible to return the system to its original state without replacing problematic components or structures at great expense (Benjamin *et al.,* 2006).

Developing new systems that are inherently corrosion resistant, either through selection and use of corrosion resistant materials or by employing appropriate corrosion preventive compounds and coatings, is one sure way to reduce total ownership costs. For effective results, these considerations must be put in place during the acquisition. Design and acquisition management practices must recognize corrosion as a risk factor to be managed (Benjamin *et al.,* 2006).

Aluminium is among the common materials used in the design of many engineering systems. It is the second most abundant element on earth, becoming an economic competitor in engineering applications as recently as the end of 19^{th} century; Figure 1.1 shows the world production of aluminium, copper and zinc for the period 1900-2002. The emergence of three important industrial developments would, by demanding material

characteristics consistent with the unique qualities of aluminium and its alloys, greatly benefit growth in the production and use of the metal (ASM, 1990).

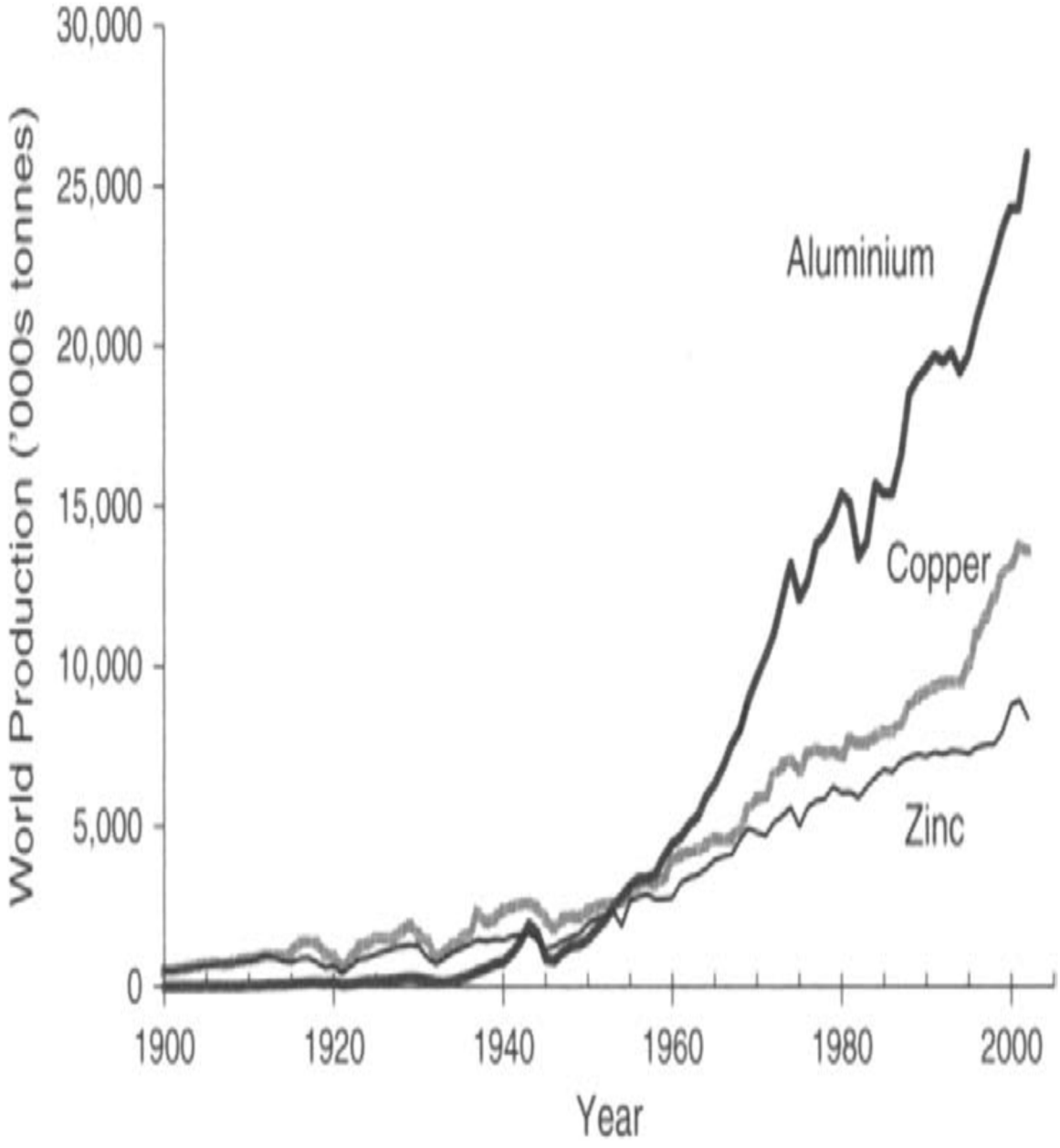


Figure 1.1: World production of Aluminium, Copper and Zinc for the period 1900-2002 (*Source*: Wills & Napier-Munn, 2006).

Aluminium possesses a combination of properties which make it an extremely useful engineering material. Aluminium has a low density (2.7 g/cm^3), making it particularly useful for transportation of manufactured products. It also has good corrosion resistance in most natural environments due to formation of a tenacious oxide film. Although pure aluminium has low strength, it can be alloyed to strength of about 960mpa. Alumnium is non-toxic and used extensively for food containers and packaging. The good electrical properties of aluminium make it suitable for many applications in the electrical industry. The relatively low price of aluminium along with its many useful properties makes this metal very important industrially, especially in the aircraft industry (William, 1990).

Aluminium is often alloyed with Copper, Zinc, Manganese, Silicon, Magnesium, Chromium, Iron e.t.c. Its alloys are much lighter and more corrosion resistant than steel, but not quite as corrosion resistant as pure aluminium (ASM, 1990). Aluminium and its alloys have remarkable economic and attractive properties for engineering applications owing to their low cost, light weight, high thermal and electrical conductivity (Elewady *et al.*, 2008). Generally, aluminium alloys are used for sheet metal work, pressure vessels, chemical equipment, hydraulic tubes, bus, track, marine and aircraft structures, pipelines and railings (William, 1990).

Aluminium copper and zinc alloys, designated as 2XXX and 7XXX series respectively, are used in many applications because of their high mechanical strength and acceptable weldability characteristics, but unfortunately their corrosion resistance is poor, except additional protection is provided. Alloy AA2024, which is precipitation-hardening type, is one of the most important alloys in the 2XXX series. The AA2024 alloy is commonly

used to make truck and aircraft wheels, truck suspension parts, aircraft fuselage and wing skins, and structural parts requiring good strength at temperature up to 150^{o}C (Féron, 2007; ASM, 1990).

However, the applications of aluminium alloys are greatly hampered by galvanic and/or crevice corrosion especially when used in corrosive environment containing halide ions such as sea water; galvanic and crevice corrosion are the most common types of damage to aluminium structures and equipment (Maria *et al.,* 2007). Sea water contains about 3.4% salt and is slightly alkaline (pH 8). It is a good electrolyte, and can cause galvanic corrosion and crevice corrosion. Corrosion in sea water is affected by oxygen content, velocity, temperature and biological organisms. The rate of corrosion in sea water at greater depths (i.e. 1 mile) is usually slower because of lower temperature and oxygen content (Fontana, 2005).

In the last part of the 20th century, most researches on corrosion were focused on the development and use of new techniques (e.g. electrochemical methods such as Linear Polarisation Resistance, Electrochemical Impedance Spectroscopy**,** Electrochemical Frequency Modulation, Chronopotentiometry, surface analysis and synchrotron radiation techniques), fundamental studies of corrosion phenomena (e.g. passivity and localized corrosion), or the properties of advanced materials e.g. amorphous metals and "stainless" Aluminium alloys (Frankel, 2003).

In the same vein, several attempts have been made in the past to solve corrosion problems of aluminium alloys by some researchers (Baek & Frankel, 2003; Frankel, 2003; Buchheit & Boger, 2002; Bard & Faulkner, 2001; Buchheit *et al.,* 1997; Buchheit, 1995). One of which is the use of corrosion inhibition compounds. Many of these compounds,

especially chromates, have been found to be toxic and costly; hence their use is strictly regulated and often prohibited. Hence, the important need to conduct research towards developing eco-friendly, cheap and non-toxic inhibitors for Aluminium and its alloys lends motivation to this research.

1.2 Statement of Research Problems

Aluminium alloys crack in moist air(susceptible to stress corrosion), halide solutions and sea water, inorganic liquids (e.g Nitric acid), gases (e.g. N_2O_4), organic liquids and organic solvents. Also failures in service have been experienced with wrought high-strength alloys in sea water. Most aluminium alloys suffer a higher rate of attack during the first year especially when exposed to the open atmosphere, but they have developed a weathered surface, the rate of attack decrease except in the case of the 2XXX series and 7XXX series. When immersed in sea water, most aluminium alloys exhibit good corrosion resistance except the 2XXX series which in most cases are protected with a barrier coating or Alclad. This series is particularly at risk of stress-corrosion cracking, especially in thick cross-section (Fontana, 2005; Baek & Frankel, 2003; Frankel, 2003; Buchheit & Boger, 2002; Bard & Faulkner, 2001; Buchheit *et al.,* 1997; Buchheit, 1995; Trethewey & Chamberlain, 1991).

1.3 Justification for the Research Work

The most common causes of damage to structures and equipment fabricated using aluminium and its alloys is galvanic and crevice corrosion. Effort has been made to tackle these problems through selecting suitable alloys for a given application, avoiding dissimilar metals, applying cathodic protection, use of alloys whose potentials are as close as possible in the environment in which they are used, and the use of inhibitors.

It has been established that soluble (hexavalent) chromates are the most effective and widely used inhibitors for controlling the corrosion of aluminium alloys in acidic and basic media (Philip, 2001). However, the toxic properties and environmental costs of chromates are well known, hence their use and disposal are therefore strictly regulated (Cook *et al.*, 2006).

Their high efficiency/cost ratio of chromates has made them standard corrosion inhibitors. Nevertheless due to their oxidizing nature, chromate concentration in a medium must be periodically checked in order to avoid undesirable corrosion, since concentrations lower than a critical value can promote pitting. Even if the chromate content is at an optimum, the presence of reducing agents in solution can cause their concentration to fall below the critical range. Moreover, an upper concentration limit must not be exceeded either in order to maintain their inhibiting properties (Dillon, 1986).

The development of effective and non-toxic alternatives to chromates remains one of the important objectives of the contemporary corrosion research. To date, there are no single inorganic or organic corrosion inhibitors, in terms of offering protection, that match chromates. However, there are many substances and other synergistic blends that have not been evaluated before as possible substitutes for chromates. Maria *et al.* (2007) evaluated the potential of rare earth diphenyl phosphate as potential substitutes for chromates in controlling the corrosion of aluminium alloys in 0.1M NaCl solution. Victoria *et al.* (2006) also used polyphrrole/aluminium flake hybrids as corrosion inhibitors for AA 2024-T3 alloy in alkaline media. These electroactrive conducting

polymers (ECPs) are potential replacement for chromates due to their conductivity and redox properties (Prissanaroon *et al.,* 2004).

Unfortunately, most of these alternative to chromates are easily leached before the onset of corrosion except incorporated with a labile bond that can be disrupted by products released from the corrosion process (Cook *et al.,* 2006).

Thus there is a need to develop alternative corrosion inhibitors with improved longevity, non-toxic and environmentally friendly. This research attempted using some plant extracts impregnated with nanoparticles as substitutes for chromates in corrosion inhibition of AA2024 aluminium alloy in simulated/artificial sea water.

1.4 Aims and Objectives

The major aim of this research was to investigate whether ***Parkia biglobosa*** (African locust bean) and ***Vitex doniana*** sweet (Black plum) leaves extracts impregnated with Boehmite nanoparticles could match the performance of Sodium Chromate as corrosion inhibitors for aluminium alloy AA2024 in artificial sea water (3.5%NaCl). Other objectives of the work included:

1. Evaluation of the corrosion characteristics of AA2024 aluminuim alloy in simulated sea water by gravimetric-based mass loss and electrochemical techniques using Linear Polarisation Resistance (LPR), Electrochemical Impedance Spectroscopy (EIS) and Chronopotentiometry.
2. Investigation of the synergistic effects of the extract-extract and extracts-nanoparticles systems on the corrosion characteristics of AA2024 aluminium alloy in simulated sea water.

3. Determination of the different metabolites in the plant extracts using proton Nuclear Magnetic Resonance (^{1}H NMR)-based metabolomics.
4. Characterization of the test coupons (AA2024 alloys) before and after the corrosion tests using the Scanning Electron Microscopy/Energy Dispersive X-Ray (SEM/EDX), X-Ray Diffractometry (XRD**)** and Raman Spectroscopy.
5. Development of model(s)/mechanism(s) of inhibition by the extracts-Boehmite nanoparticles systems from generated parameters.

1.5 Scope and Limitations of the Research

Electrochemical techniques, using Polarization Resistance (LPR), Electrochemical Impedance Spectroscopy (EIS) and Chronopotentiometry were employed to assess the influence of the extracts and extracts-Boehmite nanoparticles systems on the corrosion behaviour of the cast alloy in simulated sea water at different temperatures (30, 40, 50, 60, and 70°C). The results generated by the electrochemical techniques were compared with those obtained by gravimetric-based mass loss method. Corrosion Behaviour Diagrams (CBDs) were used to represent the results obtained. Models for the adsorption of the extracts-Boehmite nanoparticles systems onto the alloy surfaces were developed. The substrates were characterized using SEM, X-Ray XRD and Raman Spectroscopy.

Some limitations encountered while executing this work were:

1. Electrolyte composition, formed by dissolving 3.5g of NaCl in 100ml of distilled water to simulate sea water. This excluded several other constituents present in natural sea water.

2. The sample size, which was too large to make duplication of results possible.

1.6 Contribution to Knowledge

1. The possibility of using *Parkia biglobosa* (PBE*)* and *Vitex doniana* (VDE) extracts as corrosion inhibitors for high strength Aluminium alloy AA2024 was established through both classical and instrumental techniques. PBE and VDE gave room temperature Inhibition Efficiencies (IE%) of 83.30% and 74.10% respectively; which is within acceptable range of IE% for the alloy.
2. Synergistic combination of *Parkia biglobosa* (PBE) and *Vitex doniana* (VDE) extracts with Boehmite nanoparticles offered better protection and stability of adsorbed layers than other test systems. This was achieved at room temperature and optimum concentration of 30%PBE-20%VDE-0.3g Boehmite nanoparticles. Inhibition Efficiency (IE%) of 92.15% for PBE+VDE+Boehmite Nanoparticles Hybrid system compared favourably with that of Sodium Chromate, the standard/reference inhibitor, which had Inhibition Efficiency (IE%) of 92.57% .
3. The use of Boehmite Nanoparticles to improve Inhibition Efficiency, longevity and stability of adsorbed phytoconstituents of *Parkia biglobosa (PBE)* and *Vitex doniana (VDE*) was also established using chronopotentiomety.
4. The developed ecofriendly and cheap plant-based corrosion inhibitors could also serve as an alternative to un-safe chromates used in the synthesis and formulations of protective organic coatings.

CHAPTER TWO

2.0 LITERATURE REVIEW

2.1 Methods of Approach to Corrosion Phenomena

Shreir *et al.* (2000) reported that the effective use of metals as materials of construction must be based on an understanding of their physical, mechanical and chemical properties. These cannot be divorced from the environmental conditions prevailing. Any fundamental approach to the phenomena of corrosion must therefore involve consideration of the structural features of the metal, the nature of the environment and the reactions that occur at the metal/environment interface. The more important factors involved may be summarised as follows:

1. *Metal*-composition, detailed atomic structure, microscopic and macroscopic heterogeneities, stress (tensile, compressive, cyclic), etc.

2. *Environment-chemical* nature, concentrations of reactive species and deleterious impurities, pressure, temperature, velocity, impingement, etc.

3. *Metal/environment interface-kinetics* of metal oxidation and dissolution, kinetics of reduction of species in solution; nature and location of corrosion products; film growth and film dissolution, etc.

As a first approach to the principles which govern the behaviour of metal in specific environments, it is preferable to disregard the detailed structure of the metal and to consider corrosion as a heterogeneous chemical reaction which occurs at a metal/non-metal interface. Corrosion can be expressed, therefore, by the simple chemical reaction:

$$aA + bB = cC + dD \qquad (2.1)$$

A is the metal and *B* the oxidant, while *C* and *D* are the products of the reaction. The oxidants are usually chemical species in *the environment,* although it should be observed that in a complex environment the major constituents may play a very subsidiary role in the reaction (Shreir *et al.,* 2000).

2.2 Classification of Spontaneous Corrosion Reactions

The main types of corrosion reactions can be classified as follows:

1. Film-free chemical interaction in which there is direct chemical reaction of a metal with its environment. In this case, the metal remains film-free and there is no transport of oxygen.

2. Electrochemical reactions which involve transfer of charge across an interface. These electrochemical reactions can be further subdivided into:

(a) Inseparable anode/cathode type (insep. A/C). The anodes and cathodes cannot be distinguished by experimental methods although their presence is postulated by theory, e.g. the *uniform* dissolution of metals in acid, alkaline or neutral aqueous solutions, in non-aqueous solution, or in fused salts.

(b) Separable anode/cathode type (sep. *A/C)*. Certain areas of the metal can be distinguished experimentally as predominantly anodic or cathodic, although the distances of separation of these areas may be as small as fractions of a millimetre. In these reactions there will be a macroscopic flow of charge through the metal.

(c) Inter facial anode/cathode type (inter facial A/'C). One entire interface will be the anode and the other will be the cathode. Example of this phenomenon is dry corrosion in

which a metal/metal oxide interface might be regarded as the anode and the metal/oxygen interface as the cathode.

2.3 Aluminium and its Alloys

The strategic importance of Aluminium & its alloys and their susceptibilities to certain forms of corrosion are contained in the introductory aspects of this work, chapter one. The elements that are most commonly present in commercial aluminum alloys are copper, magnesium, manganese, silicon, and zinc. These elements all have significant solid solubility in aluminum, and in all cases the solubility increases with increasing temperature. The Figure below shows the Equilibrium binary solid solubility as a function of temperature for alloying elements most frequently added to aluminum.

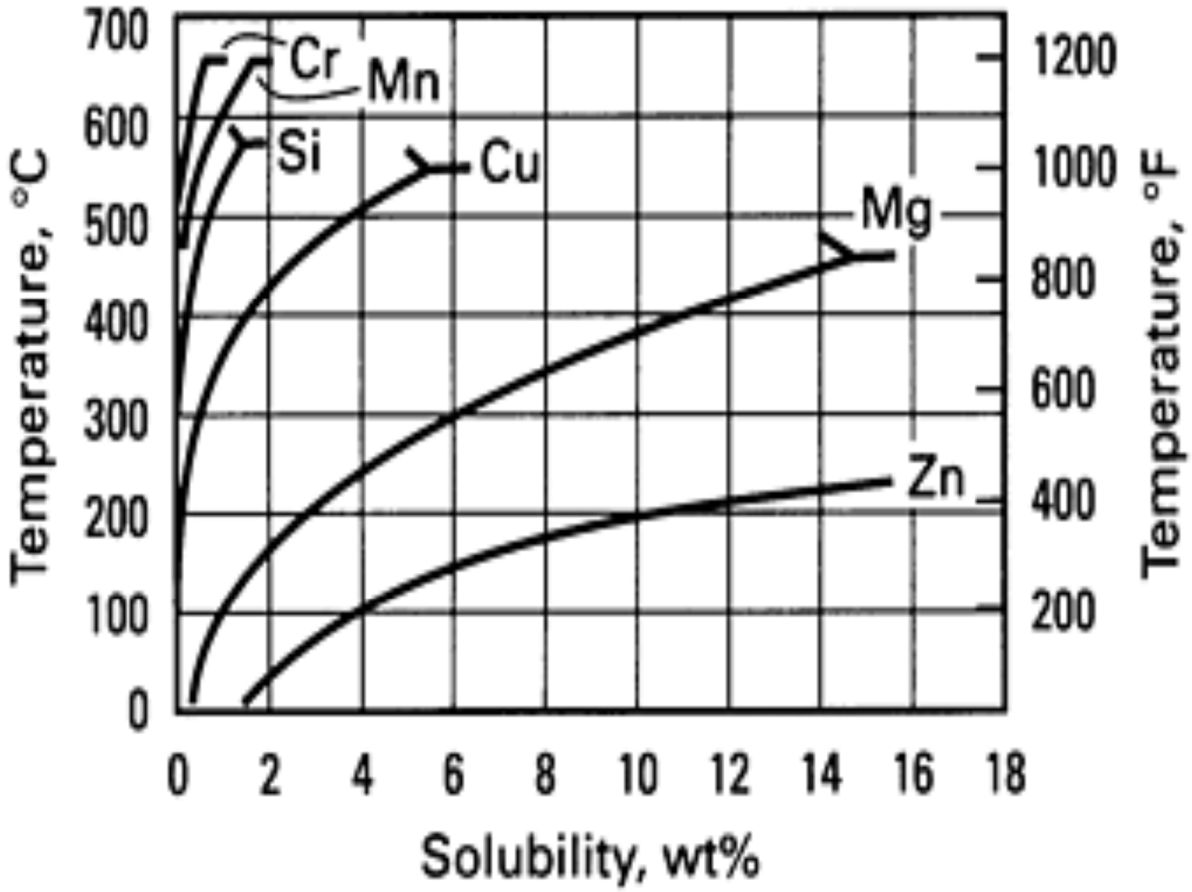


Figure 2.1: Equilibrium binary solid solubility as a function of temperature for alloying elements most frequently added to aluminum (*Source:* ASM Handbook, 1990).

2.4 Classification of Aluminum Alloys

A four-digit numerical designation system is used to identify wrought aluminum and aluminum alloys. The first digit indicates the alloy group, the second represents alloy modification, while the last two of the four digits in the 2*xxx* through 8*xxx* groups have no special significance, but serve only to identify the different aluminum alloys in the group.

Table 2.1: Classification of Wrought Aluminium & Aluminium Alloys

Series	***Major alloying element(s)***
1xxx	99.9%Al
***2xxx**	Cu
3xxx	Mn
4xxx	Si
5xxx	Mg
6xxx	Mg & Si
7xxx	Zn
8xxx	Other elements
9xxx	Unused

(*Source:* ASM Handbook, 1990).

*Copper is the principal alloying element in **2*xxx* s**eries alloys, often with magnesium as a secondary additive. These alloys require solution heat treatment to obtain optimum properties. In some instances, precipitation heat treatment (aging) is employed to further increase mechanical properties. This treatment increases yield strength, with attendant loss in elongation.

The alloys in the 2*xxx* series do not have as good corrosion resistance as most other aluminum alloys, and under certain conditions may be subject to intergranular corrosion. Therefore, these alloys in the form of sheet are usually clad with high-purity aluminum or

with a magnesium-silicon alloy of the 6*xxx* series, which provides galvanic protection of the core material. Alloys in the 2*xxx* series are particularly well suited for parts and structures requiring high strength-to-weight ratios and are commonly used to make truck and aircraft wheels, rivets, hardware, truck wheel and suspension, screw machine, aircraft fuselage and wing skins, structural and those parts requiring good strength at temperatures up to 150 °C. Except for alloy 2219, these alloys have limited weldability, but some alloys in this series have good machinability (ASM Handbook, 1990).

In particular, Alloy AA2024 has a density of 2.78g/cm^3, Electrical conductivity of 30% IACS, Young's modulus of 73GPa (10.6Msi) across all tempers and begins to melt at 500^{o}C. The non-heat treated AA2024 has a maximum tensile strength of 207-220Mpa, a maximum yield strength of no more than 14,000 Psi (96mPa) and elongation (stretch before ultimate failure) of 10-25%. This is the allowable range per applicable AMS specifications (Materials Performance Data, 2010).

2.5 Corrosion of Aluminium and its Alloys

There are several forms in which corrosion manifests. These include uniform attack, galvanic, crevice, intergranular, pitting, and Stress Corrosion Cracking (SCC). Specifically, corrosion of Aluminium and its alloys manifest in form of uniform, pitting, galvanic, intercrystalline, stress, filiform and layer corrosion (Shreir *et al.,* 2000).

Though the exact mechanisms governing corrosion of aluminium alloys are not completely understood, it is thought that the corrosion of most Aluminium/Copper alloys proceed through the following reactions:

Neutral/Alkaline/Basic Medium

At Anode

$$Al \longrightarrow Al^{3+} + 3e^- \quad (2.2)$$

At Cathode

$$O_2 + 2H_2O + 4e^- \longrightarrow 4OH^- \quad (2.3)$$

overall

$$4Al + 3O_2 + 6H_2O \longrightarrow 4Al^{3+} + 12OH^- \quad (2.4)$$

Acidic Medium

At Anode

$$Al \longrightarrow Al^{3+} + 3e^- \quad (2.5)$$

At Cathode

$$2H^+ + 2e^- \longrightarrow H_2\uparrow \quad (2.6)$$

Overall

$$2Al + 6H^+ \longrightarrow 2Al^{3+} + 3H_2\uparrow \quad (2.7)$$

A general mechanism for the dissolution of Al metal in the presence of aqueous chloride solution has earlier been postulated by Ebenso *et al.* (2008) as follows:

$$Al(s) + H_2O \longrightarrow AlOH_{ads} + H^+ + e^- \quad (2.8)$$

$$AlOH_{ads} + 5H_2O + H^+ \longrightarrow Al^{3+} + 6H_2O + 2e^- \quad (2.9)$$

$$Al^{3+} + H_2O \longrightarrow [AlOH]^{2+} + H^+ \quad (2.10)$$

$$[AlOH]^{2+} + X^- \longrightarrow [AlOHX]^+ \quad (2.11)$$

The controlling step in the metal dissolution is the complexation reaction between the hydrated cation and the anion present.

In the presence of chloride ions, the reaction will correspond to:

$$[AlOH]^{2+} + Cl^{-} \longrightarrow [AlOHCl]^{+} \quad (2.12)$$

The high strength AA2024 Aluminium alloy contains 93.74%Al-4.25%Cu-1.30%Mg-0.48%Mn-0.01%Ni-0.22%Fe (Baldini *et al.*, 1995); though other researchers (Khoshnaw & Gardi, 2007; Clarke & Varney, 1952) reported different chemical compositions from the one cited by Baldini *et al.* (1995). Generally, the corrosion behaviour of this alloy depends strongly on the cathodic activity of Cu-rich intermetallic particles such as □ phase (Al_2Cu), S phase (Al_2CuMg), and particles of varying composition containing Al, Cu, Mn, and Fe (Dimitrov *et al.,* 2000; Buchheit, 1995). During the corrosion of AA2024, Cu-containing intermetallic compounds (IMCs) act as preferred cathodic sites for oxygen reduction while the anodic sites are active S-phase particles and the Al matrix (Schmutz & Frankel, 1998). Reduction reactions at the cathodic sites lead to the development of high pH zones near IMCs and the surrounding region. The increased local pH promotes dissolution of the Al matrix near the cathodic IMCs, causing localized attack at the periphery of Cu-containing intermetallic particles, and may also result in dealloying of IMCs themselves (Ilevbare & Scully, 2001; Buchheit *et al.,* 1997).

2.6 Electrical Double Layer

When a metal *M* is immersed in an electrolyte, it oxidizes at a relatively high rate and subsequently the oxidation (dissolution) process gradually ceases and eventually stops due to build-up of charges on the metal surface. Thus, the dynamic equilibrium is attained, provided that no other complex electrochemical reactions take place. In this process, metal atoms are removed from their lattice sites to ionize as cations (M^{n+}) into the electrolyte, forming a negatively charge metal surface. If polar water molecules (H_2O) and hydrogen cations (H^+) are in the electrolyte, they are attracted by the negatively

charged metal surface to form an ionic structure (layer) which prevents other ions from the bulk solution to be part of it. This structure is a complex ionic arrangement in an electric field and has a limited thickness. Eventually, metal dissolution ceases if there is no external current flow, but it proceeds until the ionic structure is dense enough to protect and prevent the metal from reacting any further until equilibrium is reached. The ionic structure is known as the **Electrical Double Layer** (***EDL***). There are different models for explaining the interfacial structure of the electrical double layer. This layer is referred to as the Helmholtz layer which behaves like a charged capacitor. Figure 2.2 below shows an electrical double-layer model.

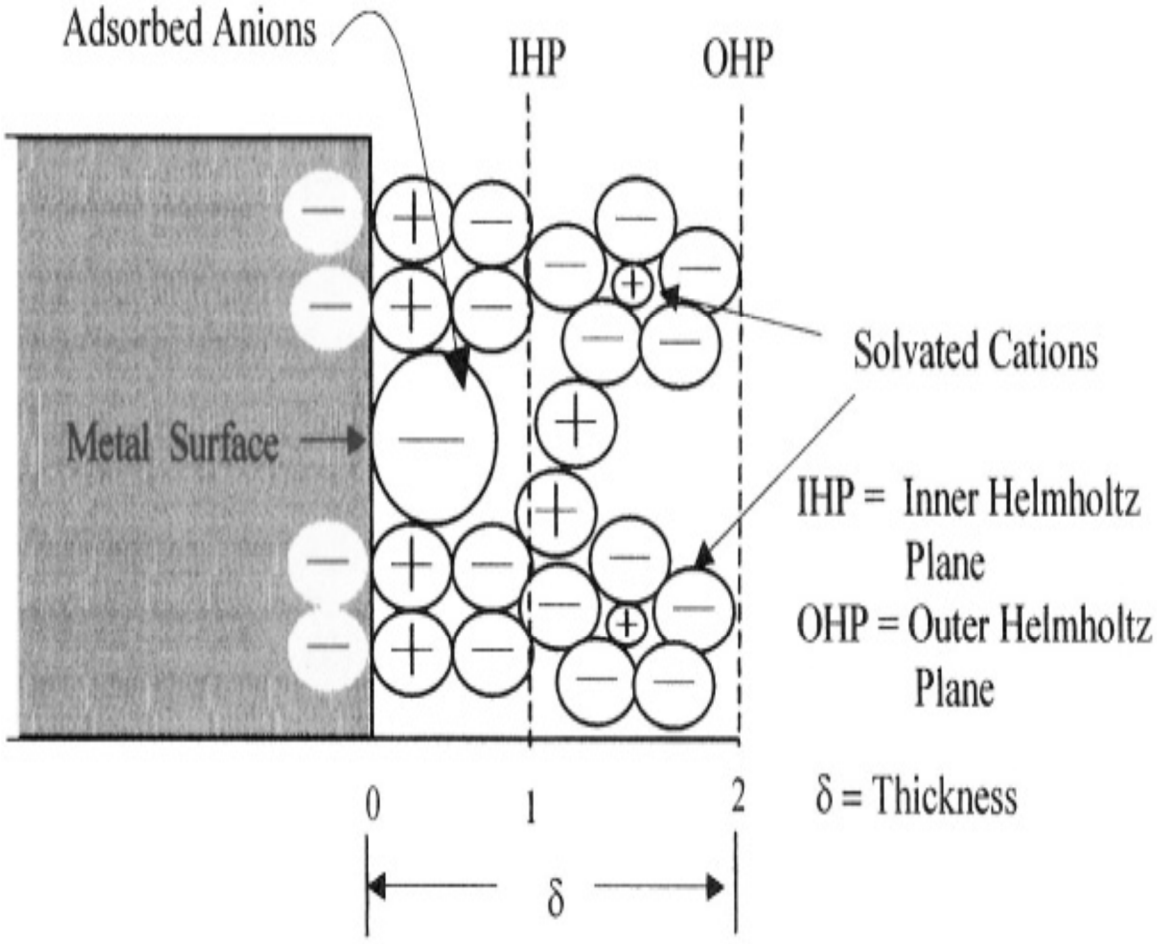


Figure 2.2: Schematic Electrical Double Layer (*Source*: Nestor, 2004).

This model indicates that some negatively charged ions are adsorbed on the metal electrode surface and polar water covers the rest of its surface, forming a protective layer. The positively charged hydrogen ion is in contact with the negatively charged metal surface (Erdey-Gruz, 1972 & Barlow, 1970). Thus, one can conclude that:

i) The **Inner Helmholtz Plane** (IHP) is an ionic layer that consists of adsorbed dipole water molecules. The majority of the anions do not penetrate this layer; some do as indicated in Figure 2.2. The inner potential on the boundary of this ionic plane is ϕ_1

ii) The **Outer Helmholtz Plane** (OHP) consists of a plane of adsorbed ions due to electrostatic forces in contact with a diffuse ionic layer at an inner potential ϕ_2

iii) The **Diffuse Layer** (DL), denoted by ϕ_3, is a thick layer located in a region of diffusely distributed ions in contact with the OHP and the bulk of solution at a potential.

2.7 Influence of Corrosion Product Deposits

Inevitably, corrosion is not a process that proceeds by straightforward, uncomplicated active dissolution, especially over extended exposure periods. Reactive materials (e.g., Fe, carbon steel, Cu, UO_2) corroding in neutral to slightly alkaline solutions ($4<pH< 9$) where oxide/hydroxide solubilities are low, tend to accumulate corrosion product deposits. These deposits will form at a rate determined by the corrosion rate of the material and the solubility of the deposit in the environment. Predicting their rate of thickening and their ability to attenuate the corrosion rate of the substrate material could be a complicated procedure. If it is assumed that the deposit is electrically insulating, this

limits the available anodic and cathodic sites to the material surface at the base of the pores.

If it is assumed also that steady-state conditions exist within the deposit, then the only film parameter that changes as corrosion progresses will be the thickness of corrosion products. As indicated in Figure 2.3, the influence of chemical parameters within the deposit (especially pH effects) is likely to separate the corrosion site (at the material/deposit interface) from the site at which the deposit forms (deposit/environment interface). Consequently, diffusion processes within the porous deposit must be involved if corrosion is to be sustained (Robert *et al*., 2003).

If a more general model is accepted, in which the corrosion product deposit is considered as a tortuous but continuous network of interconnected pores, as contained in Figure 2.4, then the diffusion path length can be significantly greater than the film thickness. Thus the key parameters influencing the corrosion rate under deposits will be the deposit porosity (ε) which determines the available surface area of material for corrosion, and the deposit tortuosity, which along with porosity will modify the fluxes of diffusing species within pores (Robert et al., 2003).

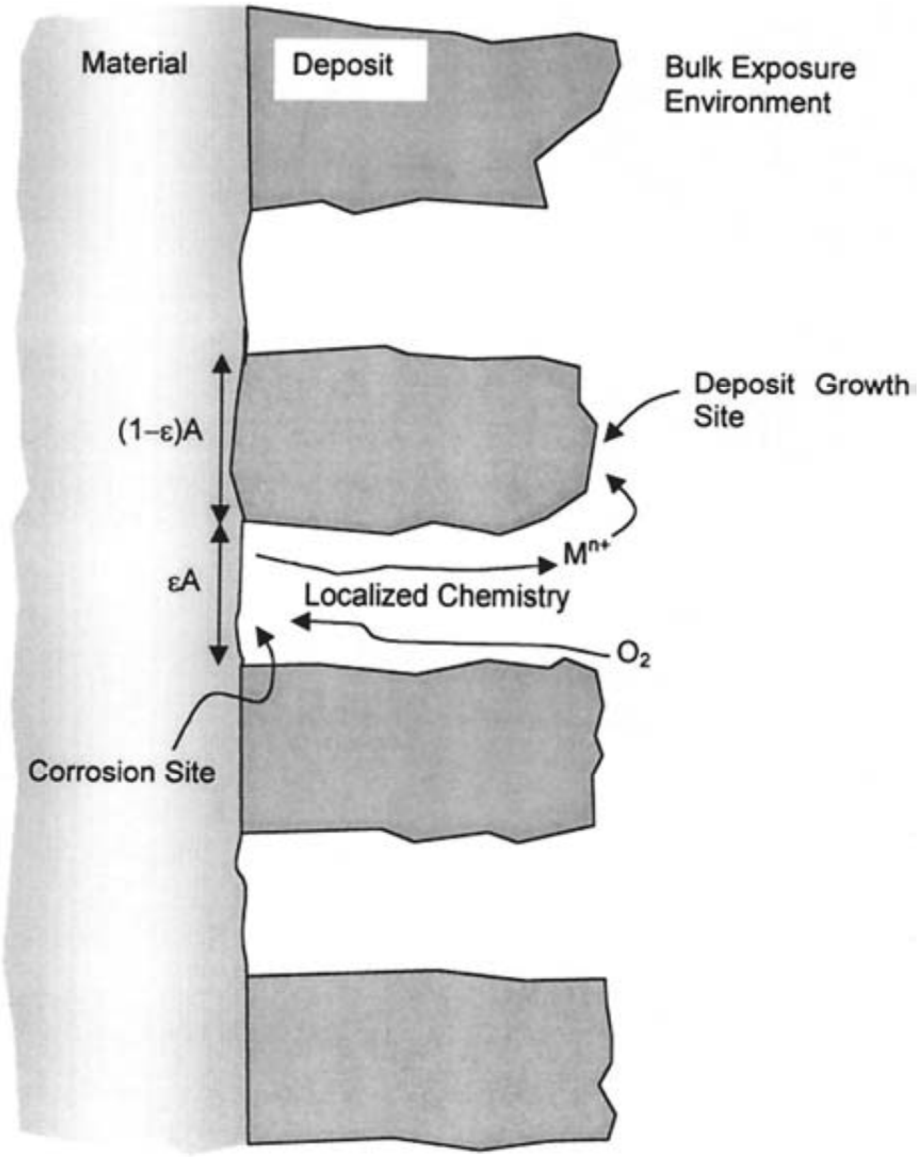


Figure 2.3**:** Schematic of an idealized corrosion product deposit on a corroding surface; *l* is the pore length, ε*A* the fraction of the surface area exposed to the corrosion environment; (1-ε*A*) is the fraction of the surface blocked by corrosion product deposit.

(*Source*: Robert *et al*., 2003).

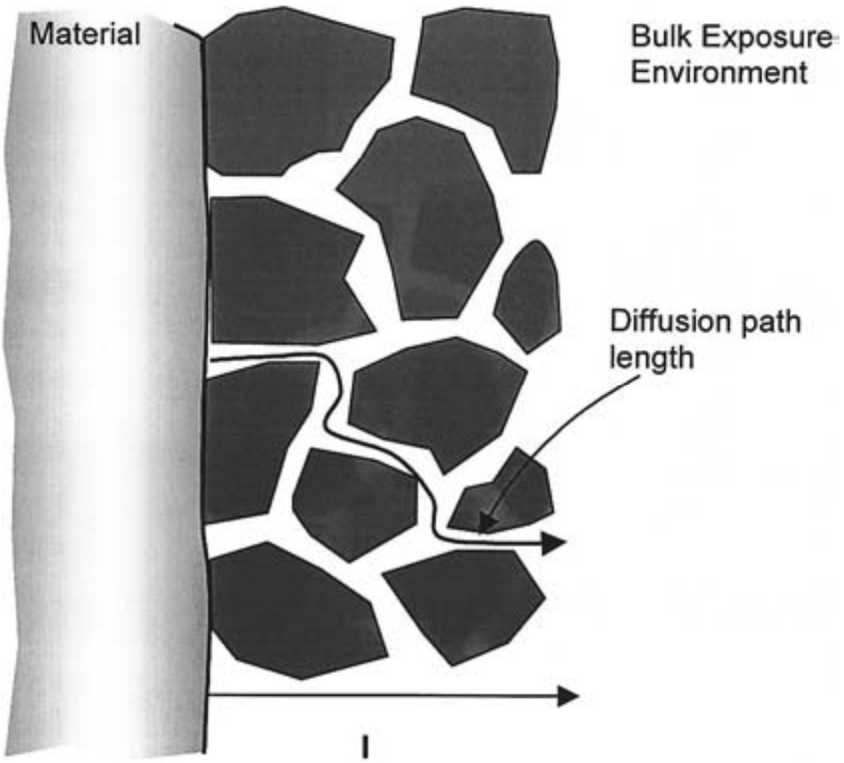


Figure 2.4: Schematic showing a corrosion product deposit composed of interconnected tortuous pores illustrating that the diffusion path length of dissolved species or dissolved oxidant through the deposit is greater than the thickness of the deposit (*Source*; Robert *et al*., 2003).

2.8 Thermodynamics and Kinetics of Corrosion

2.8.1 Thermodynamics of Corrosion; Pourbaix (*E/pH* Equilibrium) Diagrams

Thermodynamics provide a means of predicting the *equilibrium state* of a system of specified components, but provides no information on the detailed course of the reaction nor of the rate at which the system proceeds to equilibrium.

Pourbaix and his co-workers have calculated the phases at equilibrium for metal-water, M/H_2O, systems at 25^0C from the chemical potentials of the species involved in the equilibria, and have expressed the data in the form of *equilibrium diagrams* having

E vs pH., the *equilibrium potential (vs.* S.H.E.) as ordinates. These diagrams, which are analogous to the composition-temperature diagrams of alloy systems, provide a thermodynamic basis for the study of corrosion reactions, although, as emphasised by Pourbaix, their limitations in relation to practical problems must be appreciated (Pourbaix, 1973; Pourbaix, 1962). A typical Pourbaix diagram for Aluminium-H_2O system at 25^oC is shown in Figure 2.5.

The objective is to represent the relative stabilities of solid phases and soluble ions that are produced by reaction between a metal and an aqueous environment as functions of two parameters, the electrode potential, *E*, and the pH of the environment. The presentation of information in this format facilitates its application to practical problems in a wide variety of situations; including corrosion, electrodeposition, geological processes, and hydrometallurgical extraction processes.

2.8.2 Kinetics of Corrosion

The thermodynamic tendency of metals to corrode is frequently outweighed by kinetic factors that control the rate of the process so that the final position of equilibrium, i.e. complete conversion to corrosion product, is attained only slowly or not at all. The rate (or kinetics) and form of corrosion reaction will be affected by a variety of factors associated with the metal and the metal surface (which can range from a planar outer surface to the surface within pits or fine cracks), and the environment.

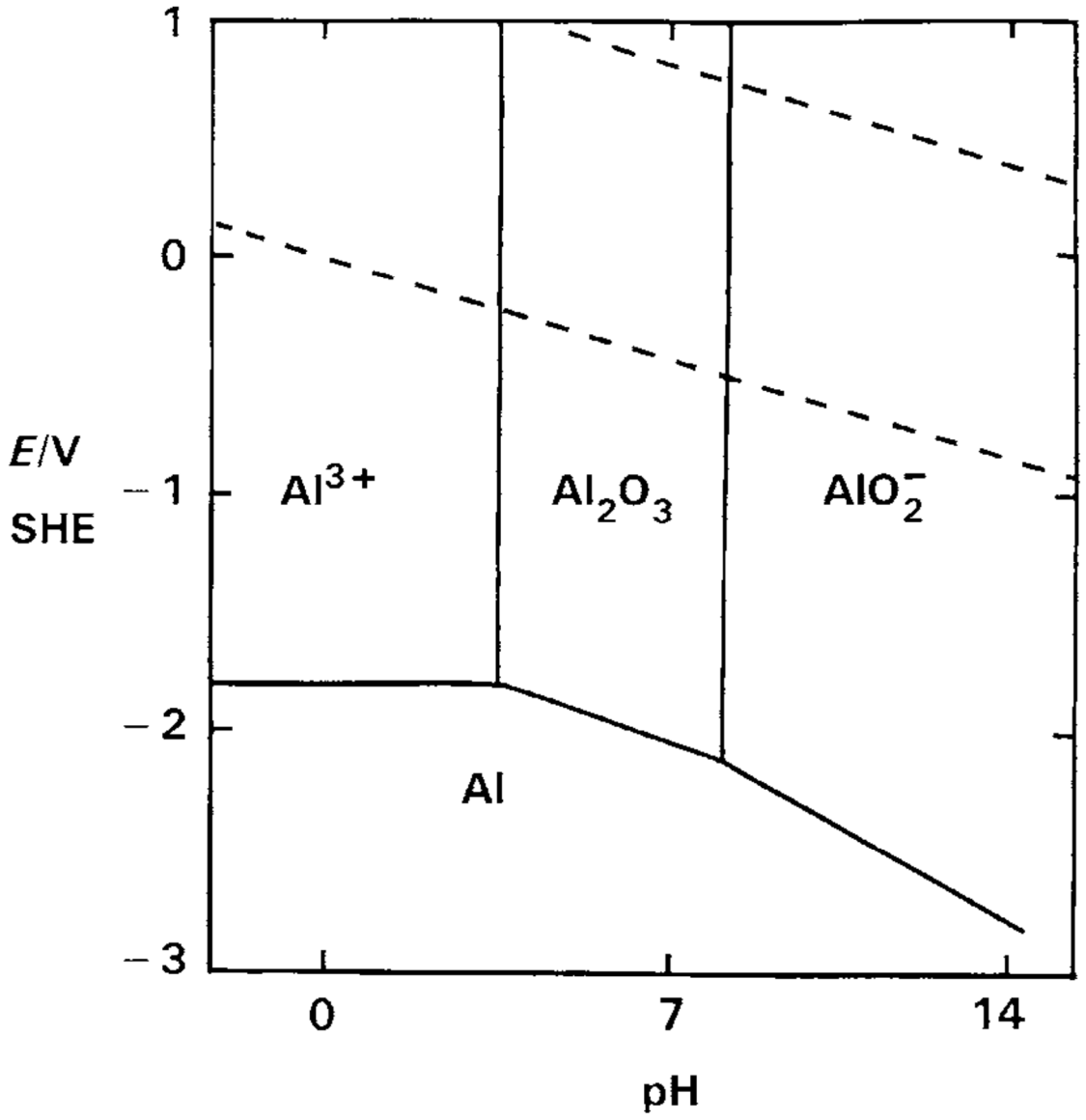


Figure 2.5: Pourbaix diagram for the Aluminium-water system at 25°C showing nominal zones of immunity, passivity and corrosion (*Source:* Pourbaix, 1962).

The rate of any transformation is controlled by the magnitude of one or more energy barriers that every chemical specie, e.g. an atom or ion, must surmount to transform to some product. These peaks are the energy maxima of intermediate transition states through which the entity must pass in transforming and the energy that must be acquired is the *activation energy*, ΔG.

The statistical distribution of energy among the particles ensures that at any instant a small but significant fraction of the particles has sufficient energy to surmount the peaks. This fraction and hence the fraction of particles transforming in a small time span, *the reaction rate*, *r*, depends on the value of the activation energy. An expression for reaction rate that applies to many reactions over moderate temperature ranges is Arrhenius' equation:

$$r = A\exp^{-\Delta G/RT} \tag{2.13}$$

To apply the equation to an electrode process, it must be restated in electrical terms. Ions transported across an electrode carry electric charge, so that the reaction rate, *r* in equation 2.13, can be replaced by an electric current, *i*. The energy of the process is the product of the charge and the potential drop, *E*, through which it is carried. Thermodynamic quantities are expressed per mole of substance and because the charge on a mole of singly charged ions is the Faraday, *F* = 96490 coulombs, the non-equilibrium free energy change, ΔG of an electrode process is:

$$\Delta G = -zFE \tag{2.14}$$

z is the charge number on the particular ion species transferred in the process.

Replacing *r* with *i* in the Arrhenius equation (equation 2.13), and considering standard condition;

$$i = K\exp^{-\Delta G^*/RT} = K\exp^{-zFE*/RT} \tag{2.15}$$

ΔG^* and E^* represent standard free energy and standard electrode potential respectively (i.e., $\Delta G^* = -zFE^*$).

The enthalpy of activation (ΔH_a) and the entropy of activation (ΔS_a) for the corrosion could be obtained by an alternative formulation of Arrhenius equation where h is Planck's constant and N is Avogadro's number. A plot of ln (i_{corr} /T) against 1/T gives a straight line with a slope of $\Delta H_a/R$ and an intercept of ln $R/Nh + \Delta S_a/R$ from which the values of ΔS_a and ΔH_a could be calculated (Lebrini *et al*., 2010).

$$I_{corr} = \frac{RT}{Nh}\exp\left(\frac{\Delta S_a}{R}\right)\exp\left(\frac{-\Delta H_a}{R}\right) \quad (2.16)$$

Tang *et al*. (2003) studied the effect of Methylene blue on the corrosion rate of mild steel in acidic medium and reaffirmed that the logarithm of the corrosion rate (log r) could be represented as a straight line function of 1/T of steel in acid medium:

$$\ln r = -\frac{E_a}{RT} + \ln A \quad (2.17)$$

r is the corrosion rate
E_a the apparent activation energy
R the universal gas constant
T the absolute temperature
A is the pre-exponential factor.

Vashi & Champaneri (1997) calculated the values of activation energy (E_a) using the Arrhenius equation:

$$\ln\left(\frac{r_2}{r_1}\right) = \left(\frac{E_a \Delta T}{RT_1T_2}\right) \quad (2.18)$$

r_1 and r_2 are corrosion rates at temperatures T_1 and T_2 respectively; $\Delta T = T_2 - T_1$.

Khamis (1990) evaluated the standard adsorption free energy (ΔG^0) by employing the following equation:

$$K = \left(\frac{1}{55.5}\right)\exp\left(\frac{-\Delta G^0}{RT}\right) \quad (2.19)$$

The free energy of adsorption (ΔG_{ads}) at different temperatures could be calculated, according to Rodosovic *et al.* (1995), using the equation:

$$\Delta G_{ads} = -RTln(55.5K) \quad (2.20)$$

$$K = \frac{\theta}{c(1-\theta)} \quad (2.21)$$

θ is the degree of coverage on the metal surface,
c is the concentration of inhibitor
K is the adsorptional equilibrium constant.
55.5 is the concentration of water in solution expressed in molar.

The standard free energy of adsorption, ΔG_{ads}, characterizes the interaction of adsorption molecules and metal surface. It is related with water adsorption/desorption equilibrium. Negative values of ΔG_{ads} ensure the spontaneity of adsorption process and stability of the adsorbed layer on the electrode surfaces. Generally, ΔG_{ads} values of around -20kJ/mol or lower are consistent with strong electrostatic interactions between inhibitor molecule and the metal surface which signifies physical adsorption (Physisorption), while those around -40kJ/mol or higher involve chemisorptions (Obot *et al*., 2009).

The standard entropy ΔS^0 can be calculated according to the basic thermodynamic equation:

$$\Delta G^0 = \Delta H^0 - T\Delta S \quad (2.22)$$

Tang *et al*. (2003) used the modified Vant Hoff equation below in evaluating the corrosion inhibition of Methylene blue in HCl acid medium:

$$1\text{n K} = \frac{-\Delta H}{RT} + \quad \text{constant} \tag{2.23}$$

The heats of adsorption, Q_{ads}, for the various inhibited systems could be calculated using the following equation (Bhajiwala & Vashi, 2001; Ekpe *et al*., 1995):

$$\text{Q}_{\text{ads}} = 2.303\text{R}\{\log\left(\frac{\theta_2}{1-\theta_2}\right) - \log\left(\frac{\theta_1}{1-\theta_1}\right)\}\frac{\text{T}_1\text{T}_2}{\text{T}_2-\text{T}_1} \tag{2.24}$$

θ_1 and θ_2 are the surface coverages at temperatures T_1 and T_2 respectively.

The nature of adsorption depends on Q_{ads} values; if the value of Q_{ads} is less than 10 KJ/mol, the adsorption is probably physical in nature and if Q_{ads} value is greater than 10 KJ/mol, the adsorption is adjudged to be chemical (Adeyemi, 2005).

2.9 Polarization

When a metal is not in equilibrium with a solution of its ions, the electrode potential differs from the free corrosion potential. In this process, the deviation from equilibrium causes an electrical potential difference between the polarized and the equilibrium (unpolarized) electrode potential. The shift in potential is called polarization and its value, **η,** is the overpotential. Thus, electrode reactions are assumed to induce deviations from equilibrium due to the passage of an electrical current through an electrochemical cell causing a change in the working electrode (*WE*) potential.

Polarisation is an extremely important corrosion parameter which enables useful statements to be made about the rate of corrosion processes. Consider the dissolution of a metal M represented by equation 2.25, if the equilibrium at an electrode is disturbed, a

net current flows across its surface displacing the potential in a direction and to an extent depending on the direction and magnitude of the current.

$$M \longrightarrow M^{z+} + ze^{-} \qquad (2.25)$$

There are three possible components of polarisation; ***activation***, ***concentration,*** and ***resistance*** polarization. Figure 2.6 is a Schematic activation activation free energy distribution for polarized and equilibrium state.

2.9.1 Activation Polarization

Activation polarization is a manifestation of the relative changes in the activation energies for dissolution and deposition, when equilibrium is disturbed. It is always a component of the total polarization, whether or not there are also significant contributions from concentration and resistance effects. The polarization is positive, i.e., *anodic*, or negative, i.e., *cathodic*, according to whether the net current is a dissolution or deposition current.

The relationship between reaction rate and overvoltage for activation polarisation is given by equation 2.26 below;

$$\eta_a = \pm \beta \log \frac{i}{i_0} \qquad (2.26)$$

$\boldsymbol{\eta_a}$ is the overvoltage,

$\boldsymbol{\beta}$ is a constant, and

$\boldsymbol{i}$ is the rate of oxidation or reduction in terms of current density.

The equation is called Tafel equation, and $\boldsymbol{\beta}$ is termed "**β slope"** or **Tafel constant.**

The value of $\boldsymbol{\beta}$ for electrochemical reactions ranges between 0.05 and 0.15 volt. In general, the value of $\boldsymbol{\beta}$ is usually 0.1 volts.

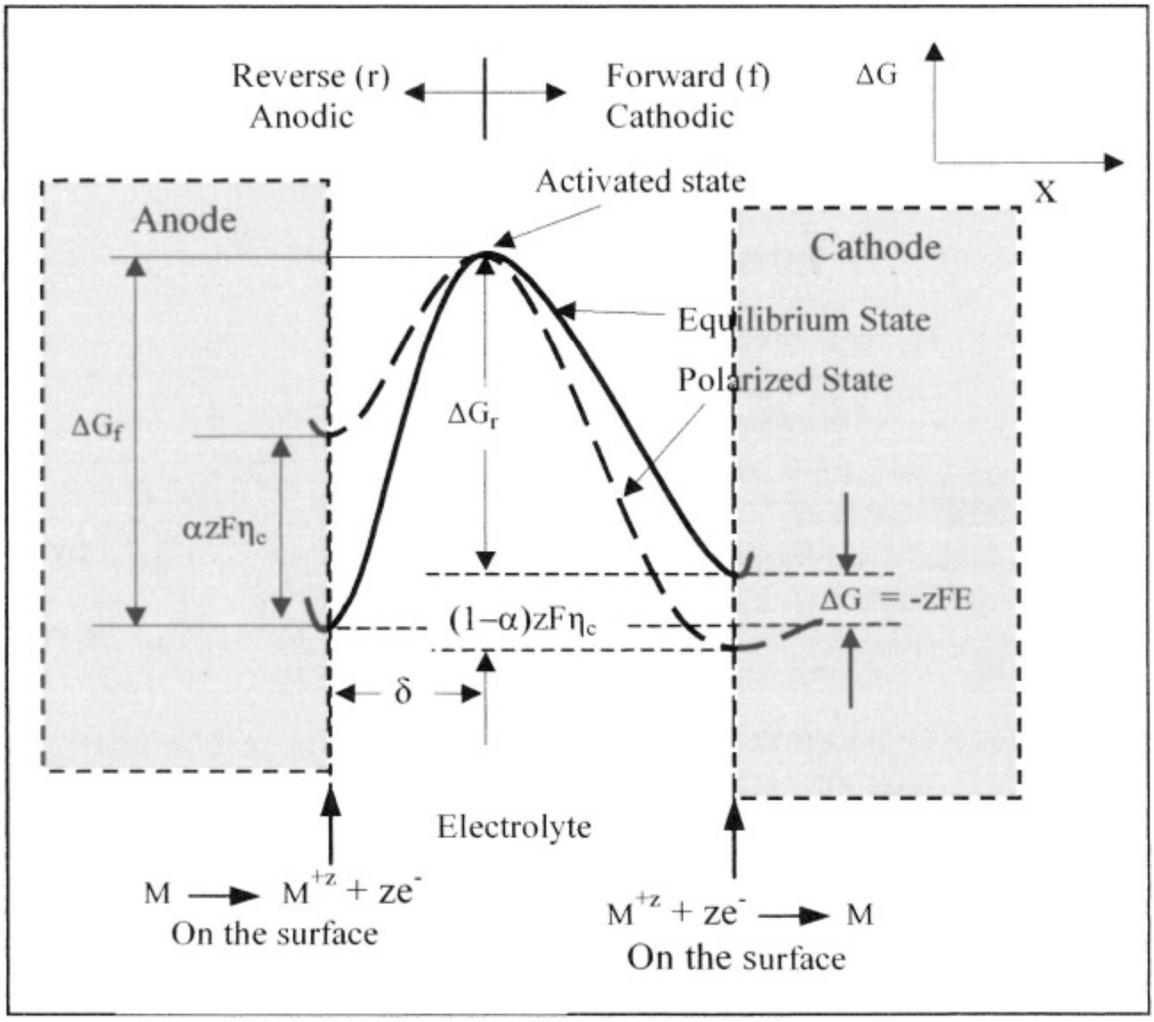


Figure 2.6: Schematic activation activation free energy distribution (*Source:* Nestor, 2004).

2.9.2 Concentration Polarization

As the potential of an electrode is altered further and further away from its equilibrium potential, the net current flowing, whether anodic, i_a , or cathodic, i_c, increases at first according to the Tafel equation. However, the current cannot be increased indefinitely because there are limits to the rate at which ions can carry charges through the solution to and from the electrode. This results in an excess potential over that predicted by the Tafel equation. The situation is illustrated in Figure 2.7. The effect arises because ions are

produced or consumed at the electrode surface faster than they can diffuse to or from the bulk of the solution. In an anodic reaction, the concentration of ions in the immediate vicinity of the electrode is raised above that in the bulk solution; conversely, in a cathodic reaction, the local concentration is depressed. As a consequence, the polarization for a given current is greater than that predicted by the Tafel equation. The excess potential is called the ***concentration polarization***, $\boldsymbol{\eta_C}$.

If we consider an electrode in which there is no activation polarisation, then the equation for concentration polarisation is

$$\eta_c = 2.3\frac{RT}{nF}\log\left(1 - \frac{i}{i_l}\right) \qquad (2.27)$$

i_l is the limiting diffusion current density

2.9.3 Resistance Polarization

In discussing activation and concentration polarization, no account was taken of ohmic resistances. For some electrode reactions, the effects of ohmic resistance can be very considerable. If a greater resistance to the flow of current is offered, the rate of corrosion is reduced. This is especially significant when the reaction, itself or a complementary reaction, produces films on the electrode surface. This type of Polarisation, caused by the electrical resistivity of the electrolyte resulting to total potential drop, is called ***Resistance Polarization***, $\boldsymbol{\eta_R}$. The degree of resistance polarisation may change as the composition of the electrolyte changes during corrosion process.

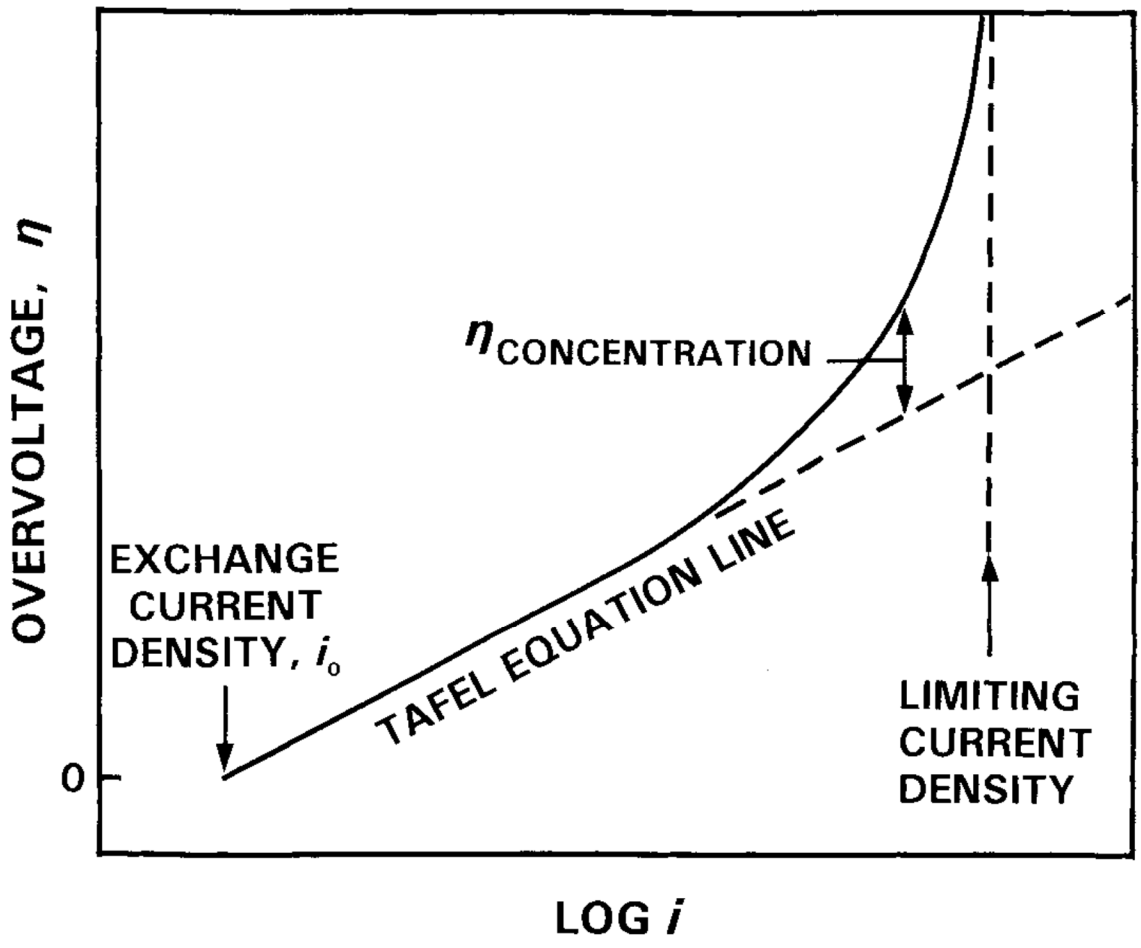


Figure 2.7: Logarithmic plot of current density, ***i*****, v.** overvoltage, **η,** for a polarized electrode, showing deviation from Tafel line and limiting current density due to concentration polarization. **η** is positive for an anodic current, i_a, and negative for a cathodic current, i_c (*Source:* David and James, 1998).

The total polarization at an electrode is therefore the sum of three components; activation, concentration and resistance polarization:

(2.28)

The effects of these forms of polarization are illustrated by the characteristics of hydrogen evolution and oxygen reduction reactions that feature prominently in corrosion processes.

2.10 Corrosion Prevention and Control Techniques

Even with the proper selection of base metals and well-designed systems or structures, there is no absolute way of eliminating all corrosion problems. Therefore, corrosion protection methods are used to additionally mitigate and control the effects of corrosion. Corrosion protection can be in a number of different forms/strategies with perhaps multiple methods applied in severe environments. Types of corrosion protection methods include proper design of structures, materials selection, use of galvanically compatible metal/alloy systems, environmental and process control, cathodic and anodic protection, surface treatments, the use of coatings and sealants and chemical treatment (inhibitor applications) (Benjamin *et al*., 2006).

2.11 Corrosion Inhibitors

The method of prevention of metal corrosion based on the use of corrosion inhibitors i.e., chemical compounds which, when present in a system at sufficient concentrations, decrease the corrosion rate has been known for several centuries (ISO, 1989). However, it was only in the middle of the twentieth century that a scientific concept about the mechanism of inhibition was known and first achievements in the direct synthesis of inhibitors was established (Kuznetsov, 2004).

Corrosion inhibitors are used in numerous systems, from water supply systems to the protection of microelectronics and contemporary military equipment. Considering that losses from metal corrosion exceed 5% of the Gross National Product in industrial countries, the application of inhibitors, which is one of the main methods of corrosion protection, should be considered as a scientific and engineering task of current interest (Kuznetsov, 2004).

2.11.1 Classification of Inhibitors

Evans (1960) simply classified corrosion inhibitors depending on whether their actions cause a decrease of the anodic reaction (oxidation-generally termed the corrosion reaction) or the cathodic reaction (reduction-hydrogen evolution or oxygen reduction reaction).

Uhlig (1963) established that there are several classes of inhibitors conveniently designated as follows: (i) Passivators (ii) Organic inhibitors (iii) Vapor phase inhibitors. Uhlig's position was corroborated by Kirk (1989) who reported that inhibitors may be classified into inorganic, organic or vapor-phase. He then noted that inorganic inhibitors may function by a mechanism different from organic or vapor-phase.

Fisher (1971) advanced a more complex classification of inhibitors based on the specific mechanism by which they achieve inhibition: interface-inhibition and electrolyte-layer inhibition. It was further suggested that interface inhibition results from substances which are adsorbed at the metal surface and decrease the rates of physical, chemical or electrochemical processes in the corrosion mechanism, while electrolyte-layer inhibition arises if an inhibitor interferes with processes which are not on the metal surface but in its vicinity such as the electrolyte layer closest to the metal surface. Fontana (2005) classified inhibitors into the following: adsorption-type, Oxidizers, hydrogen evolution poison and scavengers. Corrosion inhibitors are also classified into **Synthetic** and **Natural** corrosion inhibitors.

2.11.1.1 Synthetic corrosion inhibitors

Antropov (1972) asserted that the most commonly used inhibitors for neutral solutions are inorganic compounds of the anionic type and that corrosion inhibitors for acid

solutions are almost exclusively organic substances in the form of amino, imino, carboxyl, carbonyl and thiol groups.

Ekpe *et al.* (1995) and Onuchukwu (1990) reported the effect of organic compounds with functional groups containing hetero-atoms of oxygen (O), Sulphur (S) and Nitrogen (N), on the corrosion behaviour of steel mainly in the acid environment and concluded that these atoms adsorb onto the steel surface, thereby forming a thin film which protects the steel from acid attack.

Protection efficiency of organic inhibitors is attributed mainly to the presence of a polar group acting as an active center for adsorption on the metallic surface (Gomma and Wahdan, 1994).

Kuznetsov (1996) reported that the majority of adsorption inhibitors are organic compounds and that many researchers used the linear free energy (LFE) relationship to reveal the role of the inhibitor structure.

Martinez and Stern (2003) established that most of the well-known acid inhibitors are organic compounds that contain Nitrogen, Sulphur, Oxygen and multiple bonds in the molecules through which they adsorb onto the metal.

Tang *et al.* (2003) stated that efficient inhibitors should possess plentiful π-electrons and unshared electron pairs on either Nitrogen atoms or Sulphur atoms of the inhibitor to the d-orbitals of Iron, and by means of transference of electrons chemical adsorption may occur on the steel surface. Thus, corrosion may be suppressed by the protective film on the steel surface.

Bouklah *et al.* (2005) investigated the inhibitive ability of some organic compounds and found that those containing electronegative functional groups and π-electrons in triple or conjugated double bonds are usually good inhibitors; heteroatoms such as Sulphur, Phosphorus, Nitrogen and Oxygen as well as aromatic ring in their structures are the major adsorption centers. It was concluded that the inhibitive effect was enhanced by several Nitrogen-containing organic compounds.

Sing (1993) and Abd-El-Nabey *et al.* (1986) established that organic compounds containing both N and S atoms are of particular interest as they give better inhibition efficiency than those containing N or S alone. Among these are thiourea derivatives, which are found to be toxic and induce permeation of Hydrogen into the metal, causing Hydrogen embrittlement (Schmit, 1984).

Chromates have been used since early 1900s as means to control the corrosion of active metals. However, in 1982, the Environmental Protection Agency (EPA) has increasingly limited the use of chromate and other chromium containing compounds due to their carcinogenic effects; the hexavalent chromate is reduced to pentavalent chromate which causes the DEOXYRIBONUCLEIC ACID (DNA) damage (Cook *et al.,* 2006).

A number of studies have been undertaken concerning the suitability of various inhibitors as replacements to hexavalent chromates. Onochukwu and Oppong (1986) established that P-quinone and acetic acid could be used as inhibitors of aluminium in acidic and alkaline media. The use of diamines, carboxylic acids, complexons such as zinc phosphate, oxalates, morphine and Thiosemi-carbozide derivatives as corrosion inhibitors were reported by Al-Suhybani (1990); Moussa & El-Tagoury (1990); Wilhemsen & Grande (1988); Bairamow (1985).

Babaqi *et al.* (1989) found that 4-phenyl-1-acetophenone-3-thiosemicarbazone inhibits corrosion of aluminium in trichloro-acetic acid (TCA) at different temperatures using weight loss technique. It was reported that the efficiency increases with increasing organic additive concentration up to 7.5 x 10^{-5} M, and the maximum efficiency obtained was 87.7%, while the aluminium surface was completely covered with inhibitor molecules. However, increased additive concentration led to decrease in inhibitor efficiency which was attributed to the orientation kinetics of the adsorbed molecules. When the temperature was increased, an increase in the efficiency of the organic inhibitor was observed. Furthermore, the inhibition of aluminium corrosion in acid environment by Thiosemicarbazone derivatives (TSC) has also been reported by Ekpe *et al*. (2001); Ibbotson *et al.* (1990).

2.11.1.2 Natural Product Inhibitors

Naturally occurring materials, mostly known to be non-toxic, have found an increasing number of applications in many fields due to their chemical structures. Many researchers have investigated natural products as possible replacements to synthetic/organic inhibitors.

Investigation into the use of plants as natural inhibitors is particularly interesting because they are cheap, ecologically friendly/non-toxic and pose no threat to the environment (Ebenso *et al.,* 2004; Martinez & Stern, 2003).

Martinez (2002) established that the inhibitive effect of some plants' solution extracts was attributed to the presence of tannins in their chemical constituents. **Tannins** are natural products, characterized by their ability to precipitate proteins. Tannins are high-molecular-weight (>500) compounds with many phenolic groups, distinguished by three

principal groups; the condensed, the hydrolysable (gallotannins and ellagi-tannins) and the phlorotannins (Ramesh *et al.*, 2003). The diverse biological effects of tannins and their common occurrence in plants have created a widespread interest in their use and applications as corrosion inhibitors in various fields of interest.

Other researchers have also shown that some naturally occurring substances such as *Gmelina arborea* and *Piliostigma thonningii* (Auwal, 2008); Honey (El-Etre & Abdallah, 2000); and *Lawsonia inermis* (Al-Sahaibani, 2000) have inhibitive abilities. Ebenso *et al.* (2004) found that the leaf extracts of Pawpaw and Neem inhibited the corrosion of Aluminium in HCl; in conclusion, the adsorption obeyed Freundlish, Temkin and Florry-Huggins adsorption isotherms in all the concentrations studied at 40°C.

The anticorrosion activities of Meethi neem (*Murraya koenigii),* Amla (*Emblica officianilis*), Black Myrobalan (*Terminalia chebula*), soapberry (*Sapindus trifolianus*), and Shikakai (*Accacia conicianna*) were investigated. Corrosion inhibition has also been studied for the extracts of Beautiful swertia (*Swertia angustifolia*). Similar results were also shown by Eucalyptus (*Eucalyptus sp.*) leaves, Jambolan (*Eugenia jambolana*), sugar-apple (*Annona squamosa*), Babul (*Acacia Arabica*), Papaya (*Carica papaya*), Neem (*Azadirachta indica*) and Ironweed (*Vernonia amydalina*) were used for steel in acid media. Attap palm (*Nypa fructicans*) wurmb leaves were studied for the corrosion inhibition of mild steel in HCl media. Castor (*Ricimus communis*) leaves were studied for the corrosion inhibition of mild steel in acid media in addition to the use of herbs such as coriander, hibiscus, anis, black cumin, and garden cress as new type of green inhibitors for acidic corrosion of steel (Raja and Sethuraman, 2008).

Seeds are of great concern for corrosion inhibition studies. Tobacco (*Nicotiana*), black pepper (*Piper nigrum*), castor seeds oil (*Ricinus communis*), *acacia* gum, and lignin are good inhibitors for steel in acid medium. *Papaya*, *Poinciana pulcherrima*, Fedegoso (*Cassia occidentalis*), and Datura (*Datura stramonmium*) seeds are efficient corrosion inhibitors for steel (Raja and Sethuraman, 2008).

The anticorrosion activities of onion, garlic, and bitter gourd for mild steel in HCl media also showed good results. Oil extracts of Ginger, jojoba, eugenol, acetyleugenol, artemisia oil, and Pennyroyal (*Mentha pulegium*) are used for corrosion inhibition of steel in acid media. Berberine an alkaloid isolated from Captis was studied for its anticorrosion effect for mild steel corrosion in H_2SO_4 medium. Saps of certain plants are very useful corrosion inhibitors. Apple of Sodom (*Calotropis procera*), *Azydracta indica,* and *Auforpio turkiale* sap are useful as acid corrosion inhibitors. The extract of Datura was used as corrosion inhibitor for mild steel in acid medium. Quinine has been studied for its anticorrosive effect on carbon steel in 1M HCl. The inhibitive effect of Mosquito plant (*Occmium viridis*) extract on the acid corrosion of mild steel was studied. The inhibition effect of Winged prickly ash (*Zenthoxylum alatum*) extract on the corrosion of mild steel in aqueous Orthophosphonic acid was investigated (Raja and Sethuraman, 2008).

As a contribution to the current interest on environmentally friendly (green corrosion inhibitors), the present study investigates the inhibiting effect of leave extracts of *Parkia biglobosa* (African locust bean) and *Vitex doniana* (black plum) on Aluminium alloy AA2024 in sea water (3.5% NaCl).

2.12 Role of Surface Modified Nanoparticles in Corrosion Inhibition

Nanotechnology is the research or technology development at the atomic, molecular or macromolecular levels, in the length scale of about 1–100 nm, resulting in: **(a)** the creation and/or use of materials, structures, features, devices or systems that have novel properties and/or functions because of their size or **(b)** the ability to control or manipulate on the atomic scale. It is important to note that nanotechnology is concerned with items of small size where the size factor relates to their having "novel properties and/or functions"; the "novelty" is usually noticeable in some manner from a macro point of view (Charles, 2009). Nanotechnology offers new ways to create materials promising a degree of property control not previously possible. Nanoparticles have high surface areas (e.g. high loadings of organic corrosion inhibitors), novel surface chemistries (enhanced chemical reactivity) and offer multiple property enhancement (Kear & Strutt, 1995).

Nanomaterials are classified into **Nanostructured** materials and **Nanophase**/ **Nanoparticles** materials. The former refers to condensed bulk materials that are made of grains with grain sizes in the nanometer range, while the latter are usually the dispersive particles. Nanomaterials are a bridge that links single elements with single crystalline bulk structures (Zhong, 2000).

Daria and Dmitry (2008) fabricated a new family of active coatings using nanocontainers with a shell possessing controlled release properties that responded quickly to changes in the coating environment or the coating's integrity; the release of corrosion inhibitors encapsulated within nanocontainers is triggered by the corrosion process, which prevented the spontaneous leakage of the corrosion inhibitor out of the coating.

Pinck *et al.* (2008) studied the effect of acid (H_2SO_4) and alkaline-based surface preparations on spray deposited cerium based conversion coatings on Al 2024-T3 using Auger Electron Spectroscopy (AES) and concluded that the acid-based surface treatment appeared to expose copper rich intermetallics, thus increasing the number of cathodic sites on the surface, which led to an overall increase in the deposition rate. Additionally, acid activation increased the copper concentration at the surface of the aluminium substrate.

2.13 Synergism

The combined action(s) of two or more corrosion inhibitors to enhance inhibition efficiencies is called **Synergism/Synergy/Synergistic Effect.**

Elewady *et al.* (2008) investigated the corrosion inhibition of aluminium using the synergistic effect of some anionic surfactants and concluded that the inhibition efficiency was much more enhanced due to the synergistic effects. Ekpe *et al.* (2001) reported synergistic effect of mixtures of derivatives of thiosemicarbazone on aluminium corrosion in HCl using weight loss technique. The results from the studies showed that the combined compounds of 2-acetyl-pyridine-(4-phenylthiosemicarbarzone) (PTSC), and 2-acetylpyridine-(4-phenyl iso ethyl thiosemicarbazone) (PIETC) 2 acetylpyridine-(4-phenyl-iso-methlthiosemicarbazone) (PIMTSC) inhibit the corrosion of aluminium. The inhibition efficiency increased with increase in iso group in the mixture, which it was suggested to be due to shielding/exposing of the adsorption sites of the molecules. Makhlouf *et al.* (1996) also established that the combined action of halide ions and some selected thiols as corrosion inhibitor for mild steel pickling in H_2SO_4 is much greater (at concentration of 10^{-3} to 10^{-4}M) than either of the two inhibitors alone.

Synergism parameters could be calculated using the following relation:

$$S_I = \left| \frac{1-I_{1+2}}{1-I'_{1+2}} \right| \quad (2.29)$$

Where $I_{1+2} = (I_1 + I_2) - (I_1\ I_2)$, I_1 = inhibition efficiency of substance 1, I_2 = inhibition efficiency of substance 2, I'_{1+2} = combined inhibition efficiency of substance 1 and 2.

Synergism parameters are indication of synergistic effect existing between two inhibitors. If the value of synergism parameter is greater than one, it confirms synergistic effect existing between the two substances involved (Rajendran *et al*., 2009).

Similarly, the interaction of inhibitor molecules could also be described by introducing a parameter obtained from the surface coverage values (Θ) of the anion, cation and both. In this regard, Kazaraji *et al.* (2000) calculated the synergism parameter, S_Θ, using the following equation:

$$S_\Theta = \frac{1-\Theta_{1+2}}{1-\Theta'_{1+2}} \quad (2.30)$$

$\Theta_{1+2} = (\Theta_1 + \Theta_2) - (\Theta_1\ \Theta_2)$, Θ_1 = surface coverage by anion, Θ_2 = surface coverage by cation and Θ'_{1+2} = measured surface coverage by both anion and cation, which may be attributed to competitive adsorption.

2.14 Mechanism of Inhibition

In formulating organic inhibitor system, it is necessary to know the inhibition mechanism. It is generally accepted that organic molecules inhibit corrosion by adsorption at the metal/solution interface, with the degree of adsorption depending on the chemical structure of molecules, the chemical composition of solutions, the nature of the

metal surface, the temperature and the electrochemical potential at the metal/solution interface (Kuznetsov, 1996).

Rozenfeld, in NACE Whitney award lecture of 1981, presented a theoretical discussion and also the use of quantum chemistry calculations, X-ray Photoelectron Spectroscopy (XPS), radioactive tracers and chemical polarization as tools for studying inhibition. He asserted that inhibition can be caused by both adsorption and a phase layer on the metal surface and, in some cases, inhibition is chemical in nature. Rozenfeld's main point was that the inhibition mechanisms, irrespective of the amount adsorbed by the surface, involves changing the electrophysical properties of the surface atom by the donor-aceptor inhibitor/metal reaction, rather than screening the metal surface from the corrosive environment (Rozenfeld, 1981[b]).

Evidence presented during recent years indicates that many organic and inorganic inhibitors have become effective through interaction with several corrosion products to form a new protective phase rather than by absorption on the metal surface (Fontana, 2005).

Afanas'ev *et al.* (1989); Damaskin & Stenina (1986[b]) reported that contributions to electrostatic force can be made by "Squeezing-out" of inhibitor species from the inter-ionic space and by hydrophobic interaction of non-polar inhibitor fragments with water. Donor-acceptor interactions between a metal and an inhibitor can result in a stronger chemisorption binding of the latter to the surface.

Makhlouf *et al.* (1996) stressed that the essential features of inhibition theory indicated that organic inhibitors are capable of forming onium ions and accordingly exist in acid solutions as cations. These ions are cathodically adsorbed, thereby blanketing the

cathodic area, preventing hydrogen ions from attaching to the surface and hydrogen gas evolution.

Kuznetsov (2004) in the review of physiochemical aspect of metal corrosion inhibition in aqueous solutions cited that as a rule, cation-active inhibitors slow down cathodic reactions and active metal dissolution. It was further reaffirmed that local corrosion is more efficiently prevented by anion-active inhibitors, however, the electrostatic interaction of an inhibitor with a metal surface is not the only motive force of adsorption. Antropov *et al*. (1981) proposed a simplified approach which is found to be useful for formulating inhibitor action. Based on this, if a metal is dissolved from the active state, which is usually the case in acids, then, for moderate metal surface coverage (θ), it is possible to single out two main contributions to the corrosion inhibition efficiency, that related to changes in the ψ_1 – potential and to the surface blocking:

$$\log\psi = \text{cost.} \times \Delta\psi_1 - \log(1-\theta) \tag{2.31}$$

γ, the inhibition coefficient, is defined as:

$$\gamma = \frac{r_0}{r_i} \tag{2.32}$$

r_o and r_i are the corrosion rates in a reference solution and in a solution containing the additive inhibitor under study.

Grigoriev and Ekilik (1978) studied this problem in most detail in relation to acid corrosion, which usually occurs in the active dissolution region of potentials. Accordingly, it was shown that if the inhibitor species are small and their adsorption

increases the activation energy ($\Delta G^{\neq}$) due to the charge redistribution in the double electric layer, then the following equation is valid:

$$\log\gamma_R = \log\gamma_H + \rho\delta \qquad (2.33)$$

ρ is the reaction parameter, which is assumed to be equal to unity for a standard reaction series and depends on the nature of the reaction being studied and on the conditions under which it occurs. δ is a constant of a substituent R, which accounts for its electron-donor ($\delta<0$) or electron acceptor ($\delta>0$) effect on the reaction center in comparison with Hydrogen. γ_H and γ_R are the inhibition coefficients by the non-substituted and substituted inhibitor of the given reaction series respectively.

In general case of inhibitors capable of partial blocking of the active sites, the above equation assumes the form:

$$\log\left(\frac{\gamma_R}{\gamma_H}\right) = \rho\delta - \log\left(\frac{\theta_R}{\theta_H}\right) \qquad (2.34)$$

θ_H and θ_R are the degrees of coverage of the metal surface by the non-substituted and substituted inhibitor of the given reaction series, respectively.

The degree of coverage of the surface with the inhibiting substance can also be calculated using kinetic data. Accordingly, Rozenfeld (1981[a]) opined that the adsorbed organic substances, like the inorganic substances, put completely beyond the sphere of the anodic reaction that part of the surface which is coated with inhibitor (assuming that the rate of the anodic reaction on it drops to practically zero). Hence the following relation can be used to find the surface coverage, θ:

$$\theta = 1 - \frac{i}{i_0} \tag{2.35}$$

i and i_o are the current densities at the given potential in electrolytes with and without inhibitors respectively.

These relations are often used to calculate the degree of coverage for self-dissolution (corrosion) and data on the dissolution rates in electrolytes with (r_i) and without (r_o) inhibitors are employed.

$$\theta = 1 - \frac{r_i}{r_0} \tag{2.36}$$

Bockris *et al.* (1964) revealed that for an organic compound to be adsorbed onto the metal surface from an aqueous solution, each organic molecule has to displace n molecules of water. This led to the derivation of an equation for the standard free energy of the thermodynamic cycle for adsorption and desorption of water and organic compounds as follows:

$$\Delta G_a = \Delta G_v(org) - n\ \Delta G^o_{(w)} - RT \ln \frac{p_{(org)}}{p^n_{(w)}} + RT \ln \frac{C_s}{55.5} \tag{2.37}$$

n is the number of water molecules.

$\Delta G^o_{(w)}$ is the standard free energy of water adsorption from the solution.

$\Delta G_v(org)$ is the standard free energy of adsorption of organic compound.

$P^n{}_{(w)}$ is the vapour pressure of water at Temperature T.

$P_{(org)}$ is the vapour pressure of pure organic compound at Temperature T.

C_s is the saturation concentration of organic compound.

R is the universal gas constant.

The first two terms depend on the interaction energy of the organic compound and water with the metal surface; the third and fourth terms characterize the properties of the substance under consideration.

The role of inhibitors is to form a barrier of one or several molecular layers against acid attack. This protective action is often associated with chemical and/or physical adsorption involving a variation in the charge of the adsorbed substance and transfer of charge from one phase to the other.

According to Amitha & Bharathi (2012), the performance of an organic inhibitor is related to the chemical structure and physicochemical properties of the compound like functional groups, electron density at the donor atom, p-orbital character, and the electronic structure of the molecule. Inhibition could be due to:

(i) Adsorption of the molecules or its ions on anodic and/or cathodic sites.

(ii) Increase in cathodic and/or anodic over voltage.

(iii) The formation of a protective barrier film.

Some factors that contribute to the action of inhibitors include: chain length, size of the molecule, aromaticity/conjugation, bonding/strength of bonding to the substrate, cross-linking ability, solubility in the environment (Amitha & Bharathi, 2012).

It was also further revealed that the degree of surface coverage of adsorbed molecules was found to be influenced by the following factors:

(i) Solubility of the given compound

(ii) Presence of functional group

(iii) Interaction between adsorbed molecules

Furthermore, within a given homologous series, the contribution of the interaction between adsorbed molecules increases with their length, hence the process of adsorption and formation of protective layers on a metal substantially depend on the charges of the surface and inhibitor species (Kuznetsov, 2004).

In summary, Adsorption can be:

• Physisorption due to electrostatic attractive force between the inhibiting ions or dipoles and the electrically charged metal surface.

• Chemisorption caused by the interaction between unshared electron pairs or electrons with metals to form a coordinate type of bond. Chemisorption takes place when there are heteroatom such as P, Se, S, N and O present with lone pair electrons and/or aromatic rings in the adsorbed molecules.

• A combination of the above factors.

This is without prejudice to a publication by Kirk (1989) which classified adsorption into electrostatic, chemisorption, and π-bond (delocalised electron) types.

2.15 Adsorption Isotherms

Damaskin & Stenina (1986[b]); Damaskin *et al.* (1971) revealed that if data on the degree of surface coverage by the inhibitor is available, then an ***Adsorption Isotherm*** could be developed, and the nature of an isotherm yields valuable information about the properties of the adsorbed substances as well as their interactions with electrode surface. In short, adsorption isotherms describe the adsorption process.

Many equations have been proposed to describe the adsorption isotherm. The most frequently used isotherms include: Langmuir, Frumkin, Hill de Boer, Parsons, Temkin, Flory-Huggins, Dhar-Flory-Huggins, Freundlish, Bockris-Swinkels and the recently formulated thermodynamic/kinetic model of El-Awady and co-workers (Obot *et al.,* 2009).

For simplicity, the experimental data are most often described by the isotherm of Langmuir which is represented by the equations below:

$$K = \frac{\theta}{c(1-\theta)} \tag{2.38}$$

K is the adsorptional equilibrium constant,
c is the inhibitor concentration
θ is the surface coverage

The constant of adsorptional equilibrium K is found from the free energy of adsorption:

$$K = exp^{-\frac{\Delta\sigma}{RT}} \tag{2.39}$$

σ is the interfacial tension and R is the gas constant

The characteristic of El-Awady's kinetic/thermodynamic model, which is more recent and takes care of inherent deficiencies of the Langmuir adsorption isotherm, is given by the equation:

$$\log\frac{\theta}{1-\theta} = \log K + y \log C \tag{2.40}$$

C is the inhibitor concentration, θ is the degree of surface coverage, K_{ads} is the equilibrium constant of adsorption process and is given by the equation below:

$$K_{ads} = K^{\frac{1}{y}} \tag{2.41}$$

In this model, the number of active sites y is included. Values of 1/y less than unity imply multilayer adsorption, while 1/y greater than unity suggests that a given inhibitor molecule occupies more than one active site.

2.16 Background Information on the Substances Used as Inhibitors

2.16.1 Sodium Chromate (Na_2CrO_4)

Sodium chromate **(**Na_2CrO_4**)** is a yellow solid chemical compound used as a corrosion inhibitor in petroleum industry, dyeing auxiliary in the textile industry, wood preservative and as a diagnostic Pharmaceutical in determining red cell blood volume. It is obtained from the reaction of Sodium dichromate with Sodium hydroxide, is hygroscopic and can form tetra-, hexa-, and decahydrates. Some chromates, like other hexavalent chromium compounds, can be carcinogenic. Sodium chromate **(**Na_2CrO_4**)** is a strong oxidant and is soluble in water, producing a weakly basic solution (Rozenfeld, 1981[a]).

2.16.2 *Parkia biglobosa* (African Locust Bean) Tree

This plant occurs on a wide range of natural and semi-natural communities such as open Savannah woodlands, but it is most conspicuous and abundant in the anthropic communities, principally bush fallow and wooded farmland where cultivation is semi-permanent. The tree can also grow on rocky slopes, stony ridges or sandstone hills. It is a fire-resistant heliophyte and occurs in a diversity of agroecological zones where mean annual rainfall may be less than 400mm. It has a capacity to withstand drought conditions because of its deep root system and an ability to restrict transpiration (Keay *et al.,* 1989).

2.16.3 *Vitex doniana* Sweet (Black Plum) Tree

This is the most abundant and widespread Vitex in Savannah region, readily recognized by its long-stalked glabrous leaves, though sometimes they may be indented or

occasionally have a very short triangular tip. It is widespread in tropical Africa and the fruits are edible (Keay *et al.,* 1989).

Hausa: *dinya* Yoruba: *oori-nla* Igbo: *ucha koro* Fulani: *galbihi*

2.16.4 Boehmite Nanoparticles [AlO(OH)]

Cook *et al.* (2006) found that a material known as Boehmite fulfils the needs as a carrier for organic corrosion inhibitors. Boehmite is aluminium hydroxide oxide or aluminium oxyhydroxide and is found as one of two well defined crystalline phases- Boehmite [ϒ-AlO(OH)] and diaspore [α-AlO(OH)]. Pseudoboehmite is a hydrated form of boehmite with slightly larger d-spacing. Boehmite is an important constituent of the aluminium ore, bauxite (Greenwood & Earnshaw, 1997). In aqueous solution, the stability region of most Aluminium hydroxides is betweem pH 4 - 10 when the Al^{3+} activity is in the milli-molar range Johansson (1990).Commercial Boehmite is normally available in three forms, viz:

1. Disperal 40, unmodified Boehmite alumina.
2. Disperal OS1, modified Boehmite alumina with para-toluensulphonic acid.
3. Disperal OS2, modified Boehmite alumina with C10-C13 alkyl-benzensulphonic acid.

The unmodified commercially available Boehmite, Disperal 40, can easily be converted from its delivered form (50-50 micron agglomerates) to individual nanoparticles in water. It also has a rich and readily accessible surface chemistry (Cook *et al.,* 2006; Cook *et al.,* 2005).

2.17 Corrosion Measurement Techniques

Corrosion measurement involves the application of various techniques to determine the corrosiveness of the environment and the rate of metal loss. Corrosion measurement is

usually a quantitative method of evaluating the performance and effectiveness of corrosion control and prevention techniques. After evaluation is completed, the result obtained, feedback, is used to improve and enhance the techniques.

A variety of methods such as electrical resistance, gravimetric-based mass loss, quartz crystal microbalance-based mass loss, electrochemical and solution analysis methods enable the determination of corrosion rates. The polarization resistance method, based on electrochemical concepts, enables determination of *instantaneous* interfacial reaction rates such as corrosion rates and exchange current densities from a single experiment. The electrical resistance change, gravimetric and quartz crystal microbalance mass loss, as well as solution analysis for metallic cations provide historical or integrated mass loss information from corrosion that has occurred over some period of time. Therefore *instantaneous* rates cannot be determined from a single measurement using these other methods. Instead, the derivative of multiple measurements over time provides rate information.

In summary, the methods for corrosion measurement can be broadly divided into five categories (Yin, 2004):

1**. Non-destructive Testing Analytical Chemistry-** which includes Intelligent pigging, Ultrasonic testing, Radiography testing, Thermography, Eddy current and Magnetic flux.

2**. Analytical Chemistry-** such as pH measurement, dissolved gas (such as carbon dioxide, hydrogen sulphide and oxygen), metal ion analysis (such as Fe^{2+}, Fe^{3+}) and microbiological analysis.

3**. Fluid Electrochemistry-** consisting of AC impedance, potential measurement, potentiostatic measurement and potentiodynamic measurement.

4**. Operational Data-** including factors such as pH, pressure, temperature and velocity or flow rate.

5**. Corrosion Monitoring-** composed of techniques such as weight loss coupons, hydrogen penetration, galvanic current, electrical resistance and linear polarization.

Table 2.2 shows corrosion inspection and plant conditioning monitoring techniques while Table 2.3 represents in-plant monitoring techniques.

Table 2.2: Corrosion inspection and plant condition monitoring techniques

Acoustic Emission	Measures the location, initiation and propagation of cracks and defects under stress in metals
Dye Penetrant	Simple procedure for locating surface cracks. Requires shut down for internals
Magnetic Particle	Surface and subsurface crack and defect location, seams and Inclusions
Radiography	X-ray and gamma-ray (Co^{60}, Ir^{192}), wall thickness measurement and crack and defect location
Thermography	Identifies lack of bond, hot spots, local thinning, temperature changes due to poor/wet lagging
Ultrasonics	Indicates internal defects, porosity, lack of fusion, crack location, wall thickness
Visual Examination	Localised corrosion identification, erosion, pitting, deposit scaling and fouling problems, staining and corrosion leakage due to cracking

(*Source*: Dawson *et al.,* 2001)

Table 2.3: In-plant monitoring techniques

Weight loss Coupons*	Traditional method of limited sensitivity but used in all environments. Type of corrosion observed is an important indicator
Electrical Resistance (ER)	Measures change in probe resistance. Widely used for carbon steel fabrications in gas and liquid phases. Automated readings.
Linear Polarisation Resistance*	An electrochemical dc method used for measurement of uniform corrosion. Standard electrochemical technique. Typically requires a conductive electrolyte but some newer probes have a conductive separator between the metal probe elements.
Zero Resistance Ammetry	Established method for assessing galvanic corrosion between dissimilar metals, but can be used with nominally "identical" electrodes in some applications.
Hydrogen Probes	Measure rate of diffusion of hydrogen through steels either by means of a pressure gauge or by electrochemical techniques.
Thin Layer Activation	Measures change of radioactivity as a local irradiated area corrodes.
Electrochemical Impedance*	An ac method used for general corrosion measurements similar to LPRM. More versatile and accurate than dc measurements.
Electrochemical Noise*	A more recent technique used for assessing general corrosion and current and potential fluctuations associated with localised corrosion.

*Techniques employed in this work.
(*Source*: Dawson *et al.,* 2001).

However, for the purpose of this work, three Electrochemical (**LPR**, **OCP** and **EIS**) and Gravimetric-based mass loss techniques were used to evaluate the corrosion behaviour of the test alloy.

2.17.1 Linear Polarisation Resistance (LPR)

Linear Polarization Resistance (LPR) monitoring is an effective electrochemical method of measuring corrosion based on fluid electrochemistry. Monitoring the relationship between electrochemical potential and current generated between electrically charged electrodes in a process stream allows the calculation of the corrosion rate. LPR is most

effective in aqueous solutions, and has proven to be a rapid response technique. This measurement of the actual corrosion rate allows almost instant feedback to operators.

LPR monitoring has seen wide industry use for nearly 50 years. The major advantage to LPR monitoring is the speed in which it can provide a measurement of the corrosion rate.

Changes in the corrosion rate can typically be detected in minutes, providing an almost instantaneous measuring system. This fast response allows an operator to evaluate process changes and is particularly useful in monitoring the effectiveness of a prevention program. For example, quick feedback means that inhibitor selection and quantities can be evaluated and fine-tuned in minimal time. Another key advantage of LPR monitoring is that it can provide a qualitative pitting tendency measurement, such as whether the tendency for pitting will be shallow and infrequent, or deep and abundant. LPR monitoring can also give an indication of metal behaviour, for example when an alloy changes from a passive to an active state, thereby resulting in increased susceptibility to corrosion (Robert *et al.,* 2003).

The electrochemical cell is made up of a flask suitable for a conventional three-electrode system, comprising the working electrode, a reference electrode, counter electrode with a lid that has five holes for the reference electrode, working electrode, counter electrode, temperature measurement and an aeration/de-aeration, gas purger.

A Potentiostat is usually used for electrochemical measurements. It is generally connected to three electrodes and then to a computer which has relevant software. The Potentiostat, when started automatically, varies the potential at a steady rate between two preset potentials which generates current through the cell. The supplied current goes into the working electrode through the counter electrode. The potential of the working

electrode is thereby be measured with respect to the reference electrode. Data logging of the potential and current is done by the computer.

The corrosion rate of a material in open-circuit corrosion can be calculated from electrochemical data. The relationship is known as the Stern-Geary equation, which was published in 1957 and is based on the Wagner-Traud mixed potential theory published in 1938.

The polarization curves generated are used to study electrochemical/corrosion behavior of metals and alloys and provide several electrochemical regions of diverse physical meaning. The open circuit potential (E_{corr}), current density, Tafel slope and corrosion rate are usually obtained from the graphical presentation of the data obtained. A typical example is shown in the Figure 2.8 below:

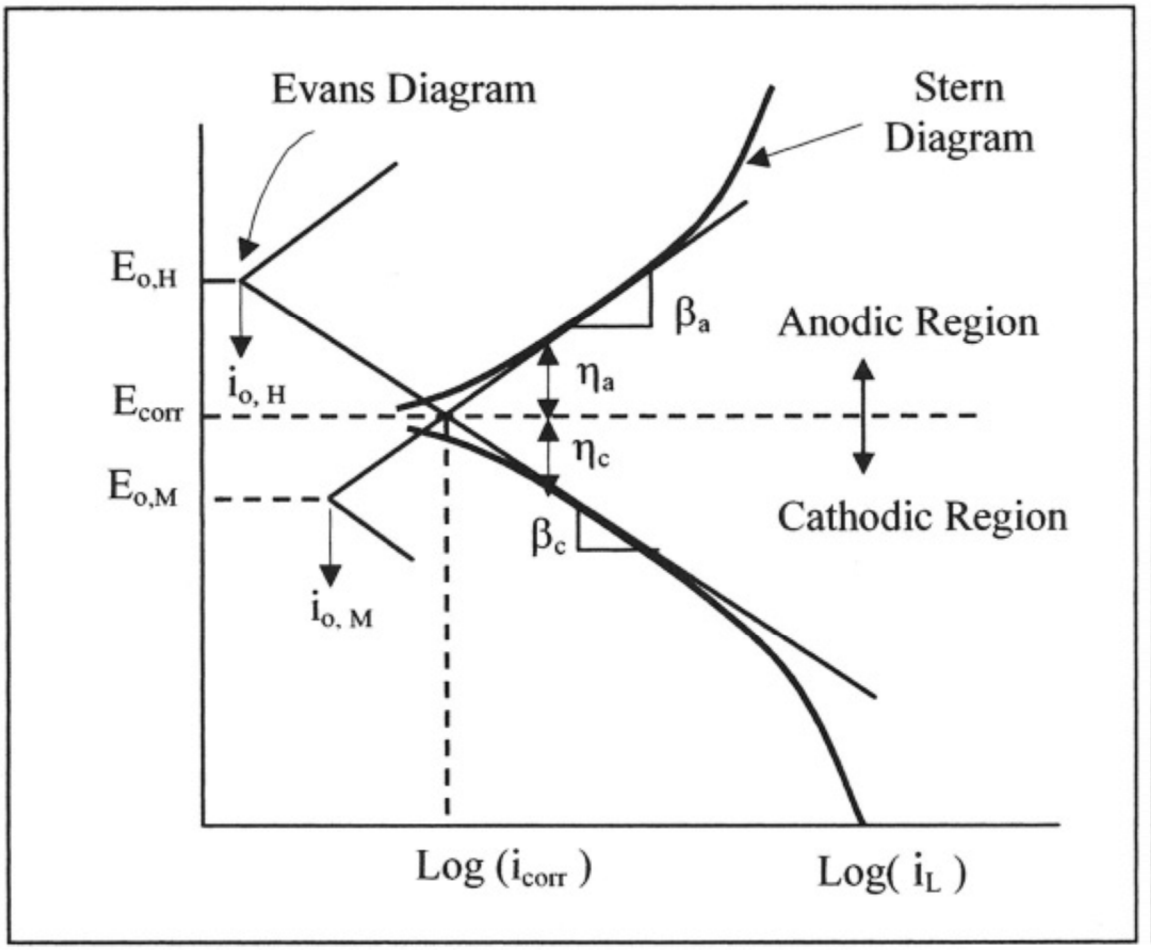


Figure 2.8: Typical polarization curve showing Tafel plot/extrapolation (*Source*: Nestor, 2004).

Corrosion parameters are calculated on the basis of potentiodynamic potential-current characteristics in the Tafel potential region ($E = E_{corr} \pm 250$ mV) and the vicinity of the corrosion potential ($E = E_{corr} \pm 15$ mV) using the mathematical equations:

——— (2.42)

——— (2.43)

These equations corresponded to linear anodic and cathodic Tafel lines. Current density i_{corr} could then be determined by extrapolating the Tafel lines to $E = E_{corr}$ or according to the Stern-Geary (1957) equation and this resulted in:

$$i_{corr} = \frac{\beta_a \beta_c}{2.303(\beta_a + \beta_c) R_p} \tag{2.44}$$

R_p is the polarization resistance, defined as the slope of a polarization curve at E_{corr};

$$R_p = \left(\frac{dE}{di}\right)_{E=E_{corr}} \tag{2.45}$$

i_{corr} is used for calculation of inhibition efficiency (IE%) based on equation 2.46 below:

$$IE\% = \left[1 - \left(\frac{i_{corr(inh.)}}{i_{corr(free)}}\right)\right] \times 100 \tag{2.46}$$

$i_{corr(free)}$ and $i_{corr(inh)}$ are the corrosion densities in absence and presence of inhibitors respectively.

The measurement of the polarization resistance is of great practical importance and is also known as linear polarization resistance (LPR) measurement, taking a linear potential-current density relationship around $\boldsymbol{E_{corr}}$. For application of the polarization resistance technique, the following limitations must be considered:

- The Open Circuit Potential must not change during the period of measurement.
- The corrosion mechanism must not change during the measurement.
- No other electrochemical reactions must occur except the corrosion reaction.
- Ohmic resistances of the system must be small compared with the polarization resistance.

2.17.2 Electrochemical Impedance Spectroscopy (EIS)

Electrochemical impedance spectroscopy (EIS) (sometimes also called AC impedance) is an electrochemical technique that surfaced in the late 1960's but did not become extensively studied until the late 1970's and early 1980's when computer-controlled laboratory equipment became the norm. Electrochemical Impedance Spectroscopy (EIS) is a non-destructive technique often used to understand the interfacial behaviour in electrochemical systems. The ability of the technique to segregate various processes, i.e., ohmic conduction, charge transfer, interfacial charging, mass transfer etc, makes it an elegant technique for electrochemical systems. While many of the idiosyncrasies of the technique are now reasonably understood, the ability to use the technique to model all corrosion systems remains elusive.

EIS is widely used to evaluate inhibitors performance, since it provides information about the corrosion process taking place on the metal surface. Particularly, it gives information about the charge transfer resistance $\mathbf{R_{ct}}$, the double layer capacitance $\mathbf{C_{dl}}$, solution resistance $\mathbf{R_s}$ as well as kinetic information. EIS has also been used in a number of areas such as battery research, estimating corrosion rates (especially low corrosion rates) and examining coatings on metal surfaces.

Briefly, this technique involves a determination of cell impedance, in response to a small (-5 mV amplitude) ac signal imposed on top of a constant DC potential (preferably at the corrosion potential with zero imposed current to minimize the DC currents), over a span of frequencies ranging typically from 10^5 kHz to 10^{-3} Hz (hence the term impedance spectroscopy). The corrosion process usually forces the measured current to be out of phase (denoted by the phase angle) with the input voltage; dividing the input voltage by

the output current furnishes the impedance. From the measured cell impedance (magnitude and phase angle) in the form of real and imaginary components and phase angle, it is possible to examine and qualitatively determine several processes such as the electronic/ionic conduction in the electrode and electrolytes, interfacial charging either at the surface films or the double-layer, charge transfer processes and the mass transfer effects, if any. The time constants for these different processes being different, their features will show up at different frequencies in the EIS spectra.

The advantages of this technique include: **i)** its nondestructive nature, since the polarization applied is low enough that linear polarization conditions (i.e., where the polarization increases linearly with current) are maintained and the rate equations are simplified accordingly, **ii)** rapid and easy measurement methods as presently possible with the advent of computer-controlled equipment such as Potentiostat and Frequency Response Analyzer (FRA) and appropriate software, which enormously simplify the data collection as well as subsequent analyses; FRA analyzes out-of-phase relationship between the input voltage and output current (Robert *et al.,* 2003). The relationships between the AC/DC impedance might be depicted as shown in Figure 2.9.

The deficiency of this technique, on the other hand, is mainly related to the difficulty in interpreting the data, i.e., in envisaging a suitable electrical equivalent circuit to represent the electrochemical system and in quantitatively determining the relevant electrical parameters that would help one to understand the response of system.

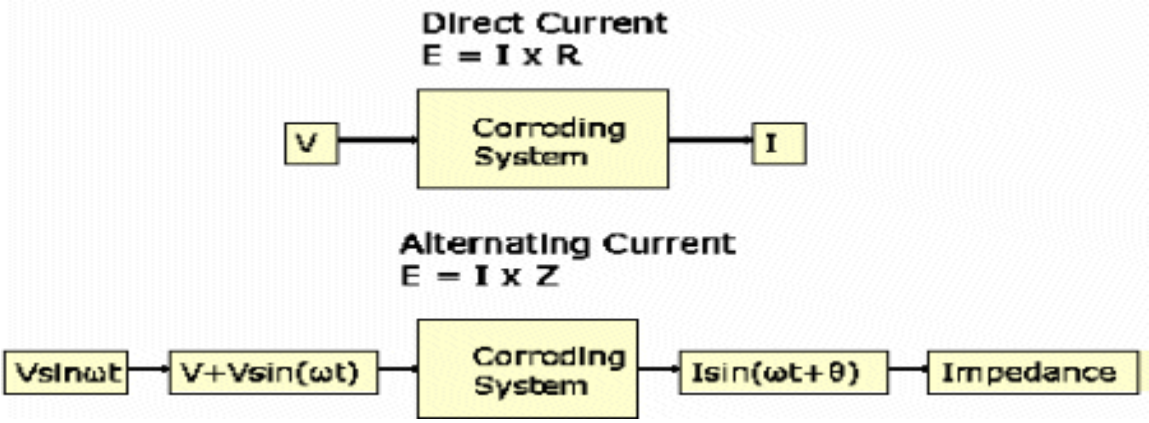


Figure 2.9: Schematic of AC/DC impedance circuit.
(*Source:* Robert *et al.,* 2003)

Most corrosion practitioners have attempted to analyze impedance spectra using combinations of analogous circuit elements. The analogous circuit components provide a way of modeling and discussing the corrosion process; they are not components of the corrosion process itself. The specific circuit elements used are the capacitor, resistor and inductor. An example of a simple circuit that can model a very passive alloy (e.g. titanium in water) is a parallel combination of a resistor and capacitor in series with a resistor as represented in Figure 2.10 below:

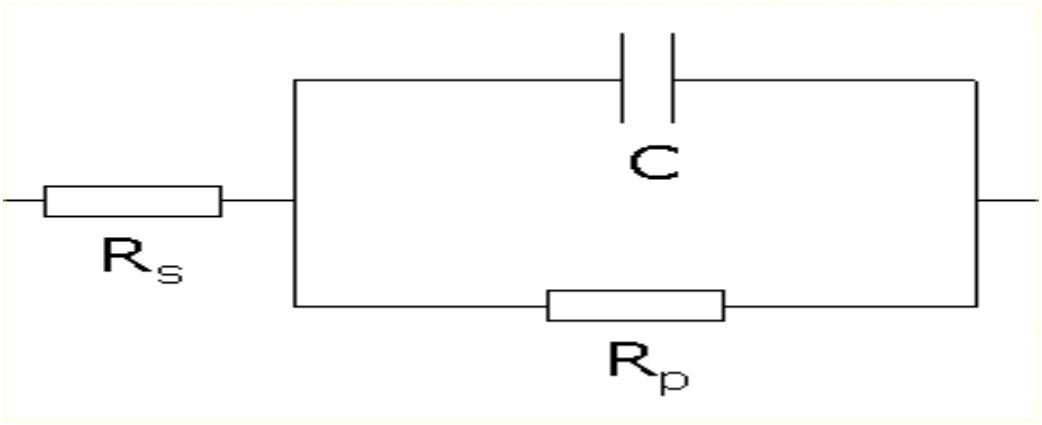


Figure 2.10: A simplified polarization resistance model circuit
(*Source*: Robert *et al*., 2003)

Sometimes impedance data obtained at the corrosion potential have the shape of a depressed semicircle with its centre on the real axis. In this case, the simplest equivalent electric circuit corresponds to a parallel combination of a capacitor and a resistor. For better quality constant phase elements (CPE), replacing the capacitor, are often used in data fitting of depressed semicircles.

2.17.3 Chronopotentiometry

Chronopotentiometry, has been known since 1900; 'Chrono' is coined from the Greek word ***Khronos***, meaning time. In this technique, a controlled current (often constant) is applied to an electrode and the electrode potential studied over a time period (electrode potential is plotted against time in ***choronopotentiogram***). Chronopotentiometry is the most basic constant current experiment, hence its importance as it gives us an insight about the stability of passive film; whether the passive film is forming, how stable it is and at which time is it more or less stable. Generally, the variation in the open circuit potential values of substrate were measured at zero applied current immediately after immersion of the substrate into an electrolyte for a specified period of time (Bard & Faulkner, 2001). Herman and Bard (1963) introduced cyclic Chronopotentiometry, in which the sign of the current is switched at regular interval. Abdulwahab (2011) used chronopotentiometric technique to study the passivity/activity of as-cast and heat-treated Al-Si-Mg alloy in simulated sea water.

2.17.4 Gravimetric-based Mass Loss Method

Though classical in nature, the gravimetric-based mass loss is still suitable for corrosion evaluation. Its advantage is that the corrosion, which has actually occurred, can be observed in a sample; allowing visual examination, physical measurements and the chemical analysis of corrosion products. Coupons can be mounted in different configurations to study different types of corrosion mechanisms, such as crevice corrosion, galvanic attack and stress corrosion (Feyisayo *et al.*, 2010; Malik *et al.*, 1994).

The mass (weight) losses of the coupons (which are test specimens of the material of interest) are determined by computing the differences between the initial mass and the final mass of the coupons at different time interval using the relationship as proposed by Fontana (2005).

$$\Delta W = W_i - W_f \tag{2.47}$$

ΔW is the mass loss (g)
W_i is the initial mass of the coupon (g)
W_f is the final mass of the coupon (g)

The corrosion rate, or the rate of material removal as a consequence of the chemical action, is an important corrosion parameter. This may be expressed as the *Corrosion Penetration Rate (CPR)* using equation 2.48 below:

$$\text{CPR} = \frac{K\Delta W}{\rho A t} \tag{2.48}$$

ΔW is the weight loss after exposure time t; $\boldsymbol{\rho}$ and A represent the density and exposed specimen area, respectively, and K is a constant, its magnitude depending on the system

of units used. The CPR is conveniently expressed in terms of either mils per year (mpy) or millimeters per year (mm/yr). In the first case, K = 534.934 to give CPR in mpy (where 1 mil = 0.001 in.), and ΔW, $\boldsymbol{\rho}$, A, and t are specified in units of milligrams, grams per cubic centimeter, square inches, and hours, respectively. In the second case, K = 87.66 for mm/yr, and units for the other parameters are the same as for mils per year, except that A is given in square centimeter (Callister, 1999).

In respect of this, the corrosion rates, inhibition efficiencies, surface coverages, activation energies and heat of adsorptions for various inhibited and uninhibited systems are computed using the conventional formulae.

The inhibition efficiency, recorded as percent inhibition (**IE%**) is calculated as follows:

$$IE\% = \left(1 - \frac{\Delta W_{corr}}{\Delta W^{0}_{corr}}\right) \text{ x } 100 \qquad (2.49)$$

ΔW_{corr} is the weight loss in the presence of an inhibitor and ΔW^{O}_{corr} is the weight loss in the absence of an inhibitor.

Quraishi & Jamal (2002) established that the percentage inhibition efficiency (IE %) at each concentration could be calculated using the following equation:

$$\text{IE\%} = \frac{r_0 - r}{r_0} \times 100 \qquad (2.50)$$

r_o and r are the corrosion rates in the absence and presence of inhibitors respectively.

2.18 Materials Characterisation

The characterisation techniques used in this work included X-Ray Fluorescence (XRF), Scanning Electron Microscopy equipped with Energy-Dispersive X-Ray Spectroscopy (SEM/EDS), X-Ray Diffractometry (XRD), Nuclear Magnetic Resonance (NMR) and Raman Spectroscopy.

2.18.1 NMR-based Metabolomic Analysis of the Plant Extracts

Nuclear Magnetic Resonance (NMR) or Proton Magnetic Resonance (PMR) spectroscopy is a powerful analytical technique used to evaluate the structures of compounds. It is also used to:

- Identify unknown compounds,
- Check for impurities and
- Study the shapes of molecules.

In medicine, magnetic resonance imaging uses **NMR** to detect the Hydrogen nuclei in the human body, especially in water and lipids. The term ***Nuclear*** interprets the technique that detects nuclei of atoms such as Hydrogen-1 (proton). The term ***Magnetic*** interprets the nuclei that act like tiny magnets that can line up either in the same direction or in opposite direction to an external magnetic field. The term ***Resonance*** is the absorption of energy in the form of radio waves with frequency corresponding to the size of energy jump as the nuclei flip from one alignment to the other (Raghupati & Sriparna, 2007).

It has been reported recently that **Nuclear Magnetic Resonance** (**NMR**) spectroscopy could be employed to determine the presence of different secondary metabolites (such as Phenolic compounds-Aromatics, Alkaloids, Flavonoids, Terpenoids, etc.) and primary

metabolites (e.g., sugars and amino acids) in plant extracts (Kim *et al.,* 2010). Nuclear Magnetic Resonance (**NMR**)-based metabolomics has many applications in plant science. Metabolomics can be used in functional genomics and to differentiate plants from different origin, or after different treatments. The main advantage of NMR metabolomic analysis is the possibility of identifying metabolites by comparing NMR data with references or by structure elucidation using two-dimensional NMR. This procedure is rapid; it takes not more than 30 minutes for sample preparation (multiple parallel) and a further 10 min for NMR spectrum acquisition (Kim *et al.,* 2010).

2.18.2 X-Ray Fluorescence (XRF).

In X-Ray Fluorescence (XRF), an X-Ray beam is used to irradiate a specimen, and the emitted fluorescent X-Rays are analyzed with a crystal spectrometer and scintillation or proportional counter. The fluorescent radiation normally is diffracted by a crystal at different angles to separate the X-Ray wavelengths and therefore to identify the elements; concentrations are determined from the peak intensities. For thin films XRF intensity-composition-thickness equations derived from first principles are used for the precision determination of composition and thickness (Brundle *et al.,* 1992)

2.18.3 Scanning Electron Microscopy/Energy-Dispersive X-Ray Spectroscopy (SEM/EDS)

For the purpose of a detailed materials characterization, the optical microscope has been supplanted by two more potent instruments, the Scanning Electron Microscope (SEM) and Transmission Electron Microscope (TEM). They have superior spatial resolution or depth of focus when compared with optical microscope (Brundle *et al.,* 1992)

When the atoms in a material are ionized by a high-energy radiation they emit characteristic X-Rays. EDS is an acronym describing a technique of X-Ray Spectroscopy that is based on the collection and energy dispersion of characteristic X-Rays. An EDS system consists of a source of high-energy radiation, usually electrons; a sample; a solid state detector, usually made from lithium-drifted silicon, Si (Li); and signal processing electronics. EDS spectrometers are most frequently attached to electron column instruments. X-Rays that enter the Si (Li) detector are converted into signals which can be processed by the electronics into an X-Ray energy histogram. This X-Ray spectrum consists of a series of peaks representative of the type and relative amount of each element in the sample. The number of counts in each peak may be further converted into elemental weight concentration either by comparison with standards or by standardless calculations (Brundle *et al.,* 1992)**.**

2.18.4 X-Ray Diffraction (XRD)

In X-Ray Diffraction (XRD), a collimated beam of X-Rays, with wavelength $\lambda \sim 0.5\text{-}2$ Å, is incident on a specimen and is diffracted by the crystalline phases in the specimen according to Bragg's law ($\lambda = 2d\sin\theta$, where d is the spacing between atomic planes in the crystalline phase). The intensity of the diffracted X-rays is measured as a function of the diffraction angle 2θ and the specimen's orientation. This diffraction pattern is used to identify the specimen's crystalline phases and to measure its structural properties, including strain (which is measured with great accuracy), epitaxy, the size and orientation of crystallites (small crystalline regions) (Brundle *et al.,* 1992)

2.18.5 Raman Spectroscopy

Raman Spectroscopy is the measurement, as a function of wave number, of the inelastic light scattering that results from the excitation of vibrations in molecular and crystalline materials. The excitation source is a single line of a continuous gas laser, which permits optical microscope optics to be used for measurement of samples down to a few μm. Raman Spectroscopy is sensitive to molecular and crystal structure; applications include chemical fingerprinting, examination of single grains in ceramics and rocks, single-crystal measurements, speciation of aqueous solutions, identification of compounds in bubbles and fluid inclusions, investigations of structure and strain states in polycrystalline ceramics, glasses, fibers, gels, and thin and thick films (Gauglitz & Vo-Dinh, 2003).

In summary, it could be seen from the literature survey that various efforts to control and mitigate corrosion of materials are been investigated. The use of corrosion inhibitors is one of the methods used in the prevention and control of corrosion. Chromates are the most effective and well-known inhibitors. However, because of their 'un-safe' nature, other comparable substitutes, either individually or in synergistic blends, are being researched/explored. Corrosion testing and evaluation techniques such as Electrochemical Quartz Crystal Microbalance (EQCM), Chronopotentiometry, LPR-that provides instantaneous corrosion rates, and EIS which is a non-destructive technique often used to understand the interfacial behaviour in electrochemical systems, gained momentum in recent times. The importance of evaluating the kinetics and thermodynamics of corrosion inhibitors with a view to understanding the mechanism of inhibitor action cannot be overemphasized. Characterisation, using tools such as SEM,

XRD, NMR, AFM, STM, SIMS, GC-MS, FT-IR e.t.c, also form part of modern corrosion research.

This research takes these modern approaches into cognisance in developing, evaluating and characterizing ecofriendly hybrid corrosion inhibiting additives (using different proportions of Boehmite nanoparticles, leave extracts of *Parkia biglobosa*-African locust bean and *Vitex doniana*-Black plum trees) as alternatives to chromate-based inhibiting additives for AA2024 aluminium alloy.

CHAPTER THREE

3.0 MATERIALS AND METHODS

3.1 Primary Materials

The primary materials used for the production of the alloy used in this research are high purity aluminium and copper wires obtained from Northern Cable Company (NOCACO), Kaduna. Alloying elements (Ferromanganese, Magnesium & Nickel) and analytical grades of Sodium chloride (NaCl) and Sodium chromate (Na_2CrO_4) were purchased over shelf from certified chemical vendors.

The unmodified Nano-sized Boehmite Alumina, Disperal 40, was sourced from the National Centre for Nano- Structured Materials (NCNSM), which is a unit in the Council for Scientific and Industrial Research (CSIR), Pretoria, South Africa. Disperal 40 was used in this work because it can easily be converted from its delivered form (50-50 micron agglomerates) to individual nanoparticles, of sizes 10^{-9} meters, in water.

3.2 Equipment, Apparatuses, Machines and Other Materials

The equipment used in this research included electric furnace, pyrometer, mechanical stirrer and a mould for casting the Aluminium alloy (AA2024). Lathe machine, brushes, grinding, polishing machines, emery papers (80, 120, 220, 800, 1000 grades), magnetic polishing papers and Diamond monocrystalline suspension (15, 6, 3 and 1μm) for micro-polishing. A desiccator for samples storage, electrodes, digital weighing balance (Mettler AE 166-Delta range), a thermostated water bath, measuring cylinders, beakers and other glass wares were also used.

The pH values of the electrolytes were monitored with a digital pH meter. The phytochemical constituents of the powdered leaves of the plants were extracted with a

Soxhlet extractor and further analysed with the aid of Nuclear Magnetic Resonance (NMR).

An Autolab Potentiostat/Galvanostat with General Purpose Electrochemical Software (GPES) version 4.9 was used for the corrosion studies using Linear Polarisation Resistance (LPR), Chronopotentiometry and Electrochemical Impedance Spectroscopy (EIS) methods. A Scanning Electron Microscopy (SEM/EDX), X-Ray Diffractometry (XRD) and Raman Spectroscopy were used to characterize the coupons before and after exposure to corrosion test environment. The chemical composition of the test alloy was analysed using X-Ray Fluorescence (XRF) machine.

3.3 Methods

3.3.1 Extraction of Some Phytoconstituents from the Plants

Extraction of the desired phytochemical constituents from the powdered plant materials was achieved through the use of a **Soxhlet extractor.** Initially, leaves of *Parkia biglobosa* and *Vitex doniana* were obtained, sun-dried and pulverized using mortar.

The resulting powder (500g) was placed in a thimble and loaded into the main chamber of Soxhlet extractor. The extractor was then placed on a flask containing ethanol (the extraction solvent), heated to reflux and the vapour flooded to the chamber housing the powder via the distillation arm of the extractor. Consequently, some of the powdered plant materials dissolved in the warm solvent was emptied by a siphon. The solvent was channeled back to the distillation flask and the cycle repeated many times for seven days to achieve maximum extraction of some of the phytoconstituents.

3.3.2 NMR-Based Metabolomic Screening of the Plant Extracts

The metabolomic analyses of the extracts were carried out using **Nuclear Magnetic Resonance** (**NMR**) to determine the presence of different secondary metabolites, such as Phenolic compounds-Aromatics, Alkaloids, Flavonoids, Terpenoids, etc., in the extracts according to the method reported by Kim *et al.* (2010).

The plant extracts were freeze dried and ultrasonicated with 1:1 CD_3OD:KH_2PO_4 buffer in D_2O for 30 minutes (multiple parallel). Then, the standard ^1H, *J*-resolved, ^1H–^1H NMR correlation spectroscopy (COSY) utilising Heteronuclear Multiple Bond Correlation (HMBC)) and chemometric methods were employed for 10 minutes in the acquisition of the NMR spectrum.

3.3.3 Production of the Test Alloy

The test alloy with compositions as contained in Table 3.1 was sand-cast according to the standard/recommended procedures used elsewhere in foundry practice. Al-4.25%Cu alloy was melted in a graphite crucible in a muffle furnace. Weighed amount of the alloy was charged into the crucible and allowed to melt completely. The melt was stirred and the temperature was raised to 700^{o}C. A covering flux was added. Proper mixing was carried out after which weighed amounts of other alloying elements were introduced into the melt. The melt was stirred thoroughly to achieve uniform distribution of the alloying elements. It was then allowed to superheat up to a temperature of 750^{o}C after which the slag produced was removed. Stirring was sustained for about 2 minutes, and then the whole melt was allowed for 2 minutes before finally casting in sand mould. The cast bars were of dimensions 20mm diameter and 300mm length. After pouring, the whole set up was allowed to solidify and cool to room temperature before removing them from the

moulds for further treatment. The cast samples were further analysed by a Siemens FK-04 X-Ray Fluorescence (XRF) machine, having Mo anode, to confirm its chemical composition**.**

Table 3.1: Nominal compositions of the test alloy.

Class of alloy	Alloy name	%Cu	%Mg	%Mn	%Ni	%Fe	%Al
2xxx	AA2024	4.25	1.30	0.48	0.01	0.22	93.74

(*Source*: Baldini *et al*., 1995)

3.4 Preparation of Solutions for Corrosion Testing

After the successful extraction of the phytochemical constituents from *Parkia biglobosa* and *Vitex doniana* using Soxhlet extractor, solutions of different concentrations of the extracts, varying amounts of Boehmite nanoparticles and fixed concentration of NaCl at 3.5% were prepared according to the permutations/combinations shown in Table 3.2.

Sodium Chromate solutions at concentrations of 0.5, 1.0 and 1.5M Na_2CrO_4 were used as control. Solutions of varying concentrations of the extracts (10, 20, 30, 40 and 50%v/v) were prepared and stored in a desiccator. From these solutions, synergistic combinations of extracts and extracts/nanoparticles through addition of 0.1, 0.2, 0.3, 0.4 and 0.5g Boehmite nanoparticles were formed.

Table 3.2: Compositions of the solutions used in the corrosion tests.

Solution	Composition
A*	3.5% NaCl solution
B	Sodium chromate + 3.5% NaCl solution
C	*Parkia biglobosa* + 3.5% NaCl solution
D	*Parkia biglobosa* + Boehmite Nanoparticles + 3.5% NaCl solution
E	*Vitex doniana* + 3.5% NaCl solution
F	*Vitex doniana* + Boehmite Nanoparticles + 3.5% NaCl solution
G	3.5% NaCl solution + *Parkia biglobosa* + *Vitex doniana*
H	Boehmite Nanoparticles + *Parkia biglobosa* + *Vitex doniana* + 3.5% NaCl solution

* Control

3.5 Pre-Corrosion Materials Characterisation

X-Ray Fluorescence, Scanning Electron Microscopy, X-Ray Diffractometry and Raman Spectroscopy were used to characterize the as-cast alloys before the corrosion tests. See section 3.8 for details.

3.6 Sample Preparation for Corrosion Testing

The working electrodes (the cast alloys) were machined to cylindrical shape coupons of dimensions 15mm x 10mm. A total of 300 coupons were used for all the tests carried out in this work. The coupons were polished with silicon carbide (SiC) grit papers of various grades (80, 120, 220, 320, 600, 800, and 1000).

3.6.1 Preparation of Samples for Gravimetric-Based Mass Loss

The coupons used for gravimetric-based mass loss were prepared according to the procedure recommended by ASTM G 1, in which a hole about 5mm was drilled at one end of the sample and a thread was attached for hanging them in the electrolytes.

3.6.2 Preparation of Samples for Electrochemical Testing

The coupons used for the electrochemical tests were attached with 20cm copper wires, mounted using epoxy mounting resin (Araldite), with the connecting copper wire protected (i.e. electrically insulated) by a rigid plastic tube extending into the mounting mould so as to offer an active flat disc-shaped surface to contact the test solutions. After mounting, they were further *Micro-polished* using Digital polishing machine (Struers TegraPol-11/TegraDoser-5) using *Dia Duo*, a Diamond suspension containing premium quality monocrystalline diamonds and cooling lubricant, of grades 15µm, 6µm 3µm and 1µm successively to obtain a mirror-like surface, degreased by immersion in boiling benzene for 5 minutes, cleaned, dried and stored in a desiccator in accordance with ASTM-G59-97 specification. Samples used for characterisation, prior to the corrosion tests, were also drawn from these.

3.7 Corrosion Testing

3.7.1 Electrochemical Techniques

Electrochemical techniques of Linear Polarisation Resistance, Chronopotentiometry and Electrochemical Impedance Spectroscopy were employed for evaluating the corrosion characteristics of the alloy. An Autolab computer-controlled Potentiostat/Galvanostat (PGSTAT 30 model, Metrohm) with an in-built General Purpose Electrochemical Software (GPES) version 4.9 was used for all the electrochemical tests carried out in this work. The test coupons were used as working electrodes (WE). The supplied current goes into the working electrode through the counter electrode (CE) made from graphite rods. All measurements were with reference to silver silver Chloride 3M KCl and taken at

room temperature (30±2^{o}C). Fresh solutions were used for each test run to avoid interference from corrosion products.

3.7.1.1 Linear Polarisation Resistance (LPR)

The electrochemical polarization measurements were taken after 30 minutes of immersion of the working electrodes into the solutions, to allow for attainment of quasi-stationary value for the Open Circuit Potential (OCP). The steady-state OCP corresponds to the corrosion potential ($\boldsymbol{E_{corr}}$) of the working electrode. A single compartment cell was used in which the working electrode was placed in the centre of the cell surrounded by the counter electrode. The auxiliary electrode was individually isolated from the test solution by a glass frit. Figure 3.1 shows a schematic representation of the linear polarisation experimental set-up.

The working electrode potentials were measured with reference to the silver silver chloride reference electrode and plotted against current in external circuit. The anodic and cathodic polarisation curves, through cathodic potential of -20mV versus $\boldsymbol{E_{corr}}$ to an anodic potential of +20mV versus $\boldsymbol{E_{corr}}$ at a scan rate of 0.125mVs^{-1}, were obtained and used to determine the polarisation resistance $\boldsymbol{R_p}$ for each experimental set-up. The linear Tafel segments of the anodic and cathodic curves were extrapolated to corrosion potential to obtain the corrosion current densities $\boldsymbol{I_{corr}}$, the anodic $\boldsymbol{\beta_a}$ and cathodic $\boldsymbol{\beta_c}$ Tafel constants were also estimated. The Inhibition Efficiencies, ***IE%,*** were calculated from the measured polarization resistance values according to the mathematical expressions respectively:

$$IE\% = \frac{R_p^i - R_p^o}{R_p^i} \text{ x } 100 \qquad (3.1)$$

is the polarisation resistance of uninhibited system.

is the polarisation resistance of inhibited system.

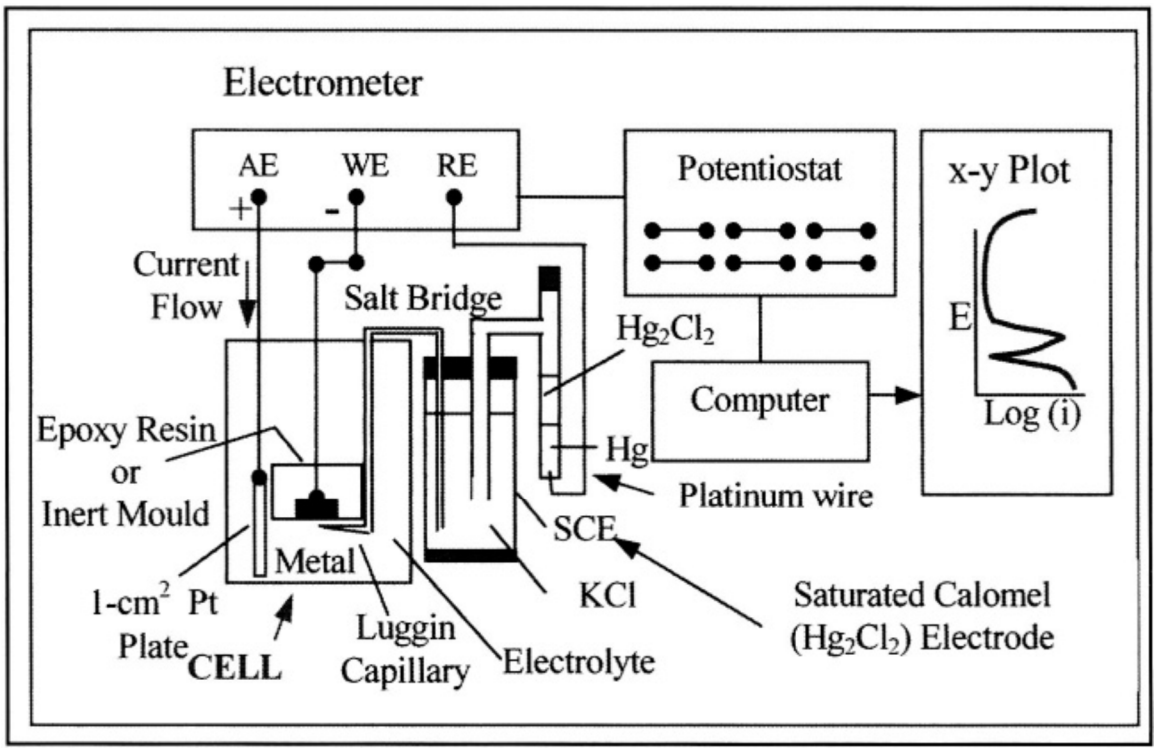


Figure 3.1: Schematic of linear polarisation experimental circuit.
(*Source*: Nestor, 2004).

3.7.1.2 Electrochemical Impedance Spectroscopy (EIS)

EIS measurements were taken using Potentiostat/Galvanostat (PGSTAT 30 model) described previously using AC signals of amplitude 5mV peak to peak at an open circuit potential (OCP), $\boldsymbol{E_{corr}}$ and in the frequency range of 100 kHz to 10 Hz. Figure 3.2 is a simplified instrumentation of the EIS experimental set-up. The data taken were analysed using an in-built NOVA software containing a Frequency Response Analyser (FRA) tool. The real part **(Z)** and imaginary part **(Z)** of the cell impedance were measured in $\boldsymbol{\Omega cm^2}$ at various frequencies and the characteristic impedance spectra generated were depicted in

the **NYQUIST** diagrams. The values for the charge transfer resistance $\mathbf{R_{ct}}$ were calculated using the diameter of the semicircle of the Nyquist plots, while the double layer capacitance magnitudes, $\mathbf{C_{dl}}$, were computed by equation 3.3 below:

$$f\{Z_{i(\max)}\} = \frac{1}{2\pi C_{dl} R_t} \tag{3.2}$$

$Z_{i(\max)}$ is the maximum cell impedance.
R_t is the charge transfer resistance.
C_{dl} is the capacitance of the double layer.
π is the phase angle.

Inhibition Efficiencies ***IE%*** and surface coverages $\boldsymbol{\theta}$ were computed using the following mathematical expressions respectively:

$$IE\% = \frac{R_t^i - R_t^u}{R_t^i} x\ 100 \tag{3.3}$$

R_t^u is the charge transfer resistance of the uninhibited system.
R_t^i is the charge transfer resistance of the inhibited system.

When a non-ideal frequency response is present, it is commonly accepted to employ distributed circuit elements in an equivalent circuit. The most widely used is constant phase element (*CPE*), which has a non-integer power dependence on the frequency. The impedance spectra for the Nyquist plots were further analysed by fitting to the equivalent circuit model shown in Figure 3.3.

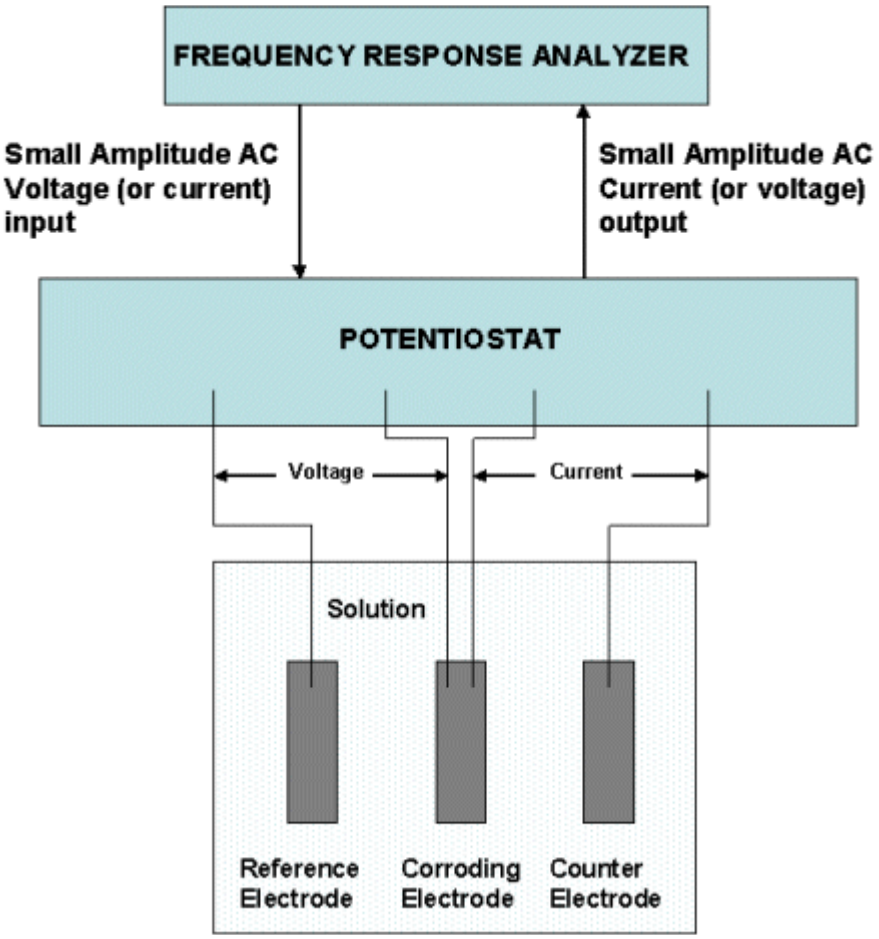


Figure 3.2: A simplified instrumentation of the EIS experimental set-up.

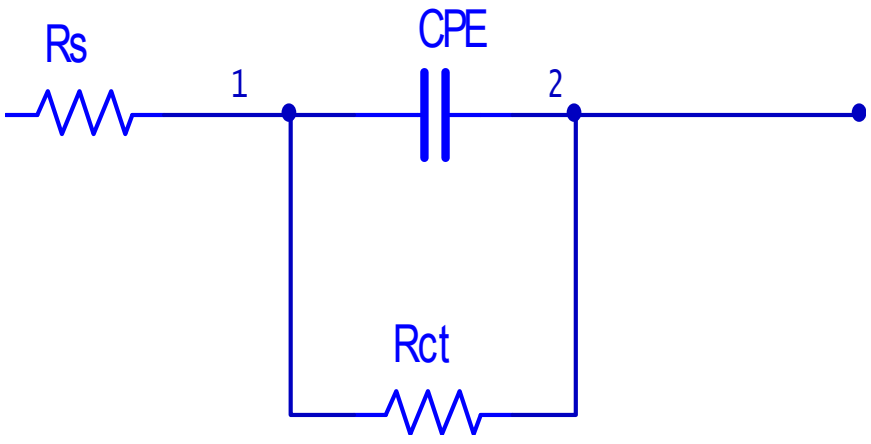


Figure 3.3: Electrochemical equivalent circuit used to fit the impedance spectra.

3.7.1.3 Chronopotentiometry

The same Potentiostat/Galvanostat (PGSTAT 30) equipment was used to measure variations in the open circuit potential of the test coupons 30 minutes after they were immersed in the different test solutions.

3.7.2 Gravimetric-Based Mass Loss

Coupons prepared for this test were weighed and fully immersed into 100ml of the different test solutions by hanging with threads as elucidated in Table 3.2. The solutions were heated to temperatures of 30, 40, 50, 60 and 70^{o}C. The coupons were left in the solutions for a period of 1 to 5 hours. After each time period, the coupons were removed from the solutions, cleaned with distilled water, dried using tissue paper and weighed. In each case, the mass losses were used to calculate corrosion rates, from which the Inhibition Efficiencies (**IE%**) were computed using equations 2.51. The pH of the solutions was monitored throughout the corrosion tests.

3.8 Post-Corrosion Materials Characterisation

After corrosion tests, the coupons were characterized using Scanning Electron Microscope (SEM/EDX), XRD and Raman Spectroscopy.

3.8.1 Scanning Electron Microscopy/ Energy Dispersive Spectrometry (SEM/EDS)

The morphological observations of the samples were carried out using a Scanning Electron Microscope model JOEL 840. At other points, a Phillips (XL30 SERIES) Environmental Scanning Electron Microscope (ESEM) equipped with a field emission gun operating between 5 and 30kV was used to assess the microstructure of the polished samples. Elemental analysis was done using Energy Dispersive Spectrometer (EDS)

(INCA Energy, IE450 system, Oxford Instrument, UK). Initially, the samples were carbon-coated before analysis in order to make their surfaces conductive.

3.8.2 X-Ray Diffraction (XRD)

X-ray diffraction analyses of the coupons before and after corrosion tests were carried out using a PW1710 Philips powder diffractometer having monochromatic Cu Kα radiation at 40kV and 20mA. This was accomplished by scraping the surface of the coupons, accumulating the powder removed in this manner on double stick tape attached to a glass. X-ray diffraction patterns **(**Diffractograms**)** were produced over a range of 2θ and between 10-80^{o}, with a step size of 0.02. Then standard diffraction data for pure phases, obtained from International Centre for Diffraction Data (ICDD, USA) database using JCPDS (Joint Committee on Powder Diffraction Standards, Swathmore, Pennsylvania, 1986) cards, were used to identify the phases present in the coupons; by comparing the measured d-spacing in the diffraction pattern and, to a lesser extent, their integrated intensities with the JCPDS cards.

3.8.3 Raman Spectroscopy

Raman experiments were conducted using a SENTERRA dispersive Raman microscope. The instrument was calibrated using a silicon wafer. A 50X magnification microscope was used to focus the 534nm excitation laser beam. The laser powder used on the samples was 5mW and the spectra of the coupons were recorded over a range of 50-3000 cm^{-1} after acquisition time of 10 s. An OPUS^{TM} software was used for data acquisition and analysis.

CHAPTER FOUR

4.0 RESULTS

4.1 X-Ray Fluorescence result of the Cast Alloy (AA2024)

Table 4.1: X-Ray Fluorescence (XRF) results of the test alloy under investigation.

Class of alloy	Alloy name	%Cu	%Mg	%Mn	%Ni	%Fe	%Al
2xxx	AA2024	4.25±0.03	1.30±0.04	0.48±0.03	0.01±0.03	0.22±0.03	93.74±0.03

4.2 NMR Spectra of ethanolic leave extracts of *Parkia biglobosa* & *Vitex doniana.*

Figures 4.1 and 4.2 depict the spectra of the Nuclear Magnetic Resonance-based metabolomics of the two plant extracts.

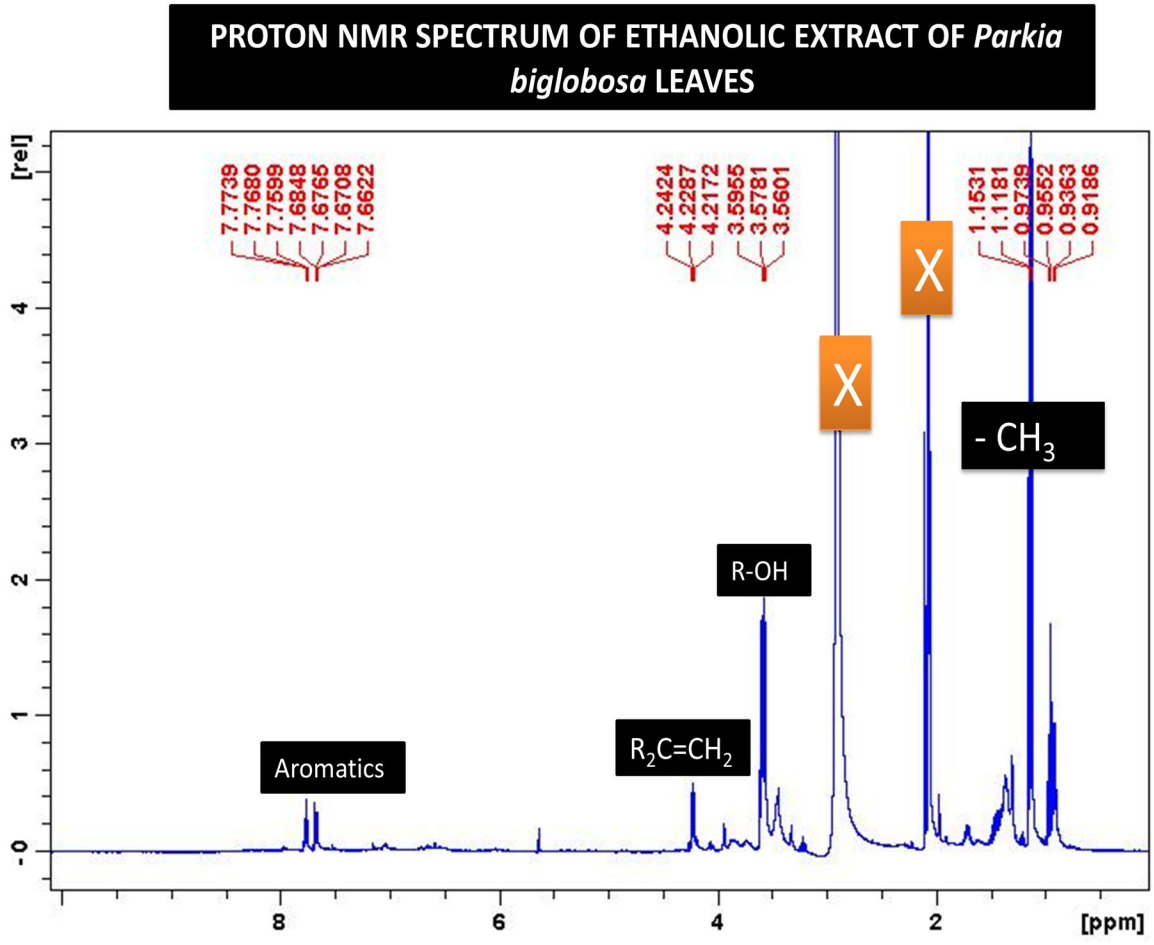


Figure 4.1: Proton NMR Spectrum of Ethanolic Extract of ***Parkia biglobosa*** (PBE) leaves extracts.

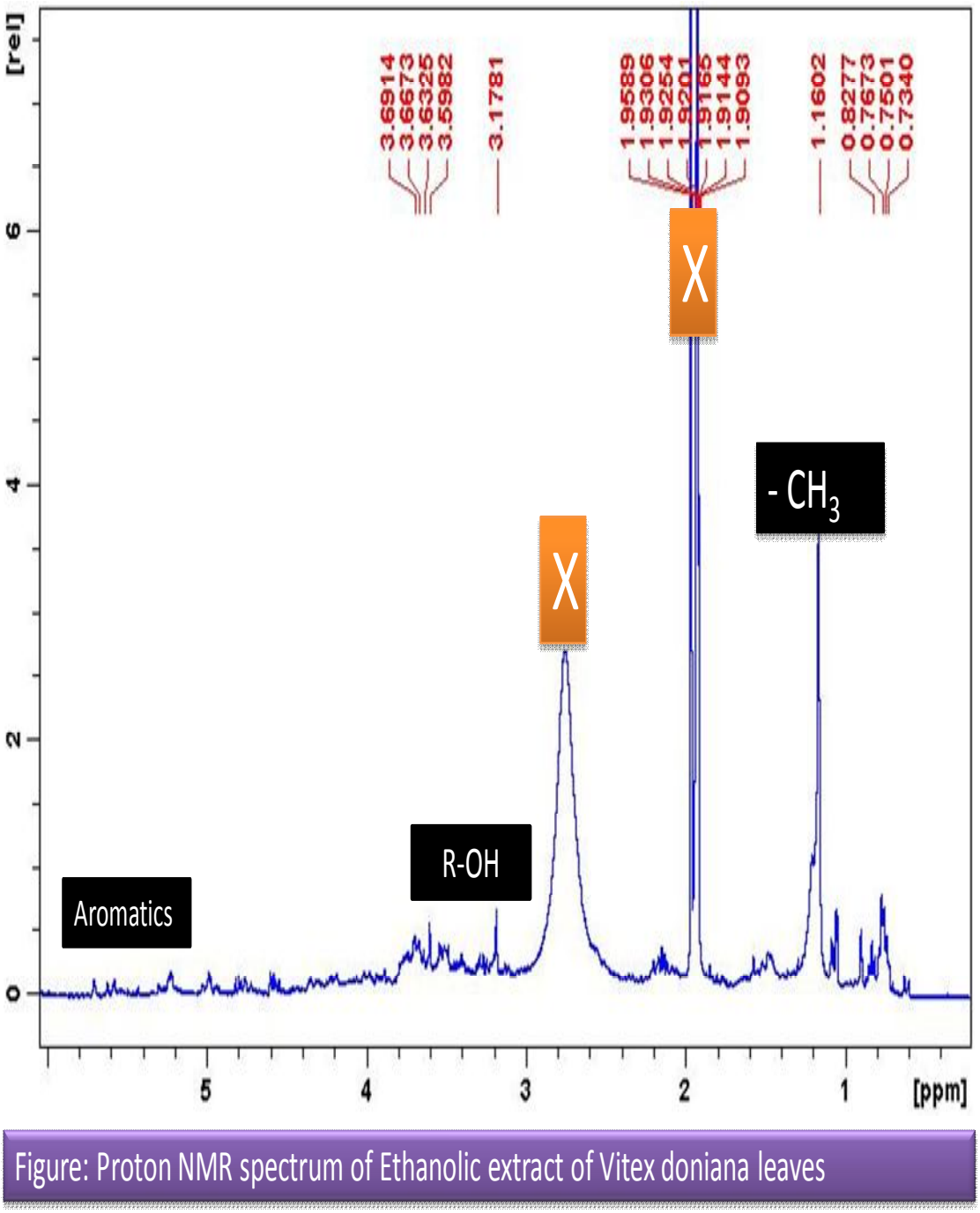


Figure: Proton NMR spectrum of Ethanolic extract of Vitex doniana leaves

Figure 4.2: Proton NMR spectrum of Ethanolic extract of ***Vitex doniana*** (V*DE*).

4.3 Corrosion Testing

4.3.1 Classical method

The visual examination & mass loss examination of the test samples were the two classical procedures employed to investigate the corrosion behaviour of the test samples.

4.3.1.1 Visual examination

Visual examination of the coupons exposed to the aggressive Sodium chloride medium was undertaken to assess the severity of the attack on the alloy.

4.3.1.2 Effect of Temperature and Concentration on Inhibition Efficiencies (IE%)

Figure 4.3 below shows the variation of corrosion rates with temperature (30-70^{o}C) for the test alloy in control (3.5%NaCl) solution.

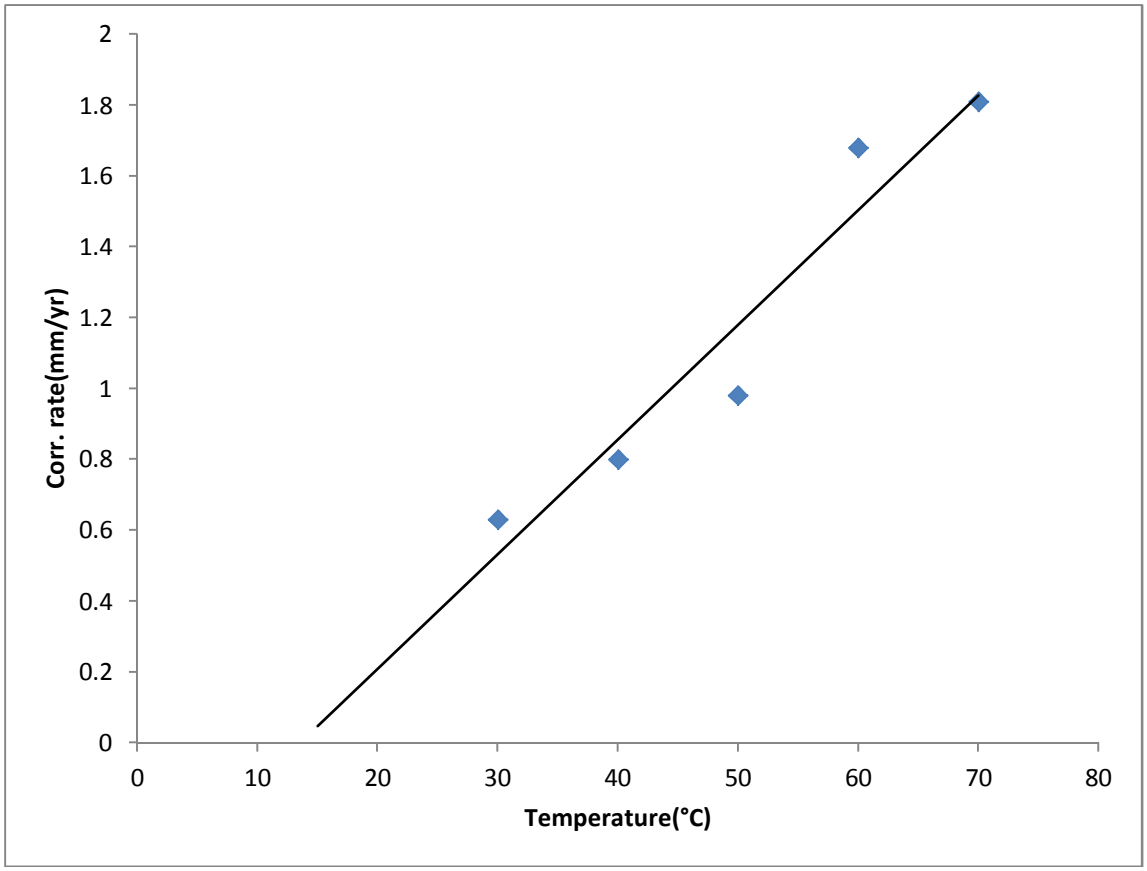


Figure 4.3: Variation of corrosion rates with temperatures for the test sample in control (3.5%NaCl) solution.

Figures 4.4-4.10 show the variation of temperature and concentration for the test alloy under the influence of different inhibiting systems investigated.

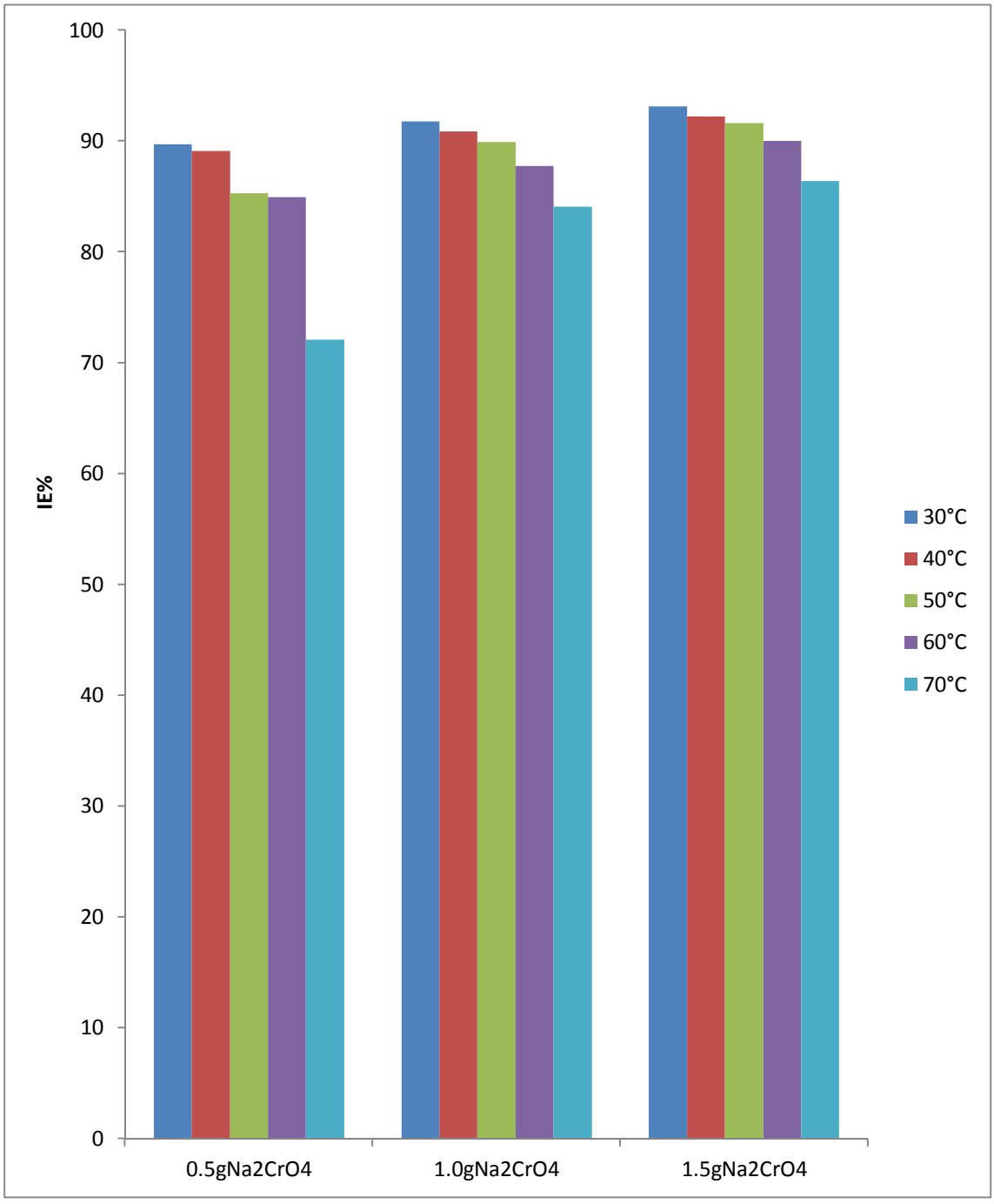


Figure 4.4: Variation of Inhibition Efficiencies (IE%) with different amounts of Na_2CrO_4 at different temperatures.

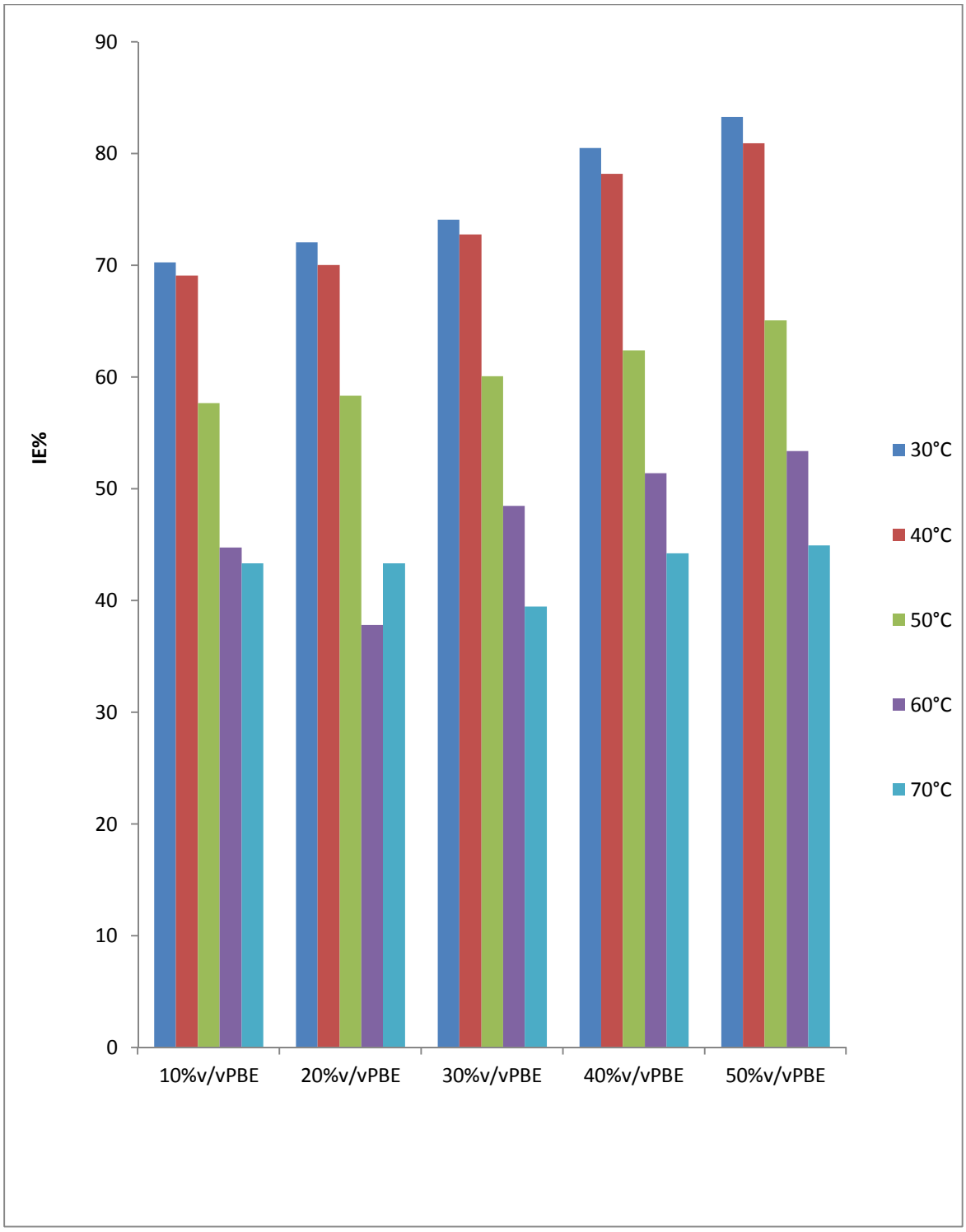


Figure 4.5: Variation of Inhibition Efficiencies (IE%) with different concentrations of *Parkia biglobosa* extracts at different temperatures.

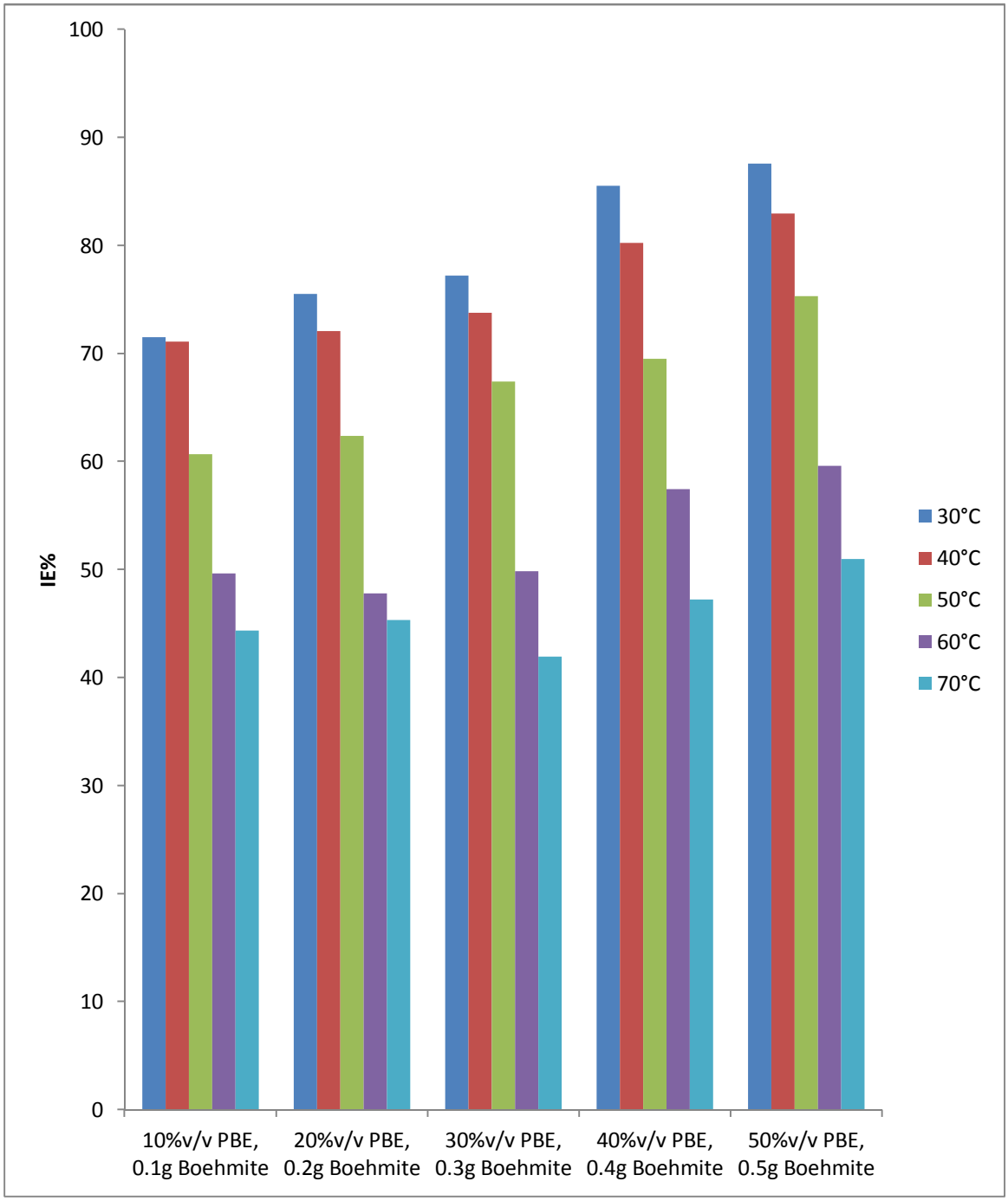


Figure 4.6: Variation of Inhibition Efficiencies (IE%) with different concentrations of *Parkia biglobosa* extracts + Boehmite Nanoparticles at different temperatures.

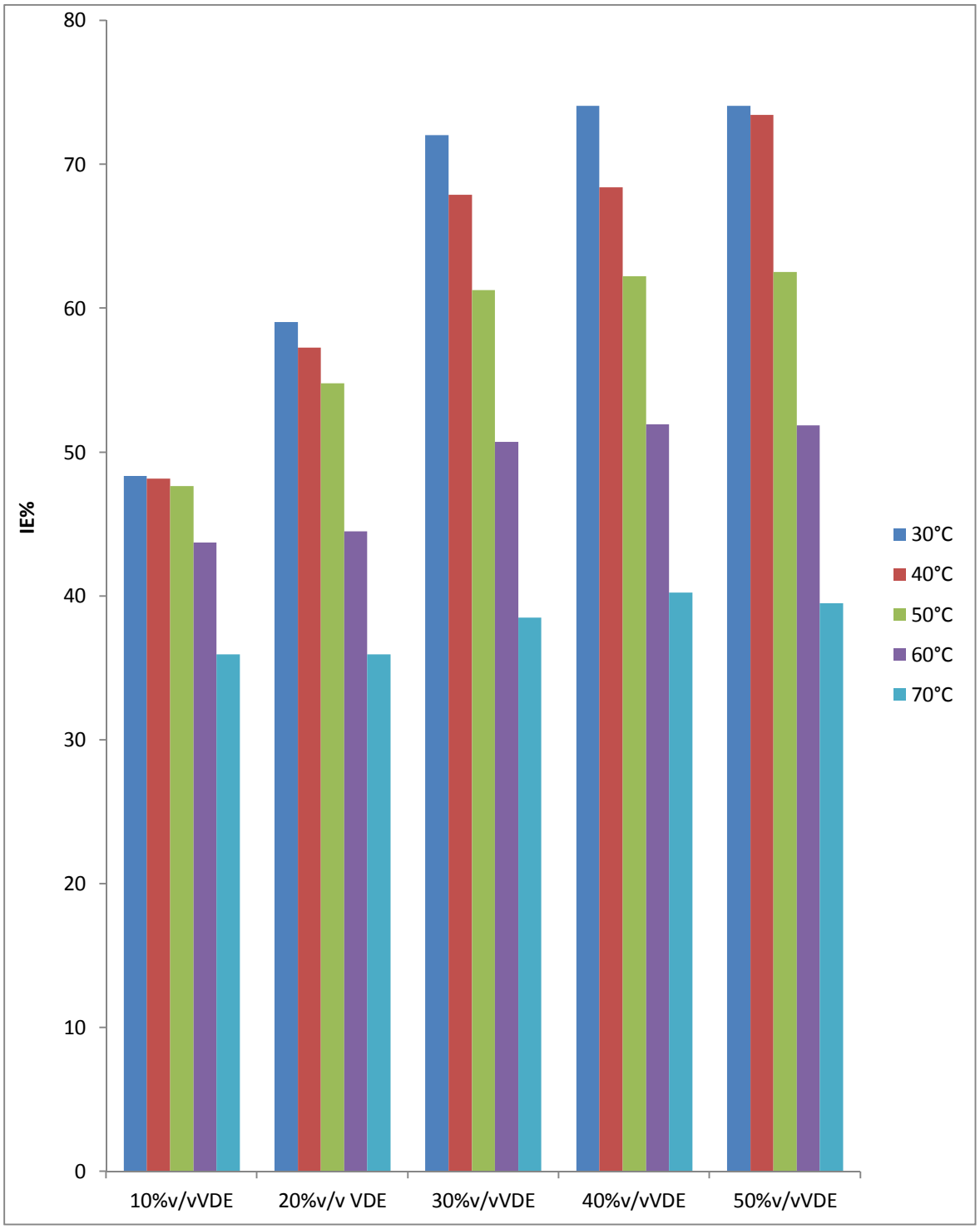


Figure 4.7: Variation of Inhibition Efficiencies (IE%) with different concentrations of *Vitex doniana* extracts at different temperatures.

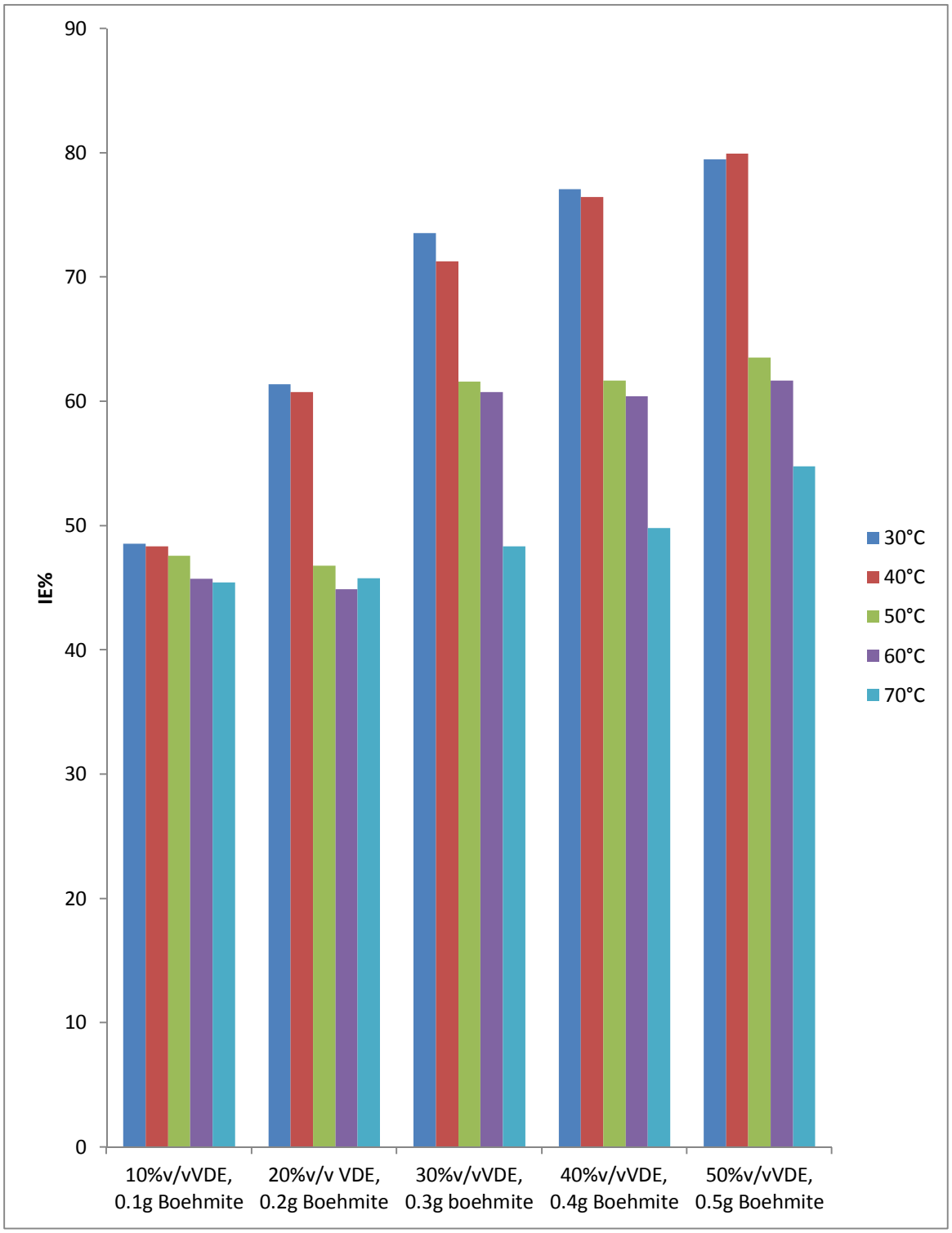


Figure 4.8: Variation of Inhibition Efficiencies (IE%) with different concentrations of *Vitex doniana* extracts + Boehmite Nanoparticles at different temperatures.

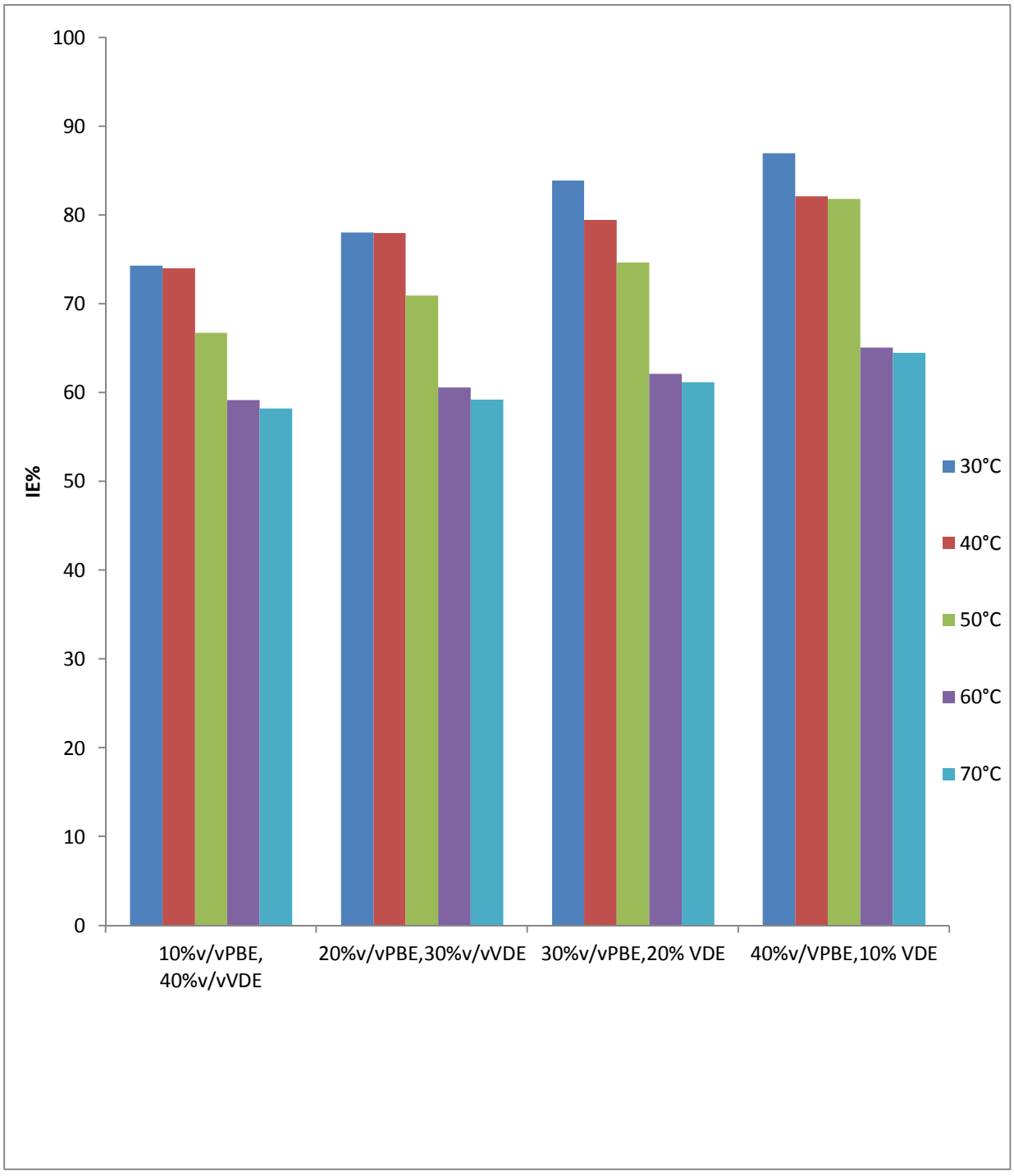


Figure 4.9: Variation of Inhibition Efficiencies (IE%) with different concentrations of *Parkia biglobosa* + *Vitex doniana* extracts at different temperatures.

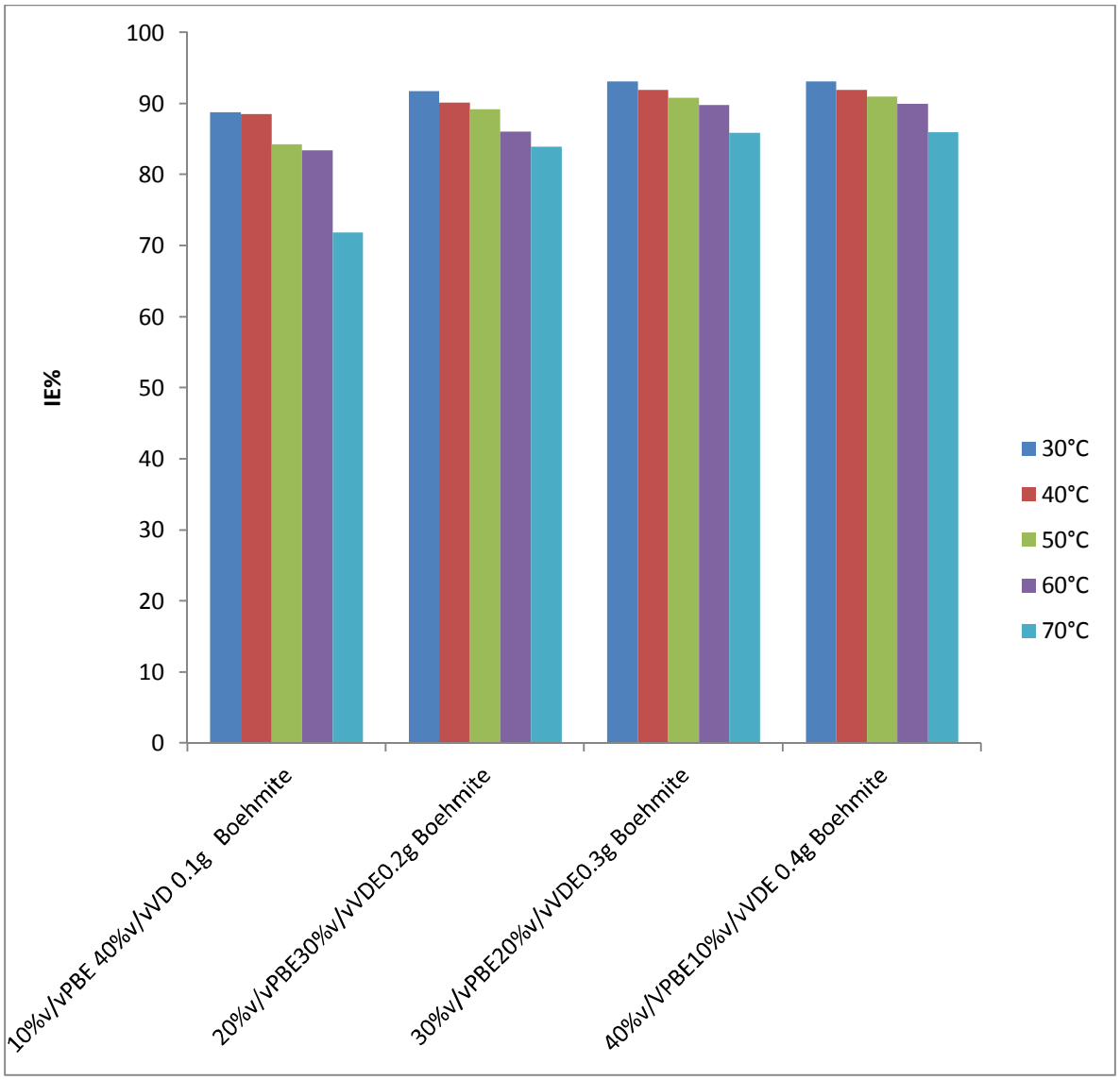


Figure 4.10: Variation of Inhibition Efficiencies (IE%) with different concentrations of *Parkia biglobosa+Vitex doniana* extracts+Boehmite Nanoparticles at different temperatures.

4.3.2 Linear Polarisation Resistance

The corrosion kinetic parameters were computed on the basis of cathodic and anodic potential versus current characteristics in the Tafel regions, shown in Figures 4.11 – 4.17. The corrosion parameters such as corrosion potential (E_{corr}), corrosion current density (j_{corr}), and cathodic (β_c) and anodic (β_a) Tafel slope are listed in Tables 4.2 - 4.8.

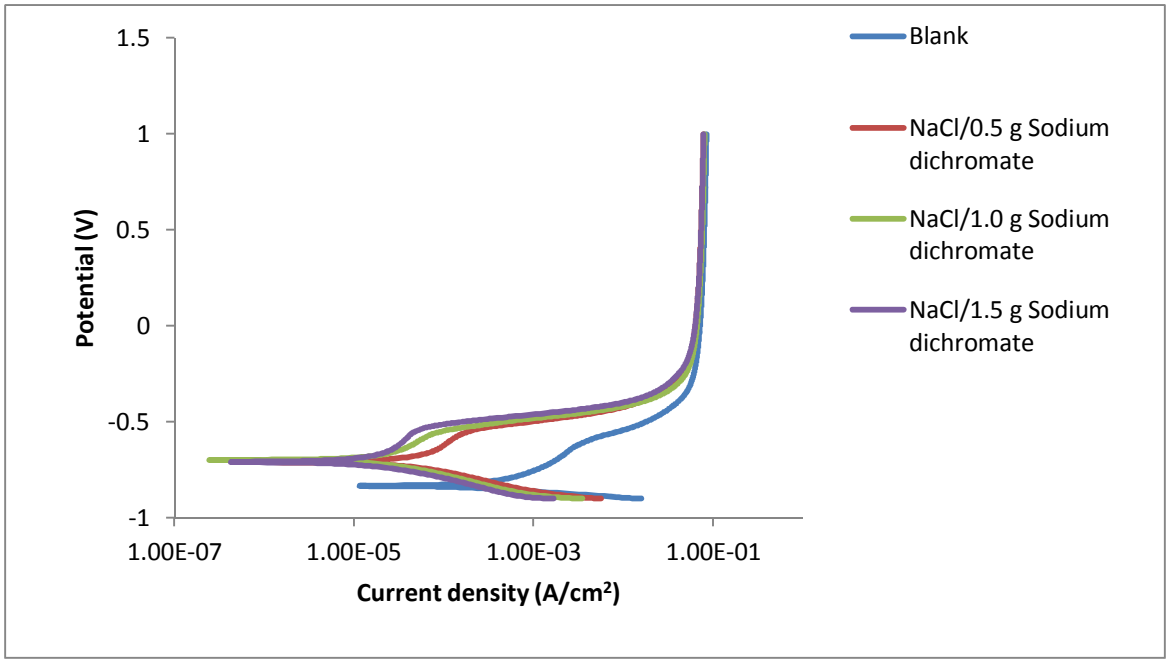


Figure 4.11: Polarisation curves for AA2024 containing different concentrations of Na_2CrO_4 at room temperature.

Table 4.2: Polarisation parameters and the corresponding Inhibition Efficiencies (IE%) for the corrosion of AA2024 Aluminium Alloy in 3.5%NaCl containing different concentrations of $NaCr_2O_4$ at room temperature.

Inh. Conc.	β_a (mV/dec)	β_c (mV/dec)	E_{corr} (mV)	j_{corr} (µA/ cm²)	i_{corr} (µA)	Corr. rate (mm/yr)	R_p(Ω)	IE%
Blank	6.37	7.48	-633	48.3	85.5	1.78	132.84	---
NaCl/0.5 g $NaCr_2O_3$	22.1	17.25	-710	1.84	3.26	0.062	1290	89.99
NaCl/1.0 g $NaCr_2O_3$	30.58	25.84	-699	1.79	3.17	0.06	1920	92.57
NaCl/1.5 g $NaCr_2O_3$	18.75	29.3	-708	0.99	1.77	0.03	2810	93.11

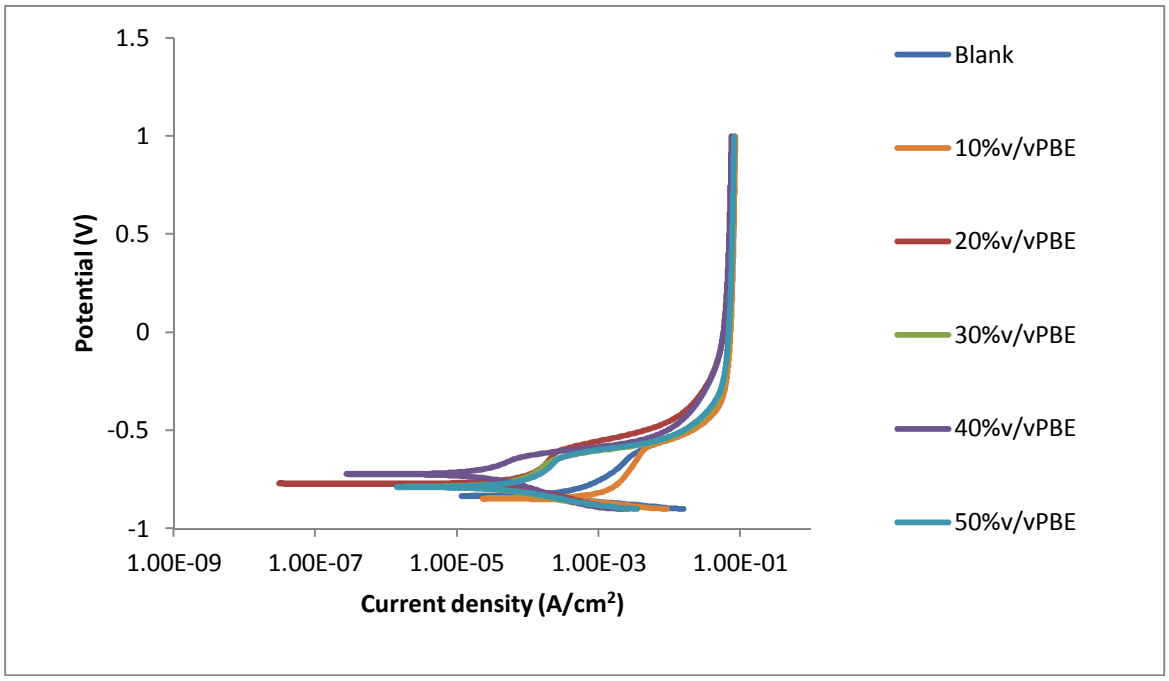


Figure 4.12: Polarisation curves for AA2024 containing different concentrations of PBE at room temperature.

Table 4.3: Polarisation parameters and the corresponding Inhibition Efficiencies (IE%) for the corrosion of AA2024 Aluminium Alloy in 3.5%NaCl containing different concentrations of PBE at room temperature

Inh. Conc.	β_a (mV/dec)	β_c (mV/dec)	E_{corr} (mV)	j_{corr} (µA/cm²)	i_{corr} (µA)	Corr. rate (mm/yr)	$R_p(\Omega)$	IE%
Blank	6.37	7.48	-633	48.3	85.5	1.78	132.84	---
10%v/v PBE	17.83	20.62	-837	17.3	30.7	0.58	135.41	67.99
20% v/v PBE	8.97	19.58	-832	15.5	27.4	0.52	97.50	71.64
30% v/v PBE	14.06	13.44	-842	10.9	19.3	0.37	154.35	72.77
40% v/v PBE	53.92	26.29	-778	5.77	10.2	0.142	749.33	81.99
50% v/v PBE	10.64	17.13	-813	4.19	7.41	0.195	3840	80.33

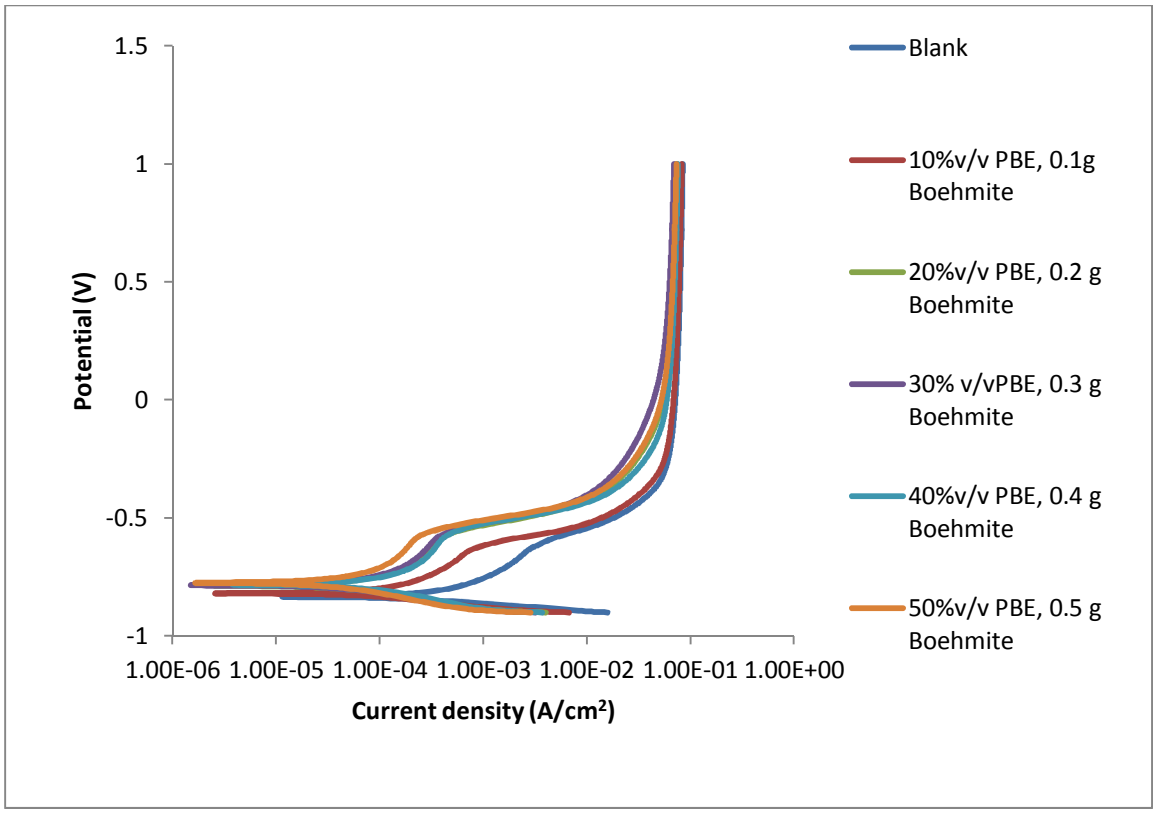


Figure 4.13: Polarisation curves for AA2024 containing different concentrations of PBE+ Boehmite at room temperature.

Table 4.4: Polarisation parameters and the corresponding Inhibition Efficiencies (IE%) for the corrosion of AA2024 Aluminium Alloy in 3.5%NaCl containing different concentrations of PBE+Boehmite at room temperature.

Inh. Conc.	β_a	β_c	E_{corr} (mV)	j_{corr}	i_{corr} (µA)	Corr. rate (mm/yr)	$R_p(\Omega)$	IE%
Blank	6.37	7.48	-633	48.3	85.5	1.78	132.84	---
10%v/v PBE+ 0.1 g Boehmite	26.96	28.94	-819	12.7	22.7	0.43	269.46	70.40
20%v/vPBE+0.2 g Boehmite	32.07	31.25	-786	6.62	11.7	0.22	526.00	74.02
30%v/v PBE+ 0.3 g Boehmite	27.93	30.59	-784	5.63	10.1	0.19	622.51	77.89
40%v/v PBE+ 0.4 g Boehmite	21.08	13.48	-782	4.75	8.40	0.16	772.1	85.99
50%v/v PBE+ 0.5 g Boehmite	18.91	27.28	-775	3.55	6.28	0.12	425.00	83.00

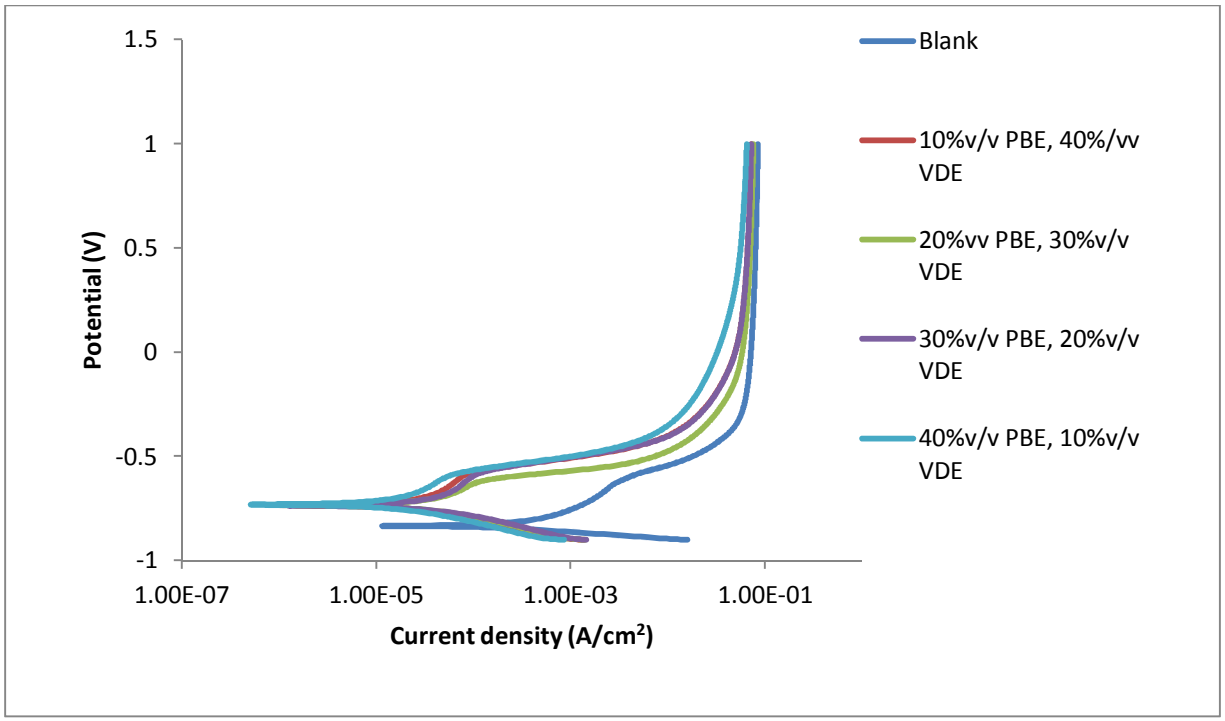


Figure 4.14: Polarisation curves for AA2024 containing different concentrations of PBE+ VDE at room temperature.

Table 4.5: Polarisation parameters and the corresponding Inhibition Efficiencies (IE%) for the corrosion of AA2024 Aluminium Alloy in 3.5%NaCl containing different concentrations of PBE+VDE at room temperature.

Inh. Conc.	**β_a**	**β_c**	**E_{corr} (mV)**	***j_{corr}* (µA/cm²)**	***i_{corr}* (µA)**	Corr. rate (mm/yr)	**R_p (Ω)**	**IE%**
Blank	6.37	7.48	-633	48.3	85.5	1.78	132.84	-- -
10%v/v PBE+ 40%v/v VDE	37.456	24.814	-732	6.36	11.3	0.08051	1537.40	73.97
20%v/v PBE+ 30%v/v VDE	26.978	19.864	-735	3.45	6.11	0.09775	918.23	71.00
30%v/v PBE+ 20%v/v VDE	28.324	24.919	-735	2.89	5.12	0.01670	1111.30	79.99
40%v/v PBE+ 10%v/v VDE	22.003	24.942	-731	2.38	4.22	0.01502	1439.30	82.98

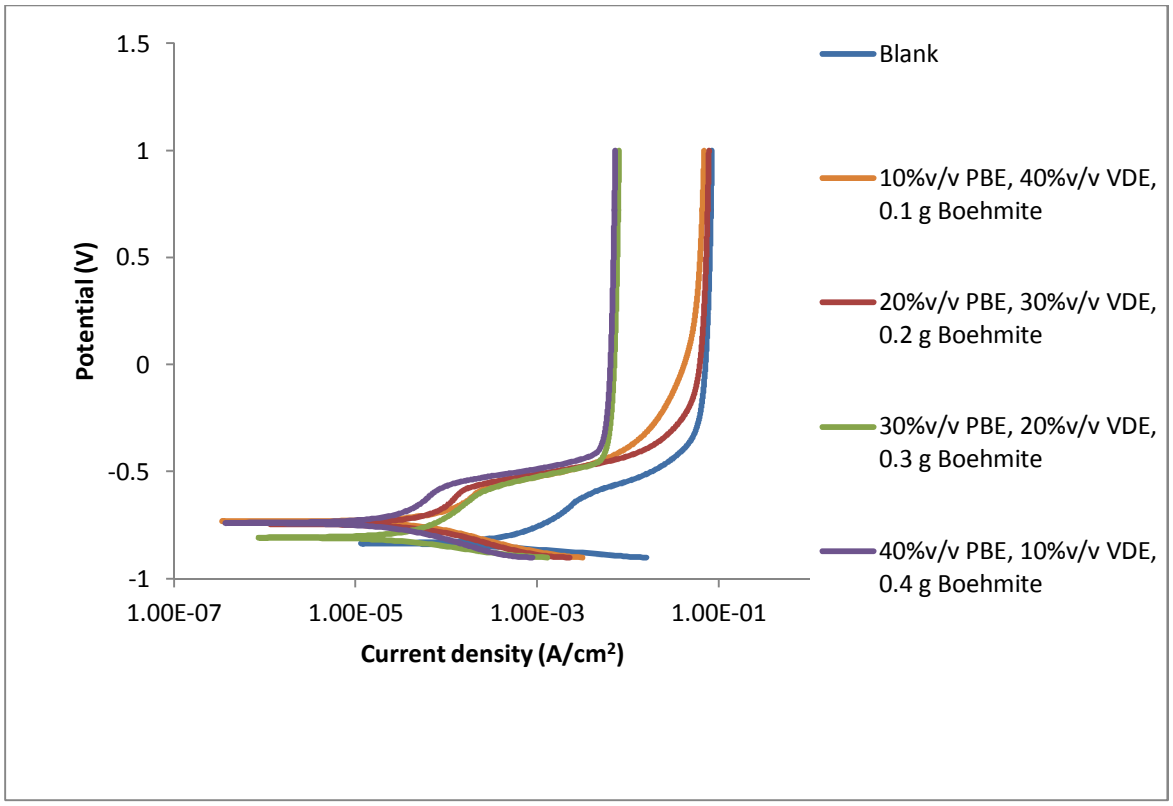


Figure 4.15: Polarisation curves for AA2024 containing different concentrations of PBE+VDE+Boehmite at room temperature.

Table 4.6: Polarisation parameters and the corresponding Inhibition Efficiencies (IE%) for the corrosion of AA2024 Aluminium Alloy in 3.5%NaCl containing different concentrations of PBE+VDE+ Nano Boehmite at room temperature.

Inh. Conc.	**β_a(mV/ dec)**	**β_c(mV /dec)**	**E_{corr} (mV)**	**j_{corr} (µA/ cm²)**	**i_{corr} (µA)**	**Corr. rate (mm/year)**	**R_p(Ω)**	**IE%**
Blank	6.37	7.48	-633	48.3	85.5	1.78	132.84	---
10%PBE+ 40%VDE+ 0.1g Boehmite	16.764	26.131	-731.6	7.06	12.5	0.2386	581.12	**88.76**
20%PBE+30 % VDE+0.2 g Boehmite	45.959	26.871	-743.1	6.34	11.2	0.2142	656.44	**91.32**
30%PBE+20 % VDE+0.3 g Boehmite	44.184	26.938	-806.6	4.86	8.60	0.1643	2444.9	**92.15**
40%PBE+10 % VDE+0.4 g Boehmite	46.413	24.721	-738.4	1.02	1.80	0.0344	2405.8	**92.13**

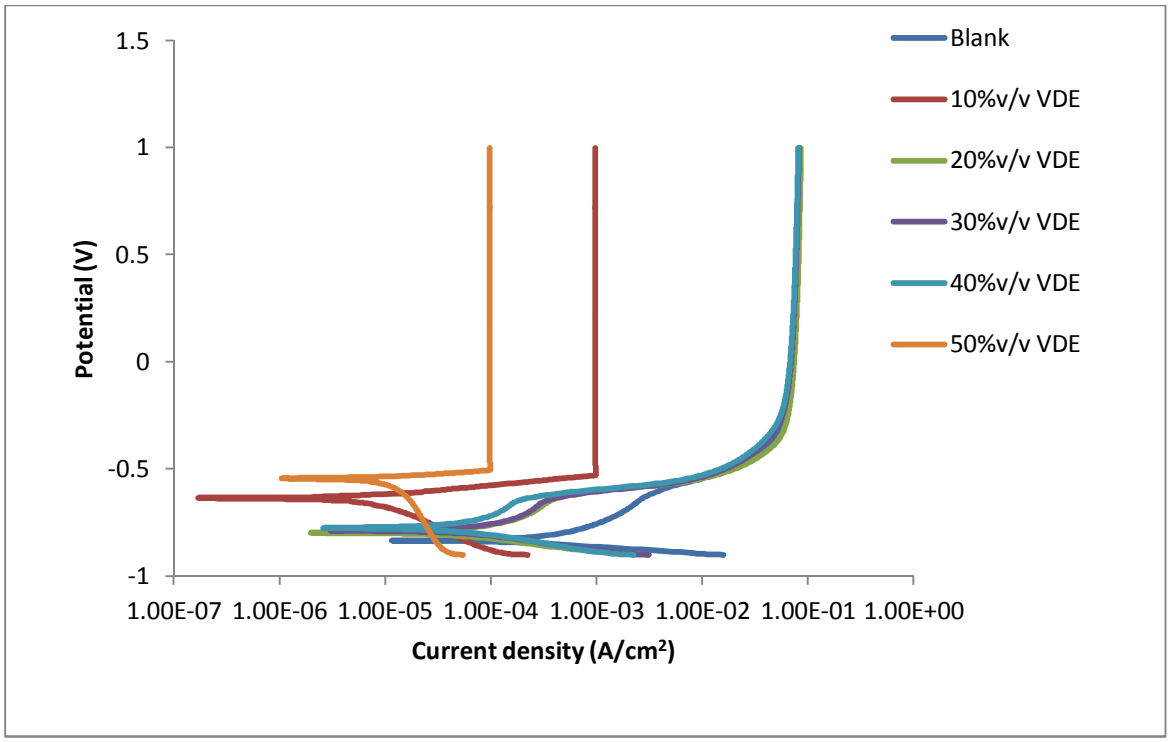


Figure 4.16: Polarisation curves for AA2024 containing different concentrations of VDE at room temperature.

Table 4.7: Polarisation parameters and the corresponding Inhibition Efficiencies (IE%) for the corrosion of AA2024 Aluminium Alloy in 3.5%NaCl containing different concentrations VDE at room temperature.

Inh. Conc.	β_a (mV/dec)	β_c (mV/dec)	E_{corr} (mV)	j_{corr} (µA/cm²)	i_{corr} (µA)	Corr rate (mm/yr)	R_p(Ω)	IE%
Blank	6.37	7.48	-633	48.3	85.5	1.78	132.84	---
10%v/v VDE	16.243	17.96	-634.98	12.03	7.872	0.16651	246.94	45.00
20% v/v VDE	8.653	21.622	-796.78	8.16	7.36	0.14061	364.46	60.02
30% v/v VDE	18.993	29.62	-786.82	7.32	6.96	0.14725	388.12	72.22
40% v/v VDE	27.102	48.603	-774.34	7.18	6.24	0.15279	570.79	71.76
50% v/v VDE	11.757	68.114	-542.56	0.493	5.90	0.06864	1211.3	71.99

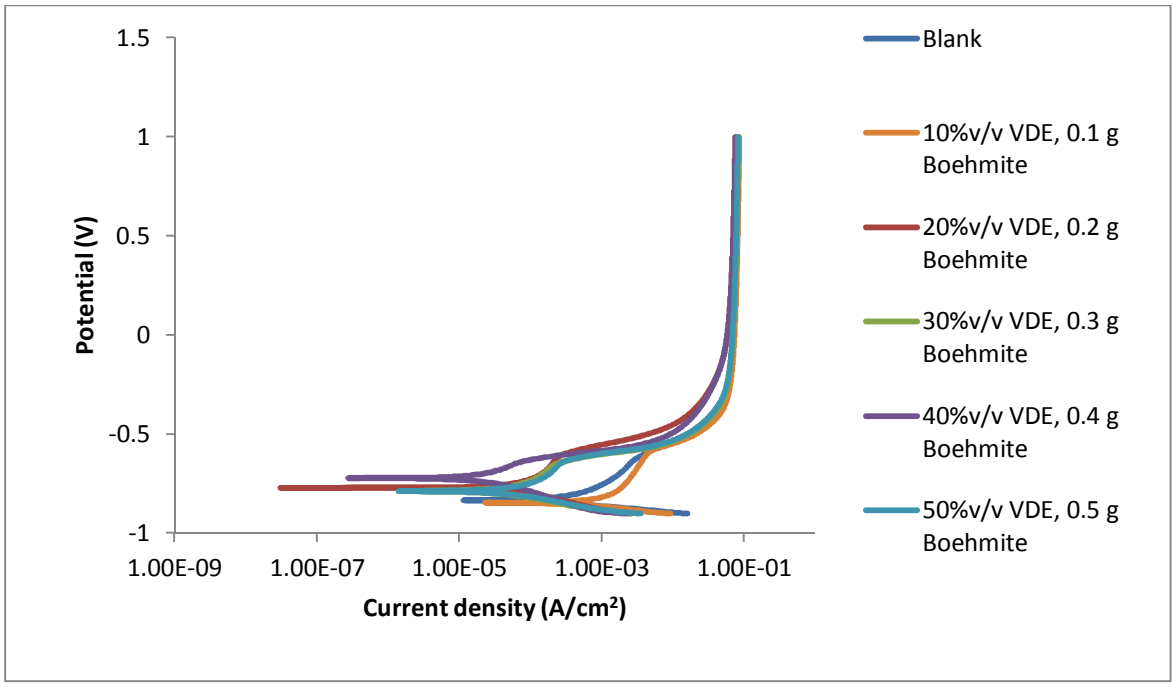


Figure 4.17: Polarisation curves for AA2024 containing different concentrations of VDE+Boehmite at room temperature.

Table 4.8: Polarisation parameters and the corresponding Inhibition Efficiencies (IE%) for the corrosion of AA2024 Aluminium Alloy in 3.5%NaCl containing different concentrations VDE+Boehmite Nanoparticles at room temperature.

Inh. Conc.	β_a (mV/dec)	β_c (mV/dec)	E_{corr} (mV)	j_{corr} (µA/cm²)	i_{corr} (µA)	Corr rate (mm/yr)	R_p (Ω)	IE%
Blank	6.37	7.48	-633	48.3	85.5	1.78	132.84	---
10%v/v VDE+0.1 g Boehmite	22.127	8.995	-846.75	23.2	30.7	1.6325	323.34	**45.89**
20% v/v VDE+0.2 g Boehmite	42.604	25.396	-770.58	8.45	15.0	0.28546	462.23	**60.46**
30% v/v VDE+0.3 g Boehmite	26.678	34.425	-786.95	5.25	9.29	0.17748	702.27	**71.04**
40% v/v VDE, 0.4 g Boehmite	37.803	20.598	-752.20	4.51	4.51	0.15248	1283.4	**76.11**
50% v/v VDE+0.5 g Boehmite	17.087	22.63	-788.14	3.95	6.99	0.13345	1604.99	**78.59**

4.3.3 Electrochemical Impedance Spectroscopy (EIS)

Figures 4.18 - 4.24 show the Nyquist diagrams for the different inhibitor systems investigated, while Tables 4.9 - 4.15 are the corresponding parameters derived from the Nyquist diagrams, in which Imaginary Impedance (**-Z′ Ω**) values were plotted against Real Impedance (**Z Ω**). The semicircle diameters in the Nyquist diagrams are related with the charge transfer resistance, $\boldsymbol{R_{ct}}$, which is equivalent to the polarization resistance $\boldsymbol{R_p}$.

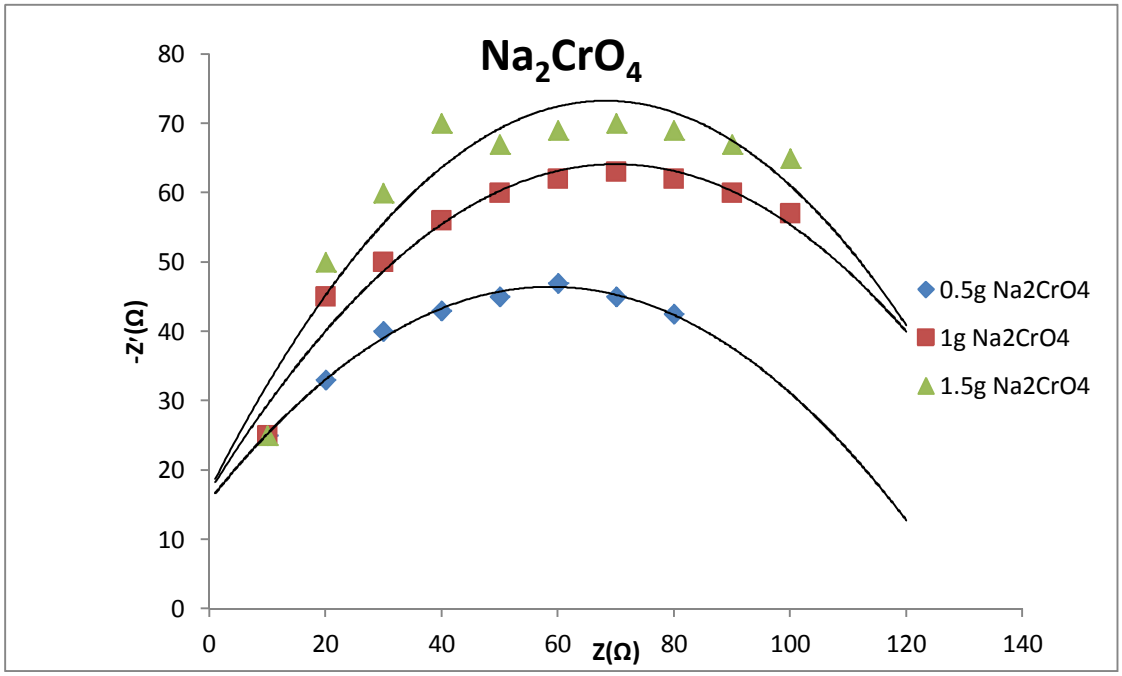


Figure 4.18: Nyquist diagram for AA2024 Aluminium Alloy Inhibited by Na_2CrO_4.

Table 4.9: Parameters obtained from Nyquist diagram for the corrosion of AA2024 coupons inhibited by Na_2CrO_4 in 3.5%NaCl solution at room temperature.

Inh. Conc. (v/v%)	R_s (Ωcm^2)	R_{ct} (Ωcm^2)	C_{dl} (µF)	IE%
0.5g Na_2CrO_4	**1.55**	**298.35**	**38.12**	**90.00**
1.0g Na_2CrO_4	**1.88**	**370.21**	**29.19**	**91.55**
1.5g Na_2CrO_4	**2.18**	**375.25**	**25.99**	**92.99**

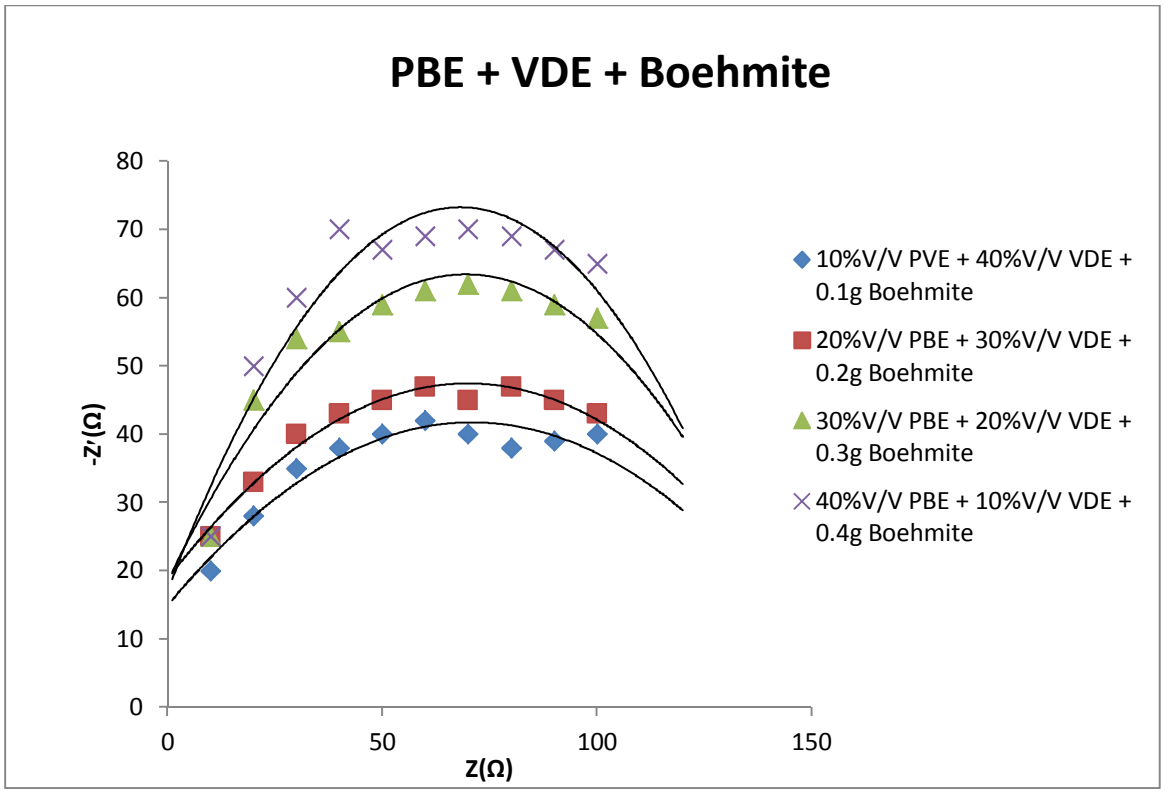


Figure 4.19: Nyquist diagram for AA2024 Aluminium Alloy Inhibited by PBE+VDE+NANO BOEHMITE system.

Table 4.10: Parameters obtained from Nyquist diagram for the corrosion of AA2024 coupons inhibited by PBE+VDE+Boehmite Nanoparticles system in 3.5%NaCl solution at room temperature.

Inh. Conc. (v/v%)	R_s (Ωcm^2)	R_{ct} (Ωcm^2)	C_{dl} (μF)	IE%
10%v/vPBE 40%v/vVDE 0.1g Boehmite	1.49	209.11	43.97	88.99
20%v/vPBE 30%v/vVDE 0.2g Boehmite	1.99	291.10	38.25	91.20
30%v/vPBE 20%v/vVDE 0.3g Boehmite	2.10	330.14	27.15	91.79
40%v/VPBE 10%v/vVDE 0.4g Boehmite	2.14	362.12	26.23	92.11

Sample

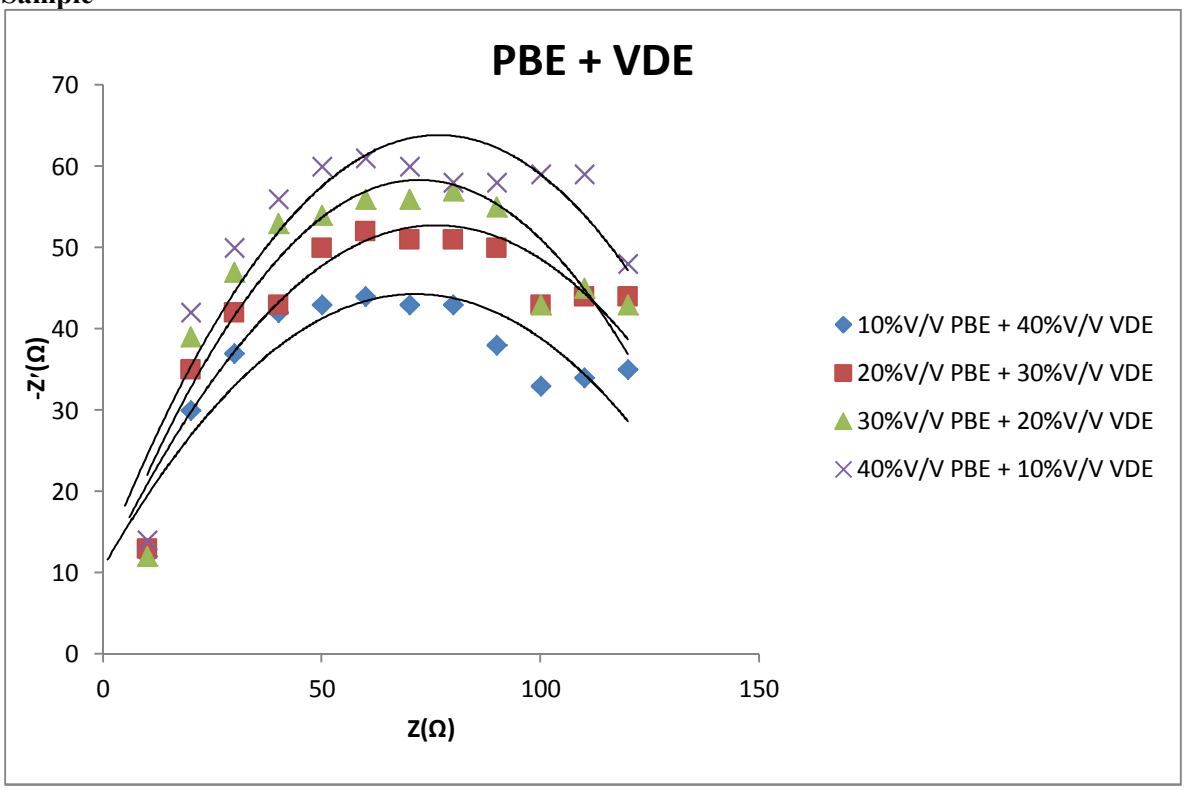


Figure 4.20: Nyquist diagram for AA2024 Aluminium Alloy Inhibited by PBE+VDE.

Table 4.11: Parameters obtained from Nyquist diagram for the corrosion of AA2024 coupons inhibited by PBE+VDE system in 3.5%NaCl solution at room temperature.

Inh. Conc. (v/v%)	R_s (Ωcm^2)	R_{ct} (Ωcm^2)	C_{dl} (μF)	IE%
10%v/vPBE 40%v/vVDE	1.27	181.11	48.11	74.12
20%v/vPBE 30%v/vVDE	1.43	191.23	37.92	70.27
30%v/vPBE 20%v/vVDE	1.71	201.17	25.25	80.19
40%v/VPBE 10%v/vVDE	1.88	211.53	24.19	82.99

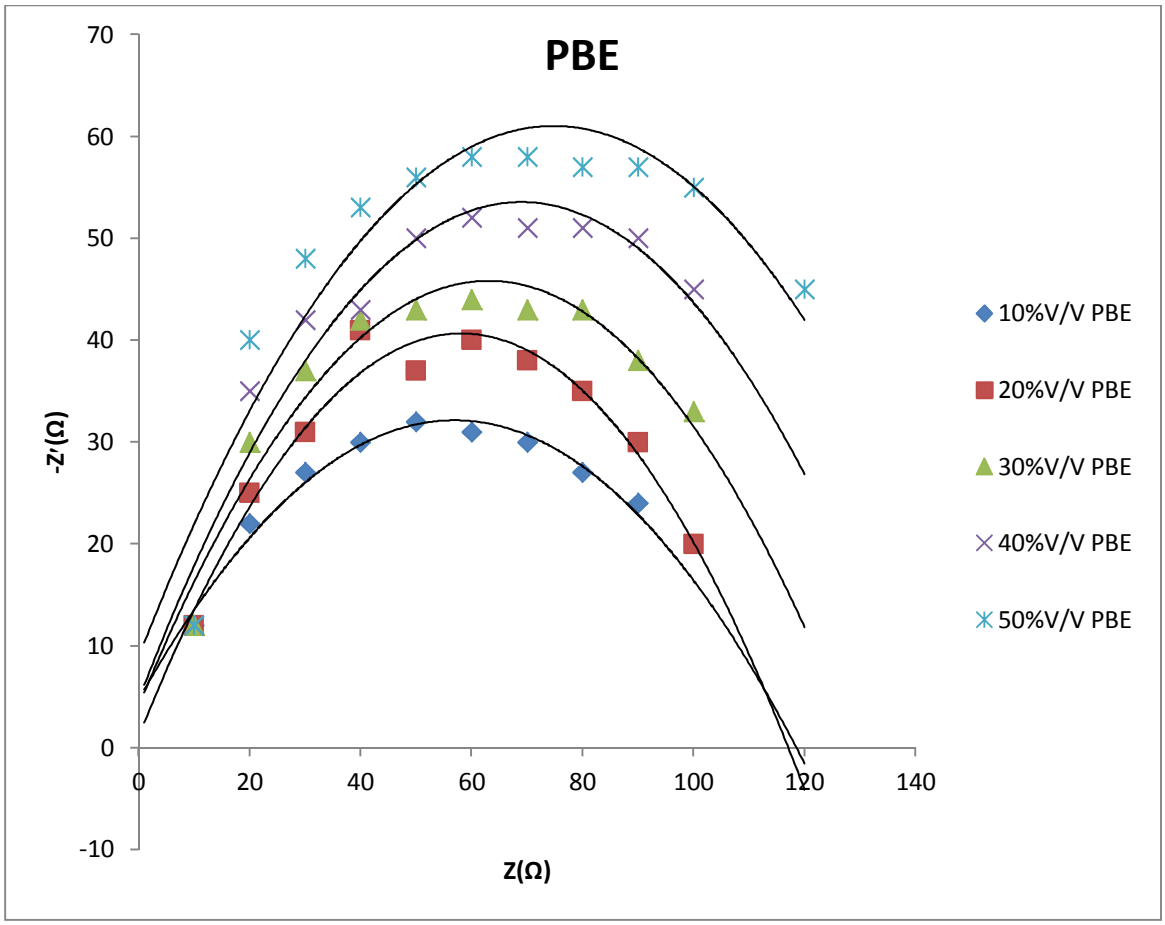


Figure 4.21: Nyquist diagram for AA2024 Aluminium Alloy Inhibited by PBE.

Table 4.12: Parameters obtained from Nyquist diagram for the corrosion of AA2024 coupons inhibited by PBE system in 3.5%NaCl solution at room temperature.

Inh. Conc. (v/v%)	R_s (Ωcm^2)	R_{ct} (Ωcm^2)	C_{dl} (μF)	IE%
10%v/vPBE	1.20	161.23	50.11	68.28
20%v/vPBE	1.36	163.99	49.17	71.19
30%v/vPBE	1.41	180.52	48.33	73.99
40%v/VPBE	1.67	181.99	46.17	80.29
50%v/VPBE	1.69	190.97	44.18	82.99

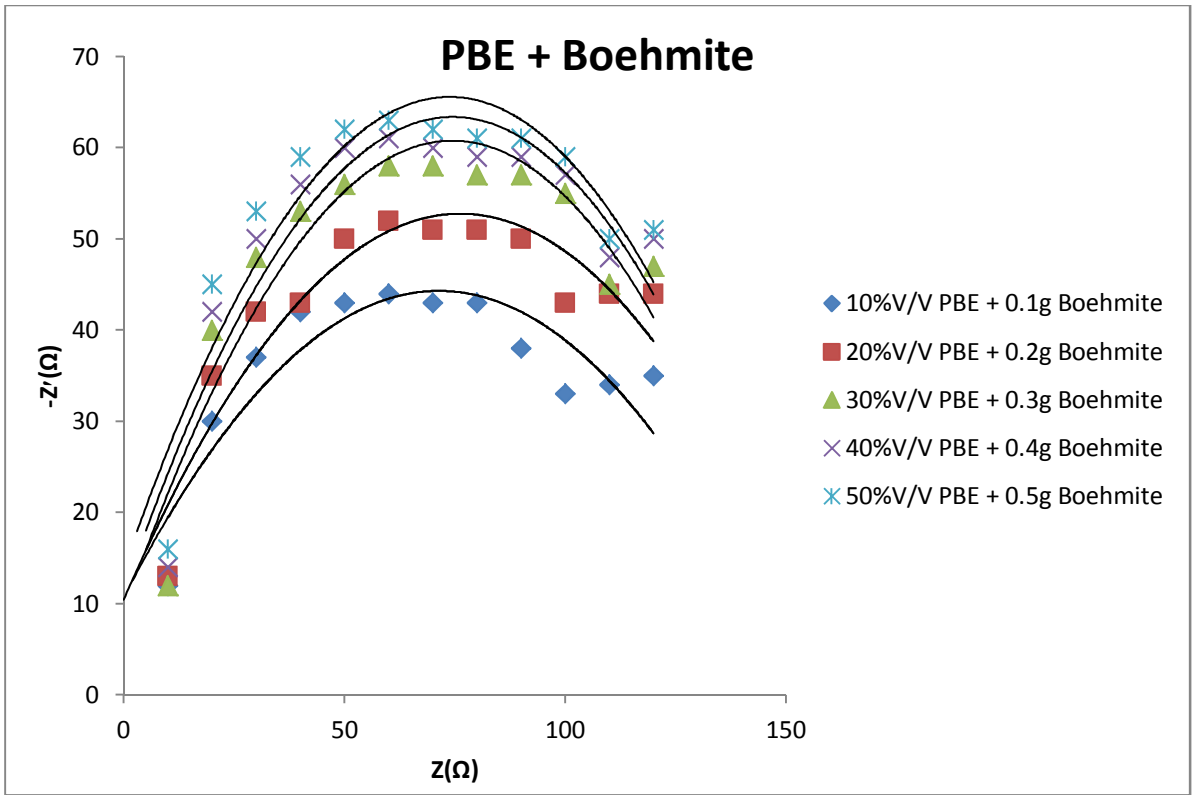


Figure 4.22: Nyquist diagram for AA2024 Aluminium Alloy Inhibited by PBE+Boehmite.

Table 4.13: Parameters obtained from Nyquist diagram for the corrosion of AA2024 coupons inhibited by PBE+ Boehmite nanoparticles system in 3.5%NaCl solution at room temperature.

Inh. Conc. (v/v%)	R_s (Ωcm^2)	R_{ct} (Ωcm^2)	C_{dl} (μF)	IE%
10%v/vPBE/Boehmite	1.38	183.11	49.23	70.51
20%v/vPBE/Boehmite	1.85	188.17	47.11	73.97
30%v/vPBE/Boehmite	1.89	197.71	40.44	78.00
40%v/VPBE/Boehmite	1.95	200.33	39.22	83.11
50%v/VPBE/Boehmite	1.99	206.27	32.33	86.26

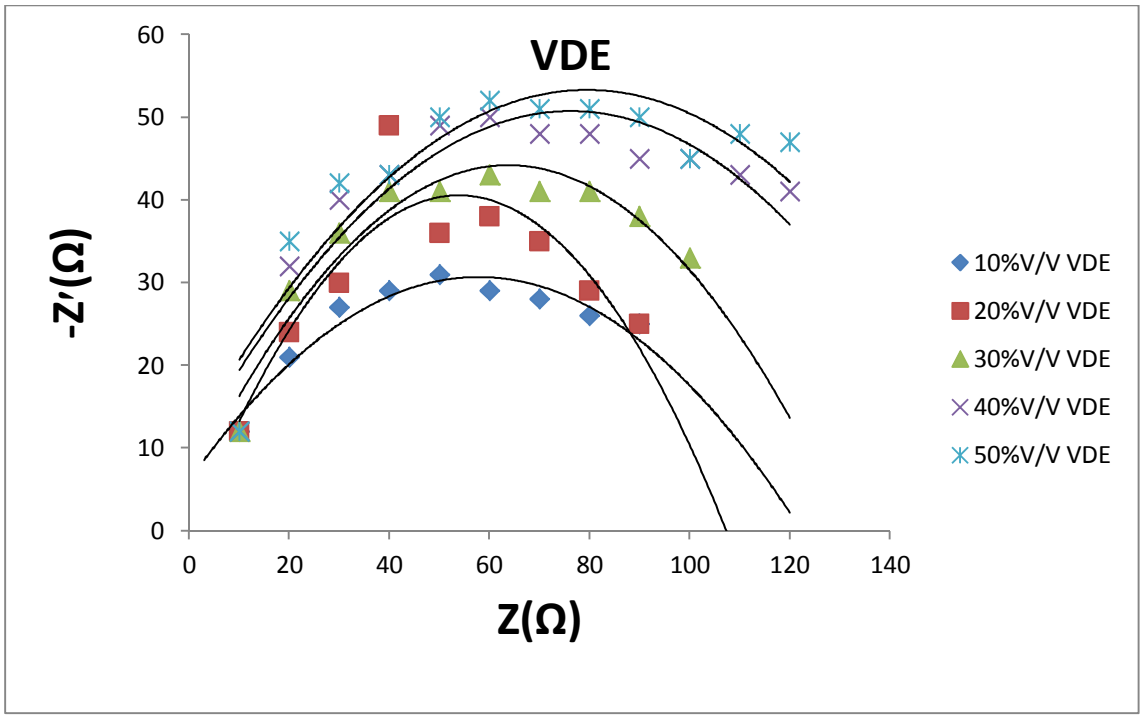


Figure 4.23: Nyquist diagram for AA2024 Aluminium Alloy Inhibited by VDE.

Table 4.14: Parameters obtained from Nyquist diagram for the corrosion of AA2024 coupons inhibited by VDE system in 3.5%NaCl solution at room temperature.

Inh. Conc. (v/v%)	R_s (Ωcm^2)	R_{ct} (Ωcm^2)	C_{dl} (μF)	IE%
10%v/vVDE	1.01	157.75	51.88	43.49
20%v/vVDE	1.09	160.79	48.17	60.00
30%v/vVDE	1.25	171.00	47.00	71.23
40%v/vVDE	1.45	175.50	43.49	71.99
50%v/vVDE	1.69	180.11	40.11	72.97

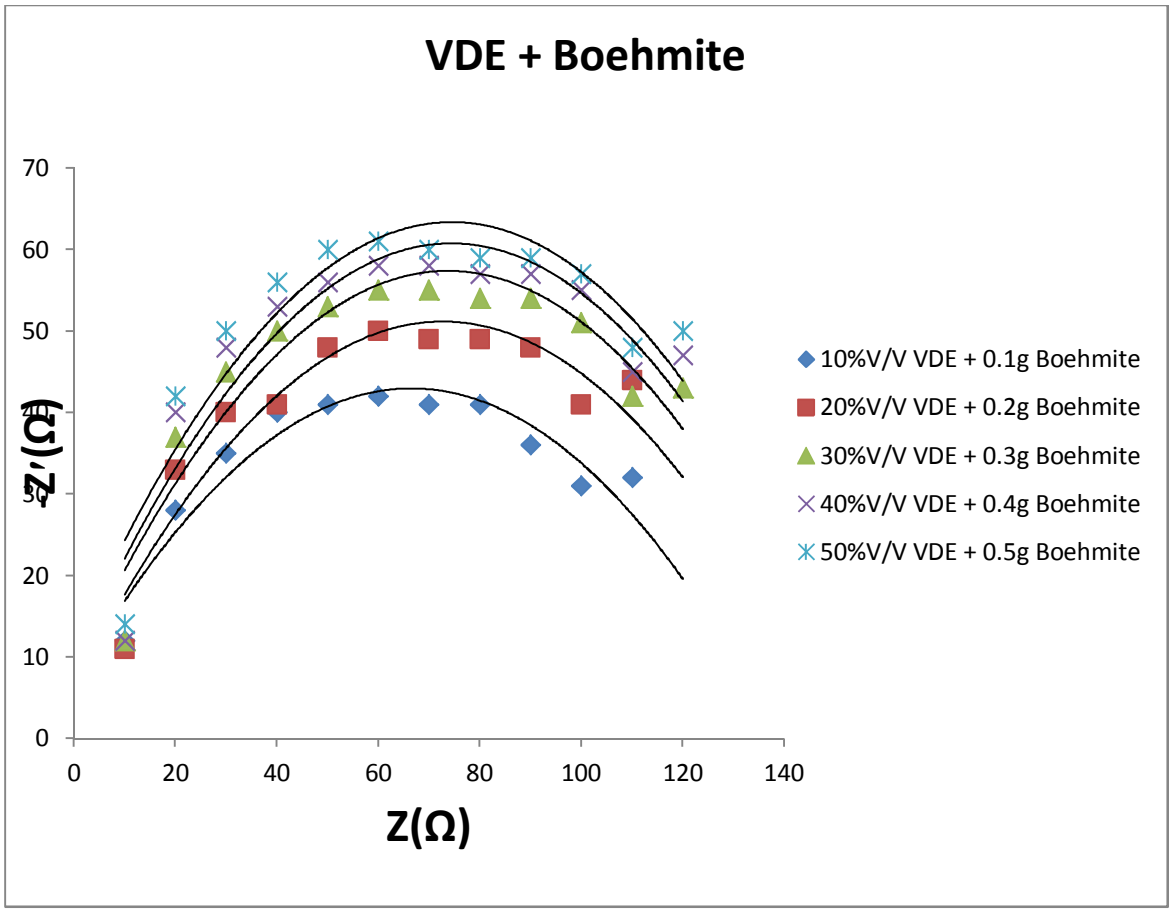


Figure 4.24: Nyquist diagram for AA2024 Aluminium Alloy Inhibited by VDE+Boehmite.

Table 4.15: Parameters obtained from Nyquist diagram for the corrosion of AA2024 coupons inhibited by VDE+Boehmite Nanoparticles system in 3.5%NaCl solution at room temperature.

Inh. Conc. (v/v%)	R_s (Ωcm^2)	R_{ct} (Ωcm^2)	C_{dl} (μF)	IE%
10%v/vVDE/Boehmite	1.28	173.95	52.93	46.79
20%v/vVDE/Boehmite	1.46	175.65	50.13	60.55
30%v/vVDE/Boehmite	1.50	180.96	49.33	71.00
40%v/vVDE/Boehmite	1.60	188.23	48.11	75.99
50%v/vVDE/Boehmite	1.86	189.99	43.11	78.99

4.3.4 Chronopotentiometric Analysis

The chronopotentiometric analyses of the test samples were carried out to determine the extent of the stability of adsorbed layers in the different systems under investigation. Figures 4.25 - 4.31 represent the chronopotentiograms of the test samples investigated.

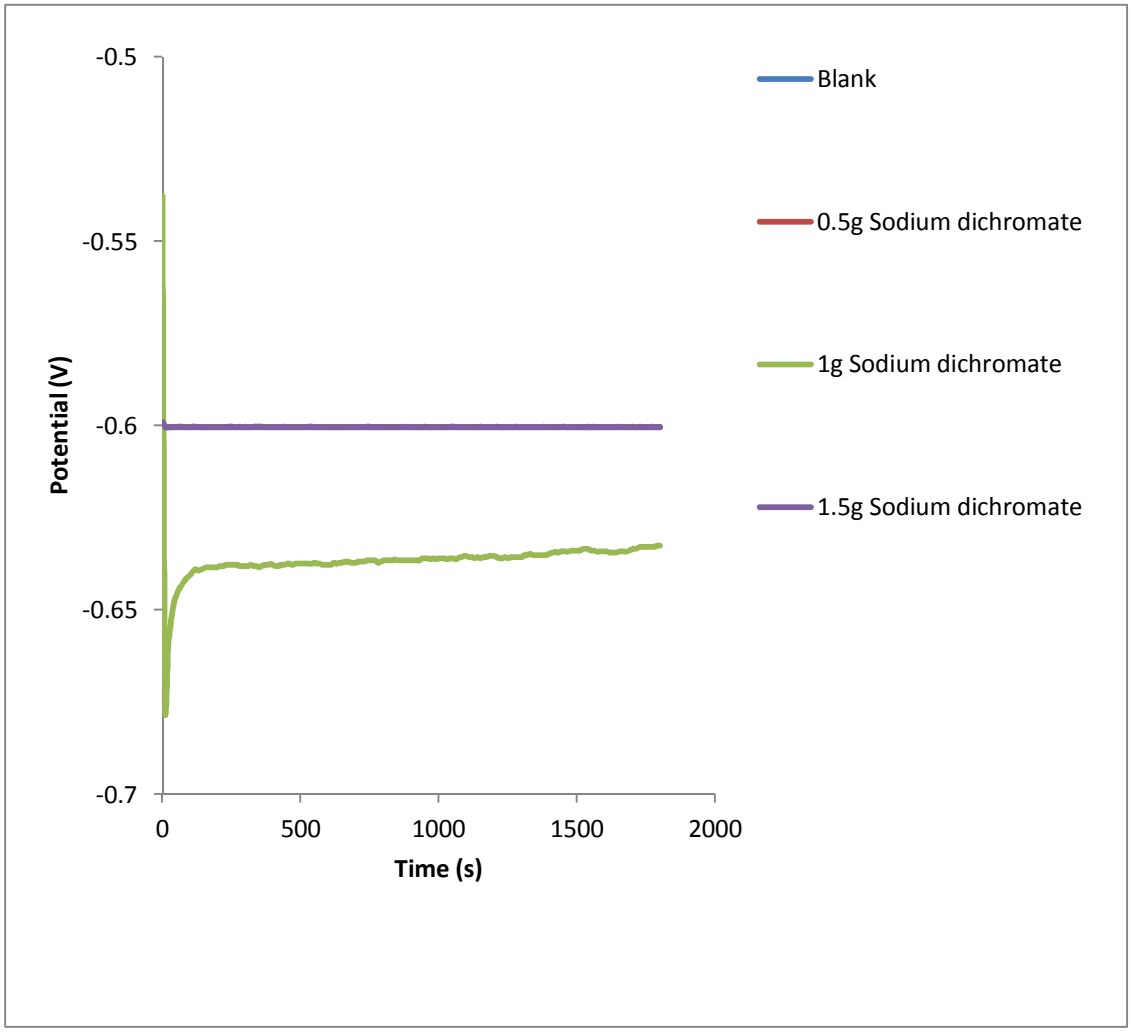


Figure 4.25: Chronopotentiograms of the test samples exposed to 3.5%NaCl+Na_2CrO_4 solution.

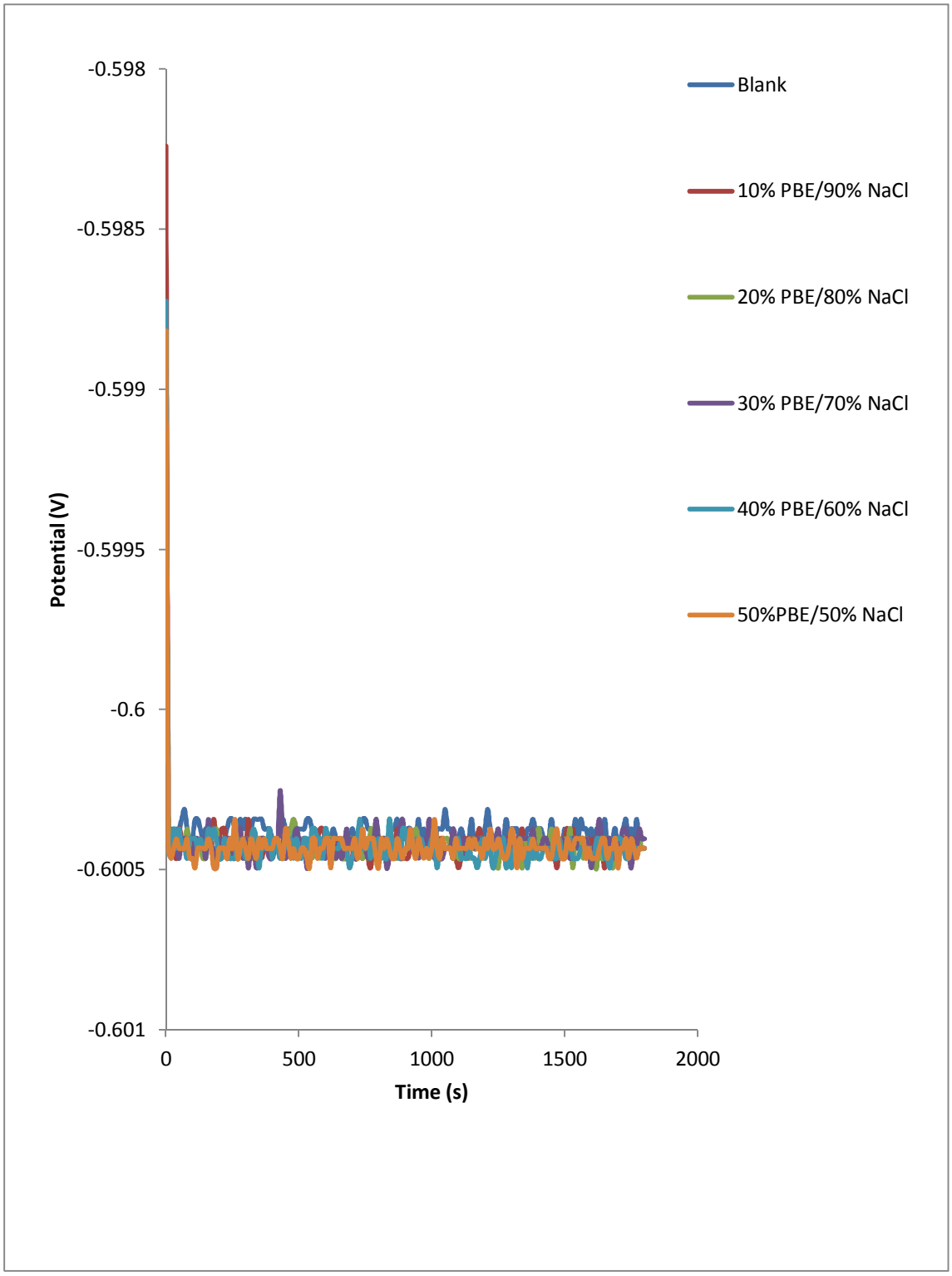


Figure 4.26: Chronopotentiograms of the test samples exposed to 3.5%NaCl+PBE solution.

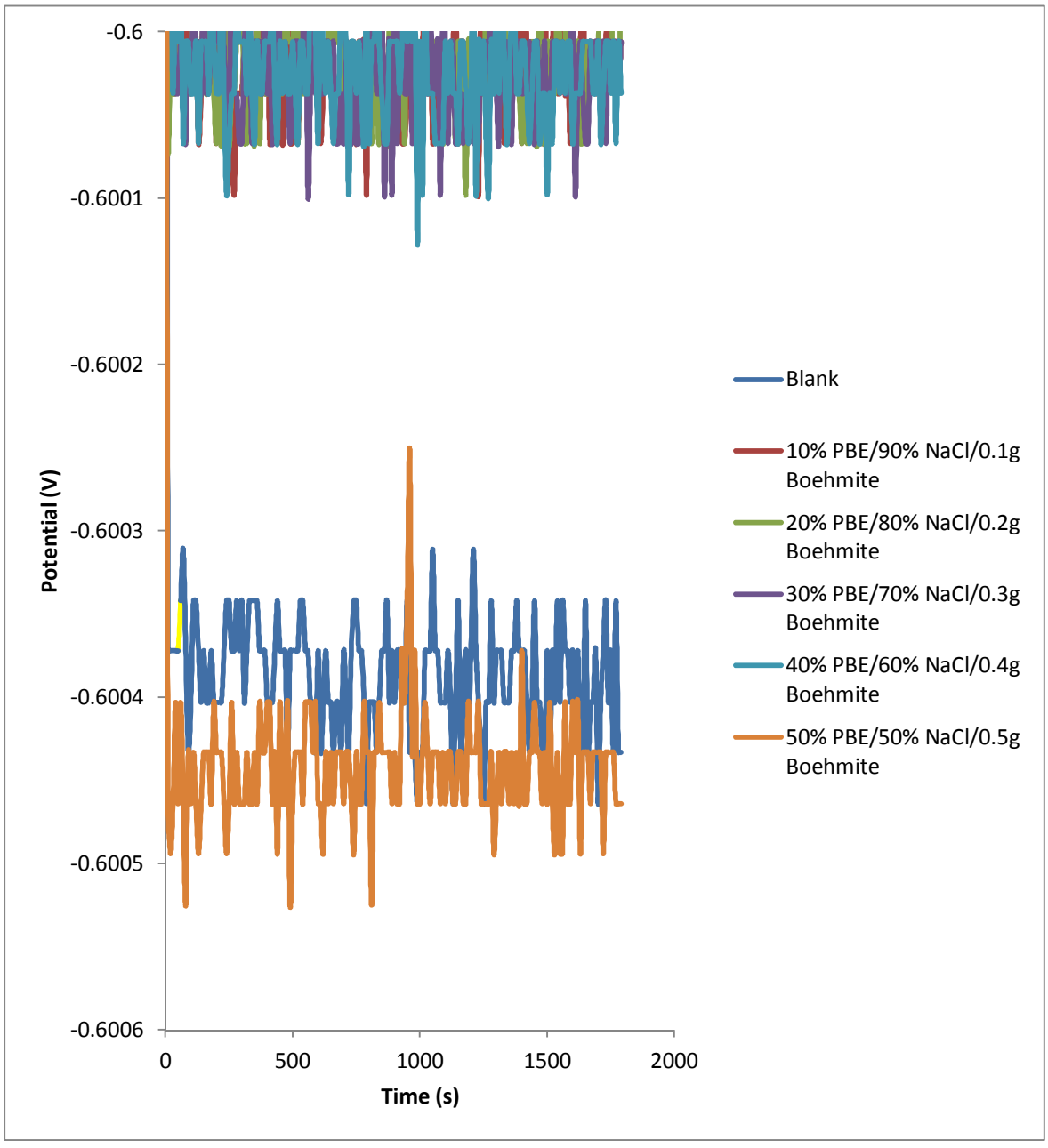


Figure 4.27: Chronopotentiograms of the test samples exposed to 3.5%NaCl+PBE+ Boehmite solution.

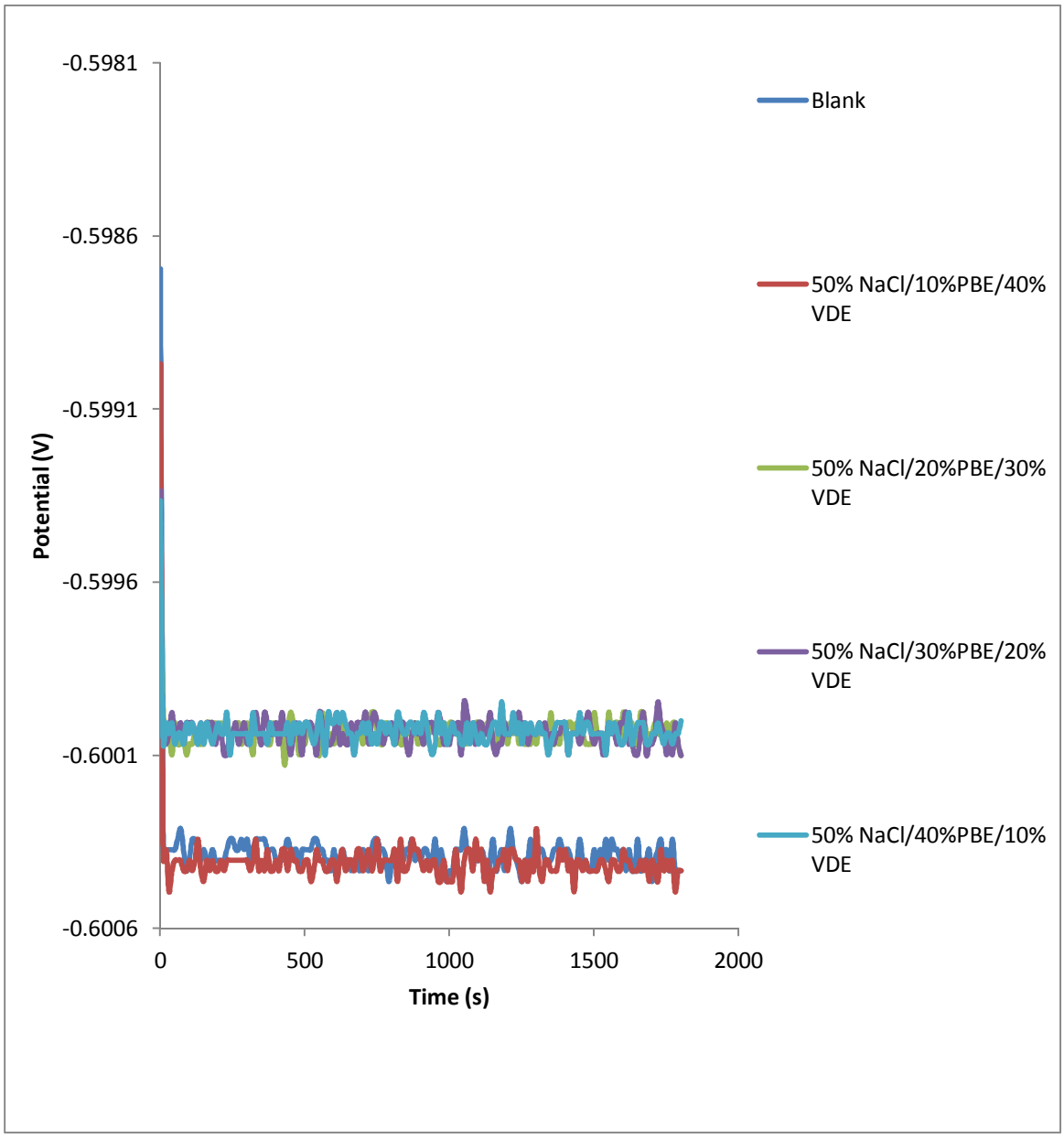


Figure 4.28: Chronopotentiograms of the tests sample exposed to 3.5%NaCl +PBE+VDE solution.

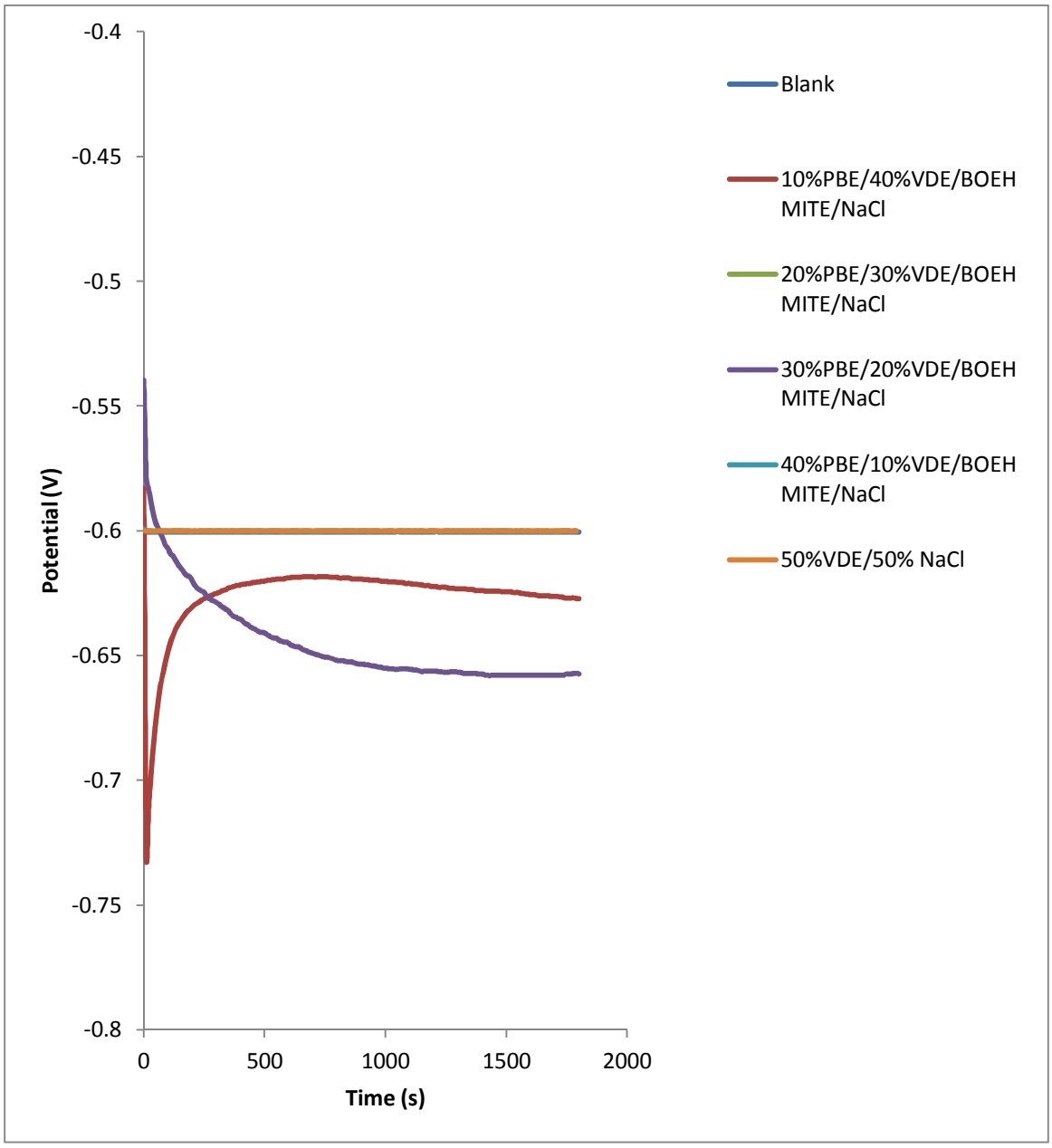


Figure 4.29: Chronopotentiograms of the test samples exposed to 3.5%NaCl+ PBE+VDE+ BOEHMITE solution.

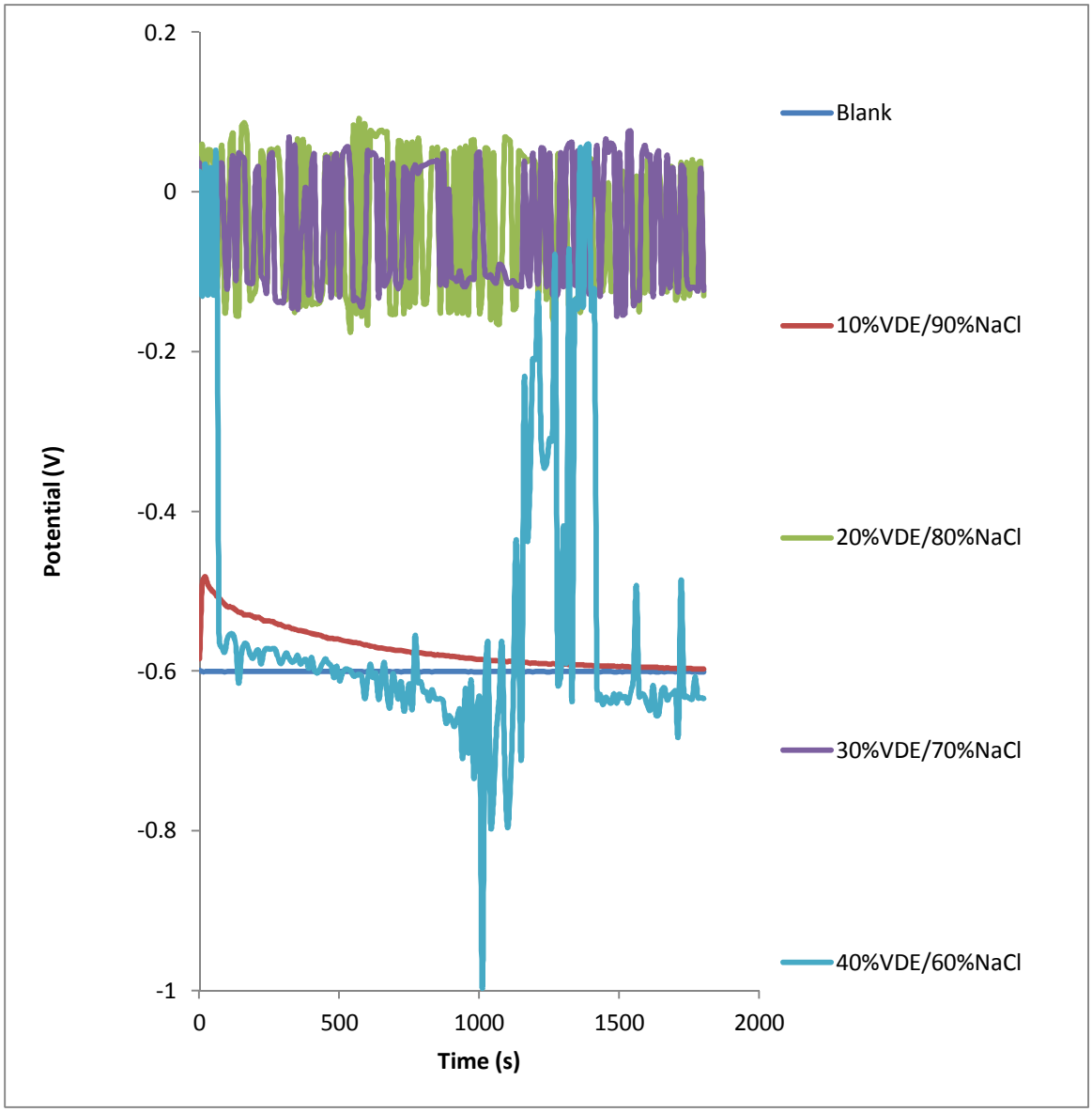


Figure 4.30: Chronopotentiograms of the test samples exposed to 3.5%NaCl+VDE solution.

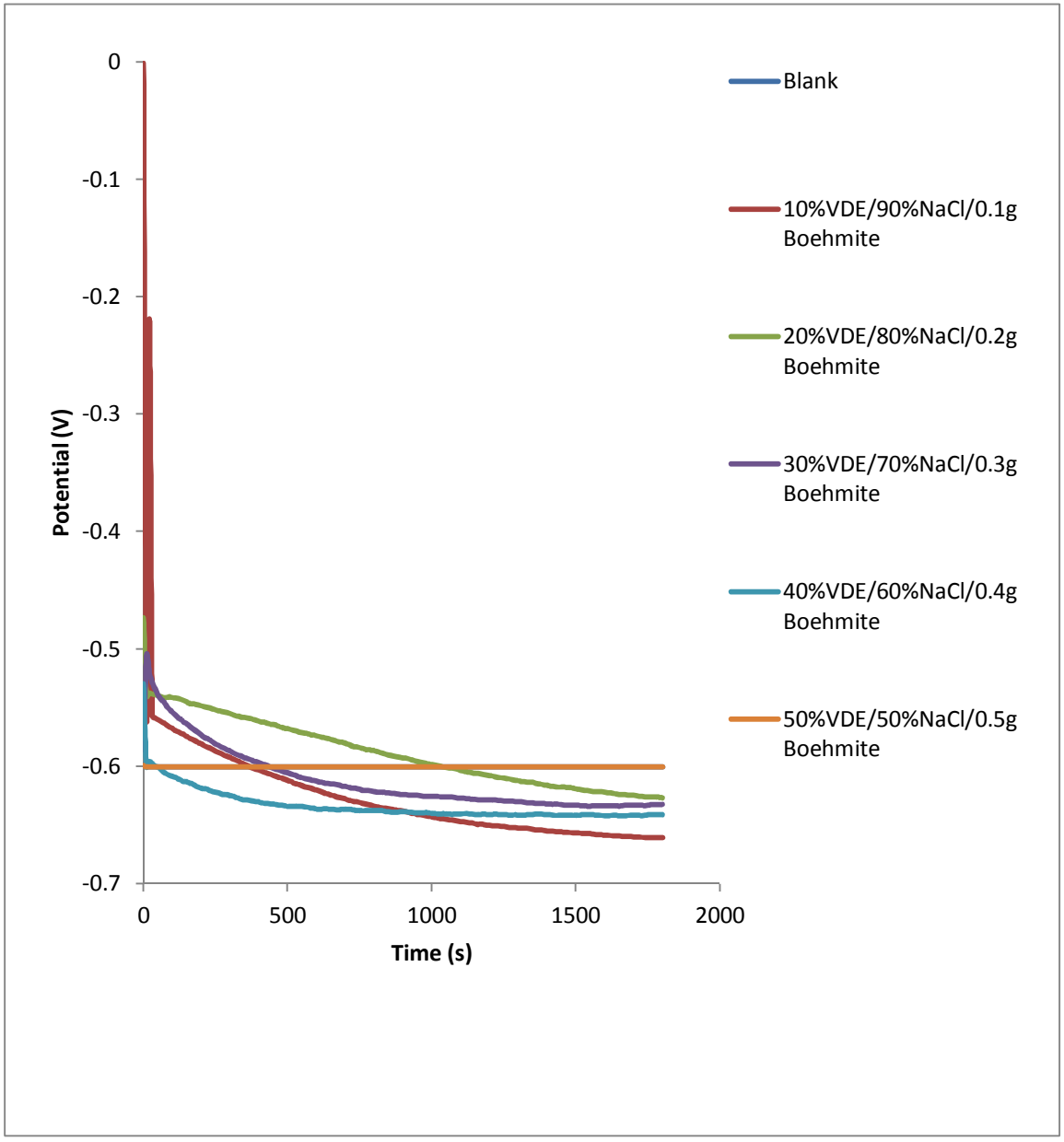


Figure 4.31: Chronopotentiograms of the test samples exposed to 3.5%NaCl+VDE+ Boehmite solution.

4.4 Kinetics and Thermodynamics Consideration

Kinetic and Thermodynamic parameters are useful tools for explaining the action of corrosion inhibition on substrates. Table 4.16 below shows some kinetic and thermodynamic parameters for the various inhibitor systems investigated at different temperatures. E_a is the activaton energy, G_{ads} adsorption energy and Q_{ads} the heat of adsorption for the various inhibited and uninhibited systems.

Table 4.16: Kinetic and thermodynamic parameters for the various inhibitor Systems at different temperatures

Inhibitor System	E_a **kJ/Mol**	ΔG_{ads} **(kJ/Mol)**					Q_{ads} **kJ/mol**
		30^0C	**40^0C**	**50^0C**	**60^0C**	**70^0C**	
SODIUM CHROMATE	89.97	-56.46	-56.81	-57.1020	-59.49	-60.77	-10.07
PBE	45.98	-36.80	-46.40	-56.84	-57.64	-58.99	-11.00
PBE+BOEHMITE	53.61	-50.67	-56.12	-46.33	-56.62	-58.79	-16.35
PBE+VDE	52.32	-38.8	-39.82	-39.49	-49.76	-38.99	-10.61
PBE+VDE+BOEHMITE	84.40	-49.20	-49.91	-49.64	-59.44	-45.87	-11.14
VDE+BOEHMITE	50.33	-40.54	-41.39	43.98	-48.33	-48.85	-10.05
VDE	42.12	-39.88	-40.97	-49.22	-53.99	-54.89	-9.99
BLANK	37.12	-	-	-	-	-	-

4.5 Elucidation of Synergism

Tables 4.17 and 4.18 show the Synergism parameters (S_θ) computed using equation 2.29 for the different extracts-extracts systems and extracts-nanoparticles systems investigated.

Table 4.17: Synergism parameter (S_θ) for different concentrations of investigated extracts-extracts (PBE+VDE) systems at different temperatures

Inh. Conc. (v/v%)	S_θ				
	30°C	40°C	50°C	60°C	70°C
10	1.604118	1.593095	1.587224	1.503781	1.368099
20	1.688514	1.640992	1.604119	1.364033	1.345124
30	1.751146	1.780625	1.633736	1.607529	1.278525
40	1.787343	1.795611	1.529630	1.596724	1.314124

Table 4.18: Synergism parameter (S_θ) for different concentrations of investigated extracts-nanoparticles (PBE+VDE+ Boehmite) systems at different temperatures

Inh. Conc. (v/v%)	S_θ				
	30°C	40°C	50°C	60°C	70°C
10	1.356882	1.352787	1.287841	1.145214	1.252822
20	1.497356	1.479300	1.226304	1.077682	1.085673
30	1.625706	1.584690	1.424930	1.234380	1.051095
40	1.754668	1.711223	1.447322	1.313069	1.130235

4.6 Adsorption Isotherms

From the data of surface coverage, adsorption isotherms were plotted and the nature of these isotherms provided insights into the properties of the adsorbed substances and their interaction with electrode surfaces.

4.6.1 Langmuir Adsorption Isotherm

Figure 4.32 are plots of log(θ/1- θ) against logC, which are linear for all the systems investigated.

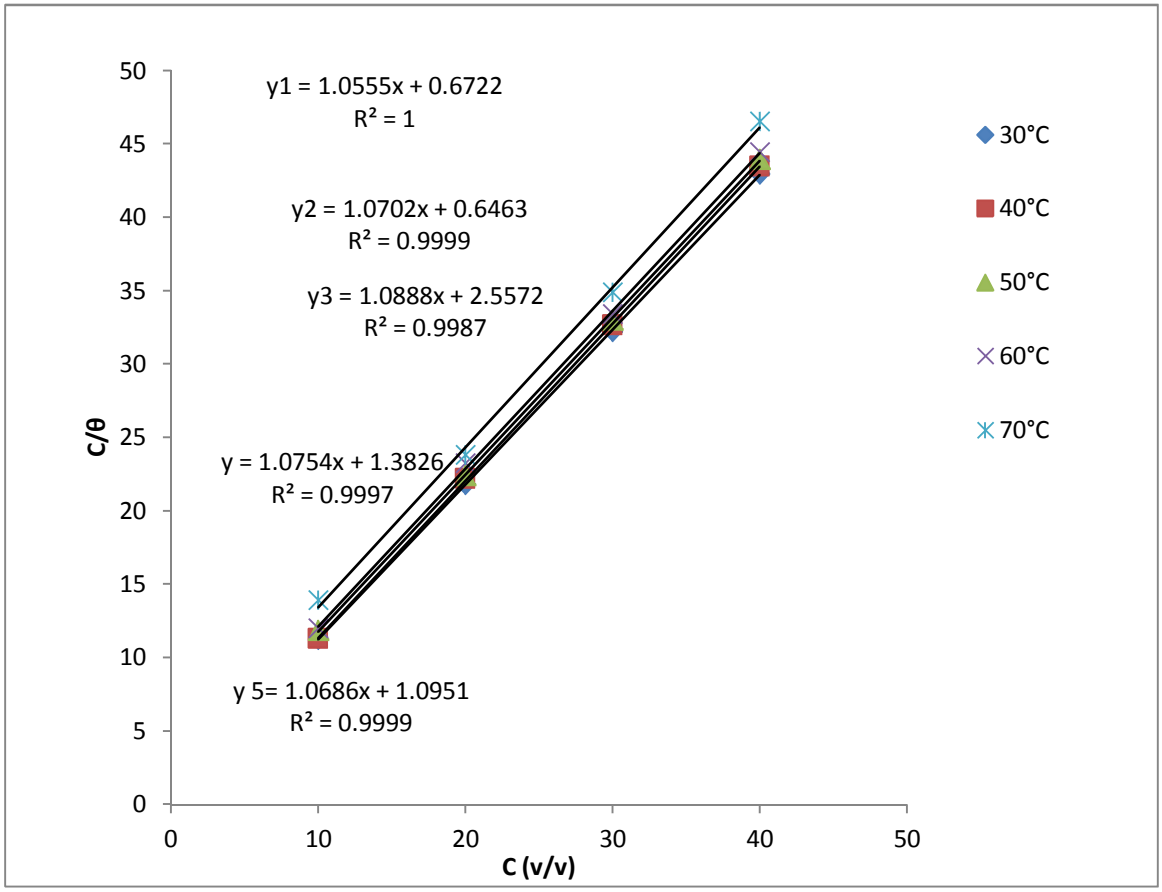


Figure 4.32: Langmuir Adsorption Isotherms for the adsorption of PBE+VDE+NANO system onto the surfaces of AA2024 coupons in 3.5%NaCl solution.

4.6.2 El-Awady's Adsorption Isotherm

Though the plots of C/Θ versus C was linear (Figure 4.33) (correlation > 0.9), for ideal Langmuir isotherm, the slight deviation of the slopes from unity, Table 4.19, can be attributed to the molecular interaction among the adsorbed inhibitor species, a factor which was not taken into consideration during the derivation of the Langmuir equation.

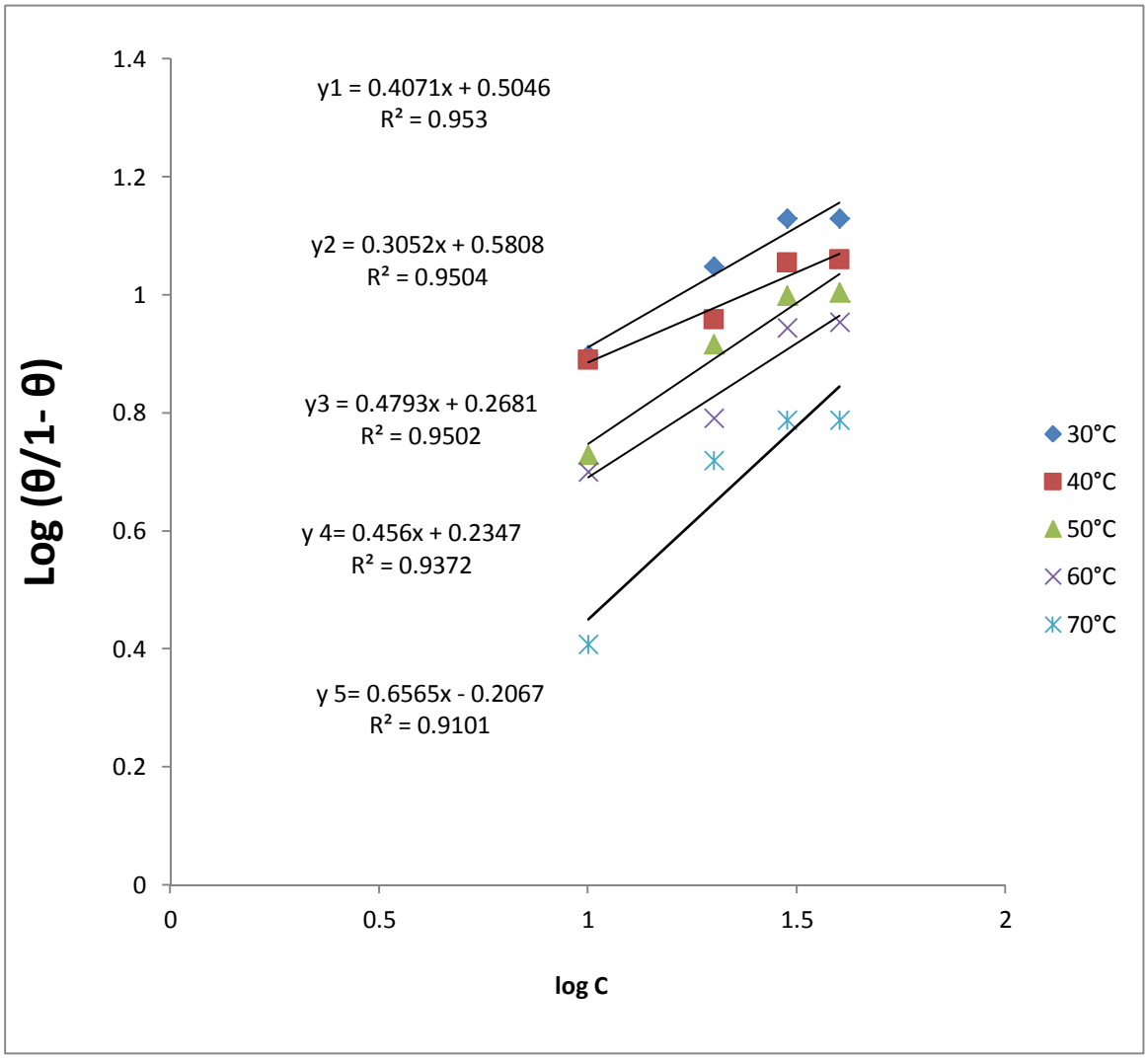


Figure 4.33: El-Awady's Adsorption Isotherms for the adsorption of PBE+VDE+NANO system onto the surfaces of AA2024 coupons in 3.5%NaCl solution.

Table 4.19: Calculated parameters from Langmuir and El-awady's Adsorption Isotherms.

Temp. (^{0}C)	**Langmuir**				**El-awady**			
	K_{ads}	ΔG_{ads} (kJ/mol)	**Slope**	**R²**	K_{ads}	ΔG_{ads} (kJ/mol)	**1/y**	**R²**
30	1.4877	-11.12	1.055	1	1.9818	-11.84	2.1231	0.953
40	1.5473	-11.09	1.070	9.9999	1.7218	-11.82	3.2765	0.950
50	0.3910	-8.26	1.088	0.9987	0.7300	-9.94	2.0864	0.950
60	0.7233	-10.22	1.075	0.9997	4.2608	-11.13	2.1930	0.937
70	0.9132	-10.19	1.068	0.9999	4.8380	-10.73	1.5232	0.890

4.7 Characterisation

Representative samples were taken from each room temperature system and characterized before and after the corrosion tests; using SEM/EDX, XRD and Raman Spectroscopy.

4.7.1 Scanning Electron Microscopy/Energy Dispersive X-Ray (SEM/EDXA)

Scanning Electron Microscopy/Energy dispersive X-ray Analysis (EDXA) was employed to study the surface morphologies of the substrates, leading to additional information about the inhibitors' interactions with substrates' surfaces. Figures 4.34 - 4.42 present SEM and EDX panorama recorded for the as-cast sample, samples exposed to artificial sea water, sodium chromate, and different extracts-extracts and extracts-nanoparticles inhibiting systems.

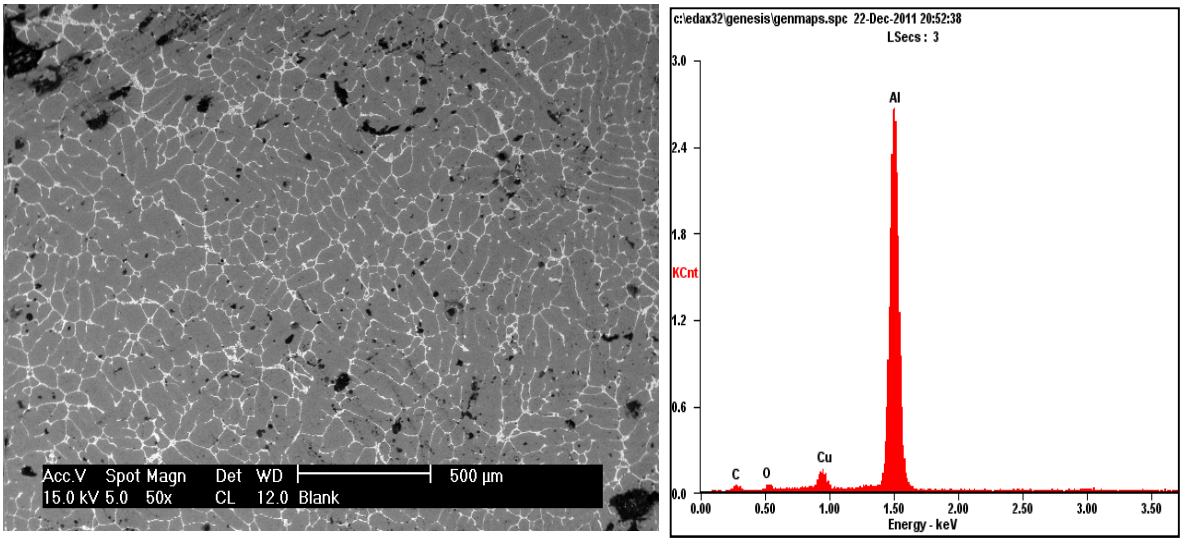


Figure 4.34: SEM Micrographs, with the corresponding EDX Spectrum, for the as-cast sample.

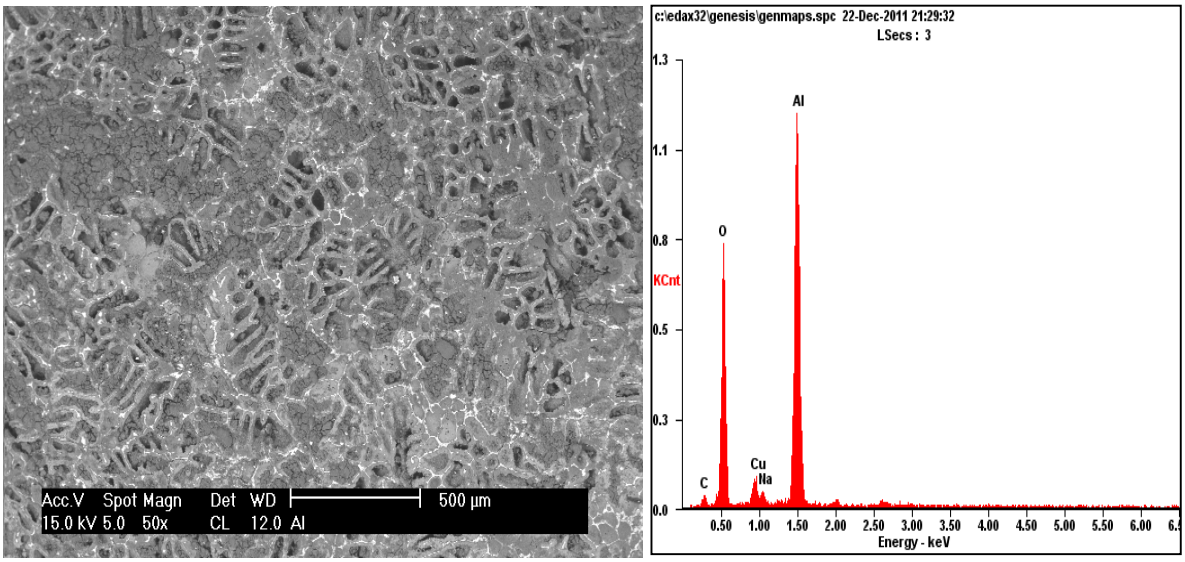


Figure 4.35: SEM Micrographs, with the corresponding EDX Spectrum, for the sample exposed to 3.5%NaCl solution.

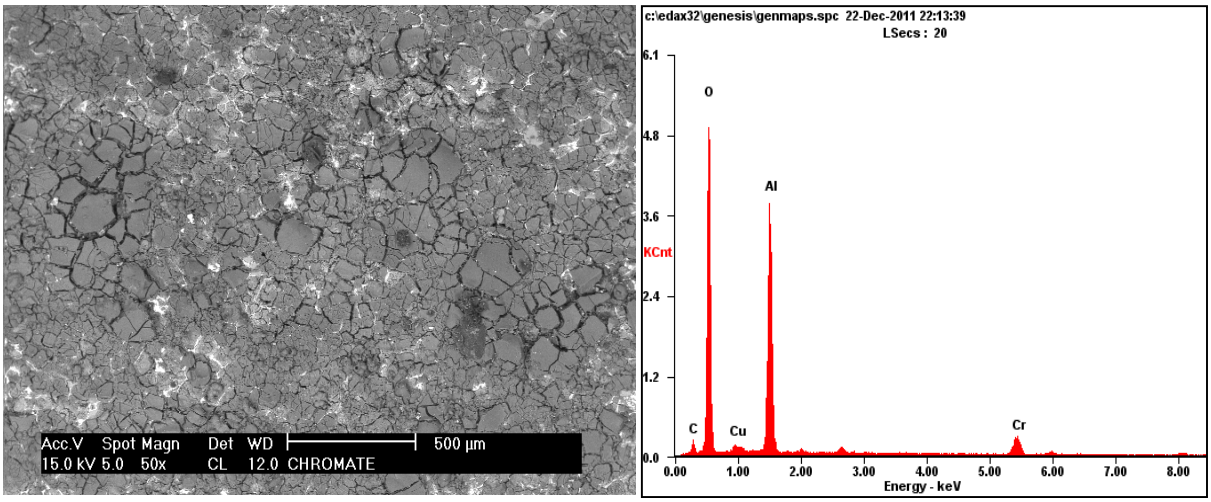


Figure 4.36: SEM Micrographs, with the corresponding EDX Spectrum, for the sample in 3.5%NaCl+Na_2CrO_4 solution.

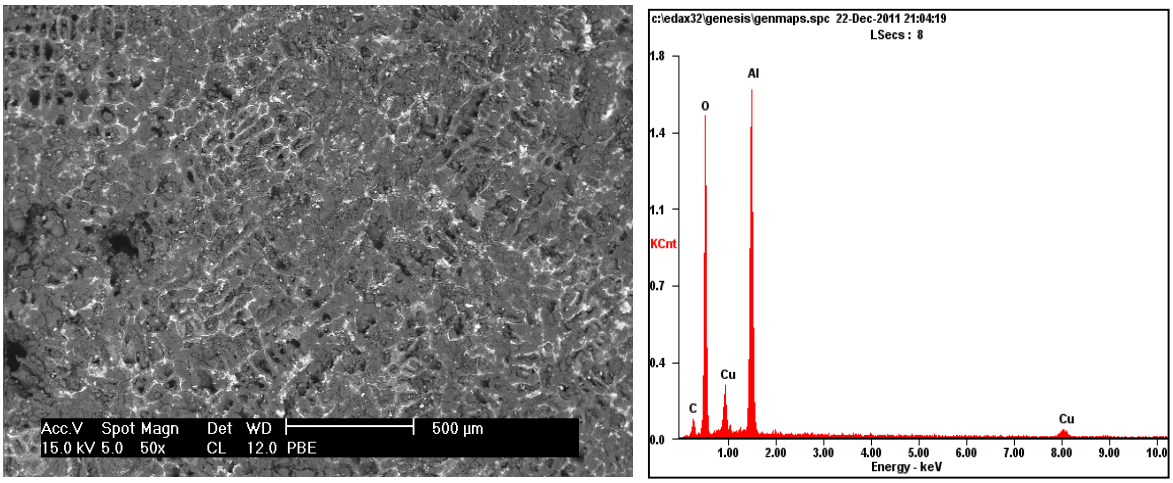


Figure 4.37: SEM Micrographs, with the corresponding EDX Spectrum, for the sample in 3.5%NaCl+PB Extracts solution.

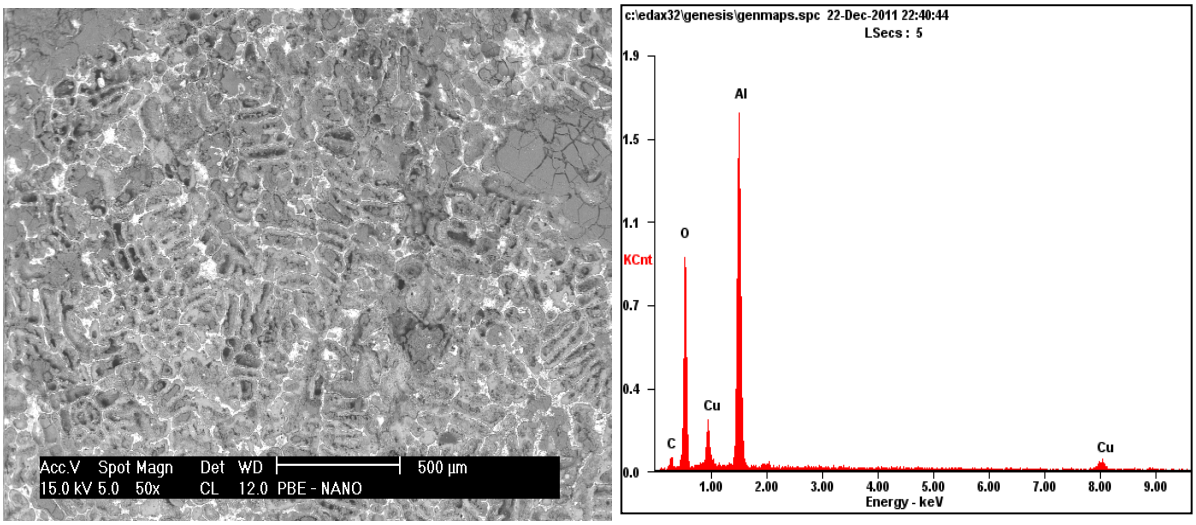


Figure 4.38: SEM Micrographs, with the corresponding EDX Spectrum, for the sample in 3.5%NaCl + PB Extracts + Boehmite Nanoparticles solution.

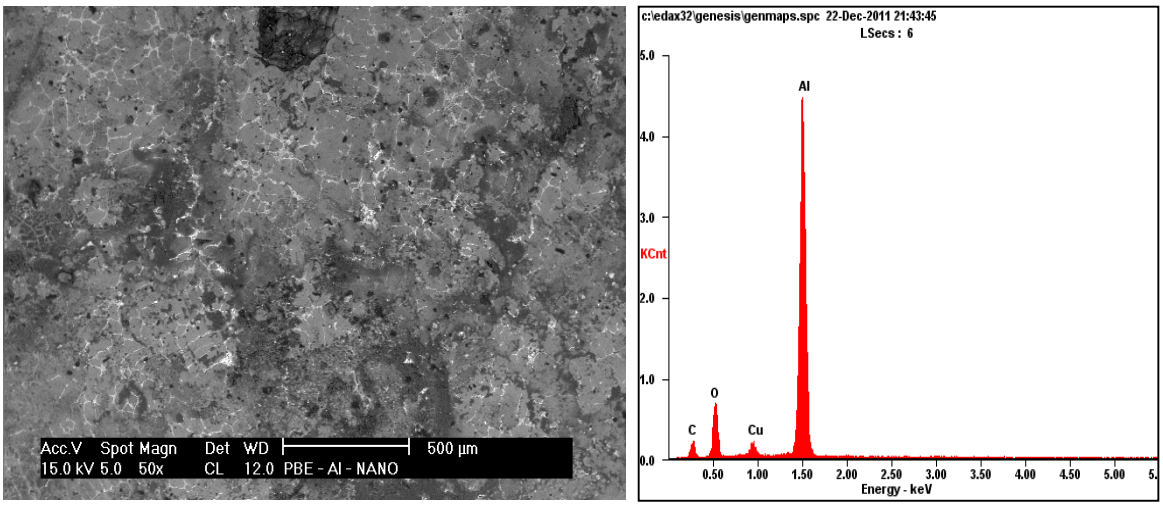


Figure 4.39: SEM Micrographs, with the corresponding EDX Spectrum, for the sample in 3.5%NaCl with PB+VD Extracts + Boehmite Nanoparticles solution.

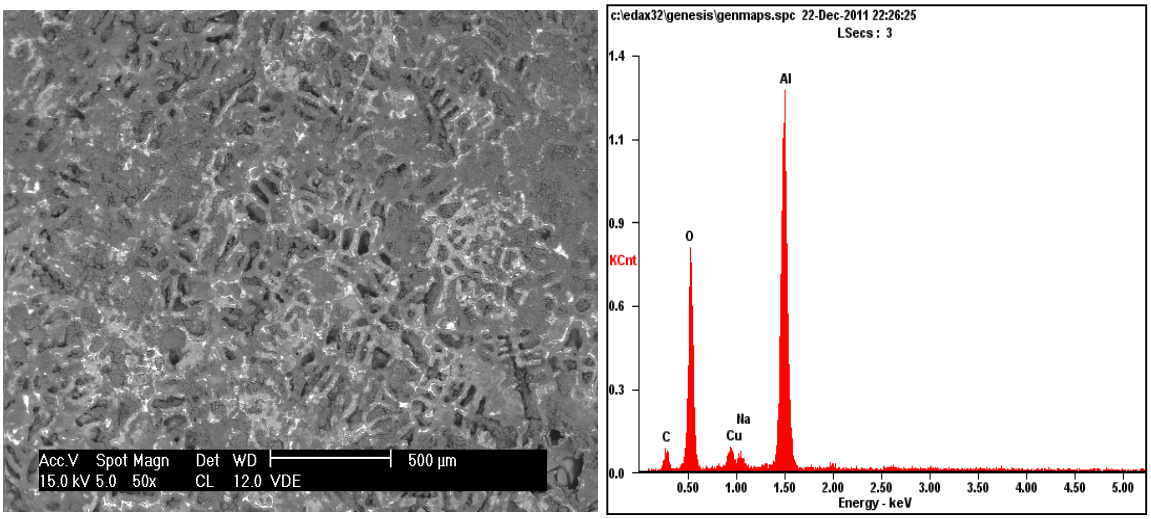


Figure 4.40: SEM Micrographs, with the corresponding EDX Spectrum, for the sample in 3.5%NaCl+VD Extracts solution.

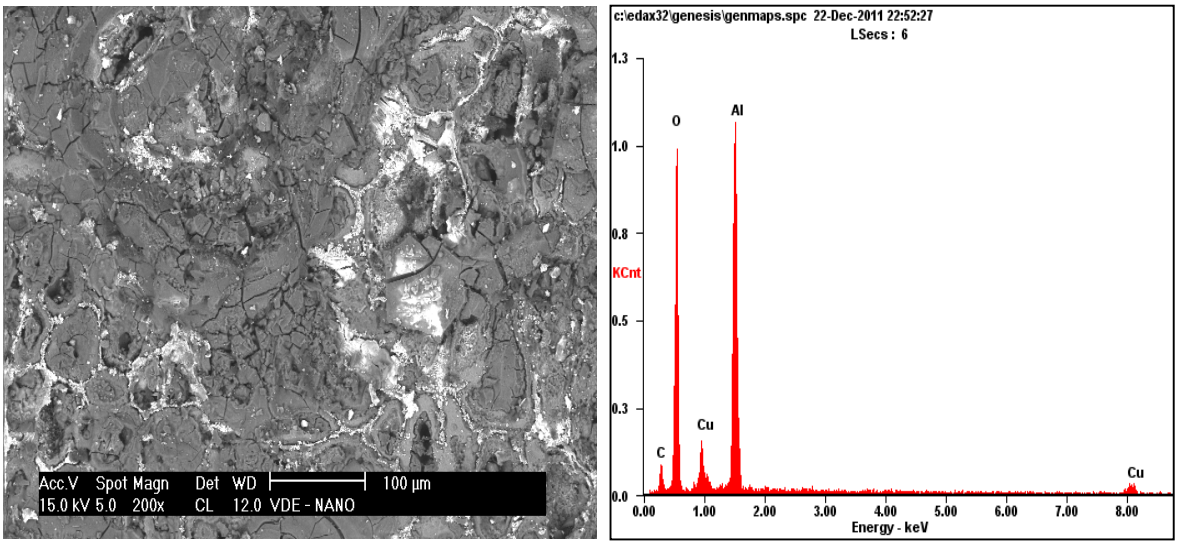


Figure 4.41: SEM Micrographs, with the corresponding EDX Spectrum, for the sample in 3.5%NaCl + VD Extracts + Boehmite Nanoparticles solution.

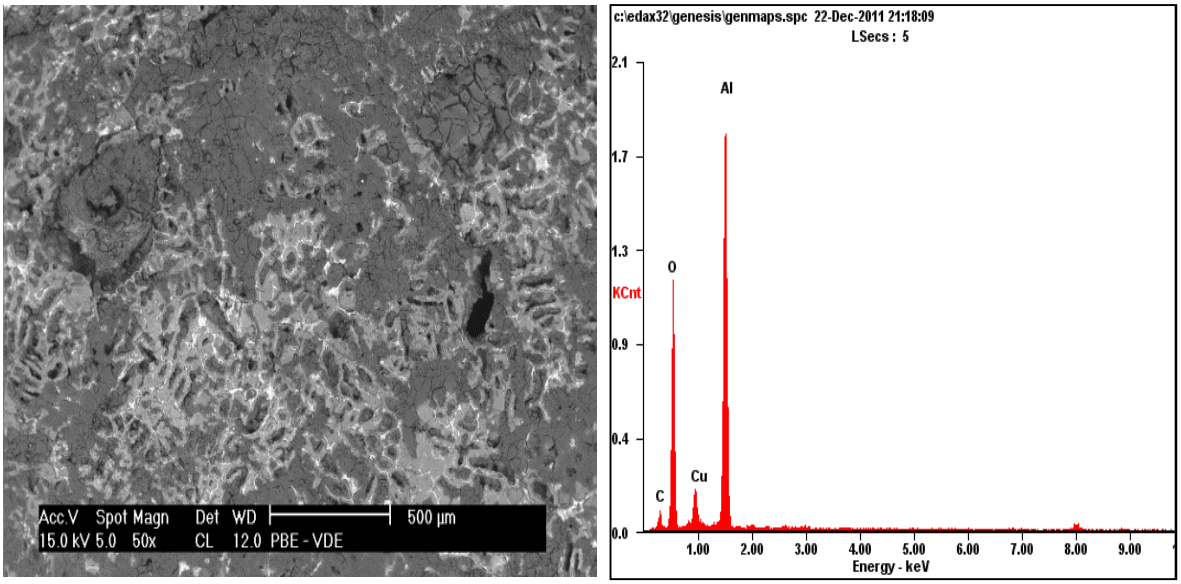


Figure 4.42: SEM Micrographs, with the corresponding EDX Spectrum, for the sample in 3.5%NaCl+PB+VD Extract solution.

4.7.2 XRD Results

The X-ray diffraction (XRD) analysis was used, in line with Jenkins and Synder (1996), for identification of crystalline phases in corrosion products and also for quantitative phase analysis based on measuring the intensity of a single diffraction line or even all the lines in the pattern. The XRD patterns generated from the different systems investigated are depicted in Figures 4.43 - 4.51, while Tables 4.20 – 4.28 contain summaries of Chemical/phases composition of the test alloy, as revealed by the XRD, in different systems investigated. The observed spectra of the systems displayed varying degrees of 2θ positions, diffraction peaks and scores which are independent of the atomic positions within the cell and entirely determined by the size and shape of the unit cell of the crystalline phase.

This might also be affected by dissolution, rearrangement of the phases and formation of other products as a result of corrosion or introduction of various inhibitive substances into the electrolytes. Because X-ray penetrated the thin layer of corrosion products, the diffractions from metallic Al, Cu, and small amounts of other elements are revealed/observed in the Diffractograms.

Table 4.20: Chemical/phases composition of the as cast alloy as revealed by the XRD.

Visible	Ref. Code	Score	Compound Name	Displacement [°2Th.]	Scale Factor	Chemical Formula
*	00-047-1424	58	Chromium Carbide	-0.191	0.340	Cr C
*	00-065-2695	62	Aluminum Copper	-0.062	0.132	Al2 Cu
*	00-037-0999	25	Iron Carbide	0.070	0.010	Fe2 C
*	00-029-0014	29	Aluminum Chromium	0.130	0.019	Al13 Cr2
*	00-025-1121	18	Aluminum Copper Iron	-0.108	0.011	Al7 Cu2 Fe

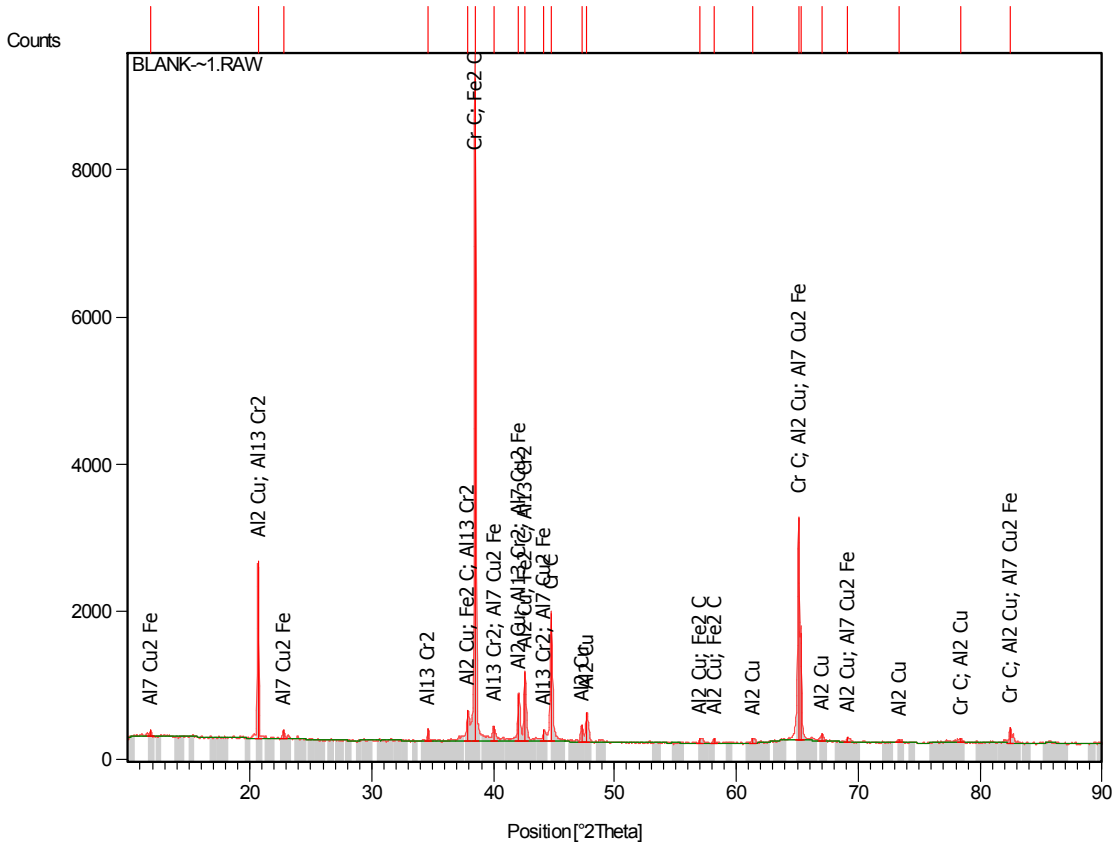


Figure 4.43: XRD pattern of the as-cast test sample.

Table 4.21: Chemical/phases composition of the test sample exposed to 3.5% NaCl solution.

Visible	Ref. Code	Score	Compound Name	Displacement [°2Th.]	Scale Factor	Chemical Formula
*	00-001-1176	46	Aluminum	-0.012	0.064	Al
*	00-049-1279	42	Aluminum Manganese	0.039	0.002	Al8 Mn5
*	00-002-1239	42	Aluminum Chromium	-0.084	0.004	Al Cr2
*	00-001-1132	27	Magnesium Aluminum	-0.135	0.004	Mg2 Al3
*	00-047-1126	28	Aluminum Iron Nickel	0.185	0.104	Al Fe0.23 Ni0.77
*	01-073-1148	30	Aluminum Magnesium	0.134	0.008	Al12 Mg17
*	00-003-0987	37	Copper Magnesium	-0.311	0.002	Cu2 Mg
*	01-089-2275	16	Chromium Aluminum Carbide	0.204	0.002	Cr2 Al C

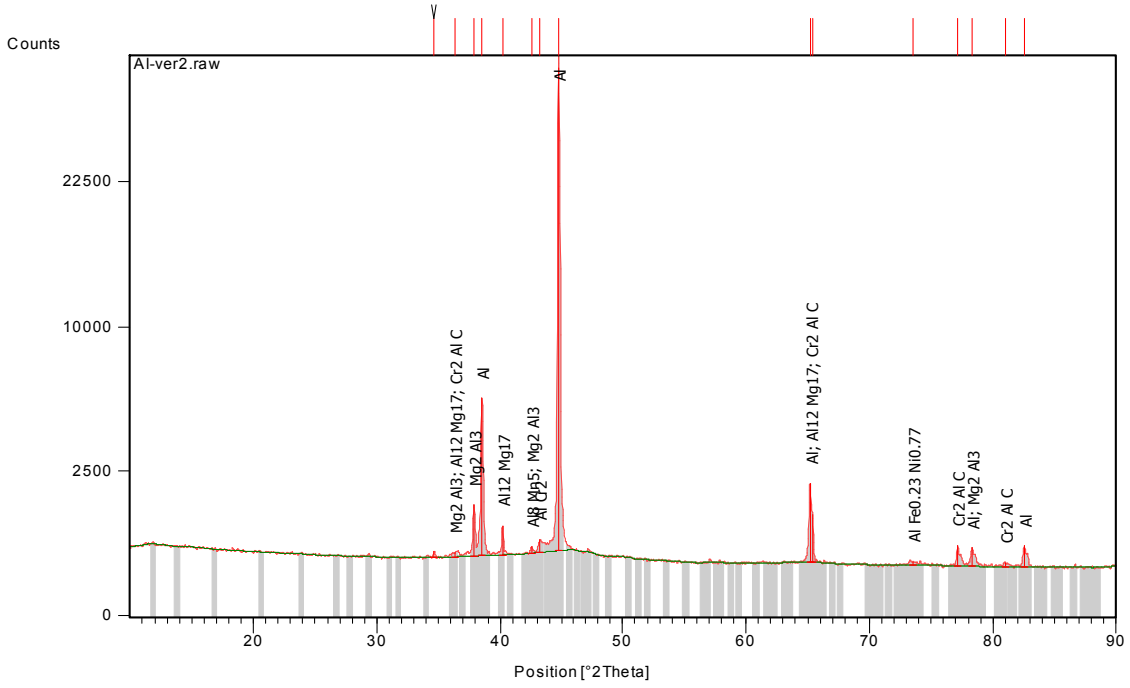


Figure 4.44: XRD pattern of the test sample exposed to 3.5%NaCl solution.

Table 4.22: Chemical/phases composition of the test sample exposed to 3.5%NaCl solution with Na_2CrO_4 as inhibitor.

Visible	Ref. Code	Score	Compound Name	Displacement [°2Th.]	Scale Factor	Chemical Formula
*	01-089-2769	67	Aluminum	0.018	1.084	Al
*	00-065-2695	61	Aluminum Copper	-0.069	0.471	Al2 Cu
*	00-044-1289	43	martensite	-0.321	0.488	C0.14 Fe1.86

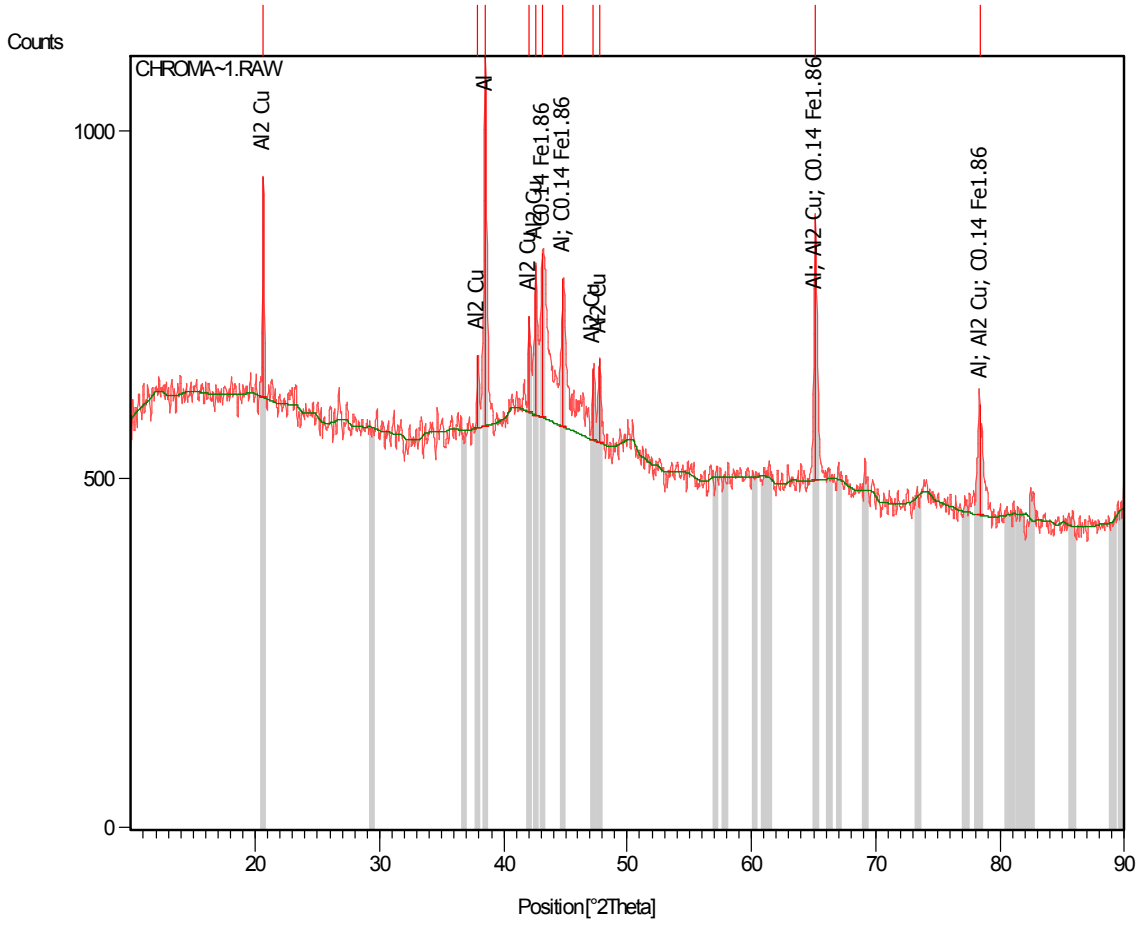


Figure 4.45: XRD pattern of the test sample in 3.5%NaCl containing Sodium chromate solution.

Table 4.23: Chemical/phases composition of the test sample in 3.5%NaCl containing PB Extracts.

Visible	Ref. Code	Score	Compound Name	Displacement [°2Th.]	Scale Factor	Chemical Formula
*	00-065-0882	51	Chromium Carbide	-0.208	0.116	Cr C
*	00-044-1289	49	martensite	-0.263	0.170	C0.14 Fe1.86
*	00-049-1279	47	Aluminum Manganese	-0.380	0.220	Al8 Mn5
*	00-040-0903	36	Aluminum Magnesium	0.199	0.057	Mg2 Al3
*	00-002-1230	30	Aluminum Chromium	0.215	0.034	Al2 Cr3
*	00-046-1194	25	Aluminum Chromium Magnesium	0.219	0.052	Mg3 Cr2 Al18
*	00-037-0999	24	Iron Carbide	0.025	0.054	Fe2 C

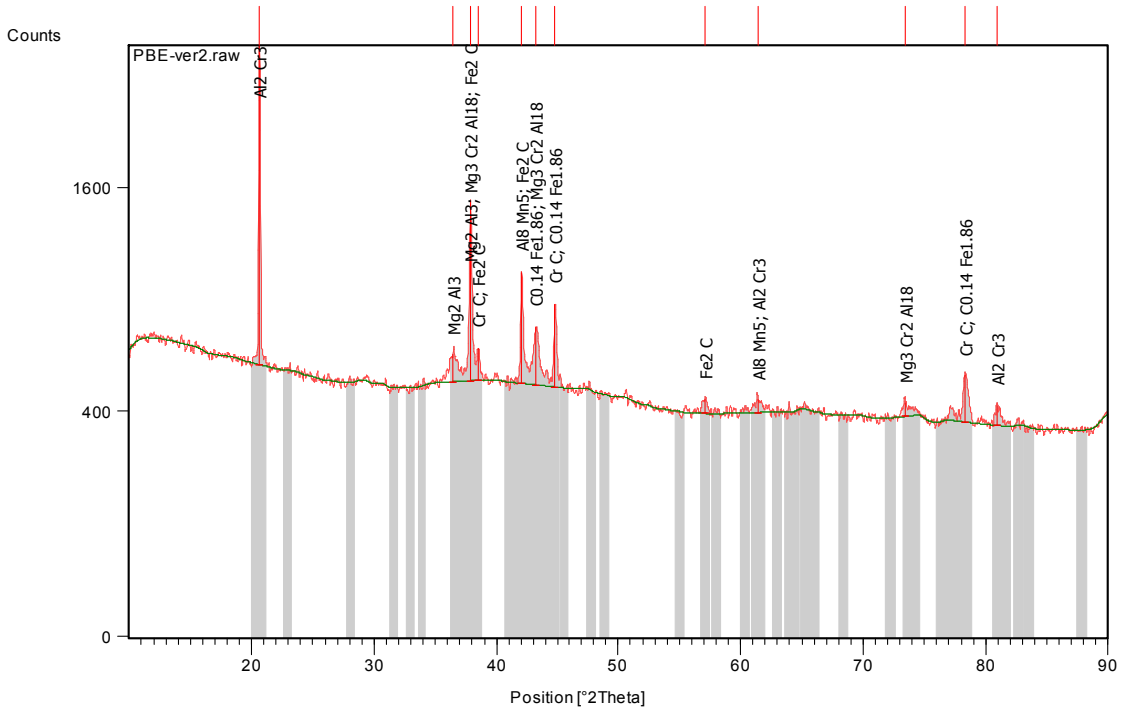


Figure 4.46: XRD pattern of the test sample in 3.5%NaCl containing PB Extracts.

Table 4.24: Chemical/phases composition of the test sample in 3.5%NaCl containing PBE+Boehmite solution.

Visible	Ref. Code	Score	Compound Name	Displacement [°2Th.]	Scale Factor	Chemical Formula
*	01-089-2769	52	Aluminum	0.046	1.056	Al
*	01-089-1980	48	Khatyrkite - synthetic	0.004	0.025	Al2 Cu
*	00-042-1074	26	Aluminum Magnesium Nickel	0.346	0.084	Al50 Mg48 Ni2
*	00-044-1289	25	martensite	-0.099	0.036	C0.14 Fe1.86
*	00-028-0014	20	Aluminum Copper Magnesium	-0.357	0.297	Al2 Cu Mg
*	01-089-4086	23	Manganese	-0.026	0.007	Mn

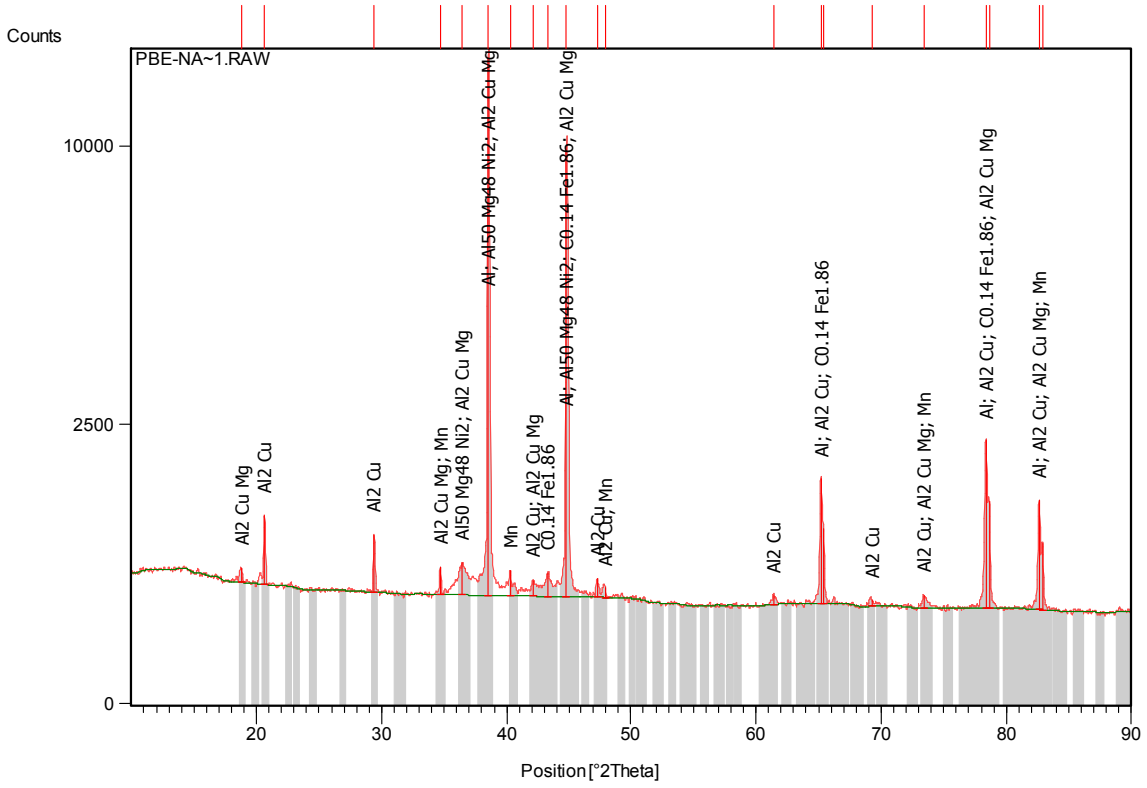


Figure 4.47: XRD pattern of the test sample in 3.5%NaCl containing PBE+BOEHMITE.

Table 4.25: Chemical/phases composition of the test sample in 3.5%NaCl containing PB+VD extracts

Visible	Ref. Code	Score	Compound Name	Displacement [°2Th.]	Scale Factor	Chemical Formula
*	01-089-4037	53	Aluminum	0.045	0.827	Al
*	00-025-0012	63	Khatyrkite, syn	0.007	0.159	Cu Al2
*	01-089-3689	34	Iron Carbide	0.109	0.072	Fe3 C
*	00-051-0799	22	Aluminum Magnesium	0.272	0.050	Al0.56 Mg0.44
*	00-049-1414	7	Aluminum Copper Magnesium	0.207	0.310	Al6 Cu Mg4
*	00-029-0043	19	Aluminum Iron	0.121	0.035	Al5 Fe2

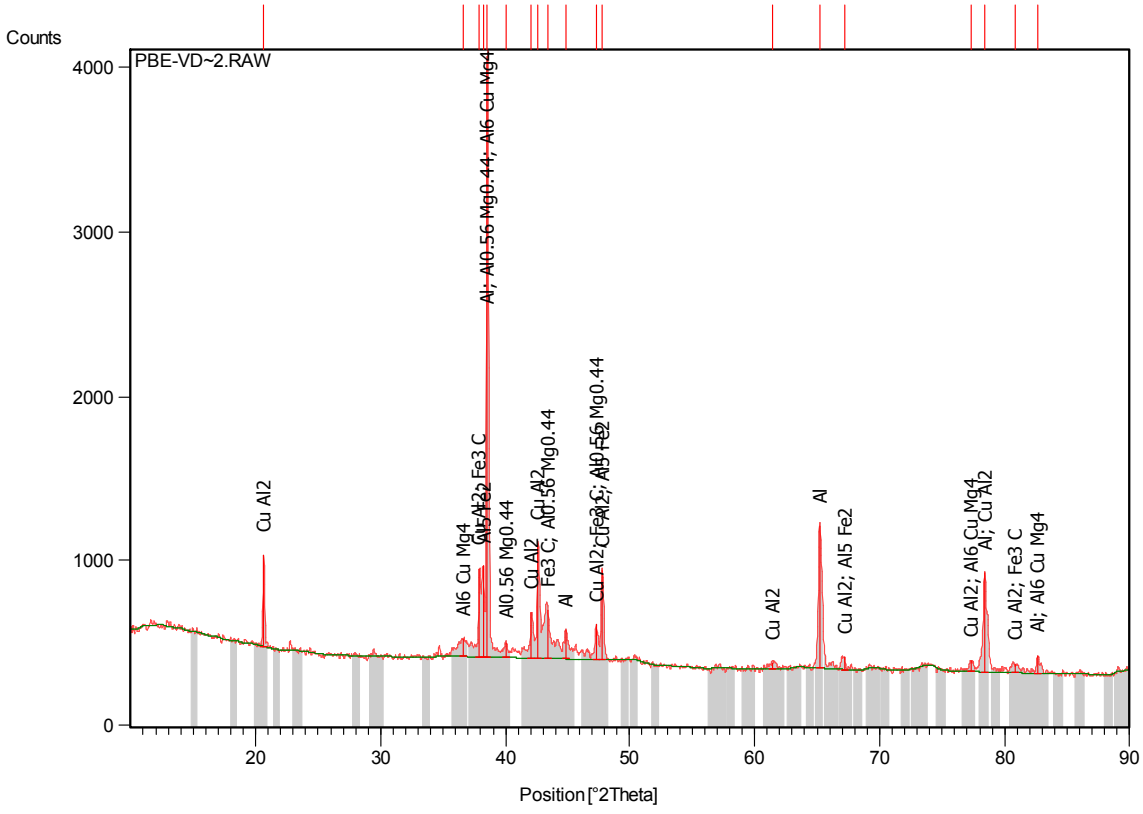


Figure 4.48: XRD pattern of the test sample in 3.5%NaCl containing PB+VD Extracts.

Table 4.26: Chemical/phases composition of the test sample in 3.5%NaCl containing PB+VD+BOEHMITE.

Visible	Ref. Code	Score	Compound Name	Displacement [°2Th.]	Scale Factor	Chemical Formula
*	00-065-2695	49	Aluminum Copper	-0.136	0.025	Al2 Cu
*	01-087-0722	48	Iron	-0.051	0.006	Fe
*	01-089-2769	34	Aluminum	-0.030	0.764	Al
*	01-075-1249	18	Magnesium Nickel	-0.015	0.004	Mg2 Ni

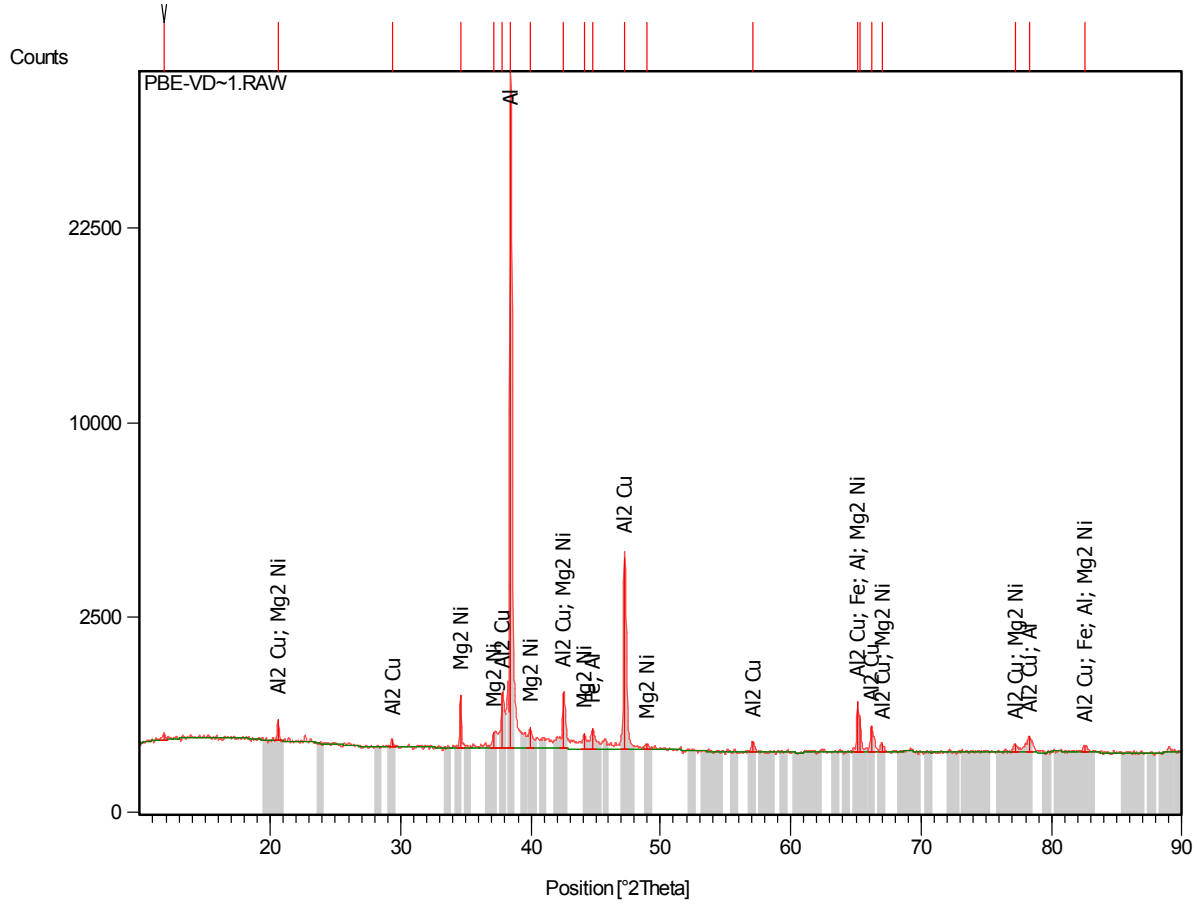


Figure 4.49: XRD pattern of the test sample in 3.5%NaCl containing PB+VD+BOEHMITE.

Table 4.27: Chemical/phase composition of the test sample in 3.5%NaCl containing VD Extracts.

Visible	Ref. Code	Score	Compound Name	Displacement [°2Th.]	Scale Factor	Chemical Formula
*	01-085-1327	52	Aluminum	0.017	1.027	Al
*	00-051-0637	36	Chromium Nickel	-0.370	0.026	Cr7 Ni3
*	01-089-4186	43	Iron	-0.318	0.009	Fe
*	00-025-0012	31	Khatyrkite, syn	0.090	0.018	Cu Al2
*	00-004-0853	13	Nickel Carbide	-0.111	0.047	Ni3 C
*	01-089-4894	13	Magnesium	0.118	0.003	Mg
*	00-001-1226	24	Copper Magnesium	-0.019	0.046	Cu2 Mg

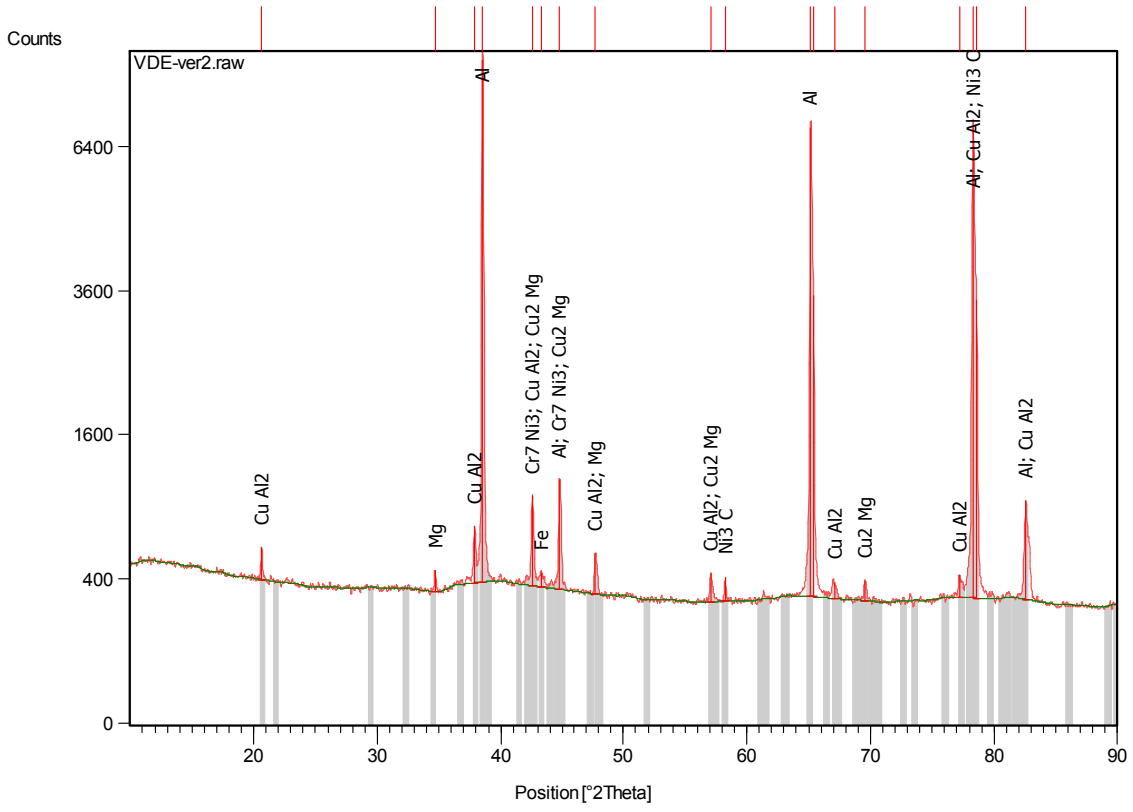


Figure 4.50: XRD pattern of the test sample in 3.5%NaCl containing VD Extracts.

Table 4.28: Chemical/phases composition of the test sample in 3.5%NaCl containing VD+BOEHMITE.

Visible	Ref. Code	Score	Compound Name	Displacement [°2Th.]	Scale Factor	Chemical Formula
*	00-047-1417	53	Taenite, syn	-0.180	0.115	(Fe , Ni)
*	00-049-1279	51	Aluminum Manganese	0.064	0.055	Al8 Mn5
*	01-087-0722	42	Iron	-0.061	0.753	Fe
*	01-089-2837	36	Aluminum	0.138	0.412	Al
*	00-065-2695	37	Aluminum Copper	-0.032	0.119	Al2 Cu
*	00-040-0903	31	Aluminum Magnesium	0.229	0.030	Mg2 Al3

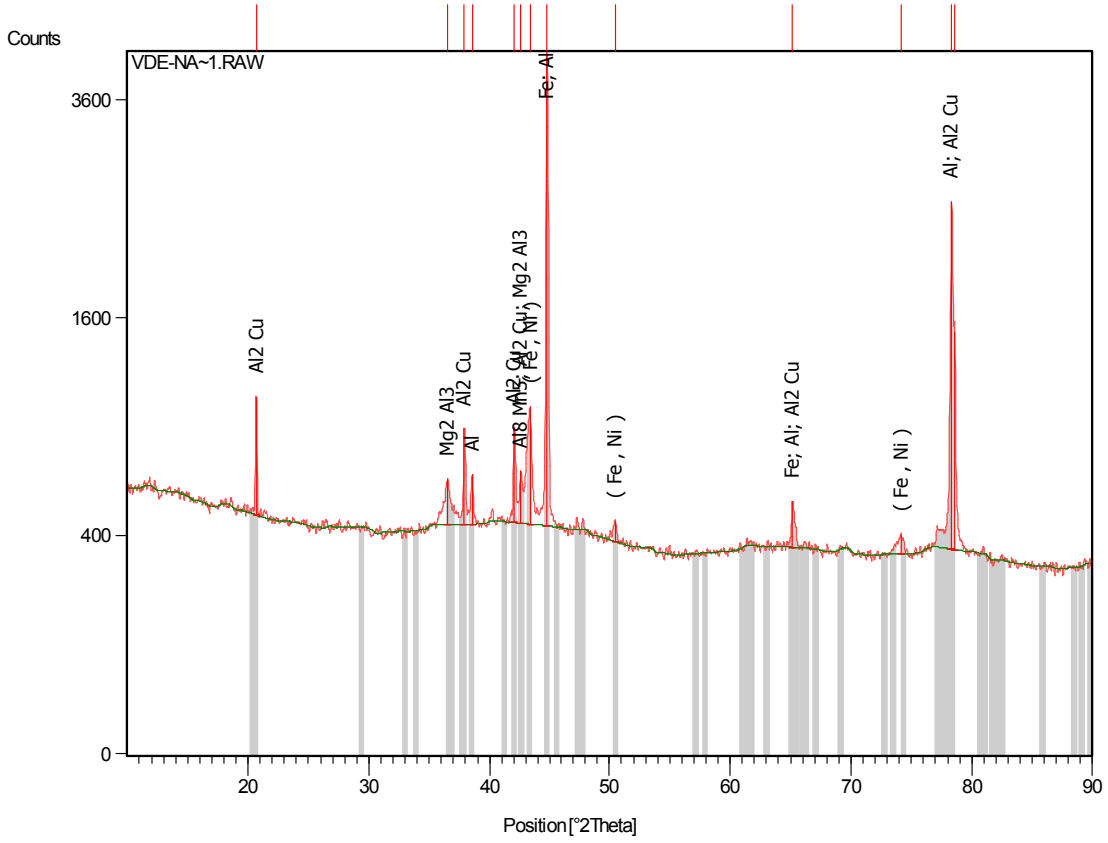


Figure 4.51: XRD pattern of the test sample in 3.5%NaCl containing VD+BOEHMITE.

4.7.3. Raman Spectroscopic Analysis

Figures 4.52 - 4.60 revealed the Raman Spectra of the test coupons for the different systems investigated. The images shown besides each Raman spectra showed the overall optical micrographs of the surface from each investigation. Raman Spectroscopy was employed to analyze very thin corrosion products which could not be analysed by XRD. In these Figures, there are some variations in Raman shifts, broadening, and surface interactions as you move from one environment to another which may be indicative of either adsorption of organic molecules onto alloy surfaces (reduction or disappearance of certain peaks) or release of certain metal ions into solution (appearance of certain peaks).

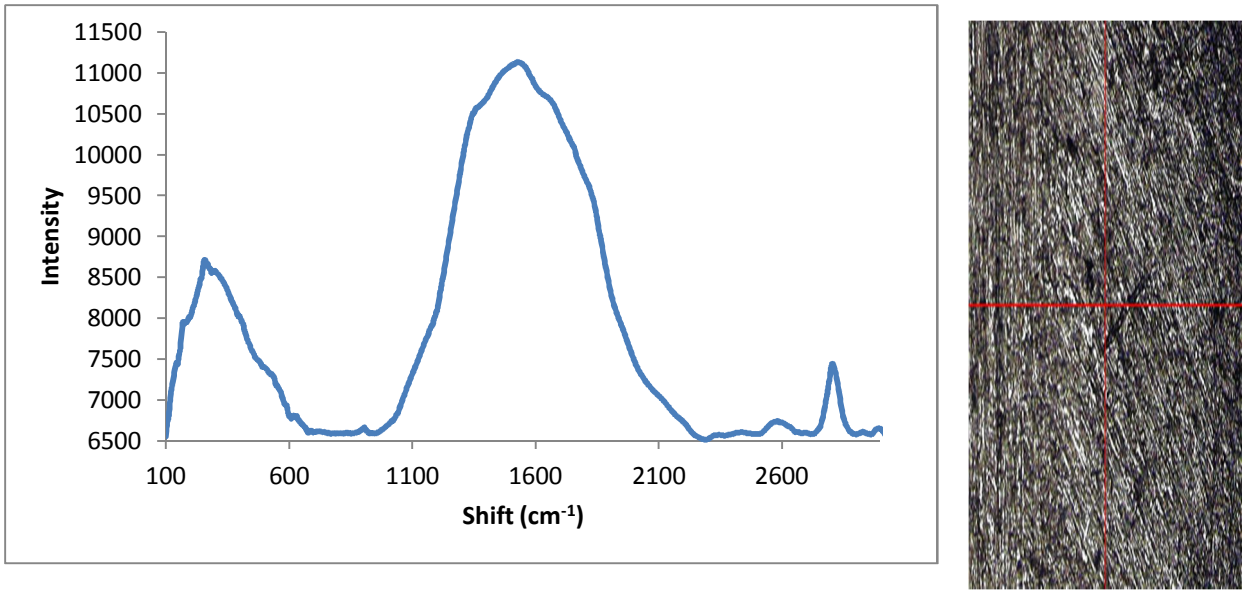


Figure 4.52: Raman Spectrum and the image of overall surface of the as-cast test alloy

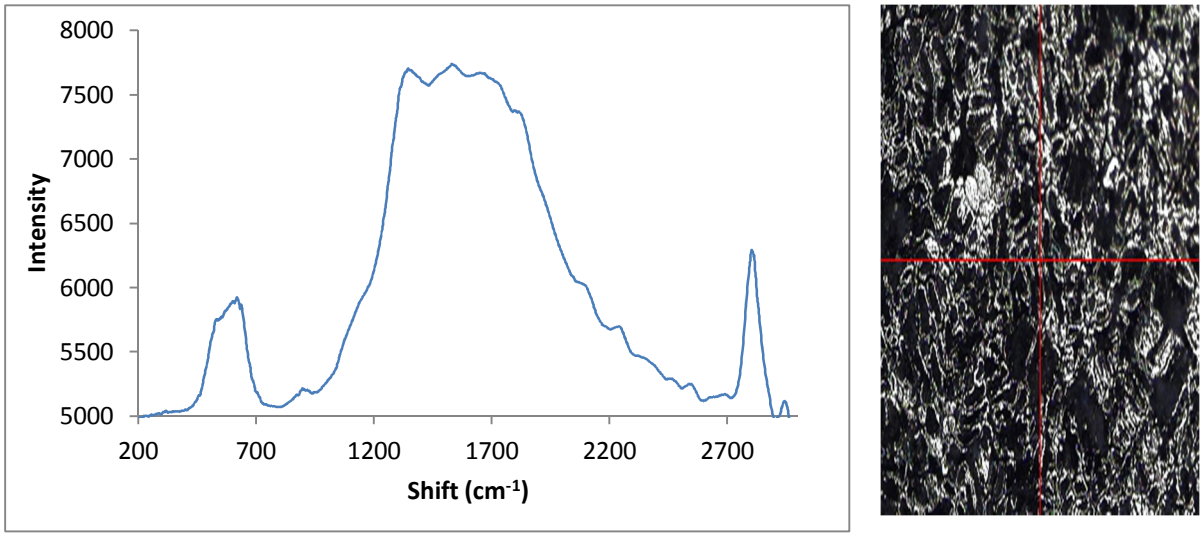


Figure 4.53: Raman Spectrum and the image of overall surface of the test alloy in 3.5%NaCl solution.

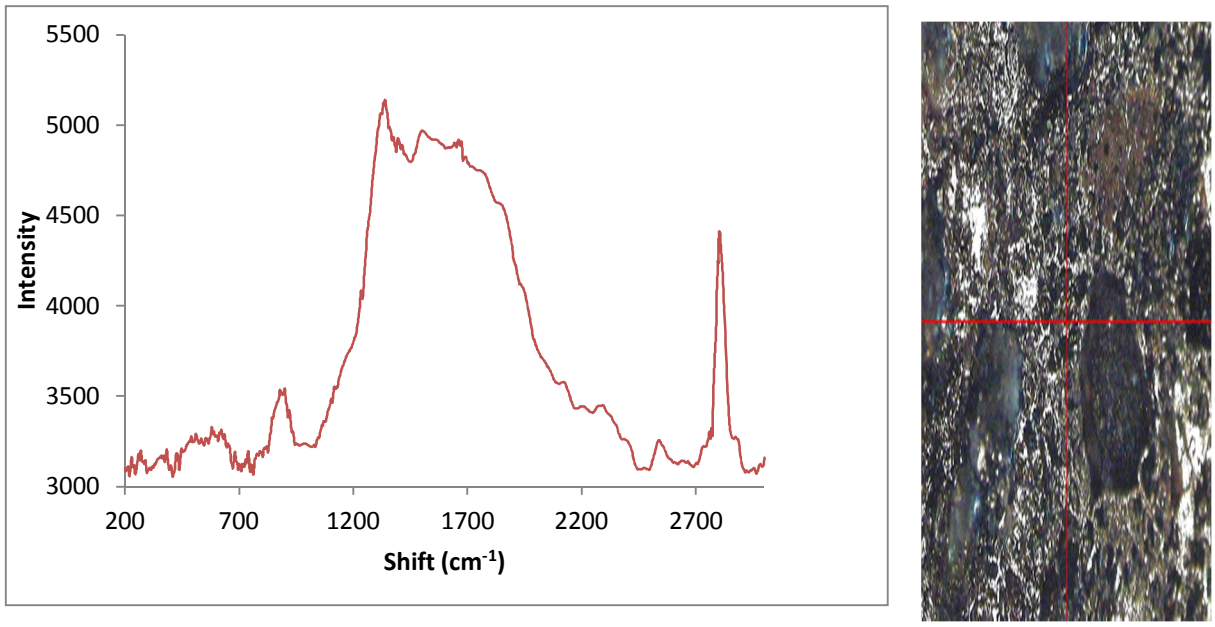


Figure 4.54: Raman spectrum and the image of overall surface of the test alloy in 3.5%NaCl and sodium chromate solution.

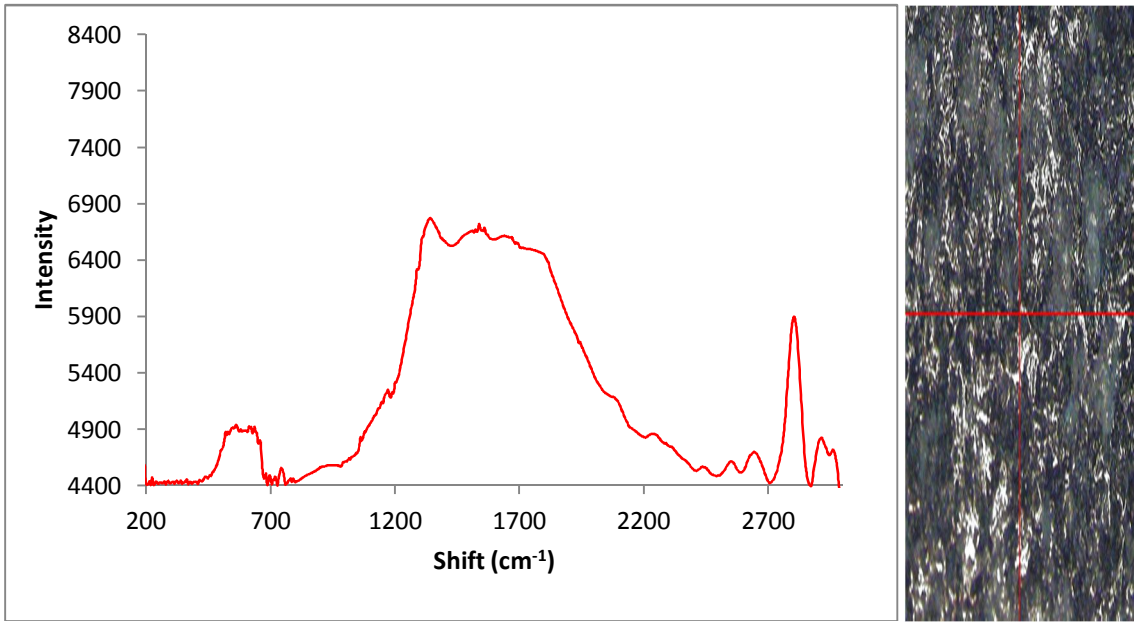


Figure 4.55: Raman spectrum and the image of overall surface of the test alloy in 3.5%NaCl and PBE solution.

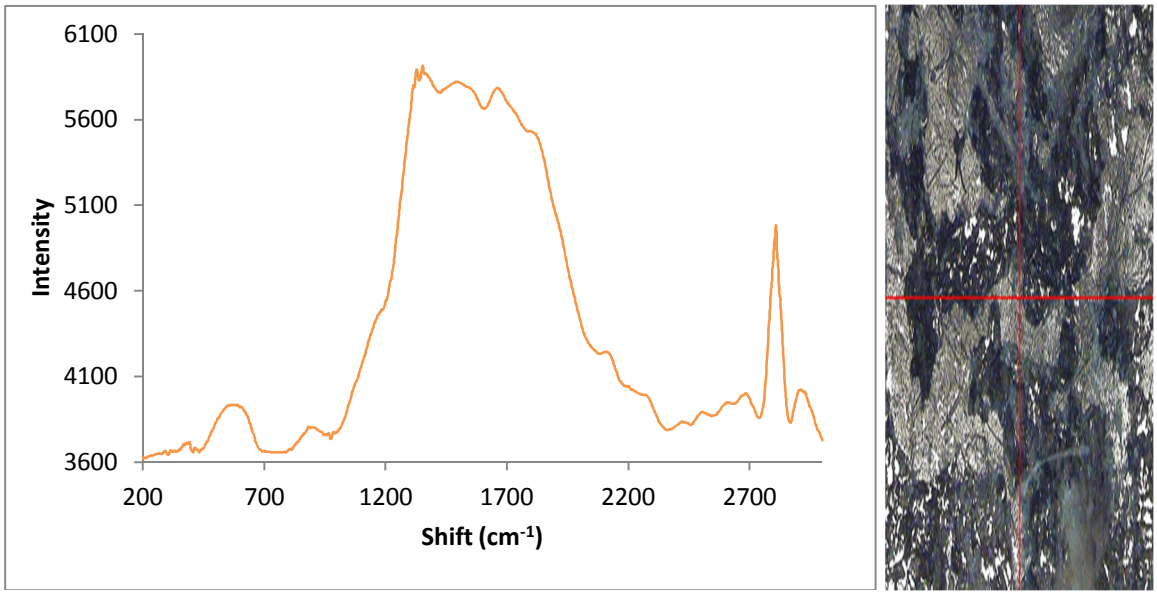


Figure 4.56: Raman spectrum and the image of overall surface of the test alloy in 3.5%NaCl and PBE+Boehmite Nanoparticles Solution.

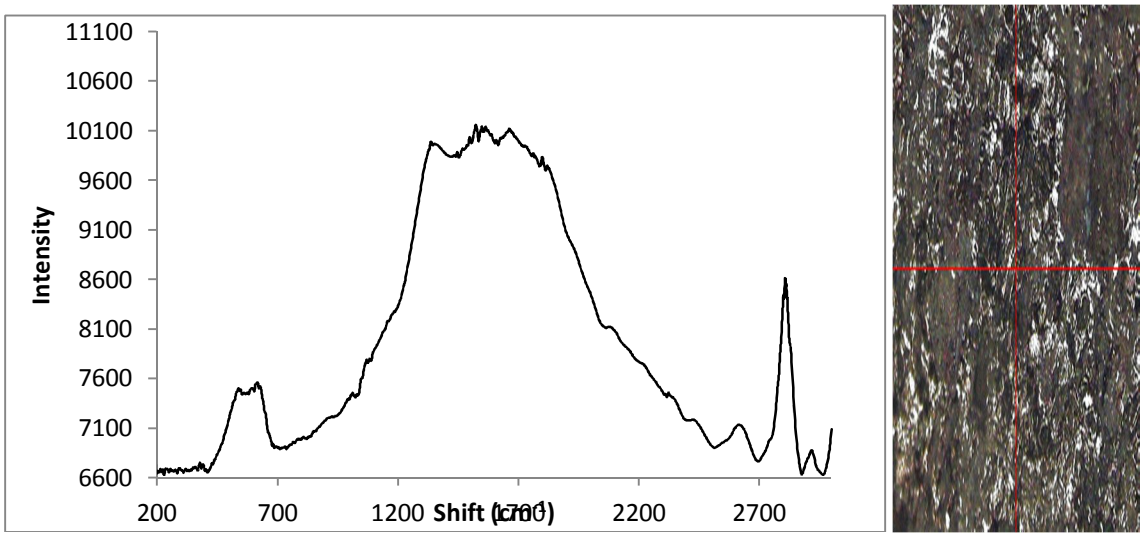


Figure 4.57: Raman spectrum and the image of overall surface of the test alloy in 3.5%NaCl and PBE+VDE solution.

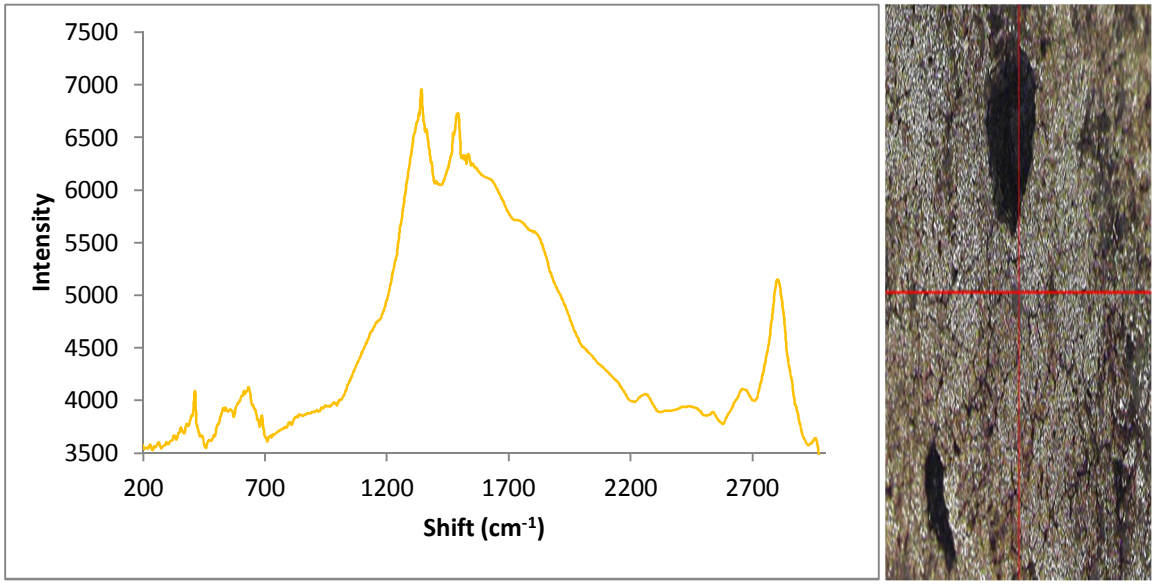


Figure 4.58: Raman spectrum and the image of overall surface of the test alloy in 3.5%NaCl and PBE+VDE+Boehmite Nanoparticles solution.

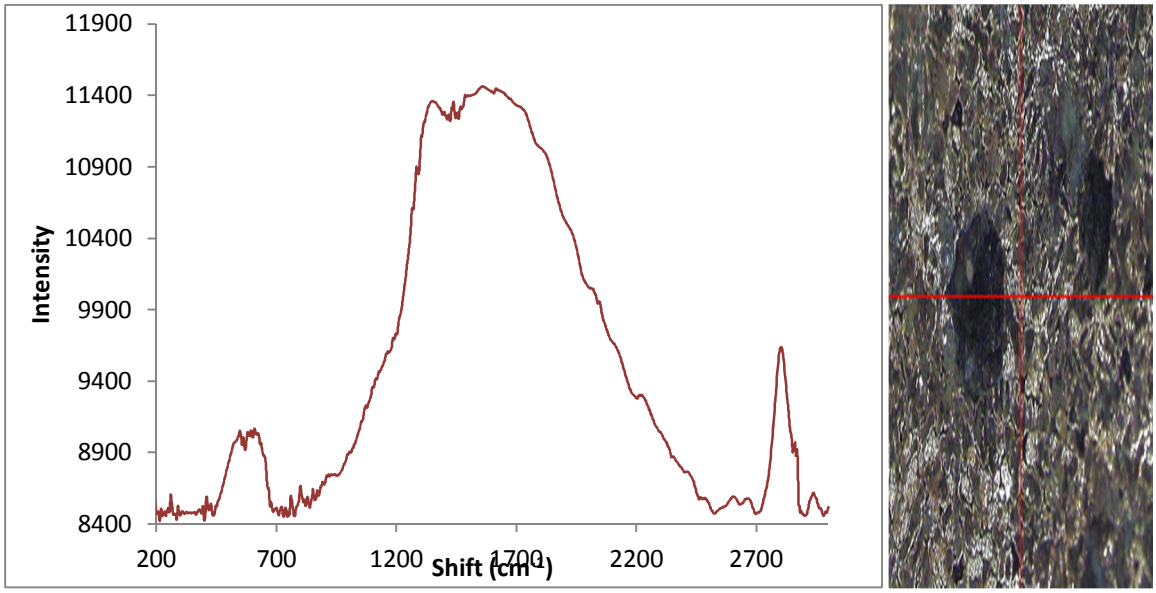


Figure 4.59: Raman spectrum and the image of overall surface of the test alloy in 3.5%NaCl and VD Extracts Solution.

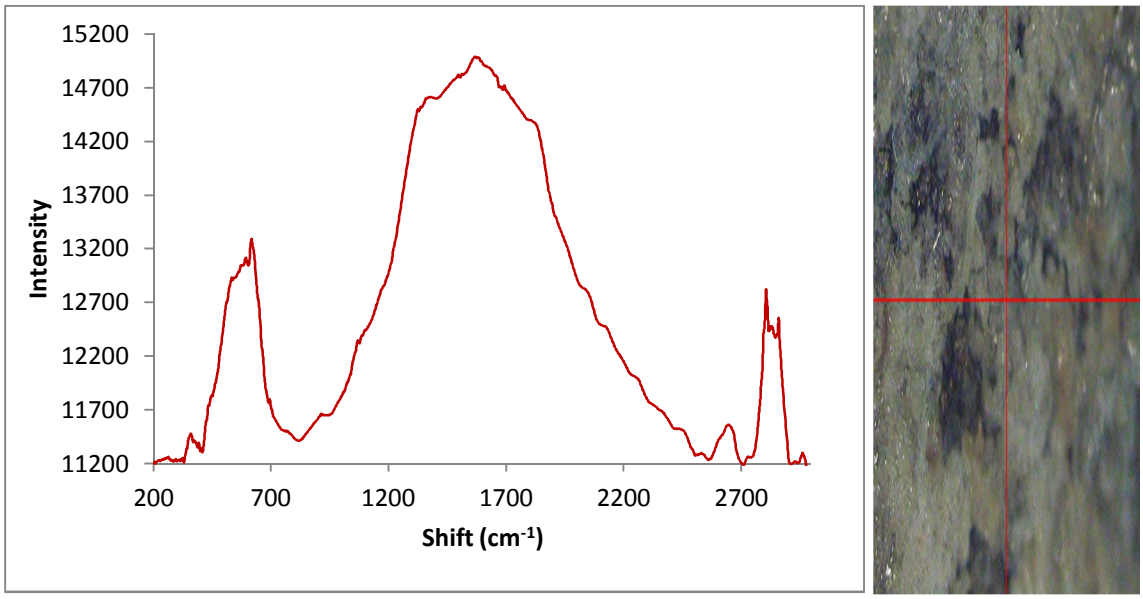


Figure 4.60: Raman spectrum and the image of overall surface of the test alloy in 3.5%NaCl and VDE+Boehmite Nanoparticles Solution.

Table 4.29: Summary of the Raman peak shifts (cm^{-1}) of the corrosion products formed on the AA2024 coupons in the different systems under investigation.

As-cast	**NaCl**	**Na_2CrO_4**	**PBE**	**PBE + BOEHMITE**	**PBE +VDE**	**PVE+ VDE+ BOEHMITE**	**VDE**	**VDE + BOEHMITE**
284	618	228	225	400	375	412	259	359
514	1342	380	562	503	537	632	290	618
696	1532	428	637	585	617	686	412	1414
914	1932	580	746	910	1336	1339	546	1618
1104	1838	679	1171	1338	1523	1492	609	2646
1288	2241	736	1342	1536	1664	2257	1348	2806
1472	2544	900	1539	1639	1798	2538	1436	2856
1690	2804	1338	2238	1657	2613	2660	2603	2959
1896	2944	1504	2438	2479	2807	2804	2660	
2072		1676	2550	2625	2917	2953	2804	
2286		2340	2643	2807			2934	
2488		2536	2804	2944				
2684		2803	2914					
2932			2963					

4.8 Analysis of Variance (ANOVA)

A two-way ANOVA system was used to evaluate the degree of variation of Inhibition Efficiencies (IE%) obtained using the three methods; Gravimetric-based mass loss, Linear Polarisation Resistance and Electrochemical Impedance Spectroscopy.

Table 4.30: Inhibition Efficiencies (IE%) obtained using LPR, EIS and Gravimetric-based mass loss (ML) for Sodium Chromate system at room temperature.

Inhibitor Conc. (v/v)	**IE%**		
	LPR	**EIS**	**ML**
0.5g Na_2CrO_4	89.99	90.00	89.72
1.0g Na_2CrO_4	91.57	91.55	91.78
1.5g Na_2CrO_4	93.11	92.99	93.15

Table 4.31: ANOVA results generated for Sodium Chromate systems at room temperature and different concentrations.

SUMMARY	*Count*	*Sum*	*Average*	*Variance*
Row 1	3	269.71	89.90333	0.025233
Row 2	3	274.9	91.63333	0.016233
Row 3	3	279.25	93.08333	0.006933
Column 1	3	274.67	91.55667	2.433733
Column 2	3	274.54	91.51333	2.236033
Column 3	3	274.65	91.55	2.9809

Table 4.32: Inhibition Efficiencies (IE%) obtained using LPR, EIS and Gravimetric-based mass loss (ML) for PBE+VDE+Boehmite system at room temperature.

Inhibitor Conc. (v/v)	**IE%**		
	LPR	**EIS**	**ML**
10%v/vPBE+40%v/vVDE +0.1g Boehmite	88.76	88.99	88.76
20%v/vPBE+30%v/vVDE +0.2g Boehmite	91.32	91.20	91.78
30%v/vPBE+20%v/vVDE +0.3g Boehmite	92.11	91.79	93.12
40%v/VPBE+10%v/vVDE +0.4g Boehmite	92.15	92.11	93.12

Table 4.33: ANOVA results generated for PBE/VDE/BOEHMITE systems at room temperature and different concentrations.

SUMMARY	*Count*	*Sum*	*Average*	*Variance*
Row 1	3	266.51	88.83667	0.017633
Row 2	3	274.3	91.43333	0.093733
Row 3	3	277.02	92.34	0.4819
Row 4	3	277.38	92.46	0.3271
Column 1	4	364.34	91.085	2.548567
Column 2	4	364.09	91.0225	1.978092
Column 3	4	366.78	91.695	4.227567

CHAPTER FIVE

5.0 DISCUSSION

5.1 X-Ray Fluorescence Result of the Cast Alloy (AA2024)

The composition of AA2024 in Table 3.1, credited to Baldini *et al*. (1995), was used in this research because of availability of the alloying elements used in casting the alloy. This is without prejudice to the work of other researchers that reported different chemical compositions for this alloy. Khoshnaw & Gardi (2007) reported a chemical composition of 93.464%Al-4.05%Cu-1.49%Mg-0.282%Si-0.034%Ti-0.62%Mn-0.02%Ni-0.04%Zn for AA2024 alloy. Smilarly, Clarke & Varney (1952) reported a composition of 92.15%Al-4.5%Cu-1.5%Mg-0.5%Si-0.5%Fe-0.5%Mn-0.10%Cr-0.25%Zn for this alloy.

The results of the XRF analysis of the as-cast sample, as revealed in Table 4.1, did not show significant deviation from the one used in the charge calculation during the process of casting the alloy.

5.2 Characterisation of the Extract by Nuclear Magnetic Resonance (NMR)

5.2.1 Parkia biglobosa.

Observation of the ^{1}H NMR spectrum in Figure 4.1 reveals some features of phenolic compounds such as flavonoids, chalcones and alkyl phenols occurring in conjunction with triterpenoids. This is because of the presence of aromatic proton as well as methine hydroxylated resonances observed in the ^{1}H NMR spectra. These resonances are common to flavonoids, chalcones and other aromatic compounds as reported in earlier works by Kim *et al*. (2010).

In the ^{1}H NMR profiles of the ethanolic extract of *Parkia biglobosa (PBE),* Methyl singlets appeared at δ_H 0.91-1.15 (leaves) with hydroxylated methine resonances at δ_H

4.21-4.24. Furthermore, hydroxylated methine resonances at δ_H 3.56 – 3.59 were evident in this spectrum of the leaves. Also present in these ^{1}H NMR spectra are aromatic proton signals at δ_H 7.66-7.77.

5.2.2 Vitex doniana

The ^{1}H NMR spectrum of the ethanolic extract of *Vitex doniana (VDE)* leaves in Figure 4.2 revealed several methyl proton signals at δ_H 0.73-0.82 with several deshielded aliphatic hydroxyl proton signals at δ_H 3.17-3.69. In addition, a signal attributed to the acetate methyl appeared at δ_H 1.16 while several aromatic proton peaks occurred at δ_H 5.00-5.95.

Observation of several terminal methyl and hydroxyl protons peaks coupled with aromatic protons peaks in the ethanolic extract of the leaves are characteristic of phenolic compounds especially alkyl phenols occurring in conjunction with triterpenoids as reported in earlier works by Kim *et al*. (2010).

In general, the predominant inhibition mechanism by plant extracts is adsorption and probable interactions of inhibitor with the electrodes or corrosion products; this is dependent on factors such as extract chemical composition, type of extraction media as well as chemical changes occurring in the extracts. Zucchi & Omar (1985) attributed the inhibitive effect of some plant extracts to the hydrolysis of protein. This has also been supported by earlier works of Singh & Quraishi (2010), Deng & Mu (2000), Noor & Al-Moubaraki (2008) and Papova *et al.* (2003).

The inhibition ability, hence adsorption, depends on the electronic structure of inhibiting molecules, steric factor, aromaticity and electron density at donor site, presence of

functional groups such as –C=O, N=N, R-OH, etc., molecular area, molecular weight of the molecule, temperature and electrochemical potential at the metal/solution interface. As can be seen from the NMR spectra of the two plant extracts, aromaticity, and presence of functional groups, such as $–CH_3$, and R-OH, were evident.

5.3 Corrosion Testing

5.3.1 Classical methods

5.3.1.1 Visual examination

Visual examination of the coupons exposed to the aggressive Sodium chloride medium revealed presence of pits, and various corrosion products. The sizes and numbers of the pits were very much reduced for the inhibited samples, most especially Sodium dichromate, Na_2CrO_4 and PBE+VDE+BOEHMITE Nanoparticles systems. Similar reductions in the numbers and sizes of pits were also observed in the samples exposed to other systems. Some of the corrosion products were visible to the naked eyes, or could be felt when touched. The shiny appearance of the coupons was compromised after exposure to the different systems, probably due to corrosion products and adsorbed substances.

a. Uninhibited samples

Figure 4.3 shows the corrosion behaviour of the test alloy in the blank (uninhibited) chloride medium obtained from Gravimetric-based mass loss. It could be observed that the Alloy is highly susceptible to corrosion in the chloride medium. This is evident from the increase in corrosion rates with increase in temperature. The observed high corrosion rates of the Alloy might not be unconnected with the high amounts of alloying additives which makes the alloy susceptible to different types of corrosion as reported in chapter one of this work.

For most applications, a corrosion penetration rate less than about 20 mpy (0.50 mm/yr) is acceptable as reported by Callister (2007). In the case of this alloy, a corrosion penetration rate of 0.63mm/yr was recorded at a temperature of 30^{o}C and this increased with increase in temperature to a value of 1.81mm/yr at 70^{o}C. Hence, there is the need for protection of this alloy since even the room temperature corrosion penetration rate is higher than the recommended value reported by Callister (2007) above. Because of the susceptibility of the alloy to uniform and localized corrosion, as reported in chapter one, the concentrations of inhibitors used were high. This is in agreement with earlier report by Phillip (2001).

5.3.1.2 Effect of Temperature and Concentration on Inhibition Efficiencies (IE%)

Figure 4.4 shows the variation of Inhibition Efficiencies (IE%) with different amounts of Na_2CrO_4 at different temperatures. Addition of different amounts of Na_2CrO_4 to the aqueous chloride medium suppressed the dissolution of the substrates at varying degrees, depending on temperature and concentration. It could be seen that at a temperature of 30^{o}C, Inhibition Efficiencies (IE%) of 89.72%, 91.78% and 93.15% were achieved through the addition of 0.5, 1.0 and 1.5g Na_2CrO_4 respectively. This confirmed that Inhibition Efficiencies (IE%) increased with increase in the amount/concentration of inhibitor; similar trends were also observed at other temperatures. This observation was earlier reported by Tang *et al.* (2003).

A general decrease of Inhibition Efficiencies (IE%) with increase in experimental temperatures could be seen clearly from Figure 4.4. The Inhibition Efficiencies (IE%) values varied from a maximum of 93.15% at 30^{o}C to a minimum of 72.10% at 70^{o}C across the different concentrations. This is because as temperature was increased,

solution agitation increased and this might have caused inhibitor desorption, resulting to a decreased surface coverage and consequently a decrease in Inhibition Efficiencies (IE%). This was supported by an earlier research by Quraishi and Jamal (2002).

The effect of temperature and concentration on the the Inhibition Efficiencies (IE%) of *Parkia biglobosa* extracts (PBE) was evaluated by weight loss method and the results shown in Figure 4.5. The Inhibition Efficiencies (IE%) increased with increase in PBE concentration and decreased with increase in temperature. This is in agreement with earlier assertion by Quraishi and Jamal (2002) that Inhibition Efficiencies (IE%) increases with increase in concentration and decreases with temperature rise.Inhibition Efficiencies (IE%) values of 70.28 and 83.30% were achieved at additive concentrations of 10%v/vPBE and 50%v/vPBE respectively, affirming that the efficiency increased with increase in concentration. This performance of this inhibitor system fall short in efficiency (IE%) compared to Na_2CrO_4 inhibitor system, the standard inhibitor used for comparing the efficiencies of the test inhibitors.

Figure 4.6 shows the variation of Inhibition Efficiencies (IE%) with different concentrations of *Parkia biglobosa* extracts and Boehmite Nanoparticles at different temperatures. The general trend of increase in corrosion rate (decrease in Inhibition Efficiencies, IE%) with increase in temperature and its increase with increase in inhibitor concentration was observed here. At the temperature of 30^{o}C, the Inhibition Efficiencies (IE%) increased from 71.52% at concentration of 10%v/vPBE+0.1g Boehmite to 87.60% at concentration 50%v/vPBE+0.5g Boehmite. Also, the Inhibition Efficiencies (IE%) decreased with increase in temperature; from 71.52% at temperature of 30^{o}C and concentration of 10%v/vPBE+0.1g Boehmite to 44.36% at the same concentration and

temperature of 70^{o}C. In a similar fashion, the Inhibition Efficiencies (IE%) also decreased from 87.60% at a temperature of 30^{o}C and concentration of 50%v/vPBE+0.5g Boehmite to 50.99% at the same concentration and temperature of 70^{o}C. This is because as temperature was increased, solution agitation increased and this might have caused inhibitor desorption, resulting to a decreased surface coverage and consequently a decrease in Inhibition Efficiencies (IE%). This was supported by an earlier research by Quraishi and Jamal (2002).

The improvement in the Inhibition Efficiency (IE%) resulting from Boehmite nanoparticles addition to PBE system might not be unconnected with the ability of the Nanoparticles to absorb the inhibitor molecules and make adsorption much faster/easier due to their high surface energy, surface loadings and high surface area as reported by Cook *et al.* (2006). Despite this, the performance of this inhibiting system did not measure up to that of the reference inhibitor, Na_2CrO_4.

Figure 4.7 shows the variation of Inhibition Efficiencies (IE%) with different concentrations of *Vitex doniana* extracts (VDE) Nanoparticles at different temperatures. The extracts of VDE inhibited the corrosion of the substrates at varying concentrations and temperature. Also, the Inhibition Efficiencies (IE%) were found to increase with increase in concentration and decrease with increase in temperature. At extracts concentration of 10v/vVDE, the efficiency of 48.35% was achieved at 30^{o}C while at the concentration of 50v/vVDE, an efficiency of 74.10% was obtained at the same temperature. A progressive decrease of efficiency with increase in temperature was noticed; the lowest values of 35.94% and 39.49%, at temperature of 70^{o}C, and concentration of 10%v/vVDE and 50%v/vVDE were respectively recorded. This

corroborates with an earlier research by Tang *et al*. (2003). The VDE inhibitor system compared less favourably with the reference inhibitor used in the test.

Figure 4.8 shows the variation of Inhibition Efficiencies (IE%) with different concentrations of *Vitex doniana* extracts and Boehmite Nanoparticles at different temperatures. Addition of Boehmite Nanoparticles to the VDE system improved its Inhibition Efficiencies (IE%). It could be observed that in a concentration of 10%v/vVDE+0.1g Boehmite Nanoparticles addition, Inhibition Efficiencies (IE%) of 48.56 and 45.44% were recorded at temperatures of 30 and 70^{o}C respectively. Similarly, in a concentration of 50%v/vVDE+0.5g Boehmite Nanoparticles, Inhibition Efficiencies (IE%) of 79.49 and 54.77% were obtained at temperatures of 30 and 70^{o}C respectively. This supports the facts that Inhibition Efficiency (IE%) increases with increase in concentration and decreases with increase in temperature, as reported by Quraishi & Jamal (2002).

The improvement in the Inhibition Efficiency (IE%) resulting from Boehmite Nanoparticles addition might not be unconnected with the ability of the Nanoparticles to absorb the inhibitor molecules and make adsorption much faster/easier due to their high surface energy, surface loadings and high surface area as reported by Cook *et al.* (2006). On a comparative note, the performance of this inhibitor system did not measure up to that of the reference inhibitor Na_2CrO_4.

Figure 4.9 shows the variation of Inhibition Efficiencies (IE%) with different concentrations of *Parkia biglobosa* and *Vitex doniana* extracts at different temperatures. It could be observed that the synergistic combinations of *Parkia biglobosa* and *Vitex doniana* produced an enhanced Inhibition Efficiencies (IE%) compared to either of the

two individual extracts alone. This was supported by an earlier work by Saratha *et al*. (2009) in which it was reported that the Inhibition Efficiencies (IE%) of some plant extracts were enhanced through Synergy. The decrease and increase of Inhibition Efficiencies (IE%) with temperature and concentration increase suggested a probable respective modes of desorption and adsorption as reported by Tang *et al.* (2003). At a synergistic concentration of 10%v/vPBE+40%v/vVDE, Inhibition Efficiencies (IE%) of 74.33% and 58.24% were achieved at 30 and 70^{o}C respectively. Similarly, the Inhibition Efficiencies (IE%) decreased as the temperature progressively increased from 30 to 70^{o}C; from 86.96 to 64.51% at 40%v/vPBE+10%v/vVDE concentration and temperature of 30 to 70^{o}C respectively. The synergistic combination of these two extracts offered good protection to the substrate, but, to a lesser extent than the one offered by the standard inhibitor, Sodium chromate.

Figure 4.10 shows the variation of Inhibition Efficiencies (IE%) with different concentrations of *Parkia biglobosa*/*Vitex doniana* extracts and amounts of Boehmite Nanoparticles at different temperatures. The performance of this inhibitor system compared favourably to that of the reference inhibitor, Na_2CrO_4. A maximum efficiency of 93.12% at 30^{o}C compared closely with 93.15% achieved with Na_2CrO_4 at the same temperature. The improvement in the Inhibition Efficiencies (IE%), resulting from Boehmite nanoparticles addition to the synergistic combination of PBE+VDE, might not be unconnected with the ability of the Boehmite Nanoparticles to absorb the inhibitor molecules and facilitate inhibition through adsorption. This was possible because of high surface energy, surface loadings and high surface area of Boehmite as reported by Cook *et al.* (2006).

Decrease in Inhibition Efficiencies (IE%) with increase in temperature is suggestive of physical adsorption mechanism and may be attributed to increase in the solubility of the protective films and of any reaction products precipitated on the surface of substrate that may otherwise inhibit the corrosion process. The physical adsorption mode does not necessarily exclude chemisorption from taking place; in many cases they occur in tandem. It may further be attributed to a possible shift of the adsorption-desorption equilibrium towards desorption of adsorbed inhibitor due to increased solution agitation, hence causing a decrease in surface coverage. Thus, as the temperature was increased, the number of adsorbed molecules decreased, leading to a decrease of Inhibition Efficiencies (IE%). This has been reported by Obot *et al.* (2009). The decrease in inhibition efficiencies with rise in temperature might also be caused by weakening of physical adsorption as advanced by Lebrini *et al.* (2010); Schorr & Yahalom (1972).

In all the systems investigated, it was possible that inhibition might not only be due to adsorption. Recent investigation has highlighted the importance of electrochemical reactions between the different ions and the substrates, leading to formation of compounds that may shield the metal from aggressive electrolyte, as the major factor in the formation of protective films.

Additionally, the interactions of inhibitors with the corrosion products may alter the electrophysical properties of surface atoms by donor-acceptor inhibitor/metal reaction, rather than in screening the metal surface from the corrosive environment. Furthermore, corrosion products may be present as a thin, well-adhering, oxidic surface film which protects the underlying metal from further corrosion by forming passive film. It is evidenced that many organic and inorganic inhibitors become effective through

interaction with one of several corrosion products to form a new protective phase rather than by adsorption onto the metal surface.

5.3.2 Linear Polarisation Resistance

In the absence of any inhibitor, i.e. in a blank sodium chloride medium, average current density and corrosion rate of 48.3μA/cm² and 1.78mm/yr were obtained respectively. The degrees of anodic (6.37mV/dec) and cathodic (7.48mV/dec) polarisation were less pronounced. Similarly, a low value of polarisation resistance of 132.84 Ω was recorded for the blank/uninhibited sample.

It was noted from Table 4.2 that addition of Sodium chromate to the chloride solution containing the substrate caused changes in corrosion potential values. This might be due to competition in the cathodic and anodic reactions caused by influence of the Sodium chromate addition as reported by Rozenfeld (1981[a]). The lower current density values (1.84, 1.79 and 0.99 μA/cm²) in the presence of inhibitors, without causing significant changes in corrosion potential, suggested that the inhibitor is a mixed-type. Both the anodic and cathodic processes were polarized, as can be seen from Figure 4.11, with the anodic processes more polarized than the cathodic ones.

The effect of the inhibitor was more pronounced on the anodic polarisation at the first two concentrations (0.5 and 1.0g/100mils); $\beta_a \neq \beta_c$ in both cases. The changes in β_a and β_c values, as shown in Table 4.2, indicated that the adsorption of Sodium chromate onto the substrate modified the mechanism of anodic dissolution as well as cathodic gaseous evolution. This also corroborated earlier findings by Frankel (2003). It could also be seen from Table 4.2 that the addition of Chromate reduced the corrosion rates; the corrosion rates were observed to decrease from 0.062 to 0.03mm/yr as the amount of inhibitor was

altered, incrementally from 0.5 to 1.5g/mils respectively. This was a marked improvement compared to the corrosion rate of 1.78mm/yr for the uninhibited sample. This consequently affected the Inhibition Efficiencies (IE%), which increased from 89.99 to 93.11% with increase in amounts of Sodium chromate. The increase in IE% values with increase in inhibitor concentration followed established trends of corrosion inhibitor functionality as reported by Kuznetsov (2004); Frankel (2003) and Tang *et al*. (2003).

Furthermore, the changes observed in the cathodic and anodic Tafel slopes were indicative of inhibitor interactions with the electrode surfaces; probably the inhibitor might adsorb and block the reaction sites at the surfaces. Hence inhibitor adsorption onto the substrates was the probable mode of corrosion inhibition mechanism. This adsorption might be substitutional in nature as reported in an earlier research by Gomma & Wahdan (1994); the adsorption of an organic adsorbate onto metal-solution interface could be attributed to a substitutional adsorption process between the organic molecules in the aqueous solution $Org_{(sol)}$ and the water molecules on the metallic surface $H_2O_{(sol)}$;

$$Org_{(sol)} + xH_2O \rightarrow Org_{(ads)} + xH_2O_{(sol)}$$

$Org_{(sol)}$ and $Org_{(ads)}$ are the organic molecules in the aqueous solutions and adsorbed on the metallic surface, respectively, $H_2O_{(ads)}$ is the water molecules on the metallic surface, and x is the size ratio representing the number of water molecules replaced by one molecule of organic adsorbate.

The observed increase in the polarization resistance $\boldsymbol{R_p}$ values (1290, 1920, 2810Ω) with increase in the concentration of the inhibitor might be due to increase in surface coverage as the inhibitor concentration was increased. This, coupled with the formation of a more coherent protective layer, retarded further dissolution of the substrates as the inhibitor

concentration was increased. This is in agreement with earlier works by Raman and Labine (1986).

Figure 4.12 above shows the Polarisation curves for AA2024 coupons containing different concentrations of *Parkia biglobosa* extracts (PBE) at room temperature, while Table 4.3 contains the Polarisation parameters, derived from the polarisation curve, and the computed values of the Inhibition Efficiencies (IE%) at various concentrations.

It could be observed from the Polarisation curve of PBE in Figure 4.12 that addition of different concentration of the PBE affected both the anodic and cathodic behaviour of the coupons at varying degrees. From the PBE Polarisation parameters contained in Table 4.3, it could be seen that both β_a and β_c values changed with increase in PBE concentration from 10%v/v to 50%v/v. This indicated that PBE addition influenced both anodic and cathodic reactions at varying degrees, the cathodic processes being more polarized than the anodic processes due to higher β_c values compared with β_a values. Since these variations did not significantly affect the corrosion potential, PBE may still be considered as a mixed-type inhibitor.

The progressive decrease in current density/corrosion rate values with increase in concentration might probably be due to the inhibitor molecules adsorption onto the substrates resulting to increased surface coverage, thereby lowering anodic dissolution and hence the observed decrease in current densities and corrosion rates. This is in agreement with earlier works of Ebenso *et al.* (2004).

It was also generally observed that the Polarisation resistance and Inhibition Efficiencies (IE%) increased with increase in inhibitor concentration. The highest IE% value of 81.99% was obtained at 40%v/v PBE concentration which also corresponded to the

highest polarisation resistance $\boldsymbol{R_p}$ value of 749.33Ω. This meant that 40%v/v was the best concentration at which PBE impeded the dissolution of the substrate and formed a coherently adsorbed layer on the substrate.

The observed increase in corrosion rate at 50%v/v PBE concentration and a corresponding decrease in the IE% value compared with the one at 40%v/v PBE concentration implied that at concentration beyond 40%v/v, PBE was in excess amount and might lead to more inhibitor molecules interacting with themselves rather than with the substrates, hence reducing competitive adsorption on the substrate surfaces. This has been established in an earlier report by Saratha *et al.* (2009).

Figure 4.13 above represents the Polarisation curves for AA2024 containing different concentrations of PBE and Boehmite nanoparticles at room temperature. It could be seen that both anodic and cathodic processes were polarized at varying degrees, depending on inhibitor concentrations. Table 4.4 contains the Polarisation parameters and the corresponding Inhibition Efficiencies (IE%) for the corrosion of the substrate (AA2024) in 3.5%NaCl containing different concentrations of *Parkia biglobosa* extracts (PBE) and different amounts of Boehmite {AlO(OH)} Nanoparticles at room temperature.

It could be seen that addition of Boehmite Nanoparticles considerably increased the anodic and cathodic $\boldsymbol{\beta}_a$ and $\boldsymbol{\beta}_c$ values. This, in effect, affected the corrosion potential, current density/corrosion rate, polarisation resistance and Inhibition Efficiencies (IE%). Nanosized-Boehmite, with its characteristic high surface energy and loading, has high affinity for other ions, thus it might have formed complexes with the inhibitor ions/molecules and facilitate adsorption, hence the increase in Inhibition Efficiencies

IE% compared with PBE system. Similar Boehmite attributes in facilitating inhibitor functionality has also been reported by Cook *et al.* (2006).

Polarisation curves for AA2024 containing synergistic combinations of *Parkia biglobosa* (PBE) and *Vitex doniana* extracts (VDE) at room temperature is given in Figure 4.14 above. Table 4.5 contained the corresponding Polarisation parameters and Inhibition Efficiencies (IE%) derived from the curve. This synergistic combination of PBE and VDE significantly affected all the parameters contained in Table 4.5. Both the anodic and cathodic processes were polarized, but the degree of the polarisation was higher for anodic than cathodic processes ($\beta_a \neq \beta_c$ at all PBE+VDE concentrations investigated), hence this synergistic combination of PBE and VDE is a mixed-type inhibitor, affecting the anodic process more than the cathodic one. Of particular importance was the Polarisation resistance and Inhibition Efficiencies (IE%) which increased considerably with increase in inhibitor concentration. The Inhibition Efficiency (IE%) of 82.98% obtained at 40%v/vPBE+10%v/vVDE concentration was found to be higher than IE% value of 81.99% obtained at 40%v/v PBE concentration and much higher than 71.99% obtained at 50%v/vVDE concentration. It could thus be inferred that the synergistic combinations of PBE and VDE enhanced Inhibition Efficiencies (IE%) mainly due to competitive adsorption/co-adsorption resulting to increased coverage. This is in accordance with an assertion by Elewady *et al*. (2008) that the combined effect of two or more inhibitive substances is greater than that of either substance alone.

Figure 4.15 is the Polarisation curve for AA2024 in different concentrations of PBE+VDE+Boehmite system at room temperature, while Table 4.6 contains the corresponding Polarisation parameters and Inhibition Efficiencies (IE%). From these

parameters, it could be seen that addition of Boehmite Nanoparticles significantly affected the corrosion behaviour of the substrates; the anodic and cathodic processes were both affected by the addition of different concentrations of PBE+VDE+Boehmite Nanoparticles as can be seen from the changes in the values of β_a and β_c in Table 4.6.

The obtained values of β_a were greater than those of β_c, infering that this inhibitor system affected the anodic processes more than the cathodic ones. Since there were no marked deviations within the values of the corrosion potential, E_{corr}, it could be inferred that the inhibitor is a mixed-type, mitigating the anodic dissolution more than the cathodic gaseous evolution.

The observed decrease in corrosion rates with increase in inhibitor concentration might not be unconnected with more interaction of inhibitor molecules with electrode surfaces and corrosion products. This probably resulted to increased surface coverages by the thin film layer of the inhibitor. It could also be seen from Table 4.6 that the addition of PBE+VDE+Boehmite reduced the corrosion rates; the corrosion rates were observed to decrease from 0.2386 to 0.0344mm/yr as the amount of inhibitor was increased. Similarly, the current densities were also found to decrease, from 7.06 to 1.02$\mu A/cm^2$, with increase in the inhibitor concentration. The values of Polarisation resistances, R_p, and the current densities increased and decreased with increase in inhibitor concentration respectively. This indicated that the additives decreased the dissolution rate of the substrates.

The Inhibition Efficiencies (IE%) were also observed to increase, from 88.76 to 92.13%, with increase in the concentrations of inhibitor. Synergistic effects among the inhibitor molecules/ions and other species might be responsible for the observed improvement of

Inhibition Efficiencies (IE%). Addition of Boehmite Nanoparticles appreciably improved the performance of this inhibitor system, mainly due to its high surface loading and surface area.

The Inhibition Efficiencies (IE%) obtained in this system compared favourably with those obtained in sodium chromate system. It could thus be inferred that of all the systems investigated, only PB+VD+Boehmite Nanoparticle system matched the performance of sodium chromate, the reference inhibitor.

The Polarisation parameters and the corresponding Inhibition Efficiencies (IE%) for the corrosion of AA2024 Aluminium Alloy in 3.5%NaCl containing different concentrations VDE at room temperature were shown in Table 4.7. Figure 4.16 represents the Polarisation curves for AA2024 containing different concentrations of VDE at room temperature. It is evident that the addition of *Vitex doniana* extracts mitigated the corrosion of the substrate at varying degree. The anodic and cathodic processes were both affected by the addition of different concentrations of VDE as can be seen from the changes in the values of $\boldsymbol{\beta_a}$ and $\boldsymbol{\beta_c}$ in Table 4.7. The obtained values of $\boldsymbol{\beta_c}$ were greater than those of $\boldsymbol{\beta}_{a,}$ suggesting that this inhibitor system affected the cathodic processes more than the anodic ones. The increase of Inhibition Efficiencies (IE%) with concentration increase could be attributed to more inhibitor interactions with electrode surfaces as the concentration was increased.

The values of Polarisation resistance, $\mathbf{R_p}$, and the current density increased and decreased with increase in inhibitor concentration respectively. This indicated that the additives decreased the dissolution rate of the substrates, probably by formation of adsorbed layers and/or interaction between the inhibitor molecules and the substrates.

The Polarisation parameters and the corresponding Inhibition Efficiencies (IE%) for the corrosion of AA2024 Aluminium Alloy in 3.5%NaCl containing different concentrations VDE+Boehmite Nanoparticles at room temperature were shown in Figure 4.17. It could be observed from the Table 4.8 that the Polarisation Resistance, R_p, and the Inhibition Efficiencies (IE%) increased with increase of inhibitor concentrations as noted earlier in other systems; IE% values increased from 45.89 to 78.59% at concentrations of 10%v/vVDE+Boehmite Nanoparticles and 50%v/vVDE+Boehmite Nanoparticles respectively.

The current densities and corrosion rates decreased with increase in the concentration of the inhibitive additive. Values for current densities decreased from 30.7 to 6.99$\mu A/cm^2$, while the corrosion rates increased from 1.6325 to 0.13345mm/yr as the concentration of the inhibitor increased from 10%v/vVDE to 50%v/vVDE. Addition of Boehmite Nanoparticles appreciably improved the performance of *Vitex doniana.*

In summary, analyses of the polarisation curves showed that no passive-active transition up to high currents. Anodic dissolution of the metal occurred at high rates and the different additive systems mitigated this dissolution of the substrates at varying degrees. The Inhibition Efficiencies obtained from polarisation measurements were found to be in agreement with those obtained from both Electrochemical Impedance Spectroscopy (EIS) and gravimetric-based mass loss.

5.3.3 Electrochemical Impedance Spectroscopy (EIS)

Figure 4.18 is the Nyquist diagram for the AA2024 substrate inhibited by Na_2CrO_4, while Table 4.9 contains the parameters obtained from the Nyquist diagram. It was evident from the Table that the Inhibition Efficiencies IE% increased with increase in Na_2CrO_4 (from 90.00 to 92.99%). The values of charge-transfer resistance, R_{ct}, and double layer capacitance $C_{dl,}$ were obtained from impedance measurements. It was also noted that addition of the Na_2CrO_4, increased the charge transfer resistance, R_{ct}, which increased from 298.35 to 375.25 Ωcm^2 as the concentration of Na_2CrO_4 was increased. From Table 4.9, it is clear that the greatest effect was observed at addition of 1.5 g sodium chromate to the sodium chloride which gave R_{ct} value of 375.25 Ωcm^2.

The capacitance of the double layer C_{dl} decreased, from 38.12 to 25.99μF, with increase in the concentration. The decrease in C_{dl} values with increase in concentration of Na_2CrO_4 could be attributed to a decrease in local dielectric constant and/or an increase in the thickness of the electrical double layer which was earlier reported by Yurt *et al.* (2002). This situation was the result of an increase in the surface coverage, which led to an increase in the Inhibition Efficiency as reported by Ambrish *et al.* (2010). The solution resistance also appreciably increased with increase in inhibitor concentration.

The Constant Phase Element (CPE), shown in the circuit of Figure 3.3, is considered a surface irregularity of the electrode causing a greater depression in the Nyquist semicircles. The CPE helped in giving a more accurate fit of the impedance data, a metal solution-interface acted as a capacitor with an irregular surface. This has been corroborated by Chauhan & Gunasekaran (2007).

The impedance spectra for Nyquist plots were analysed by fitting to the equivalent circuit model in Figure 3.3, which was used elsewhere to describe a metal/sea water interface. It is apparent from the Nyquist plots that the impedance response of the substrate in inhibited chloride solution has significantly changed after the addition of sodium chromate and that the impedance of inhibited substrate increased with increasing concentration of inhibitor. The Nyquist plots showed that on increasing concentration, the semicircle diameter also increased with attendant increase in Inhibition Efficiencies IE%.

It is apparent from Nyquist plots shown in Figure 4.19 that the impedance response of the substrate has significantly changed after the addition of PBE+VDE+BOEHMITE Nanoparticles. The impedance of inhibited substrate increased with increasing concentration of the additive, which is evident from increase in the semicircle diameters of the Nyquist plots as the concentration was increased.

Table 4.10 showed that on increasing concentration, the charge transfer resistance increased (from 209.11 to 362.12 Ωcm^2) and the double layer capacitance C_{dl} decreased, from 43.97 to 26.23 μF. The decrease in C_{dl} values with concentration increase could be attributed to a decrease in local dielectric constant and/or an increase in the thickness of the electrical double layer as established was by Yurt *et al.* (2002). From the Table 4.10, it is clear that the greatest effect was observed at addition of 40%v/vPBE+10%v/vVDE+Boehmite Nanoparticles, which gave R_{ct} value of 362.12 Ωcm^2. The solution resistance also appreciably increased with increase in inhibitor concentration.

Inhibition efficiencies were found to increase, from 88.99 to 92.11%, with inhibitor concentration. The performance of this system compared favourably with the standard.

The Inhibition Efficiencies (IE%) obtained from EIS were in good agreement with those obtained from the LPR and weight loss method.

Table 4.11 contained parameters obtained from Nyquist diagram for the corrosion of AA2024 coupons inhibited by PBE+VDE synergistic system in 3.5%NaCl solution at room temperature, while Figure 4.20 is the corresponding Nyquist diagram. The impedance of inhibited substrate increased with increasing concentration of the additive, which is evident from increase in the semicircle diameters of the Nyquist plots as the concentration was increased. The Inhibition Efficiencies IE% increased with increase in concentration of PBE+VDE system. A maximum Efficiency of 82.99% was attained at a corresponding charge transfer resistance of 211.53 Ωcm^2 and double layer capacitance of 24.19 μF. The latter and former decreased and increased with an increase in inhibitor concentration, mainly due to the shielding effect provided by the inhibitor or probable increase in the surface coverage by the inhibitor, which led to increased Inhibition Efficiencies. The solution resistance increased, from 1.27 to 1.88 Ωcm^2, with increase in inhibitor concentration.

EIS measurements were also carried out for PBE inhibitor system and the Parameters obtained from Nyquist diagram for the corrosion of the substrates in 3.5%NaCl solution at room temperature are given in Table 4.12. The Nyquist plots of this system are given in Figure 4.21. The impedance of inhibited substrate increased with increasing concentration of the additive, which is evident from increase in the semicircle diameters of the Nyquist plots as the concentration was increased.

It could be observed from the Table 4.12 that increasing additive concentration of PBE from 10%v/vPBE to 50%v/vPBE appreciably increased the solution resistance, R_s, from 1.20 to 1.69 Ωcm^2. The additive mitigated the corrosion of the substrates by increasing the charge transfer resistance R_{ct}, resulting to increase in IE% values. A maximum IE% value of 82.99% was achieved when the charge transfer resistance reached a maximum value of 190.97 Ωcm^2 in this case. This suggested that the inhibitor molecules were adsorbed onto the substrates. As the inhibitor concentration was increased, the capacitance of the double layer decreased; this decrease might not be unconnected with the formation of a thin film layer on the metal surface and increase in surface coverage.

Table 4.13 contained the parameters obtained from Nyquist diagram for the corrosion of AA2024 coupons inhibited by PBE+Boehmite Nanoparticles system in 3.5%NaCl solution at room temperature, while Figure 4.22 shows the corresponding Nyquist plots.

The IE% values increased from 70.51 to 86.26% as the concentration of PBE+Boehmite Nanoparticles was increased. Similar increases in solution resistance, R_s (from1.38 to 1.99 Ωcm^2), and charge transfer resistance, R_{ct} (from 183.11 to 206.67 Ωcm^2) were also observed. This could be due to interactions of the inhibitor molecules or ions interacting with the substrates, with probable adsorption onto them. Conversely, there was a decrease in the capacitance of the double layer, C_{dl}, from 49.23 to 32.33 μF, probably due to an increase in the surface coverage by the inhibitor, which led to an increase in the inhibition efficiency. The impedance of inhibited substrate increased with increasing concentration of the additive, which is evident from increase in the semicircle diameters of the Nyquist plots as the concentration was increased.

The parameters obtained from Nyquist diagram for the corrosion of AA2024 coupons inhibited by VDE system in 3.5%NaCl solution at room temperature were contained in Table 4.14, while the Nyquist plots for same is depicted in Figure 4.23.

From Table 4.14, it could be observed that on increasing concentration, charge transfer resistance increased from 157.75 to 180.11 Ωcm^2. Similarly, the Inhibition Efficiency IE% increased (from 43.49 to 72.97%) with increase in inhibitor concentration, mainly due to more interactions of the additive with electrode surfaces as the concentration was increased. The impedance of inhibited substrate increased with increasing concentration of the additive, which is evident from increase in the semicircle diameters of the Nyquist plots as the concentration was increased.

The double layer capacitance C_{dl} decreased from, 51.88 to 40.11 μF, with increase in concentration. The decrease in the capacitance of the double layer values with increase in concentration could be attributed to a decrease in local dielectric constant and/or an increase in the thickness of the electrical double layer as established was by Yurt *et al.* (2002). It could also probably be due to an increase in the surface coverage by the inhibitor, which led to an increase in the inhibition efficiency. The solution resistance also increased with increase in inhibitor concentration.

The parameters obtained from Nyquist diagram for the corrosion of AA2024 coupons inhibited by VDE+Boehmite nanoparticles system in 3.5%NaCl solution at room temperature are contained in Table 4.15. Figure 4.24 shows the respective Nyquist plots for the system.

Variations in the VDE+Boehmite Nanoparticles amounts affected the charge transfer resistance, solution resistance and capacitance of the double layer. The impedance of

inhibited substrate increased with increasing concentration of the additive, which is evident from increase in the semicircle diameters of the Nyquist plots as the concentration was increased. The Inhibition Efficiencies IE% increased with increasing additive concentration of the inhibitor; values obtained varied from 40.75 to 78.99%. The solution resistance also changed from 1.28 to 1.86 Ωcm^2, while the charge transfer resistance increased with increase in concentration (from 46.79 to 78.99%). This suggested that the additive retarded the dissolution of the substrates, probably by adsorbing onto them, thereby preventing further discharge of ions. From the values obtained, it could be seen that the capacitance of the double layer reduced with incremental addition of VDE+Boehmite Nanoparticles amounts, probably due to an increase in the surface coverage by the inhibitor, which led to an increase in the inhibition efficiency.

Generally, it is apparent from the Nyquist plots that the impedance response of the substrates in chloride solution has significantly changed after the additions of the different inhibitor systems. The impedance of inhibited substrates increased with increasing concentration of inhibitor. The Nyquist plots showed that on increasing concentration, the semicircle diameters also increased, with attendant increase in Inhibition Efficiencies IE%. The solution and charge transfer resistances were found to increase with increase in concentration of the different inhibitor systems. Conversely, the capacitances of the double layer were generally found to decrease with increase in inhibitor concentration. The Inhibition Efficiencies obtained from Electrochemical Impedance Spectroscopy (EIS) were found to be in agreement with those obtained from both Linear Polarisation Resistance (LPR) and gravimetric-based mass loss (ML).

5.3.4 Chronopotentiometric Analysis

From the chronopotentiograms of the samples exposed to chromate solution, Figure 4.25, it is clear that the addition of different amounts of sodium chromate affected the corrosion potential of the substrate. At a potential of -0.6V, a steady horizontal line pattern which is suggestive of the formation of a stable thin chromate film on the substrate that impedes further dissolution of the test samples was obtained. This confirmed that the adsorbed layer formed on the substrate was stable.

A look at the Chronopotentiograms in Figure 4.26 of the substrates exposed to PBE solution in presence of the chloride revealed a relatively unstable film formation on the substrate. Though high values of IE% were achieved, the adsorbed layers formed, at the prevailing experimental conditions, were not very stable. The instability of the adsorbed layers might partly be as a result of their inability to block active micro pits and partly due to more interactions among the different inhibiting species than between these species and the substrates.

The Chronopotentiograms shown in Figure 4.27 were for test samples exposed to 3.5%NaCl+PBE+Boehmite solution at various concentrations. It could be clearly seen that there are marked irregularities in the Chronopotentiograms at all the concentrations studied under this system, accompanied by a wide gap in the corrosion potential. This indicated that the adsorbed layers were not stable. The instability was suggestive of the fact that the force of attraction/interaction among the different inhibiting molecules far outweighs that between the species and the substrates, in conjunction with a report by Elewady *et al*. (2008).

The chronopotentiograms for the synergistic combination of PBE+VDE were schematically represented in Figure 4.28 above. It could be observed from the Figure that there were two distinct overlaps of the chronopotentiograms at varying potentials, with each accompanied by small irregularities, suggestive of the fact that the adsorbed layers on the substrate were not very stable. The instability of the adsorbates, in this case, was lower than that reported in the previous case of Figure 4.27, hence the relatively low intensity of the irregularities seen in the chronopotentiogram above (Figure 4.28). This is suggestive of the fact that there were low-keyed interactions among the inhibitor species and the substrates but not strong enough to form stable adsorbed layers on the substrates.

In the case of the substrate exposed to 3.5%NaCl + PBE+VDE+ BOEHMITE solution, Figure 4.29, it could be observed that a marked stability, as epitomized by a straight line parallel to the abscissa, was obtained at potential of -0.6V. This was an indication of appreciable stability of the adsorbed film on the substrate. It could also be seen that only three chronopotentiogram lines were visible, which was indicative of co-adsorption phenomena taking place at same potential. This system compared favourably with the Sodium chromate system, the reference inhibitor.

Figure 4.30 represents the Chronopotentiograms of the test samples exposed to 3.5%NaCl +VDE solution. It is evident that there was an observed stability at -0.6V for the additive concentration of 40%v/vVDE in the aqueous chloride solution. Irregular chronopotentiogram was obtained for the substrate exposed to the blank aqueous chloride solution, indicating either the inability of the adsorbed layer to completely cover the substrate or the tenacity of the micro pits contained in the substrate. These combined to

make the film unstable. Similar attributes were also noted on the substrates exposed to 20% and 30%v/vVDE in chloride medium.

The Chronopotentiograms, Figure 4.31, of the test samples exposed to 3.5%NaCl+VDE+Boehmite solution at various inhibitor concentrations revealed an appreciable stability of the adsorbed films onto the substrate under investigation, at a potential of -0.6V and inhibitor concentration of 50%v/vVDE+0.5g Boehmite in aqueous NaCl solution.

In summary, it could be inferred that addition of different inhibiting systems resulted in the formation of adsorbed layers/films, which stifled further dissolution of the substrates. As contained in the various chronopotentiograms discussed above, some of these adsorbed layers were stable, but others were not. The irregularities recorded in some chronopotentiograms is suggestive of the fact that the adsorbed layers were not robust enough to confer lasting and stable corrosion protection to the substrates in the aggressive aqueous chloride environment.

5.4 Effect of the Boehmite Nanoparticles on the Performance of the Plant Extracts

It has earlier been reported, equations 2.2-2.12, that the controlling step in the Aluminium dissolution is the complexation reaction between the hydrated cation and the anion present. In the presence of chloride ions, the reaction will correspond to equation 2.12:

$$[AlOH]^{2+} + Cl^{-} \longrightarrow [AlOHCl]^{+}$$

Introduction of the Boehmite nanoparticles might have probably created an unbalance field of force, thereby allowing inhibitor molecules to be adsorbed onto the substrate

surfaces and decrease their surface energy, hence resulting in increased Inhibition Efficiency (IE%). This observation was also reported by Cook *et al.* (2006).

Furthermore, in the initial stage of sea water corrosion, since the pH of the interface between the substrate and aggressive solution was equal to that of the bulk sea water, Al met the thermodynamic condition of formation of hydroxide (equation 2.8) that could nucleate on the substrate. The resulting Nano-deposited product blocked active sites, by competitive adsorption, thereby preventing further dissolution of the metal; hence the reduction in corrosion rates. Thus Boehmite Nanoparticles addition favoured the continuous extraction of the dissolved Al; which was made easier because of its high surface loading, large specific area and high surface energy. Earlier work reported by Cook *et al.* (2006) corroborated this.

From thermodynamic perspective, the metallic cation, Al in this case, react with OH^- to precipitate, at which instant the concentration products in the electrolyte exceeded the solubility product of them. During this precipitation, the solid crystal nuclei with certain critical size would first be produced in the electrolyte and then the crystal nuclei gradually grow by amalgamating the metallic cations and OH^- in the electrolyte. In the deposition process, the crystal nuclei constantly form and continually grow up until the product of the metallic cations and OH^- was equal to solubility product of it building up to the equilibrium state. At this state, the adsorbed layer is stable and the efficiency of the inhibition enhanced. This is in agreement with findings by Yan (2001).

Hence, it is probably that the Boehmite nanoparticles reinforced the hybrid matrices by absorbing inhibitor ions, releasing them during contact with moisture and thus offering effective self-healing properties; by protecting the reactive groups of the corrosion

inhibitors and then releasing them at the on-set of corrosion. This probably helped prevent premature depletion of the inhibitor reservoirs thereby increasing their longevity and improving the overall inhibition efficiencies.

5.5 Kinetics and Thermodynamics Consideration

Table 4.16 contained some kinetic and thermodynamic parameters for the different systems investigated. The activation energies of the inhibited systems, as contained in Table 4.16, were computed using equation 2.18 and found to be greater than that of the uninhibited system. This indicated that the inhibitors were more effective at room temperature, and the efficiencies of Inhibition decreased with temperature increase. The high values of Activation Energies **(E_a)** of 89.97 and 84.40 kJ/mol for sodium chromate and PBE+VDE+BOEHMITE systems, respectively, indicated efficient inhibiting actions of the two systems which could be attributed to the thickening of the electrical double layer. Since the presence of the inhibitors caused a change in the values of the apparent activation energies, such a change indicated a change in the rate determining step brought about by the presence of various chemical components and phytoconstituents of the inhibitors. This meant that the adsorption processes took place easily and that some of the adsorbed layers were stable. This tallied with earlier work by Chetouani *et al.* (2004).

Thermodynamic model could well be used to explain the corrosion inhibition of the different systems under investigation. The adsorption free energies (ΔG_{ads}) and adsorption heats (Q_{ads}) were calculated using equations 2.20 and 2.24 respectively. The Q_{ads} values for the different systems investigated were tabulated in Table 4.16.

The negative values of the free energies of adsorption (ΔG_{ads}) suggested strong interactions among inhibitor molecules, whereas low ΔG_{ads} implied that the adsorptions

of the different inhibiting systems onto the substrates were spontaneous. The increase in free energies with temperature was indicative of the fact that the adsorption was unfavorable with increase in experimental temperatures as a result of desorption of inhibitors molecules from the surfaces of the substrates as established by Tang *et al.* (2003).

The ΔG_{ads} values obtained for all the systems were more negative than -40 kJ/mol which suggested strong electrostatic interaction/charge sharing between the charged molecules and the charged metal to form a coordinate bond, indicating chemisorption as reported by Bouklah *et al.* (2005); Bilgic and Sahin (2001).

The negative values of the heats of adsorption **(Q_{ads})** suggested that the adsorption and hence inhibition efficiencies decreased with rise in temperature. Positive Q_{ads} values implied that the physical adsorption equilibrium is usually rapid and the process readily reversible, whereas in Chemisorption, the occurrence of chemical reaction at the metal surface makes the process relatively slow and not readily reversible.

The obtained values of heat of adsorption (Q_{ads}) values were more negative than -10KJ/mol suggesting predominance of chemical adsorption at the metal surface, even though physical adsorption might as well played a role in inhibition. This is in good agreement with earlier report by Ebenso *et al.* (2004).

It could thus be concluded that the different values of ΔG_{ads} for the inhibitor systems investigated were indicative that their inhibition properties depended on the ability of hetero atoms in their molecules to donate electrons to the metal surface, thereby forming a coordinate bond.

5.6 Elucidation of Synergism

In both cases, as contained in Tables 4.17 and 4.18, all the obtained values for the Synergism parameters were close to or more than unity, which suggested enhanced Inhibition Efficiencies, were obtained by combining the plant extracts and/or addition of Boehmite Nanoparticles. This was mainly due to the synergistic effect, aided by competitive adsorption among different inhibitor molecules and other ions which in effect might have lead to the formation of complex(s) and their subsequent adsorption onto the substrates; hence the increase in coverage and, correspondingly, efficiencies. Similar findings were also reported by Rajendran *et al*. (2009).

5.7 Adsorption Isotherms

From the data of surface coverage, adsorption isotherms were plotted and the nature of these isotherms provided insights in to the properties of the adsorbed substances and their interaction with electrode surfaces. The degree of surface coverages (**θ**) for the different systems investigated were evaluated using equation 2.52. The increase in surface coverage with increasing inhibitor concentration could be attributed to more inhibitor molecules adsorption onto the substrate surfaces when inhibitor concentration was increased which agrees with findings by Tang *et al.* (2003).

5.7.1 Langmuir Adsorption Isotherm

Figures 4.32 are plots of log(θ/1- θ) against logC, which are linear for all the systems investigated. These suggested that the adsorption of inhibitor compounds/molecules onto the coupon surfaces followed the Langmuir adsorption isotherm, in which case the adsorption of the inhibitor molecules belonged to a monolayer adsorption, i.e the adsorbed film/layer was no more than a monolayer thick, assuming that the lateral interactions between the inhibitor molecules were ignored.

5.7.2 El-Awady's Adsorption Isotherm

Though the plots of C/Θ versus C was linear (Figure 4.33) (correlation > 0.9), for ideal Langmuir isotherm, the slight deviation of the slopes from unity, Table 4.19, can be attributed to the molecular interaction among the adsorbed inhibitor species, a factor which was not taken into consideration during the derivation of the Langmuir equation.

Langmuir, in developing his Isotherm, assumed that:

- The metal surface contains a fixed number of adsorption sites and each site holds one adsorbate;
- ΔG_{ads} is the same for all sites and it is independent of Θ;
- The adsorbates do not interact with one another, ie. there is no effect of lateral interaction of the adsorbates on ΔG_{ads}

Though the linearity of the Langmuir plot may be interpreted to suggest that the experimental data for the systems obeyed the Langmuir adsorption isotherm, the considerable deviation of the slope from unity shows that the isotherm cannot be strictly applied. These observations on Langmuir's Isotherms were forwarded by Villamil *et al*. (1999), and also adopted by El-awady.

The El-Awady's kinetic/thermodynamic model, represented by eqn. 2.40, which is more recent, was employed to take care of inherent deficiencies of the Langmuir adsorption isotherm. In this model, the numbers of active sites '***y***' were calculated (equation 2.41) and found to vary from 1.52 to 3.2. These suggested that the given inhibitor molecule occupied more than one active site; values of 1/y less than one imply multilayer adsorption, while 1/y greater than one suggests that a given inhibitor molecule occupies more than one active site as reported by Obot *et al.* (2009).

5.8 Characterisation

5.8.1 Scanning Electron Microscopy/Energy Dispersive X-Ray (SEM/EDXA)

The SEM micrographs of the as-cast specimen shown in Figure 4.34 revealed compact films, with evidence of porous or micro cracks, along the grain boundaries, which allowed the diffusion of electrolytes. The presence of these micro cracks might not be unconnected with thermal stresses generated during the cooling & solidification of the alloy and also due to the presence of high amount of alloying elements in the alloy as reported by Buccheit & Boger (2001). The EDX spectrum of the as-cast sample revealed the presence of signals of Al (at energy level of 1.5keV) at much more higher energy level than Cu, O and C. All the EDX spectra contained Carbon, likely from the charge materials used in the production of the alloy, principally Ferromanganese.

Inspection of the SEM micrographs, Figure 4.35, of the sample exposed to the chloride solution in the absence of an inhibitor revealed that chloride ions cause severe attack on the surfaces of the test alloy, AA2024. The white patches might be as a result of the sodium chloride and also different concentrations of Cu-containing compounds. The corrosion products, relatively coarse, bridge around the dealloyed S-particle remnants. The disappearance of the grain boundaries might not be unconnected with the deposition of corrosion products, as can be seen from relatively coarse particles in the micrograph. The appearance of heteroatom of O at an energy level of 0.5keV, on EDXS spectrum, and a count of 0.82 was indicative of the fact that the limiting step in the corrosion of this alloy, AA2024, was the mass transport of oxygen, which generated the OH^-. In pure chloride medium, the cathodic corrosion rate on Al-4%Cu was slightly higher than that of

pure Al due to the increased ORR (Oxygen Reduction Reaction) rate. However, even though the ORR rate was much larger on Al_2Cu intermetallics, less cathodic corrosion occurred. This assertion was reported in earlier work by Baek and Frankel (2003).

Figure 4.36 shows the SEM Micrographs, with the corresponding EDX Spectrum, for the sample exposed to 3.5%NaCl+Na_2CrO_4 solution. The appearance of Cr at a very high energy level (5.5keV) in the EDX spectrum was indicative of adsorption of sodium chromate onto the substrate thereby retarding its dissolution. The micrograph contained coarse particles, which were indicative of deposition of some compounds onto the substrate surfaces, hence the absence of the grain boundaries. The white patches were due to Cu-containing compounds, with the corrosion products bridging around dealloyed S-particle remnants as established by Hatch (1984). The increased counts of Oxygen observed from the EDX spectrum was probably due to oxidizing nature of chromates culminating to thickening of chromium oxide layer which stifled cathodic reaction. It was also due to the thickening of other oxide films on Cu and $Al_{20}Cu_2(MnFe)_3$, resulting in increased corrosion resistance. This reduced cathodic corrosion might have affected the reduced ORR rate on Cu-rich intermetallic particles by preventing further exposure of catalytic metal Cu on the surface as reported by Ilevbare and Scully (2001).

The SEM Micrographs, with the corresponding EDX Spectrum, for the sample in 3.5%NaCl+PB Extracts solution was shown in Figure 4.37. The micrograph contained coarse particles embedded within relatively fine ones, shielding the grain boundaries. The relatively dark nature of the micrograph might be as a result of the adsorption of the phytoconstituents of *Parkia biglobosa* extracts onto the substrate surface. This stifled the

anodic dissolution, resulting in a decreased corrosion rate. The major centers of adsorption were heteroatom of O, which was found at energy level and count of about 0.5keV and 1.6 respectively. The presence of metallic Cu at another energy level of 5.5keV might probably be due to intermetallics of Al_2Cu and/or Al_2CuMg. This might have changed the conductivity of the oxide film on these intermetallics, thereby enhancing the kinetics of ORR on this phase to the extent that the limiting step of this phase could be mass-transfer-limited Oxygen reaction as was established by Buccheit and Boger (2002).

Figure 4.38 shows the SEM Micrographs, with the corresponding EDX Spectrum, for the sample in 3.5%NaCl + PB Extracts + Boehmite Nanoparticles solution. The high surface loadings of Boehmite nanoparticles facilitated the adsorption of *Parkia biglobosa* extracts and improved its efficiency. The micrograph contained mixtures of coarse and fine grains embedded within the matrix. The brightness of the micrograph was partly due to Cu-containing intermetallics and partly due to the Boehmite nanoparticles. The presence of metallic Cu at another energy level of 5.5keV might probably be due to intermetallics of Al_2Cu and/or Al_2CuMg. This might have changed the conductivity of the oxide film on these intermetallics, thereby enhancing the kinetics of ORR on this phase to the extent that the limiting step of this phase can be mass-transfer-limited Oxygen reaction as was established by Buccheit and Boger (2002).

The SEM Micrographs, with the corresponding EDX Spectrum, for the sample exposed to 3.5%NaCl with PB+VD Extracts + Boehmite Nanoparticles solution is shown in Figure 4.39. The microstructure principally contained fine grains with few coarse grains

embedded within them, accompanied by reduced visibility of the grain boundaries. The dull appearance of the micrograph was as a result of synergistic co-adsorption of the various phytoconstituents of *Parkia biglobosa* and *Vitex doniana* extracts onto the alloy surface. The Boehmite nanoparticles provided a flat form for adsorption to proceed at a faster rate, aided by synergistic contribution of the two extracts. EDX spectrum recorded O at energy level and conts of 0.5keV and 0.9 counts respectively. It was probable that adsorption took place through the O atoms as reported by Gomma and Wahdan (1994).

Figure 4.40 revealed the SEM Micrographs, with the corresponding EDX Spectrum, for the sample in 3.5%NaCl+VD Extracts solution. Coarse grains dominated the micrograph, the dark patches in bright background were suggestive of the influence of the *Vitex doniana* extracts and the Boehmite nanoparticles on the corrosion rate of the substrate. The signals from the EDX spectrum revealed heteroatom of O atom at 0.5 counts, this served as adsorption centers onto which the phytoconstituents of the extracts were adsorbed and consequently retarded dissolution of the substrate. This corroborated earlier findings by Bouklah *et al*. (2005)

Again, the influence of *Vitex doniana* extracts and Boehmite nanoparticles addition on the surface morphology of the substrate is shown in the SEM micrograph of Figure 4.41. The grains were predominantly coarse, due to probable interactions of the corrosion products with the extracts. The inhibiting additives stultified the corrosion rate of the substrate by adsorption of phytoconstituents of the extracts onto the alloy surface, the

heteroatoms of O, shown on the EDX spectrum, were the major adsorption centers. This is similar to an earlier research by Bouklah *et al*. (2005).

Figure 4.42 shows SEM Micrographs, with the corresponding EDX Spectrum, for the sample in 3.5%NaCl+PB+VD Extract solution. The microstructure here revealed a mixure of fine and coarse grains. The dark patches were indicative of synergistic co-adsorption of the two extracts onto the alloy, which took place through heteroatoms of O, the major adsorption centers.

In summary, the SEM micrographs of the as-cast specimen showed compact films, with evidence of porous or micro cracks which allowed the diffusion of electrolytes. The presence of these micro cracks might not be unconnected with thermal stresses generated during the cooling & solidification of the alloy and also due to the presence of high amount of alloying elements. In the micrographs of inhibited samples, there were evidences of interference of corrosion products with the additive inhibitors to form new phases, which as proposed by Rozenfeld (1981), was a plausible mechanism for the action of the inhibitors, and not just adsorption or co-adsorption. This might have also explained the coarseness contained in most of the SEM micrographs.

The galvanic coupling between the Al matrix and the secondary phases and intermetallic compounds might be responsible for the observed pits in the test samples. This was reported earlier by Buchheit & Boger (2002) in which it was cited that pitting is more pronounced for the Al-Mg-Si and Al-Cu-Mg, with pits averaging about 5-35μm in depth.

Generally, Cu scatters much more effectively than either Al or Mg; hence the bright regions in the SEM micrographs might have contained elevated concentrations of Cu. The corrosion products bridge around a dealloyed S-particle remnants. This observation is similar to an earlier one reported by Buchheit & Boger (2002); Hatch (1984).

The EDX spectrum of the uninhibited surface clearly indicates the presence of Al and Cu signals, the major constituent elements in the alloy. Signals of Al, Cu and O are also observed in all the spectra, at varying intensities. Hence, the use of the different inhibitive additives decreased the extent of corrosion damage of the alloy at varying degrees. This observation confirmed that addition of an inhibitor to the tested solution resulted in formation of adsorbed layer of inhibitor on the metal surface which suppressed the corrosion process. This correlates with an earlier research work as reported by Morad *et al.* (1995).

5.8.2 XRD Results

A summary of the chemical compositions/phases present for the as-cast samples is contained in Table 4.20. In the XRD pattern/Diffractogram of the as-cast, as shown in Figure 4.43, prominent peaks were observed at 2θ position of 21.5^{o}, 38.5^{o}, 43.5^{o}, 45^{o} and 65^{o}, with respective peak heights of 2800, 7500, 1000, 2000 and 2500 counts; corresponding to Al_2Cu; Al_3Cr_2, $Al_2Cu;Fe_2C;Al_3Cr_2$, $Al_{13}Cr_2$; Al_7Cu_2Fe, $Al_3Cr_2;Al_7Cu_2Fe$ and $CrC;Al_2Cu$; Al_7Cu_2Fe.

The XRD pattern showed that different phases containing aluminium, copper, magnesium and iron were the major ingredients making up the structures of the as-cast alloy. These phases are independent of the atomic positions within the cell and entirely determined by the size and shape of the unit cell of the crystalline phase.

The XRD pattern of the sample exposed to the 3.5%NaCl, Figure 4.44, showed a marked increase in the peaks' heights compared to the as-cast peak. A summary of the chemical compositions/phases present for the sample exposed to 3.5% NaCl is contained in Table 4.21. The observed peaks in the Diffractograms were found at 2θ position of 38.5^{o}, 45.5^{o} and 66.5^{o} at 5000, 25000 counts respectively. These showed that sodium chloride has pronounced effect on the corrosion properties of the substrates, AA2024 Aluminium Alloy. The aggressiveness of the chloride might be responsible for the appearance and disappearance of some phases; dissolution, rearrangement of phases and formation of other products as a result of corrosion or introduction of various inhibitive substances into the electrolytes as reported by Dimitrov *et al.* (2000).

The corrosion behaviour of the test alloy is heavily dependent on the formation of these phases and intermetallic compounds formed as observed from the Diffractograms in Figure 4.44. In particular, the corrosion behaviour strongly depend on the cathodic activity of Cu-rich intermetallic particles such as □ phase (Al_2Cu), S phase (Al_2CuMg), and particles of varying composition containing Al, Cu, Mn, and Fe. This correlated with the findings by Dimitrov *et al.* (2000) and Buchheit (1995).

Despite these, the XRD spectrum showed that aluminium, copper and iron were the elements making up the phase structures of the alloy exposed to the chloride medium. These phases, as stated above, were independent of the atomic positions within the cell and entirely determined by the size and shape of the unit cell of the crystalline phase.

The Cu-containing intermetallic compounds (IMCs) acted as preferred cathodic sites for oxygen reduction while the anodic sites are active S-phase particles and the Al matrix, this has also been reported by Schmutz & Frankel (1998).

Reduction reactions at the cathodic sites led to the development of high pH zones near IMCs and the surrounding region. The increased local pH promoted dissolution of the Al matrix near the cathodic IMCs, causing localized attack at the periphery of Cu-containing intermetallic particles, and may also result in dealloying of IMCs themselves. This assertion was earlier on reported by Ilevbare & Scully (2001) and Buchheit *et al.* (1997).

In homogeneous dissolution, both Al and Cu are dissolved during alloy dissolution, followed by Cu repleting. S-phases contained less Cu than θ phase and typically exhibited a more active corrosion potential in the Chloride solution; hence the exhibition of minor structural reorganization by surface and volume diffusion.

The XRD spectrum of the coupons exposed to the chloride solution with sodium chromate as an inhibitor, shown in Figure 4.45, revealed distinct phase of Al_2Cu and Al occurring in tandem at different scores and counts; (20, 900), (38.5, 1300), (44, 800), (65, 900), (78, 600). A summary of the chemical compositions/phases present for the sample exposed to 3.5%NaCl+Na_2CrO_4 solution is contained in Table 4.22. The reduction in number of distinct phases here could be attributed to the shielding effect of the chromate and the formation of a protective film which might have prevented the dissolution and redistribution of many phases. This conforms to earlier works by Dimitrov *et al*. (2000). It could be observed from the Diffractograms that addition of Na_2CrO_4 had suppressed

the formation of IMCs, this indicated that the shielding effect of the inhibitor is pronounced; probably Physisorption and Chemisorption.

Prominent scores and their peaks are depicted Table 4.23 and Figure 4.46 in the case of chloride + PBE systems. Al_2Cr_3 at a score range of 20-21.5 and counts of above 1600; CrC, $Fe_2Mg_2Al_3$, $Mg_3Cr_2Al_{18}$ and Fe_2C at a score and counts of about 38 and 1600 respectively. Other intermetallics present were Al_8MnS and Fe_2C at a score and counts of 41 and 1100 respectively. Many of these IMCs were found at other scores and counts.

The Cu-containing intermetallics (IMCs) were the preferred cathodic sites for oxygen reduction, while the anodic sites were the active S-phase particles (Al_2CuMg) and the Al matrix. Dissolution of the anodic sites might have affected the overall composition of the intermetallics (IMCs). Hence, addition of PBE to the chloride media altered the configuration of the IMCs, infering that the corrosion mechanism of the substrates was influenced by the extracts addition. Compared to the standard inhibitor (Na_2CrO_4), this inhibitor system contained more Mg-containing IMCs, which were anodic.

Figure 4.47 shows the XRD pattern of the test sample in 3.5%NaCl containing PBE+BOEHMITE. The characteristic intermetallic phases observed in the spectrum and contained in Table 4.24 were Al, Al_2Cu, $Al_{50}Mg_{48}Ni$, Al_2CuMg e.t.c. obtained at different scores and counts. The reduction in the number of anodic Mg-containing intermetallics might be due to the influence of Boehmite nanoparticles, which served to conserve the *Parkia biglobosa* extracts, hence the improvement in Inhibition Efficiencies (IE%).

XRD pattern of the test sample in 3.5%NaCl containing PB+VD Extracts is shown in Figure 4.48. The different phases with their compositions are contained in Table 4.25. The predominant phases $CuAl_2$, Fe_3C, $Al_{0.56}Mg_{0.44}$, Al_6CuMg_4 and Al_5Fe_2 were found at different counts and scores. The synergistic effect of the two extracts, *Parkia biglobosa* and *Vitex doniana*, might have influenced the corrosion behaviour of the substrate, through redistribution of the phases and/or the IMCs. This inhibitor system did not measure up to performance of the standard inhibitor, probably due to its inability to contain Mg-containing IMCs, which are generally known to be anodic.

Table 4.26 shows the Chemical/phases composition of the test sample in 3.5%NaCl containing PB+VD+BOEHMITE. Predominant phases observed were Al_2Cu, Al, Fe and Mg_2Ni at different scores and counts shown in Figure 4.49. The synergy between *Parkia biglobosa* and *Vitex doniana* coupled with the influence of Boehmite nanoparticles affected the electrode kinetics-corrosion rates. From the marked reduction in the number of phases, it could be deduced that this inhibiting system acted as a protective barrier film for anodic dissolution; stifling the formation of S-phase particles and other anodic IMCs. This inhibiting system compared favourably with standard inhibitor, sodium chromate, in that it recorded a marked reduction in the number of Mg-containing anodic sites and the S-phases, which derive the dissolution of Al-Cu alloys.

Figure 4.50 represents XRD pattern of the test sample in 3.5%NaCl containing *Vitex doniana* (VD) extracts, while Table 4.27 shows the chemical/phase composition of the

test sample in 3.5%NaCl containing VD extracts. The effect of this inhibiting system in dissolution and redistribution of phases is evident from Table 4.6h. The various chemical/phase compositions recorded were Al, Cr_7Ni_3, Fe, $CuAl_2$, Ni_3C, Mg and Cu_2Mg. The presence of appreciable number of anodic sites (Al, Cu_2Mg, Fe, $CuAl_2$ and Mg) might be the reason for the low Inhibition Efficiencies recorded for this system.

Table 4.28 revealed the chemical/phase compositions for the samples exposed to the VD+ Boehmite inhibiting system, while Figure 4.51 revealed the main diffraction peaks. The main constituents found were (Fe, Ni), Al_8Mn5, Fe, Al, Al_2Cu and Mg_2Al_3. The predominance of anodic phases {(Fe, Ni), Al_8Mn5, Fe, Al and Mg_2Al_3} was suggestive of the fact that the inhibiting system did not appreciably offer a protective barrier against the aggressive electrolyte. This resulted in low Inhibition Efficiency (IE%), making the performance of this inhibiting system far below that of the standard inhibitor, sodium chromate.

Carbon, Chromium and Cobalt are present as impurities in the alloy, hence the appearance of some diffraction peaks containing compounds/intermetallics of these elements. Their source might be from the charge materials used in the production of the alloy, principally Ferromanganese and Aluminium.

The corrosion behaviour of the test alloy is heavily dependent on the formation of different phases and intermetallic compounds formed as observed from the Diffractograms. In particular, the behaviour strongly depends on the cathodic activity of Cu-rich intermetallic particles such as □ phase (Al_2Cu), S phase (Al_2CuMg), and

particles of varying composition containing Al, Cu, Mn, and Fe. This relates to the findings by Dimitrov *et al.,* 2000 and Buchheit, 1995.

The Cu-containing intermetallic compounds (IMCs) acted as preferred cathodic sites for oxygen reduction while the anodic sites are active S-phase particles and the Al matrix, as reported by Schmutz & Frankel, 1998. Reduction reactions at the cathodic sites led to the development of high pH zones near IMCs and the surrounding region. The increased local pH promotes dissolution of the Al matrix near the cathodic IMCs, causing localized attack at the periphery of Cu-containing intermetallic particles, and may also result in dealloying of IMCs themselves. This assertion was earlier on corroborated by Ilevbare & Scully, 2001 and Buchheit *et al.,* 1997.

Addition of an inhibitor retarded the dissolution of Al and other anodic and cathodic sites at varying degrees as enunciated in the Inhibition Efficiency (IE%) diagrams. These suggested that the inhibitor functionality is enhanced by its ability to donate unshared electron pair from its d orbital to the anodic sites, formatting strong electrostatic force with the substrate. This assertion was also reported by Kuznetsov *et al.,* 1996.

The XRD pattern of inhibited surfaces showed the main phases observed previously, in the as-cast, but the intensity of the peaks became weak compared to those detected in the absence of inhibitor. It can be noted from the comparative Diffractograms that addition of the optimum concentration of the studied inhibitor systems lead to a noticeable attenuation in the heights of the characteristic peaks of the main phases present in the alloy. This supports earlier conclusion by Ralph and Daniel (2008). Furthermore, the height/intensity of the phase peak correlated with its concentration in the sample, so the observed decrease in the height of the corrosion product phase could be considered as a

semi-quantitative indication for the suppression of the corrosion process and hence gave good evidence for the inhibitive effect of the studied inhibitor system. However, the inability of the X-ray pattern to detect inhibitor surface films might either be due to its poor crystallinity or due to the fact that the films were very thin. This correlates with earlier findings by Khaled *et al.,* 2012.

From all the XRD spectra investigated, it could be concluded that differences in peaks were attributed to different lattice parameters and crystallographic orientations. Increase in peak intensities after exposure to the different electrolytes/systems indicated higher crystallinity of corrosion products, and might have been responsible for the differences in corrosion properties of the investigated substrates as reported by Feyisayo (2009). This also confirmed observations from the Raman spectra.

Critical look at the Diffractograms also revealed that both the anodic and cathodic IMCs were affected by the adsorbed inhibitor systems. This confirmed that the action of the inhibitor affected both the anodic and cathodic reactions through competitive adsorption; hence they are mixed type inhibitor systems. The overlap of some peaks in the Diffractograms is suggestive of the fact that the phases formed belong to the same crystal systems and space groups; they are the same but differing qualitatively. This assertion has been reported elsewhere by Birol (2009).

In the context of Al-Cu alloy corrosion in a chloride medium, the □-phase, Al_2Cu, is often considered to be the prototypical IMC particle. The Cu-rich phases could either be active or noble with respect to the matrix phase depending on the IMC composition. There were wide varieties of phases/precipitates/IMCs, most of which were cathodic;

hence a feasible mechanism for the inhibition process can be envisaged. This has also been reported by Buchheit & Boger (2001) and Dillon (1986).

If the dissolution were assumed to be homogeneous, then both Al and Cu would dissolve during alloy dissolution, followed by Cu repleting. Structural reorganization by surface and volume diffusion might have been responsible for the formation of a variety of the IMCs phases noted in the Diffractograms. This has also been suggested by Modolfo (1976) and Buchheit & Boger (2001).

The presence of magnesium in the alloy might be responsible for lowering the solubility of Cu in the test alloy, and large fractions of constituent S, □ and other IMCs (containing different proportions of Al, Mg, Mn, Fe, Ni e.t.c) might also lower the solid solution of Cu concentration; these IMCs might be more resistant to dissolution than S and □, and may concentrate, bind and prevent Cu release during the dissolution. Earlier work by Boger (2000) also cited this.

5.8.3. Raman Spectroscopic Analysis

Raman spectra are not obviously dependent on the chemical and physical environment of the samples being examined. Whether the molecules are in a gaseous, liquid, solid or polymeric form is not easily apparent from the spectrum, but the physical state does affect the overall strength and band shape. In general, crystalline solids give sharp, strong spectra whilst liquids and vapours tend to have much weaker spectra; this is in agreement with earlier publication by Ewen and Geoffrey (2005).

Figure 4.52 shows the Raman spectrum and the image of overall surface for the as-cast test alloy. The Raman shifts of the as-cast alloy showed peaks within the range 280-2940 cm^{-1}. The broad peaks ranging from about 1000 to 2000 cm^{-1} shift might be indicative of the thickness/crystallinity of phases formed during the cooling and solidification of the alloy as reported by Ewen and Geoffrey (2005). The shift 284 cm^{-1} was assigned to Fe_2O_3, while the shift around 514 cm^{-1} was assigned to $Fe_{3-x}O_4$, in line with reference to McCarty and Boehme (1989). The shift at 1104 was suggestive of Al_2O_3 as reported by Guevara-Lara *et al.* (2007). Both shift at 1288 and 1450 cm^{-1} were indicative of Fe_2O_3 as reported by McCarty and Boehme (1989).

Raman Spectrum and the image of overall surface of the test alloy in 3.5%NaCl solution were shown in Figure 4.53. The Raman spectra of the corrosion products of the AA2024 in 3.5%NaCl were observed at the range 610-2950 cm^{-1}. The broad peaks ranging from about 1000 to 2000 cm^{-1} shift might be indicative of the thickness/crystallinity of the corroded materials as reported by Ewen and Geoffrey (2005). The shifts at 618 might be indicative of NiO, as contained in a research by Chang *et al.* (1992). The shifts at 1342 and 1532 cm^{-1} might have revealed the presence of $Fe_{0.4}Cr_{1.6}O_{0.3}$ and Fe_2O_3 respectively as established by McCarty and Boehme (1989). The broad peaks ranging from about 1000 to 2000 cm^{-1} shift might be indicative of the thickness/crystallinity of the corroded materials as reported by Ewen and Geoffrey (2005).

Raman spectrum and the image of overall surface of the test alloy in 3.5%NaCl and sodium chromate solution were represented in Figure 4.54 above. In Na_2CrO_4 system, the

Raman shifts range from 220 to 2810 cm^{-1}. The broad peaks ranging from about 1000 to 2000 cm^{-1} shift might be indicative of the thickness/crystallinity of the corroded materials as reported by Ewen and Geoffrey (2005). The presence of NiO at shift 428 cm^{-1} or 736 cm^{-1} has been confirmed with reference to an earlier work by Guevara-Lara *et al.* (2007). $Fe(OH)_2$ and □-Fe_2O_3 has also been reportedly identified at respective shifts of 428 cm^{-1} and 679 cm^{-1} by Gui and Devine (1991). At a shift of 1338 cm^{-1}, either $Fe_{0.4}Cr_{1.6}O_{0.3}$ or $FeCr_2O_4$ was envisaged. This has been supported with reference to Gui and Devine (1991).

Figure 4.55 shows the Raman spectrum and the image of overall surface of the test alloy in 3.5%NaCl and PBE Solution. For the PBE system, the Raman shifts were found within the range 220-2970 cm^{-1}. The broad peaks ranging from about 1000 to 2000 cm^{-1} shifts might be indicative of the thickness/crystallinity of the corroded materials as reported by Ewen and Geoffrey (2005). Specifically, the peak at 225 cm^{-1} shift is inferred to contain α-Fe_2O_3, while one at shift 746 cm^{-1} contained □-Fe_2O_3 with reference to Gui and Devine (1991). Similarly, the bands at 746 and 1342 cm^{-1} were adjudged to contain NiO and $Fe_{0.4}Cr_{1.6}O_{0.3}$ respectively with reference to the work of Gui and Devine (1991). The bands around 1342 cm^{-1} were attributed to δ(CH) modes, while those around 1539 were assigned to ring stretching vibrational modes, probably due to organically adsorbed phytoconstituents from the *Parkia biglobosa* (PB) extracts. This inference is in agreement with earlier works by Silvia *et al.* (2010).

Figure 4.56 shows the Raman spectrum and the image of overall surface of the test alloy in 3.5%NaCl and PBE+Boehmite Nanoparticles Solution. The shifts in this system range

from 400 to 2950 cm^{-1}. With reference to the work of McCarty and Boehme (1989) Shifts of 503 cm^{-1}(Fe_3O_4) 585 cm^{-1} (NiO), 910 cm^{-1}($Fe_2Cr_2O_4$), and 1338 cm^{-1}($Fe_{0.4}Cr_{1.6}O_{0.3}$) were adjudged to be present. The broad peaks ranging from about 1000 to 2000 cm^{-1} shifts might be indicative of the thickness/crystallinity of the corroded materials as reported by Ewen and Geoffrey (2005). The bands around 1339 cm^{-1} were attributed to δ(CH) modes, while those around 1536 and 1639 cm^{-1} are assigned to ring stretching vibrational modes, probably due to organically adsorbed phytoconstituents, from the *Parkia biglobosa* (PB) extracts, onto the substrate. This inference is in agreement with earlier works by Silvia *et al.* (2010).

The Raman spectrum and the image of overall surface of the test alloy in 3.5%NaCl and PBE+VDE solution were shown in Figure 4.57 above. The Raman shifts of this system were observed within the range 370 to 2920 cm^{-1}. The broad peaks ranging from about 1000 to 2000 cm^{-1} shift might be indicative of the thickness/crystallinity of the corroded materials as reported by Ewen and Geoffrey (2005). The bands around 1336 cm^{-1} were attributed to δ(CH) modes, while those around 1523 and 1664 cm^{-1} are assigned to ring stretching vibrational modes, probably due to organically adsorbed phytoconstituents from the *Parkia biglobosa* (PB) extracts. This inference is in agreement with earlier works by Silvia *et al.* (2010).

Figure 4.58 above shows the Raman spectrum and the image of overall surface of the test alloy in 3.5%NaCl and PBE+VDE+Boehmite Nanoparticles solution. The observed shifts for this system range from 410 to 2960 cm^{-1}. The bands around 632 and 686 cm^{-1} were respective attributes of □-Fe_2O_3 and NiO with reference to Gui &Devine (1991); Chang

et al. (1992). The bands around 1339 and 1492 cm^{-1} were assigned to ring stretching vibrational modes, attributed to δ(CH) modes, probably organic adsorbed phytoconstituents, from the *Parkia biglobosa* and *Vitex doniana* extracts, onto the substrate. This inference is in agreement with earlier works by Silvia *et al.* (2010). The broad peaks ranging from about 1000 to 2000 cm^{-1} shift might be indicative of the thickness/crystallinity of the corroded materials as reported by Ewen and Geoffrey (2005).

Figure 4.59 shows the Raman spectrum and the image of overall surface of the test alloy in 3.5%NaCl and VD Extracts Solution. Raman band were observed within the range 250 to 2940 cm^{-1}. The broad peaks ranging from about 1000 to 2000 cm^{-1} shift might be indicative of the thickness/crystallinity of the corroded materials as reported by Ewen and Geoffrey (2005). The band around 259 and 290 cm^{-1} shift might be attributed to α-Fe_2O_3 as reported by Gui & Devine (1991) and McCarty and Boehme (1989). The shifts around 412, 546 and 609 cm^{-1} might be indicative of NiO presence as reported by Guevara-Lara *et al.* (2007). The bands around 1348 cm^{-1} were attributed to δ(CH) modes, while those around 1436 cm^{-1} were assigned to ring stretching vibrational modes, probably due to organically adsorbed phytoconstituents, from the *Vitex doniana* (VD) extracts, onto the substrate. This inference is in agreement with earlier works by Silvia *et al.* (2010).

The Raman spectrum and the image of overall surface of the test alloy in 3.5%NaCl and VDE+Boehmite Nanoparticles Solution were shown in Figure 4.60. The Raman shifts observed under this inhibiting system range from 350 to 2960 cm^{-1}. Traces of $[MoO_{24}]^{-6}$ were suggested to be present at 359 cm^{-1} by Guevara-Lara *et al.* (2007), while McCarty

and Boehme (1989) reported NiO at shifst of around 618 cm^{-1}. The broad peaks ranging from about 1000 to 2000 cm^{-1} shift might be indicative of the thickness/crystallinity of the corroded materials as reported by Ewen and Geoffrey (2005). The bands around 1414 and 1618 cm^{-1} were assigned to ring stretching vibrational modes, probably organic adsorbed phytoconstituents, from the *Parkia biglobosa* and *Vitex doniana* extracts, onto the substrate. This inference is in agreement with earlier works by Silvia *et al.* (2010).

A Summary of the Raman peak shifts (cm^{-1}) of the corrosion products formed on the substrates (AA2024 coupons) for the different systems investigated is given in Table 4.29. Generally, similarities among the Raman shifts of all the substrates investigated were observed. From the spectral patterns, there were variations in Raman shifts, broadening, and surface interactions. These might be indicative of either adsorption of organic molecules onto the alloy surface, leading to reduction or disappearance of certain peaks, or release of certain metal ions into solution, leading to appearance of certain peaks. SEM/EDX and XRD examination of the substrate surfaces also revealed these variations at varying degrees, depending on the electrolyte/system under investigation.

5.9 Analysis of Variance (ANOVA)

Table 4.30 shows the Inhibition Efficiencies (IE%) obtained using LPR, EIS and Gravimetric-based mass loss (ML) for Sodium Chromate system at room temperature. Table 4.31 represents a simple two-way ANOVA generated for Sodium Chromate system at room temperature and different concentrations used to evaluate the degree of variation of Inhibition Efficiencies (IE%) obtained using different methods of assessing the corrosion characteristics of the test coupon.

It could be observed that the degree of variations were much lower along the rows (0.025233, 0.016233 and 0.006933) than the columns (2.433733, 2.236033 and 2.9809), suggesting that at the same experimental temperature and concentration, the results obtained from both Chemical (gravimetric-based mass loss) and Electrochemical methods (Linear Polarisation Resistance and Electrochemical Impedance Spectroscopy) were in good agreement. The generally high degree of variance column-wise was indicative of the fact that the Inhibition Efficiencies (IE%) increased with concentration increase as was established earlier through researches by Quraishi and Jamal (2002).

Inhibition Efficiencies (IE%) obtained using LPR, EIS and Gravimetric-based mass loss (ML) for PBE+VDE+Boehmite system at room temperature were shown in Table 4.32. The data from a simple two-way ANOVA, for samples exposed to PBE+VDE+Boehmite Nanoparticle systems at room temperature and different concentrations respectively, were shown in Table 4.33. The data were generated from the Inhibition Efficiencies (IE%) obtained from three methods (Linear Polarisation Resistance and Electrochemical Impedance Spectroscopy). .

It was observed that the degree of variance were much lower along the rows (0.017633, 0.093733, 0.4819 and 0.3271) than the columns. This implied that the results obtained from both Chemical (gravimetric-based mass loss) and electrochemical methods (Linear Polarisation Resistance and Electrochemical Impedance Spectroscopy) were in good agreement at the same experimental temperature and concentration. Similarly, the generally high degree of variance column-wise implied that the Inhibition Efficiencies (IE%) increased with increase concentration as reported by Tang *et al*. (2003).

CHAPTER SIX

6.0 SUMMARY, CONCLUSIONS AND RECOMMENDATIONS

6.1 Summary

The influence of two plant extracts, *Parkia biglobosa* (African locust bean) and *Vitex doniana* (Black plum), on the electrochemical corrosion behaviour of as-cast AA2024 aluminium alloy exposed to simulated sea water (3.5%NaCl solution) was investigated at different temperatures (30, 40, 50, 60 and 70^{o}C). The test alloy, AA2024, was produced by the conventional sand casting method and analysed by X-Ray Fluorescence (XRF) to ascertain its composition. Gravimetric-based mass loss and electrochemical methods using Linear Polarisation Resistance (LPR) and Electrochemical Impedance Spectroscopy (EIS) were employed in the investigation. Assessments of the stability of adsorbed layers on the substrates were carried out using Chronopotentiometry.

The phytoconstituents of the plants were extracted using Soxhlet extractor and analysed by the ^{1}H NMR-based metabolomics technique. The NMR spectra of the two plant extracts investigated showed presence of aromaticity, functional groups, such as –CH_3, and R-OH, which are some attributes of corrosion inhibitors. *Parkia biglobosa* has high density/concentration of aromatics and other functional groups, compared with *Vitex doniana* as revealed by ^{1}H NMR spectrum.

The extracts were prepared in different concentrations of 10, 20, 30, 40 and 50%v/v. Boehmite nanoparticles (Disperal 40) were added in different amounts (0.1, 0.2, 0.3, 0.4, and 0.5g) to optimize the performance of the extracts as corrosion inhibitors, and also improve their longeivities.

Comparison of the performances of the different extract-extract and extract-Nanoparticle systems were also made on the basis of Inhibition Efficiencies (IE%), determined from

both chemical (Gravimetric-based mass loss) and electrochemical techniques (Linear Polarisation Resistance and Electrochemical Impedance Spectroscopy). Only PBE+VDE+Boehmite Nanoparticle synergistic system was found to compare favourably with Sodium chromate, the reference inhibitor against which the effectiveness of the different inhibitor systems (single, binary and ternary) was compared. An optimum IE% of 92.15% for PBE+VDE+Boehmite Nanoparticles system compared favourably with IE% of 92.57% for Sodium Chromate. The adsorbed films of Sodium Chromate and PBE+VDE+Boehmite Nanoparticles systems were found to be stable around -0.6V when evaluated by Chronopotentiometry.

Kinetic and thermodynamic data generated suggested co-adsorption through a combination of both Physisorption and Chemisorption mode of interaction between the inhibitors and the substrates. The linearity of Langmuir adsorption Isotherms further supported adsorption proposition, while the El-Awady's adsorption Isotherms consolidated the Langmuir's model by calculating the number of active sites; obtained values greater than unity inferred that the inhibitor molecules blocked more than one active site. The synergism parameters were found to be greater than unity, affirming synergy among the inhibitor molecules/ions.

Characterisation of the electrode surfaces, using SEM/EDX, XRD and Raman Spectroscopy gave insights into the inhibition mechanism. SEM/EDX panorama clearly revealed differences between inhibited and uninhibited surface morphologies of the substrates. In the micrographs of inhibited samples, there were evidences of interference of corrosion products with the additive inhibitors to form new phases, which as proposed by Rozenfeld (1981), was a plausible mechanism for the action of the inhibitors, and not

just adsorption or co-adsorption. This might have also explained the coarseness contained in most of the SEM micrographs.

The XRD pattern of inhibited surfaces showed the main phases observed previously, in as-cast sample, but the intensity of the peaks became weak compared to those detected in the absence of inhibitor. It was also noted from the comparative Diffractograms that addition of the optimum concentration of the studied inhibitor systems lead to a noticeable attenuation in the heights of the characteristic peaks of the main phases present in the alloy. This suggested marked interactions of inhibitor molecules with electrode surfaces; adsorption/co-adsorption onto the substrates, interactions with the electrode surfaces and corrosion products.

Raman spectroscopic analyses were found to be particularly helpful when examining the surfaces of the substrates inhibited by the plant extracts. From the Raman spectral patterns, there were variations in Raman shifts, broadening, and surface interactions. These might be indicative of either adsorption of organic molecules onto the alloy surface, leading to reduction or disappearance of certain peaks, or release of certain metal ions into solution, leading to appearance of certain peaks.

All the characterisation techniques gave insights into the influence of the inhibitive systems on the electrodes/substrates; through morphological revelations, phase identifications and other thin corrosion products elucidation.

Inhibition Efficiency (IE%) results obtained from Linear Polarisation Resistance, Electrochemical Impedance Spectroscopy and Gravimetric-based mass loss were compared using ANOVA statistical tool and found to be in good agreement.

6.2 Conclusions

From the results of this investigation, the following conclusions were arrived at;

1. The plant extracts exhibited reasonable degree of Inhibition Efficiencies (IE%). The IE% values increased with increase in concentrations, and decreased with temperature increase in all the concentration and temperature ranges investigated. *Parkia biglobosa* extracts (IE% 83.30%) performed better than *Vitex doniana* extracts (IE% 74.1%); this could probably be due to higher density/concentration of aromatics and other functional groups compared with *Vitex doniana* as revealed by the ^{1}H NMR-based metabolomics technique.
2. Addition of Boehmite Nanoparticles appreciably improved the performance of these extracts, by enhancing synergy among the different inhibitor components. Probably, the Boehmite nanoparticles reinforced the hybrid matrices by absorbing inhibitor ions/reactive groups, releasing them during contact with moisture and thus offering effective self-healing properties through adsorption, interactions with the electrode surface and corrosion products**.**
3. Of all the methods used to evaluate the inhibitive ability of the substances against the test alloy, Linear Polarisation Resistance (LPR) was found to be the best, followed by Electrochemical Impedance Spectroscopy (EIS) and Gravimetric-based mass loss. Results obtained from electrochemical methods were found to be in good agreement with those obtained from Gravimetric-based mass loss.
4. All the inhibitor systems investigated affected both the anodic and cathodic processes, at varying degrees, suggesting that they are mixed type inhibitors. This is evidenced from anodic and cathodic Tafel constants obtained from the Linear

Polarisation Resistance (LPR) measurements of the different systems investigated**.**

5. Characterisation of the test coupons, via examination of the electrode surfaces, using SEM/EDX, XRD and Raman Spectroscopy supported the results obtained from corrosion studies; that the different plant extracts, extract-extract and extract-nanoparticles systems investigated inhibited the corrosion of AA2024 in artificial sea water at varying degrees through interactions with the substrate surfaces and corrosion products.
6. Synergistic combination of *Parkia biglobosa* and *Vitex doniana* with Boehmite nanoparticles offered better protection system and stability of adsorbed layers than other systems. Its performance matched that of the standard/reference inhibitor, i.e. sodium chromate.
7. Optimum concentration of the synergistic system of *Parkia biglobosa*+*Vitex doniana*+Boehmite nanoparticles was found to be 30%PBE+20%VDE+0.3g Boehmite nanoparticles, with obtained IE% values of 92.15%.

6.3 Recommendations

Based on the findings arrived at this work, the following recommendations are offered;

1. More plant species should be explored for use as corrosion inhibitors, so as not to be too dependent on particular specie(s), as continued exploitation of limited species threatens the ecosystem.
2. The possibility of using these extracts in the synthesis and formulation of protective organic coating should be taken as a matter of urgent interest.

3. Investigation into more potent ways of preserving plant extract materials, when used as inhibitors, with a view to improving their biodegradability and longevity limits should be carried out.
4. Semi-empirical approaches employing the Density Functional Theory (DFT) and Quantum Chemical Methods (QCM) should be applied to model the functionality of the different systems investigated. Other Mathematical Modeling approaches for assessing corrosion inhibitor functionality such as Monte Carlo, Genetic Function Approximation (GFA), and Extreme Value Analysis (EVA) should also be applied to ascertain the validity or otherwise of the results obtained in this work.
5. Nanoscience and technology is a new frontier with multidisciplinary applications; from water treatment to cancer theraphy. Hence, it is important to sensitise and educate the populace, especially scientists and engineers, on potential applications of this multidisciplinary frontier of knowledge.

REFERENCES

Abdulwahab, M. (2011). *The effect of multi-step thermal ageing treatment on the hardness and corrosion characteristics of A365.0-type Al-Si-Mg alloy.* An unpublished Ph.D Dissertation, Department of Metallurgical and Materials Engineering, Ahmadu Bello University, Zaria, Nigeria.

Abd-El-Nabey, B. A., Khamis, E., Thompson, G. E. and Dawson, J. L. (1986) *Surface Coating Technology*, 2:87. *In:* Rozenfeld, I.L. (1981[a]). *Corrosion Inhibitors.* McGraw-Hill Inc. Ltd., USA. 1st edition, pp27-221.

Adeyemi, O. O. (2005). Effect of temperature and concentration on protective action of 5-membered heterocycles on acid corrosion of brass. *Nigerian Journal of Corrosion Science and Technology, 3: 41-43.*

Afanas'ev, B.N., Akulova, Y.P. and Charykov, N.A. (1989)[a] *Zashch. met.,* 34:303. *In:* Rozenfeld, I.L. (1981[a]). *Corrosion Inhibitors.* McGraw-Hill Inc. Ltd., USA. 1st edition, pp27-221.

Al-Sahaibani, H. (2000). Evaluation of extracts of Henna leaves as environmentally friendly corrosion inhibitors for metals. *Materials Science and Technology,* 31(12): 1060-1063.

Al-Suhybani, A.A. (1990). *Corrosion prevention and control,* 37: 11-16. *In:* Rozenfeld, I.L. (1981[a]). *Corrosion Inhibitors.* McGraw-Hill Inc. Ltd., USA. 1st edition, pp27-221.

Amitha, R. B. E. and Bharathi, B. J. B. (2012). Green Inhibitors for Corrosion Protection of Metals and Alloys: An Overview. *International Journal of Corrosion,* doi:10.1155/2012/380217.

Antropov, L. I., Makushin, E. M. and panasenko, V. F. (1981). *Inhibitors of metal corrosion*. Tekhnika, Kiev,3rd edition, pp21-76.

American Soceity of Metals Handbook (1990). *Properties and Selection: Non-ferrous Alloys and special purpose materials*. Printed in the USA, vol. 2, pp 17-19.

Auwal, K. (2008). *Effects of organic resins and plant extracts on corrosion rate of medium carbon steel in H_2SO_4 acid medium.* An unpublished M.Sc. thesis, Department of Metallurgical and Materials Engineering, Ahmadu Bello University, Zaria.

Babaqi, A.S., El-Basiounyi, M.S. and Abdulla, R.M. (1989). *Bulletin of society of chemists,* 3: 297-300. France. *In:* Antropov, L. I., Makushin, E. M. and panasenko, V. F. (1981). *Inhibitors of metal corrosion.* Tekhnika, Kiev,3rd edition, pp21-76.

Badini, C., Manna, F. and Verne, E. (1995). *Materials Science & Engineering*. John Wiley & sons, New York, 3rd edition, pp185-191.

Baek, Y. and Frankel, G. S. (2003). Electrochemical Quartz Crystal Microbalance study of corrosion of phases in AA2024. *Journal of the Electrochemical Soceity, 15(1): B1-B9.*

Bairamow, A.K. (1985) *Corrosion Science,* 25: 69-73. *In:* Antropov, L. I., Makushin, E. M. and panasenko, V. F. (1981). *Inhibitors of metal corrosion*. Tekhnika, Kiev,3rd edition, pp21-76.

Bard, A. J. & Faulkner, L. R. (2001). *Electrochemical Methods*. John Wiley, New York.

Barlow, C. A. Jr. (1970). *The Electrical Double Layer. In:* Henry E. (1970). *Physical Chemistry: an Advanced Treatise*, vol. IXA/Electrochemistry, Academic Press, New York.

.

Benjamin, D. C., Richard, A. L., David, H. R. (2006). Corrosion control and monitoring; a program management guide for selecting materials. *Advanced Materials, Manufacturing and Testing Information Analysis Center (AMMTIAC)*, New York, USA pp1-19.

Bereket G., Ogretir C. and Ozsahim C. (2004). *Journal of Molecular Structures (THEOCHEM)* 663: 173. *In:* Buchheit, R. G. and Boger, R. K. (2002). *Copper redistribution and surface enrichment due to the dissolution of Al-Cu alloys*. Seminar paper, Fontana Corrosion Center, Ohio State University, Columbus, USA.

Bhajiwala, H. M. and Vashi, R. T. (2001) *Bulletin of Electrochemistry,* 17(10):441. *In:* Kuznetsov, Y.I., Thomas, J.G.N. and Mercer, A.D. (1996). *Organic inhibitors of corrosion of metals.* Plenum publishing co., Austria. pp 35-70.

Bilgic, S. and Sahim, M (2001) *Materials Chemistry & Physics.* 70:290. *In:* Kuznetsov, Y.I., Thomas, J.G.N. and Mercer, A.D. (1996). *Organic inhibitors of corrosion of metals.* Plenum publishing co., Austria. pp 35-70.

Birol, Y. (2009). Response to artificial ageing of dendritic and globular Al-7.5%-Mg alloys. *Journal of alloys & compounds,* 484:164-167.

Bockris, J.O.M. and Drazk, D.; (1972) *Electrochemical Science*. Taylor and Francis Ltd., London pp 250-251. *In:* Damaskin, B.B., Petrii, O.A. and Batrakov, V.V. (1971). *Adsorption of Organic Compounds on Electrodes*. Plenum Press, New York.

Bockris, J.O.M, Green, M. and Swinkels, D.A. (1964). *Journal of Electrochemistry.* 3:736. *In:* Clark, D. S. and Varney, W. R. (1952). *Physical Metallurgy for Engineers*. D. Van Nostrand Company Inc., pp 12-47.

Boger, R. K. (2000). *Copper release from corroding Al-Cu alloy measured using a Rotating Ring Disc Electrode*. M.Sc. thesis, Ohio University, USA.

Bouklah, M., Hammouti, B. and Benkaddour, M. (2005). Corrosion Inhibition of steel in HCl acid by new bipyrazole derivatives. *Pigment* and *Resin Technology*, 34(4): 197 – 202.

Brundle, C. R., Evans, C. A. Jnr. and Wilson, S. (1992). *Encyclopedia of Materials characterization; surfaces, interfaces, thin films*. Butterworth-Heinemann publishing inc., USA. pp70-427.

Buchheit R. G. (1995). *Journal of the Electrochemica Society,* 142, 3994. *In:* Damaskin, B.B., Petrii, O.A. and Batrakov, V.V. (1971). *Adsorption of Organic Compounds on Electrodes*. Plenum Press, New York.

Buchheit, R. G. and Boger, R. K. (2002). *Copper redistribution and surface enrichment due to the dissolution of Al-Cu alloys*. Seminar paper, Fontana Corrosion Center, Ohio State University, Columbus, USA.

Buchheit R. G., Grant R. P., Hlava P. F., McKenzie B., and Zender G. L. (1997). *Journal of the Electrochemical Society,* 144: 2621. *In:* Damaskin, B.B., Petrii, O.A. and Batrakov, V.V. (1971). *Adsorption of Organic Compounds on Electrodes*. Plenum Press, New York.

Callister W. D. Jnr. (2007). *Material Science and Engineering; an Introduction.* John Wiley and sons inc. USA, 7th edition, pp622-631.

Chang, S. C., Leugers, M. A. and Bare, S. R. (1992). Surface chemistry of Magnesium Oxide-supported Molybdenum oxide; an in-situ Raman spectroscopic study. *Physical Chemistry, 96:10358-10365.*

Charles, R. (2009). Nano Know-How. *Chemical Engineering,* 112 (2): 34-39.

Chauhan, L. R. and Gunasekaren, G. (2007). Corrosion inhibition of mild steel by plant extract in dilute HCl medium. *Corrosion Science*, 49:1143-1161.

Chetouani, A., Hammouti, B. and Benkaddour, M. (2004). Corrosion inhibition of iron in HCl acid solution by jojoba oil. *Pigment and Resin Technology,* 33(1): 26-31.

Clark, D. S. and Varney, W. R. (1952). *Physical Metallurgy for Engineers*. D. Van Nostrand Company Inc., pp 12-47.

Cook, R. L., Elliot, B. J, Devito-Luebben, S., Myers, A. W. and Smith, B. M. (2005). Surface modified particles by multi-step Michael-type addition and process for the preparation thereof. *United States patent* 6,887, 517.

Cook, R. L., Myers, A. W. and Elliot, J. E. (2006). Chromate-free on-demand releasable corrosion inhibitors for Aluminium alloys. *Corrosion Science.*

Cuilei, I. (1990). *Methodology for analysis of vegetable drugs*. UNIDO.

Damaskin, B.B. and Stenina, E.V. (1986[b]). *Electrochemistry,* 22:315. *In:* Damaskin, B.B., Petrii, O.A. and Batrakov, V.V. (1971). *Adsorption of Organic Compounds on Electrodes*. Plenum Press, New York.

Damaskin, B.B., Petrii, O.A. and Batrakov, V.V. (1971). *Adsorption of Organic Compounds on Electrodes*. Plenum Press, New York.

Daria, V.A. & Dmitry, G.S. (2008). Smart self-repairing protective coatings. *Materials today,* 11(10): 24-30.

David, T. and James, T. (1998). *Corrosion Science and Technology*. CRC press LLC, USA. pp85-124.

Dawson, J., Bruce, K. and John, D. G. (2001). *Corrosion risk assessment and safety management for offshore processing facilities.* Prepared for Capcis Limited, Manchester, United Kingdom **by HSE** books. pp31-53.

Deng, L. S., Fu, H. and Mu, G. (2009). *Corrosion Science,* 51; 620. *In:* Kuznetsov, Y.I. (2004). Physicochemical aspects of metal corrosion inhibition in aqueous solutions. *Russian Chemical Reviews*, 73(1): 75-87.

Dillon, C. P. (1986). *Corrosion Control in the Chemical Process Industries*. McGraw-Hill, New York, 1st edition, pp267.

Dimitrov N., Mann J. A., Vukmirovic M., and Sieradzki K. (2000). *Journal of the Electrochemical Society,* 147, 3283. *In:* Damaskin, B.B., Petrii, O.A. and Batrakov, V.V. (1971). *Adsorption of Organic Compounds on Electrodes*. Plenum Press, New York.

Ebenso, E. E., Alemu, H., Umoren, S. A., Obot I. B. (2008). *International Journal of Electrochemical Sciences,* 3: 1325. *In:* Ebenso, E.E., Ekpe, U.J., Umoren, S., Ekerete, J., Abiola, O.K., Oforka, N.C. and Martinez, S. (2004). Corrosion inhibition studies of some plant extracts on Aluminium in acidic medium. *Journal of Corrosion Science and Technology,* 1 (1): 96-101.

Ebenso, E. E., Ekpe, U. J., Umoren, S., Ekerete, J., Abiola, O. K., Oforka, N. C. and Martinez, S. (2004). Corrosion inhibition studies of some plant extracts on Aluminium in acidic medium. *Journal of Corrosion Science and Technology,* 1 (1): 96-101.

Ebenso, E. E., Okafor, P. C., Ita, B. I. Offiong, O. E., Ibok, U. J. and Ekpe, U. J. (2001). *Bulletin of Electrochemistry,* 17:457-464. *In:* Damaskin, B. B., Petrii, O. A. and Batrakov, V. V. (1971). *Adsorption of Organic Compounds on Electrodes*. Plenum Press, New York.

Ekpe, U.J., Ibok, U.I. Ita, B.I. Offiong, O.E. and Ebenso, E.E. (1995). *Materials Chemistry and Physics,* 40:87. *In:* Gomma, G. K. and Wahdan, M. H.(1994). Effect of temperature on the acidic dissolution of copper in the presence of amino acids. *Materials Chemistry and Physics*, vol. 39(2): 142– 148.

Ekpe, U. J., Okafor, P. C., Ebenso, E. E., Offiong, O. F and Ita, B. I. (2001). *Bulletin of Electrochemsitry,* 17:131-135. *In:* Gomma, G. K. and Wahdan, M. H.(1994). Effect of temperature on the acidic dissolution of copper in the presence of amino acids. *Materials Chemistry and Physics*, vol. 39(2): 142– 148.

El-Etre, A.Y. and Abdallah, M. (2000). Natural honey as corrosion inhibitor for metals and alloys II. *Corrosion Science,* 42(4): 731-738.

Elewady, G.Y., El-Said, I.A., and Fouda, A.S. (2008). Anion surfactants as corrosion inhibitors for Aluminium dissolution in HCl solution. *International Journal of Electrochemical science,* 3:177-190.

Elliot, J. and Cook, R. (2007). Nanoparticle-based corrosion inhibitors for Aerospace Aluminium. *NACE Tri-Service Conference*, 3-7.

Erdey-Gruz, T. (1972). *Kinetics of Electrode Processes*. Wiley-Interscience, John Wiley & Sons Inc., New York, pp 442.

Evans, R. U. (1960). *The Corrosion and Oxidation of Metals*. Edward Arnold Publishers Ltd., 2nd edition, pp. 135.

Evans, W. C. (1996). *Trease and Evan's pharmacognosy.* W.B. Saunders Co. Ltd. London, 14th edition. pp 15-775.

Ewen, S. and Geoffrey, D. (2005). *Modern Raman Spectroscopy; a Practical Approach*. John Wiley And Sons Ltd., West Suxxes, England, pp 5-119.

Féron, D. (2007). Corrosion behaviour and protection of copper and aluminium alloys in seawater. *European Federation of Corrosion, Woodhead publishing limited, Cambridge, England. No. 50* pp3-117.

Feyisayo, V. A. (2009). *A comparison of the corrosion behaviour of 444 Ferritic and 316 Austenitic stainless steels in acidic media*. MSc. Dissertation, University of Witswatersrand, pp27-125.

Fisher, J. T. (1971). Corrosion Inhibitors, Corrosion Chemistry. *American Chemical Society*, *89: 270.*

Fontana, M. G. (2005). *Corrosion Engineering*. McGraw-Hill Inc, 2nd Edition New York, pp33-341.

Frankel, G.S. (2003). Corrosion science in the 21st century. *Journal of Corrosion Science and Engineering,* 6(CO28).

Gauglitz, G. and Vo-Dinh, T. (2003). *Handbook of Spectroscopy*. WILEY-VCH Verlag GmbH & Co. KGaA, Weinheim, pp72-397.

Gökhan, G. (2008). The use of quantum chemical methods in corrosion inhibitor studies. *Corrosion Science*, 50 (2008): 2981–2992.

Gomma, G. K. and Wahdan, M. H.(1994). Effect of temperature on the acidic dissolution of copper in the presence of amino acids. *Materials Chemistry and Physics*, vol. 39(2): 142– 148.

Greenwood, N. N. and Earnshaw, A. (1997). *Chemistry of Elements*. Butterworth and Heinemann, 2nd Edition.

Grigoriev, V.P. & Ekilik, V.V. (1978). *Chemical Structure and Protective action of corrosion inhibitors.* (Rostov-on-Don: Rostov State University).

Guevara-Lara, A., Bacaud, R. and Vrinat, M. (2007). Highly active NiMo/TiO_2-Al_2O_3 catalysts: influence of the preparation and the activation conditions on the catalytic activity. *Applied Catalysts, 328:99-108.*

Gui, J. and Devine, T. M. (1991). In-situ vibrational spectra of the passive film on Iron in buffered Borate solution. *Corrrosion Science, 32: 1105-1124.*

Hagerman, A. E. (1988). Extraction of tannins from fresh and preserved leaves. *Journal of Chemical Ecology*, 14 : 453 – 461.

Hatch, J. E. (1984). Aluminium: Properties and Physical Metallurgy. *American Soceity for Metals*, Metals park, OH, USA.

Herman, H. B. & Bard, A. J. (1963). *Anlalytical Chemistry*, 35:1121. *In:* Clark, D. S. and Varney, W. R. (1952). *Physical Metallurgy for Engineers*. D. Van Nostrand Company Inc., pp 12-47.

Ibbotson, G.E. and Marshall, A. (1990). Chemical inhibitors for corrosion control. G. G. Clubley Ed., *Royal Society of Chemists,* U.K.

Ilevbare O. and Scully J. R. (2001). *Corrosion (Houston),* **57**, 134. *In:* Baek, Y. and Frankel, G. S. (2003). Electrochemical Quartz Crystal Microbalance study of corrosion of phases in AA2024. *Journal of the Electrochemical Soceity, 15(1): B1-B9.*

ISO (1989). *International Standard Organization,* 8044.

Jenkins, R. and Snyder, R. L.(1996). *Introduction to X-Ray Powder Diffractometry*. John Willey& Sons Inc., New York.

Johansson, L. G. (1990). *Marine Chemistry.* **30**, pp113. *In:* Damaskin, B.B., Petrii, O.A. and Batrakov, V.V. (1971). *Adsorption of Organic Compounds on Electrodes*. Plenum Press, New York.

Jones, D. A. (1996). *Principles and prevention of corrosion*. Prentice-Hall Inc., USA. pp 75-153.

Kazaraji, A., Keertit, S., Aride, J., Bougrin, K. and Soufiaoui, M. (2000). *Bulletin of Electrochemistry,* 16(3):97. *In:* Kuznetsov, Y. I., Thomas, J. G. N. and Mercer, A. D. (1996). *Organic inhibitors of corrosion of metals.* Plenum publishing co., Austria. pp 35-70.

Kear, B. H. and Strutt, P. R. (1995). Chemical processing and applications for nano-structured materials. *Nanostructured materials,* 6(1-4): 227-236.

Keay, R. W. J., Onochie, C. F. A. and Standfield, D. P. (1989). A revised version of Nigerian Trees. Clarendon press. Oxford, pp 234, 438.

Kendig, M., Cunningham, L., Warren, S. Jean-Jaquet (1995). *NACE International* Annual Conference, Charlottesville, VA, March 27-29, pp 1.

Khaled, Z. M., Hamdy, A. and Abbas, M. (2012). A Pharmaceutically Active Compound as Corrosion Inhibitor for Carbon Steel in Acidic Medium: Electrochemical and Thermodynamic Studies. *Research Journal of Pharmaceutical, Biological and Chemical Sciences, 3(2):912-918.*

Khamis, E. (1990). *Corrosion*, 6:476. *In:* Rozenfeld, I.L. (1981[a]). *Corrosion Inhibitors*. McGraw-Hill Inc. Ltd., 1st edition, pp 115-232.

Khoshnaw, H. and Gardi, M. (2007). *Materials & Corrosion*, 58(5). *In:* Kuznetsov, Y.I. (2004). Physicochemical aspects of metal corrosion inhibition in aqueous solutions. *Russian Chemical Reviews*, 73(1): 75-87.

Kim, H. K., Young, H. C. & Robert, V. (2010). NMR-based metabolomic analysis of plants. *Nature,* doi:10.1038/nprot.2009.23

Kirk, O. (1989). *Encyclopedia of Chemical Technology*, 4: 289-3000.

Kuznetsov, Y.I. (2004). Physicochemical aspects of metal corrosion inhibition in aqueous solutions. *Russian Chemical Reviews*, 73(1): 75-87.

Kuznetsov, Y.I., Thomas, J.G.N. and Mercer, A.D. (1996). *Organic inhibitors of corrosion of metals.* Plenum publishing co., Austria. pp 35-70.

Laurence, M. H. and Christopher, J. M. (2007). *Experimental organic chemistry: Principles and Practice* (Illustrated ed.). pp. 122-125.

Lebrini, M., Robert, F. and Roos, C. (2010). Inhibition Effect of Alkaloids Extract from *Annona Squamosa* Plant on the Corrosion of C38 Steel in Normal Hydrochloric Acid Medium. *International Journal of Electrochemical Sciences,* 5: 1698 - 1712

Levine I.N. (1991). *Quantum Chemistry*, Prentice Hall, New Jersey.

Mahran, G.H., El-Alfy, T.S., Ahmed, M.S. and Hanna, G. (1980). *Journal of African Medicinal plants,* 3:35-45.

Makhlouf, M. Th., El-Shatory, S. A. and El-Said, A. (1996). The synergistic effect of halide ions and some selected thiols as a combined corrosion inhibitor for pickling of mild steel in sulphuric acid solution. *Materials chemistry and Physics*, 4:76-82.

Malik, A. U., Andijani, I. N. and Ahmed, S. (1994). *Corrosion monitoring in SWCC plants-Al Khafji plant. Research & Development center, Al-Jubail and Madeeh Al-Khalidi and Khalid A.* Al-Maaeeli AL-Khatji Desalination plant. Technical report,30:1040-1056.

Maria, F. Tracey, M., Anthony, H. and Grant, V.R. (2007). Rare earth diphenyl phosphates as corrosion inhibitors for Aluminium alloys. *Corrosion Science, 41:37-49.*

Marsh, J. and Teh, T. (2007). Conflicting Views: CO_2 Corrosion Models, Corrosion Inhibitor Availability Philosophies, and the Effect on Subsea Systems and Pipeline Design. *Soceity of Petroleum Engineers*, SPE 109209, Presentation at Offshore Europe, Aberdeen, Scotland, UK.

Martinez, S. (2002). *Material chemistry and physics*, 77:97. *In:* Martinez, E. (2002). Some advances in corrosion inhibition*. Materials Chemistry and Physics, 77(97).*

Martinez, S. and Stern, I. (2003). Journal of applied electrochemistry, 31:973. *In:* Martinez, E. (2002). Some advances in corrosion inhibition. *Material chemistry and physics,* 77(97).

Materials Performance Data (2010): 2024 Aluminium alloy.

Maxey, B. (1954). *Corrosion Inhibitor checklist*. pp 230-234.

McCarty, K. F. and Boehme, D. R. (1989). A Raman study of the system $Fe_{3-}xCr_xO_4$ and $Fe_{2-}xCr_xO_3$. *Solid State Chemistry, 79:19-27.*

Modolfo, L. F. (1976). *Aluminium alloys: structures and properties*. Butterworths, London. pp 499.

Morad, M., Morvan, J. and Pagetti, J.(1995). *Proceedings of the Eighth European Symposium on Corrosion Inhibitors* (8SEIC), Sez V, Suppl. N. 10, Ann. Univ. Ferrara, NS, pp. 159.

Moussa, M.N. and El-Tagoury, M. M. (1990). *Anti-corrosion method and materials,* 37: 4-8. *In:* Rozenfeld, I.L. (1981[a]). *Corrosion Inhibitors*. McGraw-Hill Inc. Ltd., 1st edition, pp 115-232.

NACE 3C194 (1994). Economics of Corrosion. *NACE International*, Houston, Texas.

Nestor, P. (2004). *Electrochemistry and Corrosion Science.* Kluwer Academic Publishers, New York. pp34-67.

Noor, E.A. and Al-Moubaraki, A.H. (2008). *Materials Chemistry & Phys*ics, 110: 145. *In:* Al-Sahaibani, H. (2000). Evaluation of extracts of Henna leaves as environmentally friendly corrosion inhibitors for metals. *Materials Science and Technology,* 31(12): 1060-1063.

Obot, I. B., Obi-Egbedi, N.O. and Umoren, S. A.(2009). Adsorption Characteristics and Corrosion Inhibitive Properties of Clotrimazole for Aluminium Corrosion in Hydrochloric Acid. *International Journal of Electrochemical Sciences,* 4: 863-877.

Onochukwu, I. and Oppong, F. W. (1990). *Corrosion Science*, 26:919-926. *In:* Raman and Labine (1986). Reviews on Corrosion Inhibitor Science and Technology. *NACE, TX* 1(11): 20.

Phillip, A. S. (2001). *Corrosion Engineering Handbook*. McGraw-Hill Inc., 2nd edition. New York, vol 1, pp 140-176.

Pierre, R.B. (2000). *Handbook of corrosion Engineering*, McGraw-Hill Companies, Inc. New York. pp 1001-1009.

Pinck, W., Geng, S., O'keefe, M., Fahrenhottz, W. and O'Keefe, T. (2008). Effects of acid and alkaline based surface preparations on spray deposited cerium based conversion coatings on Al-2024 T3. *Applied Surface Science*, 225(7): 4061-4065.

Papova, A., Sokolova, E. and Christov, M. (2003). *Corrosion Science,* 45: 33. *In:* Kuznetsov, Y.I., Thomas, J.G.N. and Mercer, A.D. (1996). *Organic inhibitors of corrosion of metals.* Plenum publishing co., Austria. pp 35-70.

Pourbaix, M. (1962). *Atlas of Potential/pH Diagrams.* Pergamon, Oxford and CEBELCOR (Centre Beige D'etude de Ia Corrosion) Rapports Techniques.

Pourbaix**,** M.(1973). *Lectures on Electrochemical Corrosion.* Plenum Press, New York, London.

Prissanaroon, W., Brack, N., Pigram, P.J. and Liesegang, J. (2004). *Journal of Synthetic metals.In:* Buchheit, R. G. and Boger, R. K. (2002). *Copper redistribution and surface enrichment due to the dissolution of Al-Cu alloys*. Seminar paper, Fontana Corrosion Center, Ohio State University, Columbus, USA.

Quraishi, M. A. and Jamal, D. (2002). Inhibition of Mild Steel Corrosion in the presence of fatty acid triazoles. *Journal of Applied Electrochemistry*, 32:425-430.

Raghupati, M. and Sriparna, D. (2007). *Engineering Chemistry*. New age Int'l. (p) ltd., New Delhi. pp527-578.

Raja, P. B. and Sethuraman ,M.G.(2008). Natural products as corrosion inhibitor for metals in corrosive media-a review. *Materials Letters*, 62 (1):113–116.

Rajendran, S., Agasta, M., Rama, D. M., Shyamala, D. B., Rajam, K. and Jeyasundari, J. (2009). Corrosion inhibition by an aqueous extract of Henna leaves *(Lawsonia inermis L.). Zastita Materijala 50, broj 2.* UDC:620.193.4-20.

Ralph, P. I. A. and Daniel, J. S.(2008). Characterization of Corrosion on Outdoor-Exposed Aluminum Metal-Matrix Composites as a Function of Reinforcement Specie and Volume Fraction. *Materials Research Directorate,* ARL George Hawthorn and Lloyd H. Hihara, University of Hawaii, pp19-51.

Raman and Labine (1986). Reviews on Corrosion Inhibitor Science and Technology.

NACE, TX 1(11): 20.

Ramesh, S.P., Vinod, K.P., Kumer, P. and Sethuraman, G.N. (2003). *Bulletin of Electrochemistry,* 17: 3. *In:* Rozenfeld I. L.(1981[b]). New data on the mechanism of metals protection with inhibitors. *Corrosion*, 37:371-377.

Robert, G. K., John, R. S., David, W. S. and Rudolph, G. B. (2003). *Electrochemical Techniques in Corrosion Science and Engineering*. Marcel Dekker, Inc, New York, USA, pp205-255.

Rodosovi, J., Kliskic, M., Aljinovic, L.J. and Vuko, S. (1995). *Proceedings of 8th European Symposium on "Corrosion Inhibition".* Ann University, Ferrara, Italy. pp 817.

Rozenfeld, I.L. (1981[a]). *Corrosion Inhibitors*. McGraw-Hill Inc. Ltd., 1st edition, pp 115-232.

Rozenfeld I. L.(1981[b]). New data on the mechanism of metals protection with inhibitors. *Corrosion*, 37:371-377.

Saratha, R., Priya, S. V. and Thilagavathy, p. (2009). Investigation of *Citrus aurantiifolia* leaves extracts as corrosion inhibitor for mild steel in HCl. *E-Journal of Chemistry;* 6(3): 785-795.

Schmit, G. (1984). *The British Corrosion Journal*, 19:165. *In:* Damaskin, B.B., Petrii, O.A. and Batrakov, V.V. (1971). *Adsorption of Organic Compounds on Electrodes*. Plenum Press, New York.

Schmutz P. and Frankel G. S.(1998). *Journal of Electrochemical Society,* 145, 2285. *In:* Raman and Labine (1986). Reviews on Corrosion Inhibitor Science and Technology. *NACE, TX* 1(11): 20.

Schorr, M. and Yahalom, J. (1972). The significance of the energy of activation for the dissolution reaction of metal in acids. *Corrosion Science*, vol. 12(11): 867–868.

Shreir, L.L., Jarman, R.A. and Burstein, G. T. (2000). *Corrosion: metal/environment reactions*. Butterworth-Heinemann, 3rd Revised edition. Boston. Vol. 1 pp.

Silva, G.L., Lee, I. and Kinghorn, A.D. (1998). S*pecial problems with the extraction of plants. In:* Cannell(1995). *Methods in Biotechnology (Natural product isolation)*. R.J.P (Ed) Humana press, New Jersey. pp 245-364.

Silvia B., Victoria G., Federica P., and Anna M. M. (2010). Surface-enhanced Raman spectroscopy (SERS) on silver colloids for the identification of ancient textile dyes. Part II: pomegranate and sumac. *Journal of Raman spectroscopy*, 42:465-473.

Singh, A. K. & Quraishi, M.A. (2010). *Corrosion Science,* 52: 152. *In:* Singh, A., Singh, V. K. and Quraishi, M. A. (2010). Aqueous Extract of Kalmegh (*Andrographis paniculata*) Leaves as Green Inhibitor for Mild Steel in Hydrochloric Acid Solution. *International Journal of Corrosion*, Article ID 275983; doi:10.1155/2010/275983.

Singh, A., Singh, V. K. and Quraishi, M. A. (2010). Aqueous Extract of Kalmegh (*Andrographis paniculata*) Leaves as Green Inhibitor for Mild Steel in Hydrochloric Acid Solution. *International Journal of Corrosion*, Article ID 275983; doi:10.1155/2010/275983.

Sing, I. (1993). *Corrosion*, 49:473. *In:* Damaskin, B.B., Petrii, O.A. and Batrakov, V.V. (1971). *Adsorption of Organic Compounds on Electrodes*. Plenum Press, New York.

Stern, M. and Geary, A. I. J. (1957). Electrochemical Polarisation: A Theoretical Analysis of the Shape of Polarisation Curves. *Journal of Electrochemical Society,* 104:56.

Tang, L., Guannan, M. and Guangheng, L. (2003). The effect of neutral red on the corrosion inhibition of cold-rolled steel in 1M HCl acid. *Corrosion Science,* 45: 2251-2261.

Trethewey, K. R. and Chamberlain, J. (1991). Corrosion for students of Science and Engineering. Longman scientific and technical publishers, New York. 2nd Edition, pp 50-121.

Uhlig, H.H. (1963). Corrosion and Corrosion Control; an introduction to corrosion science and Engineering. John-Willey and Sons, Inc., 2nd edition, pp. 224-238.

Vashi, R.T. and Champaneri, V.A. (1997). *Indian Journal of Chemical Technology,* 4(180). Raman and Labine (1986). Reviews on Corrosion Inhibitor Science and Technology. *NACE, TX* 1(11): 20-28.

Victoria, J. G., Xiaoning, Q., Chris, V., Katharine, G. and Alice, H. (2006). Polyprrole/Aluminium flake hybrids as corrosion inhibitors for Al 2024-T3 *Corrosion Science.*

Villamil, R.F.V., Corio, P. Rubin J.C and. Agostinho S.M.I. (1999). *Journal of Electroanalytical Chem*istry, 472:112. *In:* Kuznetsov, Y.I. (2004). Physicochemical aspects of metal corrosion inhibition in aqueous solutions. *Russian Chemical Reviews*, 73(1): 75-87.

Wilhemsen, W. and Grande, A. P. (1988) *Acta Electrochemica,* 33: 927-932. *In:* Rozenfeld, I.L. (1981[a]). *Corrosion Inhibitors*. McGraw-Hill Inc. Ltd., 1st edition, pp 115-232.

William, F.S. (1990). *Materials Science and Engineering*. McGraw-Hill publishing Co., 2nd Edition New York. pp 508-525.

Wills, B. A. and Napier-Munn, T. J. (2006). *Mineral Processing and Technology*. Elsevier Science & Technology Books Publishers, 7th edition, pp 2.

Welz, B. and Sperling, M. (1999). *Atomic Absorption Spectrometry*, Wiley-VCH, Weinheim, Germany, ISBN 3-527-28571-7.

Yan, L. (2001). Formation of non-crystalline corrosion products on Zn-Al alloy coating exposed to sea water. *Corrosion science, 43:1793-1800.*

Yin J. Y. (2004). *Green Inhibitors for Corrosion Control: A Study on the Inhibitive Effects of Extracts of Honey and Rosmarinus Officinalis L. (Rosemary).* M.Sc. thesis, University of Manchester Institute of Science and Technology.

Yurt, A., Bereket, A., Balaban, A. and Erk, B. (2005). Effect of Schiff bases containing pyridyl group as corrosion inhibitors for low carbon steel in 0.1 M HCl. *Journal of Applied Electrochemistry; 33(12): 1025-1032.*

Zhao, T. P. & Mu G. N. (1999). *Corrosion Science*. pp 1937 – 1944. *In:* Kuznetsov, Y.I., Thomas, J.G.N. and Mercer, A.D. (1996). *Organic inhibitors of corrosion of metals.* Plenum publishing co., Austria. pp 35-70.

Zhang S.G., Lei W.M., Xia Z., Wang F. Y.(2003). *Journal of Molecular Structures (THEOCHEM)* 632: 46. *In:* Rozenfeld I. L.(1981[b]). New data on the mechanism of metals protection with inhibitors. *Corrosion*, 37:371-377.

Zhong, L. W. (2000). *Characterisation of Nanophase Materials. Part 1: Technical Approaches.* WILEY-VCH Verlag GmbH & Co. KGaA, Weinheim, pp 2.

APPENDICES

- **XRD**
- **SEM/EDXS**
- **INHIBITION EFFICIENCIES & SURFACE COVERAGES**
- **INHIBITION EFFICIENCIES COMPARISM**

APPENDIX I: EXPERT HIGH SCORE PROGRAMME AND JCPDS CARDS USED TO OBTAIN INFORMATION ON XRD PATTERNS AND RELATED INFORMATION.

X'Pert HighScore	**X'Pert HighScore Report**	date: 09/24/13



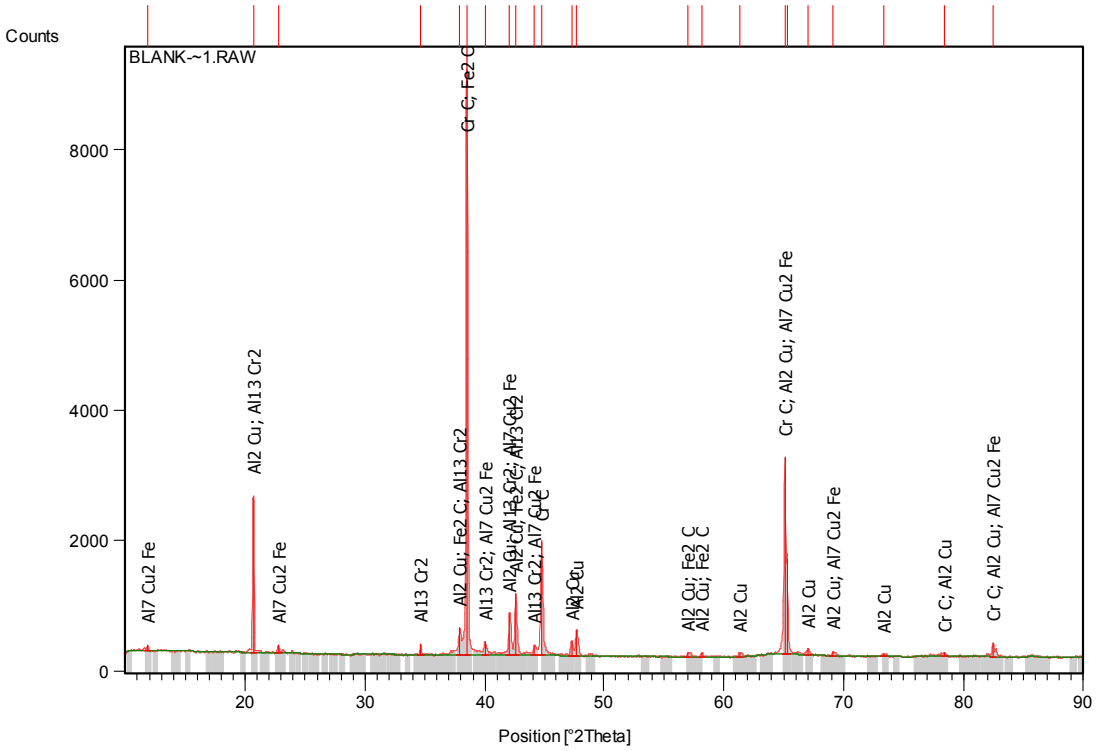
Distribution:

Name	**Function**	**0.1**	**0.5**	**1.0**
N.N.-999	Masterking Group Manager (MGM)	✓		
N.N.-998	Product Ontwikkelt Manager (POM)	✓		
N.N.-1	(AS)			✓

N.N.-2	(DS)			✓
N.N.-3	(BS)			✓
T.P.	Supervisor All Coding			✓

Sample Identification	**As-cast Sample**
Measurement Date / Time	01/10/12 13:32:56
Raw Data Origin	BRUKER-binary V3 (.RAW)
Scan Axis	Gonio
Start Position [°2Th.]	10.0020
End Position [°2Th.]	90.0040
Step Size [°2Th.]	0.0260
Scan Step Time [s]	37.0000
Scan Type	CONTINUOUS
Offset [°2Th.]	0.0000
Divergence Slit Type	Fixed
Divergence Slit Size [°]	1.0000
Specimen Length [mm]	10.00
Receiving Slit Size [mm]	0.1000
Measurement Temperature [°C]	25.00
Anode Material	Cu
Generator Settings	30 kV, 10 mA
Diffractometer Type	Unknown
Goniometer Radius [mm]	141.00
Dist. Focus-Diverg. Slit [mm]	91.00
Incident Beam Monochromator	No
Spinning	No

Graphics: (Bookmark2)



Peak List: (Bookmark 3)

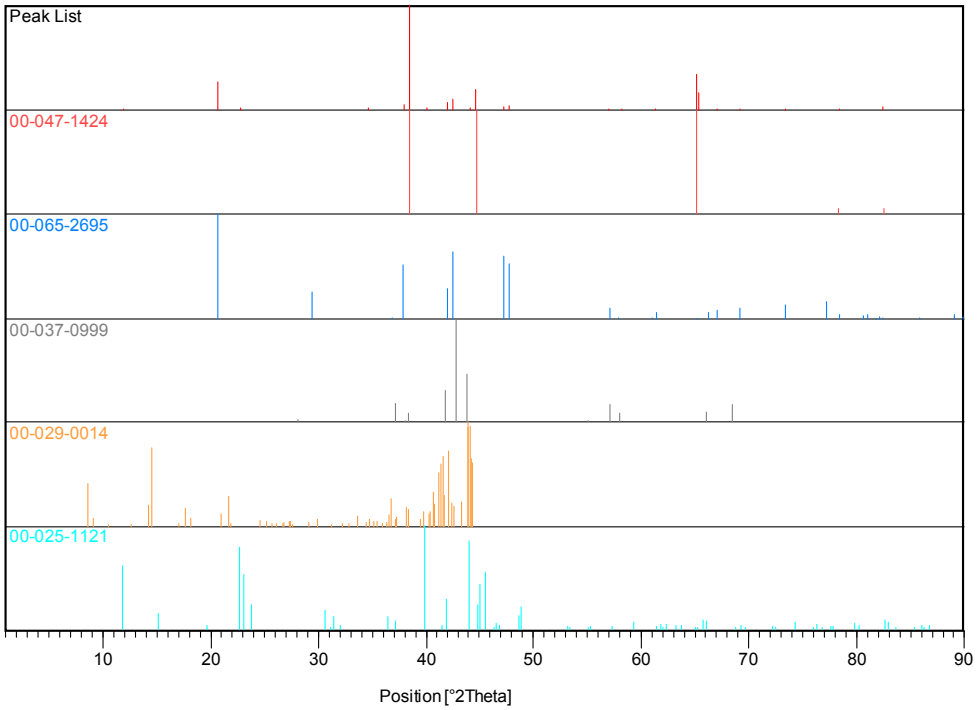
Pos. [°2Th.]	Height [cts]	FWHM [°2Th.]	d-spacing [Å]	Rel. Int. [%]	Tip width [°2Th.]	Matched by
11.8781	75.34	0.1535	7.45073	0.84	0.1560	00-025-1121
20.6710	2390.27	0.1279	4.29699	26.60	0.1300	00-065-2695; 00-029-0014
22.7575	113.30	0.1535	3.90753	1.26	0.1560	00-025-1121
34.6301	170.32	0.1023	2.59027	1.90	0.1040	00-029-0014
37.8777	412.77	0.1791	2.37532	4.59	0.1820	00-065-2695; 00-037-0999; 00-029-0014
38.4588	8987.56	0.2047	2.34076	100.00	0.2080	00-047-1424; 00-037-0999
40.0021	198.52	0.2047	2.25394	2.21	0.2080	00-029-0014; 00-025-1121
42.0577	640.61	0.2047	2.14841	7.13	0.2080	00-065-2695; 00-029-0014; 00-025-1121
42.5625	931.90	0.1791	2.12409	10.37	0.1820	00-065-2695; 00-037-0999; 00-029-0014
44.1363	160.23	0.1791	2.05194	1.78	0.1820	00-029-0014; 00-025-1121
44.7022	1732.74	0.2303	2.02727	19.28	0.2340	00-047-1424
47.3096	219.68	0.1791	1.92144	2.44	0.1820	00-065-2695
47.7346	387.33	0.2558	1.90532	4.31	0.2600	00-065-2695

57.0222	51.59	0.3582	1.61509	0.57	0.3640	00-065-2695; 00-037-0999
58.1841	51.77	0.3070	1.58558	0.58	0.3120	00-065-2695; 00-037-0999
61.3165	59.56	0.3070	1.51188	0.66	0.3120	00-065-2695
65.1036	3021.42	0.1248	1.43162	33.62	0.1040	00-047-1424; 00-065-2695; 00-025-1121
65.3155	1438.32	0.0936	1.43100	16.00	0.0780	
67.0590	93.72	0.2496	1.39455	1.04	0.2080	00-065-2695
69.1376	68.75	0.3120	1.35761	0.76	0.2600	00-065-2695; 00-025-1121
73.3879	35.86	0.7488	1.28912	0.40	0.6240	00-065-2695
78.3916	55.28	0.6240	1.21888	0.62	0.5200	00-047-1424; 00-065-2695
82.4677	213.07	0.1248	1.16865	2.37	0.1040	00-047-1424; 00-065-2695; 00-025-1121

Identified Patterns List: (Bookmark4)

Visible	Ref. Code	Score	Compound Name	Displacement [°2Th.]	Scale Factor	Chemical Formula
*	00-047-1424	58	Chromium Carbide	-0.191	0.340	Cr C
*	00-065-2695	62	Aluminum Copper	-0.062	0.132	Al2 Cu
*	00-037-0999	25	Iron Carbide	0.070	0.010	Fe2 C
*	00-029-0014	29	Aluminum Chromium	0.130	0.019	Al13 Cr2
*	00-025-1121	18	Aluminum Copper Iron	-0.108	0.011	Al7 Cu2 Fe

Plot of Identified Phases: (Bookmark 5)



Document History: **(Bookmark 6)**

Insert Measurement:
- Scan name = "BLANK-~1.RAW"
- Modification time = "2012/01/11 11:21:26 AM"
- Modification editor = "Anthony"

Interpolate Step Size:
- Step Size = "Derived"
- Modification time = "2012/01/11 11:21:26 AM"
- Modification editor = "Anthony"

Smooth:
- Type of smoothing = "Polynomial"
- Polynomial type = "Cubic"
- Convolution range = "9"
- Modification time = "2012/01/11 11:21:40 AM"
- Modification editor = "Anthony"

Search Peaks:
- Minimum significance = "1.50"
- Minimum tip width = "0.01"
- Maximum tip width = "1.00"
- Peak base width = "2.00"
- Method = "Minimum 2nd derivative"
- Modification time = "2012/01/11 11:21:44 AM"
- Modification editor = "Anthony"

Search-Match:
- Data source = "Profile and peak list"
- Restriction = "Restriction set"
- Description = "Default - All ref. patterns possible"
- All of: elements = "C, Na, Mg, Al, Cr, Mn, Fe, Ni, Cu"
- At least one of: elements = ""

- None of: elements = "H, He, Li, Be, B, N, O, F, Ne, Si, P, S, Cl, Ar, K, Ca, Sc, Ti, V, Co, Zn, Ga, Ge, As, Se, Br, Kr, Rb, Sr, Y, Zr, Nb, Mo, Tc, Ru, Rh, Pd, Ag, Cd, In, Sn, Sb, Te, I, Xe, Cs, Ba, La, Ce, Pr, Nd, Pm, Sm, Eu, Gd, Tb, Dy, Ho, Er, Tm, Yb, Lu, Hf, Ta, W, Re, Os, Ir, Pt, Au, Hg, Tl, Pb, Bi, Po, At, Rn, Fr, Ra, Ac, Th, Pa, U, Np, Pu, Am, Cm, Bk, Cf, Es, Fm, Md, No, Lr, D, T"

- Maximum no. of elements = "9"

- Skip marked as deleted by ICDD = "No"

- Skip marked as deleted by a user = "No"

- Quality marks set = ""

- Subfiles = ""

- Scoring schema = "Multi phase"

- Auto residue = "Yes"

- Match intensity = "Yes"

- Demote unmatched strong = "Yes"

- Allow pattern shift = "Yes"

- Two theta shift = "0"

- Identify = "Yes"

- Max. no. of accepted patterns = "20"

- Minimum score = "50"

- Search depth = "10"

- Min. new lines / total lines = "100"

- Minimum new lines = "5"

- Minimum scale factor = "0.1"

- Modification time = "2012/01/11 11:21:54 AM"

- Modification editor = "Anthony"

Search-Match:

- Data source = "Profile and peak list"

- Restriction = "Restriction set"

- Description = "Default - All ref. patterns possible"

- All of: elements = ""

- At least one of: elements = "C, Na, Mg, Al, Cr, Mn, Fe, Ni, Cu"

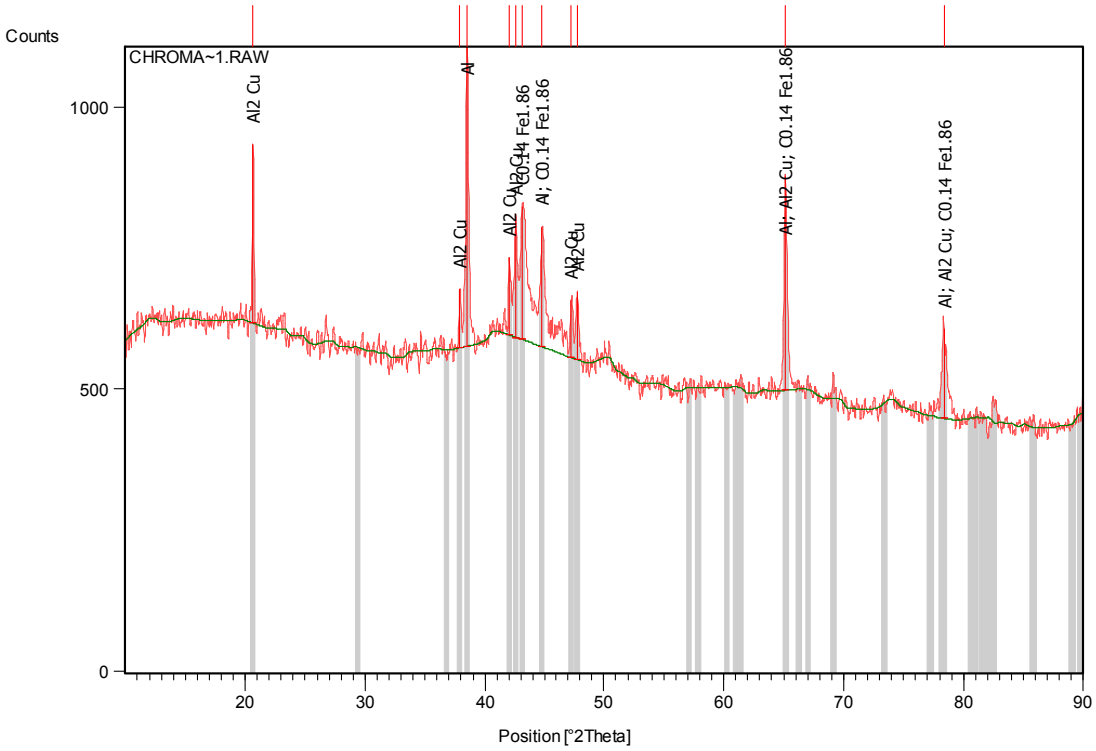
- None of: elements = "H, He, Li, Be, B, N, O, F, Ne, Si, P, S, Cl, Ar, K, Ca, Sc, Ti, V, Co, Zn, Ga, Ge, As, Se, Br, Kr, Rb, Sr, Y, Zr, Nb, Mo, Tc, Ru, Rh, Pd, Ag, Cd, In, Sn, Sb, Te, I, Xe, Cs, Ba, La, Ce, Pr, Nd, Pm, Sm, Eu, Gd, Tb, Dy, Ho, Er, Tm, Yb, Lu, Hf, Ta, W, Re, Os, Ir, Pt, Au, Hg, Tl, Pb, Bi, Po, At, Rn, Fr, Ra, Ac, Th, Pa, U, Np, Pu, Am, Cm, Bk, Cf, Es, Fm, Md, No, Lr, D, T"

- Maximum no. of elements = "9"
- Skip marked as deleted by ICDD = "No"
- Skip marked as deleted by a user = "No"
- Quality marks set = ""
- Subfiles = ""
- Scoring schema = "Multi phase"
- Auto residue = "Yes"
- Match intensity = "Yes"
- Demote unmatched strong = "Yes"
- Allow pattern shift = "Yes"
- Two theta shift = "0"
- Identify = "Yes"
- Max. no. of accepted patterns = "20"
- Minimum score = "50"
- Search depth = "10"
- Min. new lines / total lines = "100"
- Minimum new lines = "5"
- Minimum scale factor = "0.1"
- Modification time = "2012/01/11 11:26:39 AM"
- Modification editor = "Anthony"

Anchor Scan Parameters: (Bookmark1)

Sample Identification	**Sample exposed to Sodium Chromate (Na_2CrO_4)**
Measurement Date / Time	01/10/12 14:12:26
Raw Data Origin	BRUKER-binary V3 (.RAW)
Scan Axis	Gonio
Start Position [°2Th.]	10.0020
End Position [°2Th.]	90.0040
Step Size [°2Th.]	0.0260
Scan Step Time [s]	37.0000
Scan Type	CONTINUOUS
Offset [°2Th.]	0.0000
Divergence Slit Type	Fixed
Divergence Slit Size [°]	1.0000
Specimen Length [mm]	10.00
Receiving Slit Size [mm]	0.1000
Measurement Temperature [°C]	25.00
Anode Material	Cu
Generator Settings	30 kV, 10 mA
Diffractometer Type	Unknown
Goniometer Radius [mm]	141.00
Dist. Focus-Diverg. Slit [mm]	91.00
Incident Beam Monochromator	No
Spinning	No

Graphics: (Bookmark2)



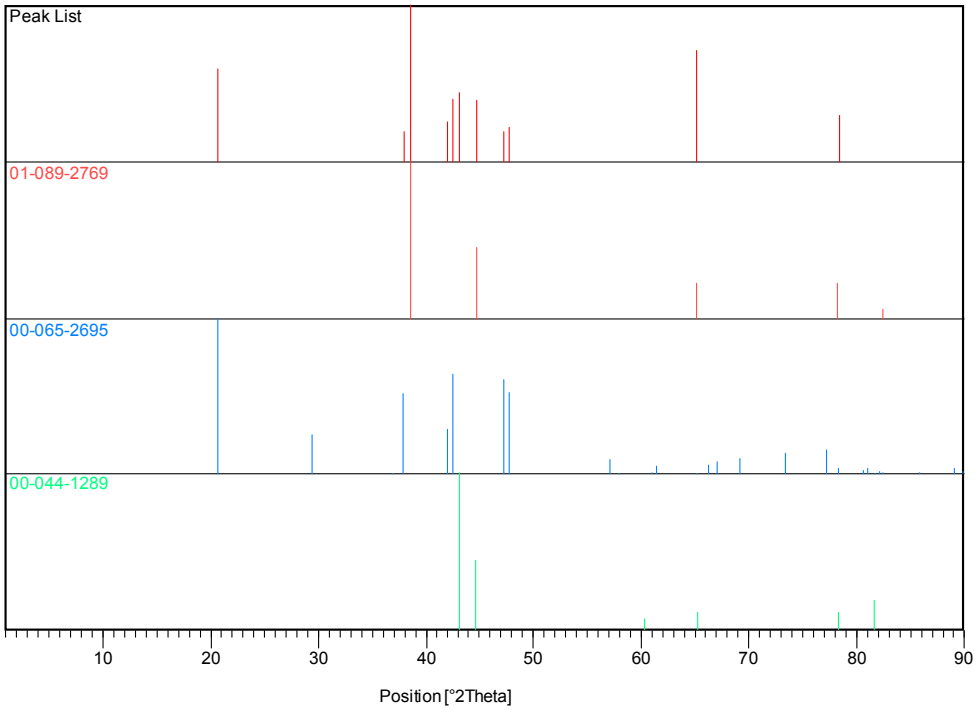
Peak List: (Bookmark 3)

Pos. [°2Th.]	Height [cts]	FWHM [°2Th.]	d-spacing [Å]	Rel. Int. [%]	Tip width [°2Th.]	Matched by
20.6592	315.41	0.1279	4.29943	59.20	0.1300	00-065-2695
37.9098	102.94	0.1535	2.37339	19.32	0.1560	00-065-2695
38.5007	532.74	0.1279	2.33831	100.00	0.1300	01-089-2769
42.0427	136.17	0.1535	2.14914	25.56	0.1560	00-065-2695
42.5718	214.30	0.1535	2.12365	40.23	0.1560	00-065-2695
43.1037	233.55	0.3582	2.09867	43.84	0.3640	00-044-1289
44.7556	210.71	0.2558	2.02497	39.55	0.2600	01-089-2769; 00-044-1289
47.2965	101.26	0.2047	1.92195	19.01	0.2080	00-065-2695
47.8152	119.15	0.2047	1.90230	22.37	0.2080	00-065-2695
65.1344	380.30	0.1535	1.43219	71.38	0.1560	01-089-2769; 00-065-2695; 00-044-1289
78.3751	158.08	0.3744	1.21910	29.67	0.3120	01-089-2769; 00-065-2695; 00-044-1289

Identified Patterns List: (Bookmark4)

Visible	Ref. Code	Score	Compound Name	Displacement [°2Th.]	Scale Factor	Chemical Formula
*	01-089-2769	67	Aluminum	0.018	1.084	Al
*	00-065-2695	61	Aluminum Copper	-0.069	0.471	Al2 Cu
*	00-044-1289	43	martensite	-0.321	0.488	C0.14 Fe1.86

Plot of Identified Phases: (Bookmark 5)



Document History: (Bookmark 6)

Insert Measurement:

- Scan name = "CHROMA~1.RAW"
- Modification time = "2012/01/11 11:22:04 AM"
- Modification editor = "Anthony"

Interpolate Step Size:

- Step Size = "Derived"
- Modification time = "2012/01/11 11:22:04 AM"
- Modification editor = "Anthony"

Smooth:

- Type of smoothing = "Polynomial"
- Polynomial type = "Cubic"
- Convolution range = "9"
- Modification time = "2012/01/11 11:22:17 AM"
- Modification editor = "Anthony"

Search Peaks:

- Minimum significance = "1.50"
- Minimum tip width = "0.01"
- Maximum tip width = "1.00"
- Peak base width = "2.00"
- Method = "Minimum 2nd derivative"
- Modification time = "2012/01/11 11:22:21 AM"
- Modification editor = "Anthony"

Search-Match:

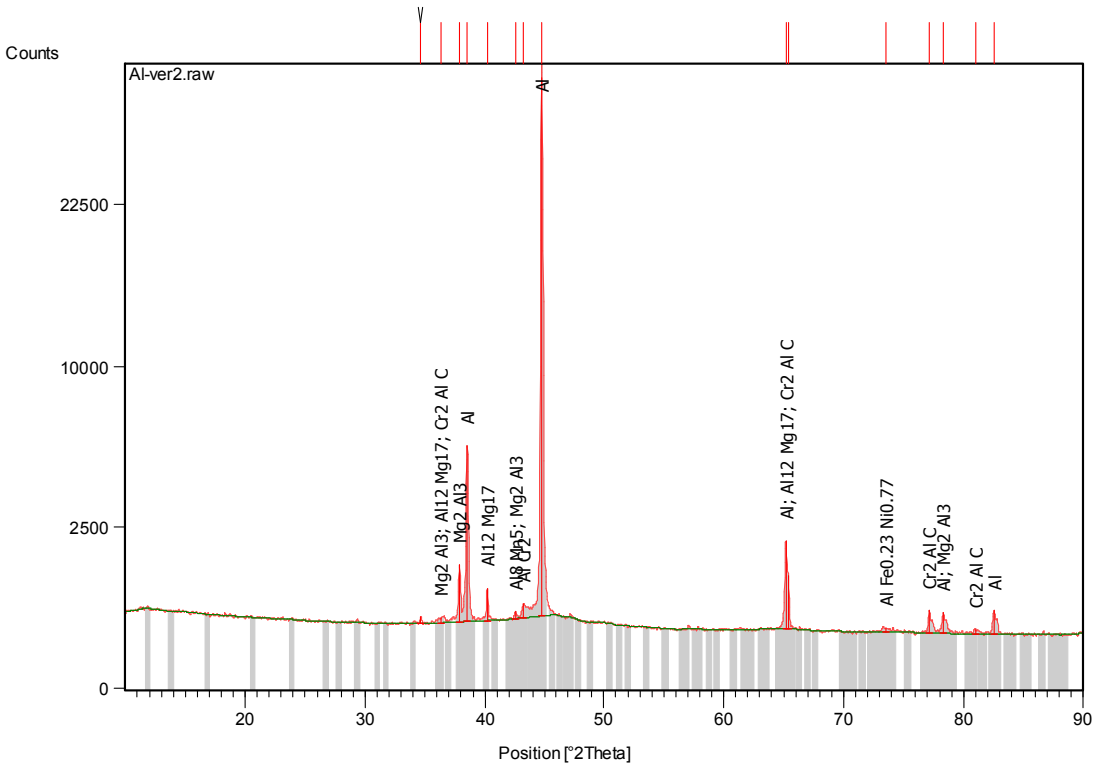
- Data source = "Profile and peak list"
- Restriction = "Restriction set"
- Description = "Default - All ref. patterns possible"
- All of: elements = ""
- At least one of: elements = "C, Na, Mg, Al, Cr, Mn, Fe, Ni, Cu"

- None of: elements = "H, He, Li, Be, B, N, O, F, Ne, Si, P, S, Cl, Ar, K, Ca, Sc, Ti, V, Co, Zn, Ga, Ge, As, Se, Br, Kr, Rb, Sr, Y, Zr, Nb, Mo, Tc, Ru, Rh, Pd, Ag, Cd, In, Sn, Sb, Te, I, Xe, Cs, Ba, La, Ce, Pr, Nd, Pm, Sm, Eu, Gd, Tb, Dy, Ho, Er, Tm, Yb, Lu, Hf, Ta, W, Re, Os, Ir, Pt, Au, Hg, Tl, Pb, Bi, Po, At, Rn, Fr, Ra, Ac, Th, Pa, U, Np, Pu, Am, Cm, Bk, Cf, Es, Fm, Md, No, Lr, D, T"
- Maximum no. of elements = "9"
- Skip marked as deleted by ICDD = "No"
- Skip marked as deleted by a user = "No"
- Quality marks set = ""
- Subfiles = ""
- Scoring schema = "Multi phase"
- Auto residue = "Yes"
- Match intensity = "Yes"
- Demote unmatched strong = "Yes"
- Allow pattern shift = "Yes"
- Two theta shift = "0"
- Identify = "Yes"
- Max. no. of accepted patterns = "20"
- Minimum score = "50"
- Search depth = "10"
- Min. new lines / total lines = "100"
- Minimum new lines = "5"
- Minimum scale factor = "0.1"
- Modification time = "2012/01/11 11:23:32 AM"
- Modification editor = "Anthony"

Anchor Scan Parameters: (Bookmark1)

Sample Identification	**Sample exposed to NaCl**
Measurement Date / Time	01/10/12 13:46:18
Raw Data Origin	BRUKER-binary V3 (.RAW)
Scan Axis	Gonio
Start Position [°2Th.]	10.0020
End Position [°2Th.]	90.0040
Step Size [°2Th.]	0.0260
Scan Step Time [s]	37.0000
Scan Type	CONTINUOUS
Offset [°2Th.]	0.0000
Divergence Slit Type	Fixed
Divergence Slit Size [°]	1.0000
Specimen Length [mm]	10.00
Receiving Slit Size [mm]	0.1000
Measurement Temperature [°C]	25.00
Anode Material	Cu
Generator Settings	30 kV, 10 mA
Diffractometer Type	Unknown
Goniometer Radius [mm]	141.00
Dist. Focus-Diverg. Slit [mm]	91.00
Incident Beam Monochromator	No
Spinning	No

Graphics: (Bookmark2)



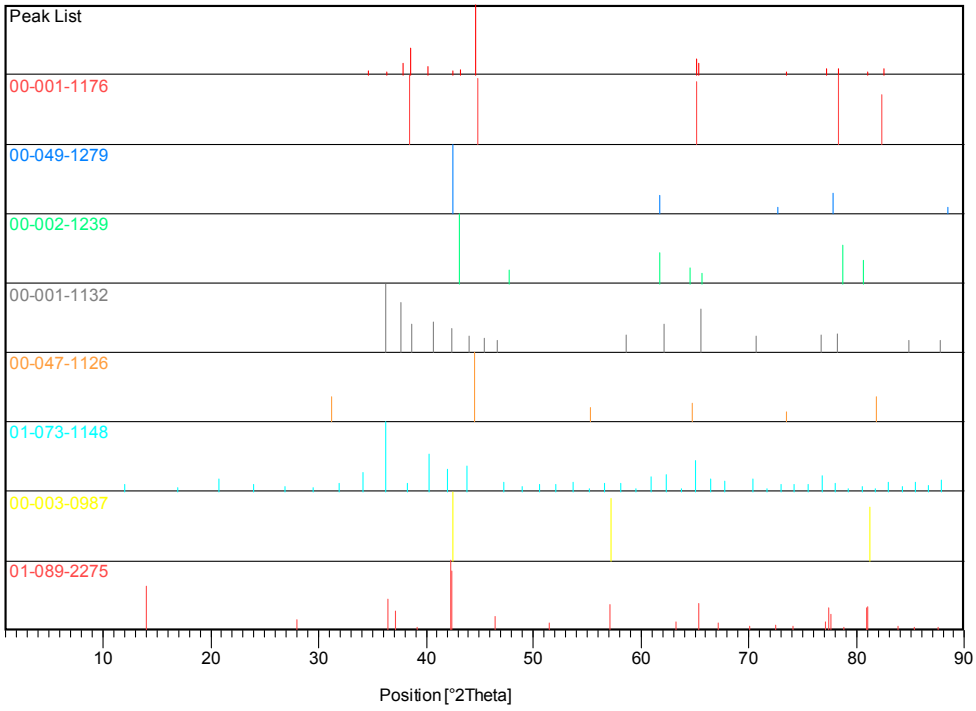
Peak List: (Bookmark 3)

Pos. [°2Th.]	Height [cts]	FWHM [°2Th.]	d-spacing [Å]	Rel. Int. [%]	Tip width [°2Th.]	Matched by
34.6471	93.78	0.1535	2.58904	0.27	0.1560	
36.3263	67.10	0.6140	2.47312	0.19	0.6240	00-001-1132; 01-073-1148; 01-089-2275
37.8579	1027.57	0.1535	2.37652	2.91	0.1560	00-001-1132
38.5018	5183.51	0.1791	2.33824	14.68	0.1820	00-001-1176
40.1846	511.89	0.1023	2.24412	1.45	0.1040	01-073-1148
42.5316	98.01	0.1535	2.12556	0.28	0.1560	00-049-1279; 00-001-1132
43.2170	210.14	0.2558	2.09343	0.59	0.2600	00-002-1239
44.6889	35319.87	0.1791	2.02784	100.00	0.1820	00-001-1176
65.1793	1739.50	0.1560	1.43014	4.92	0.1300	00-001-1176; 01-073-1148; 01-089-2275
65.3935	871.38	0.0936	1.42948	2.47	0.0780	
73.4956	43.41	0.9984	1.28749	0.12	0.8320	00-047-1126
77.1512	297.75	0.1560	1.23535	0.84	0.1300	01-089-2275
78.3075	260.10	0.1872	1.21998	0.74	0.1560	00-001-1176; 00-001-1132
81.0671	43.98	0.7488	1.18527	0.12	0.6240	01-089-2275
82.5343	305.09	0.1872	1.16788	0.86	0.1560	00-001-1176

Identified Patterns List: **(Bookmark4)**

Visible	Ref. Code	Score	Compound Name	Displacement [°2Th.]	Scale Factor	Chemical Formula
*	00-001-1176	46	Aluminum	-0.012	0.064	Al
*	00-049-1279	42	Aluminum Manganese	0.039	0.002	Al8 Mn5
*	00-002-1239	42	Aluminum Chromium	-0.084	0.004	Al Cr2
*	00-001-1132	27	Magnesium Aluminum	-0.135	0.004	Mg2 Al3
*	00-047-1126	28	Aluminum Iron Nickel	0.185	0.104	Al Fe0.23 Ni0.77
*	01-073-1148	30	Aluminum Magnesium	0.134	0.008	Al12 Mg17
*	00-003-0987	37	Copper Magnesium	-0.311	0.002	Cu2 Mg
*	01-089-2275	16	Chromium Aluminum Carbide	0.204	0.002	Cr2 Al C

Plot of Identified Phases: (Bookmark 5)



Document History: (Bookmark 6)

Insert Measurement:

- Scan name = "Al-ver2.raw"
- Modification time = "2012/01/11 11:17:21 AM"
- Modification editor = "Anthony"

Interpolate Step Size:

- Step Size = "Derived"
- Modification time = "2012/01/11 11:17:21 AM"
- Modification editor = "Anthony"

Smooth:

- Type of smoothing = "Polynomial"
- Polynomial type = "Cubic"
- Convolution range = "9"
- Modification time = "2012/01/11 11:17:40 AM"
- Modification editor = "Anthony"

Search Peaks:

- Minimum significance = "1.50"
- Minimum tip width = "0.01"
- Maximum tip width = "1.00"
- Peak base width = "2.00"
- Method = "Minimum 2nd derivative"
- Modification time = "2012/01/11 11:18:00 AM"
- Modification editor = "Anthony"

Search-Match:

- Data source = "Profile and peak list"
- Restriction = "Restriction set"
- Description = "Default - All ref. patterns possible"
- All of: elements = "C, Na, Mg, Al, Cr, Mn, Fe, Ni, Cu"
- At least one of: elements = ""

- None of: elements = "H, He, Li, Be, B, N, O, F, Ne, Si, P, S, Cl, Ar, K, Ca, Sc, Ti, V, Co, Zn, Ga, Ge, As, Se, Br, Kr, Rb, Sr, Y, Zr, Nb, Mo, Tc, Ru, Rh, Pd, Ag, Cd, In, Sn, Sb, Te, I, Xe, Cs, Ba, La, Ce, Pr, Nd, Pm, Sm, Eu, Gd, Tb, Dy, Ho, Er, Tm, Yb, Lu, Hf, Ta, W, Re, Os, Ir, Pt, Au, Hg, Tl, Pb, Bi, Po, At, Rn, Fr, Ra, Ac, Th, Pa, U, Np, Pu, Am, Cm, Bk, Cf, Es, Fm, Md, No, Lr, D, T"

- Maximum no. of elements = "9"

- Skip marked as deleted by ICDD = "No"

- Skip marked as deleted by a user = "No"

- Quality marks set = ""

- Subfiles = ""

- Scoring schema = "Multi phase"

- Auto residue = "Yes"

- Match intensity = "Yes"

- Demote unmatched strong = "Yes"

- Allow pattern shift = "Yes"

- Two theta shift = "0"

- Identify = "Yes"

- Max. no. of accepted patterns = "20"

- Minimum score = "50"

- Search depth = "10"

- Min. new lines / total lines = "100"

- Minimum new lines = "5"

- Minimum scale factor = "0.1"

- Modification time = "2012/01/11 11:21:26 AM"

- Modification editor = "Anthony"

Search-Match:

- Data source = "Profile and peak list"

- Restriction = "Restriction set"

- Description = "Default - All ref. patterns possible"

- All of: elements = ""

- At least one of: elements = "C, Na, Mg, Al, Cr, Mn, Fe, Ni, Cu"

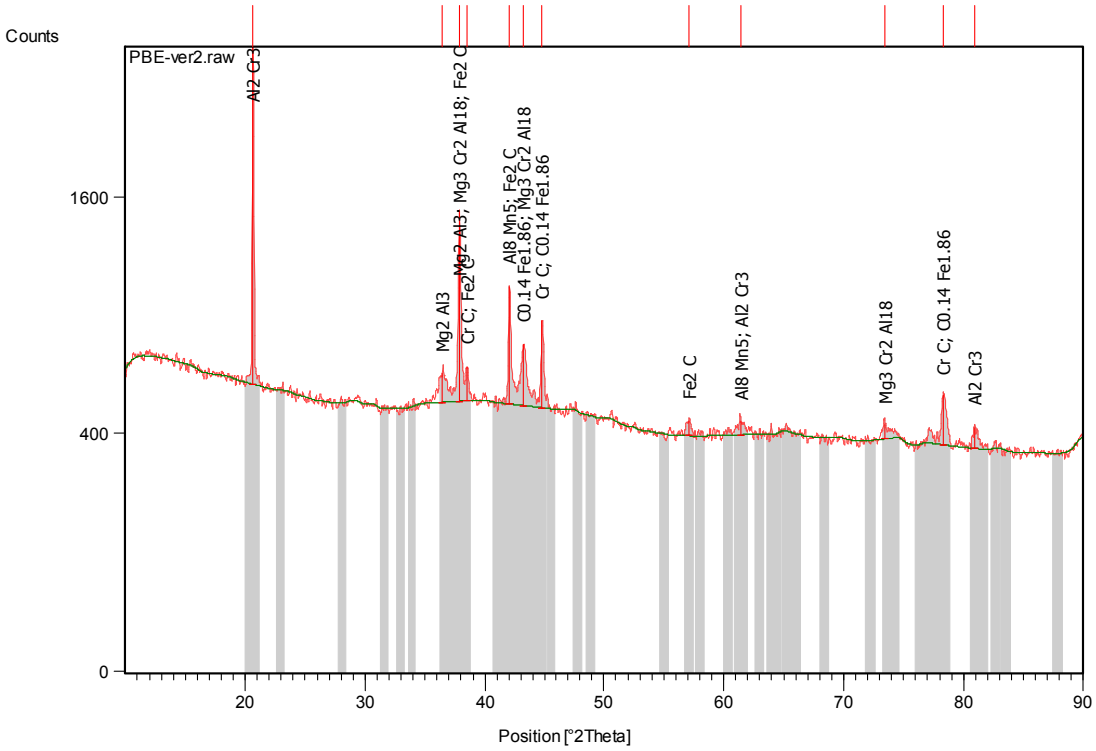
- None of: elements = "H, He, Li, Be, B, N, O, F, Ne, Si, P, S, Cl, Ar, K, Ca, Sc, Ti, V, Co, Zn, Ga, Ge, As, Se, Br, Kr, Rb, Sr, Y, Zr, Nb, Mo, Tc, Ru, Rh, Pd, Ag, Cd, In, Sn, Sb, Te, I, Xe, Cs, Ba, La, Ce, Pr, Nd, Pm, Sm, Eu, Gd, Tb, Dy, Ho, Er, Tm, Yb, Lu, Hf, Ta, W, Re, Os, Ir, Pt, Au, Hg, Tl, Pb, Bi, Po, At, Rn, Fr, Ra, Ac, Th, Pa, U, Np, Pu, Am, Cm, Bk, Cf, Es, Fm, Md, No, Lr, D, T"

- Maximum no. of elements = "9"
- Skip marked as deleted by ICDD = "No"
- Skip marked as deleted by a user = "No"
- Quality marks set = ""
- Subfiles = ""
- Scoring schema = "Multi phase"
- Auto residue = "Yes"
- Match intensity = "Yes"
- Demote unmatched strong = "Yes"
- Allow pattern shift = "Yes"
- Two theta shift = "0"
- Identify = "Yes"
- Max. no. of accepted patterns = "20"
- Minimum score = "50"
- Search depth = "10"
- Min. new lines / total lines = "100"
- Minimum new lines = "5"
- Minimum scale factor = "0.1"
- Modification time = "2012/01/11 11:30:59 AM"
- Modification editor = "Anthony"

Anchor Scan Parameters: (Bookmark1)

Sample Identification	**Sample exposed to PBE**
Measurement Date / Time	01/10/12 13:18:08
Raw Data Origin	BRUKER-binary V3 (.RAW)
Scan Axis	Gonio
Start Position [°2Th.]	10.0020
End Position [°2Th.]	90.0040
Step Size [°2Th.]	0.0260
Scan Step Time [s]	37.0000
Scan Type	CONTINUOUS
Offset [°2Th.]	0.0000
Divergence Slit Type	Fixed
Divergence Slit Size [°]	1.0000
Specimen Length [mm]	10.00
Receiving Slit Size [mm]	0.1000
Measurement Temperature [°C]	25.00
Anode Material	Cu
Generator Settings	30 kV, 10 mA
Diffractometer Type	Unknown
Goniometer Radius [mm]	141.00
Dist. Focus-Diverg. Slit [mm]	91.00
Incident Beam Monochromator	No
Spinning	No

Graphics: (Bookmark2)



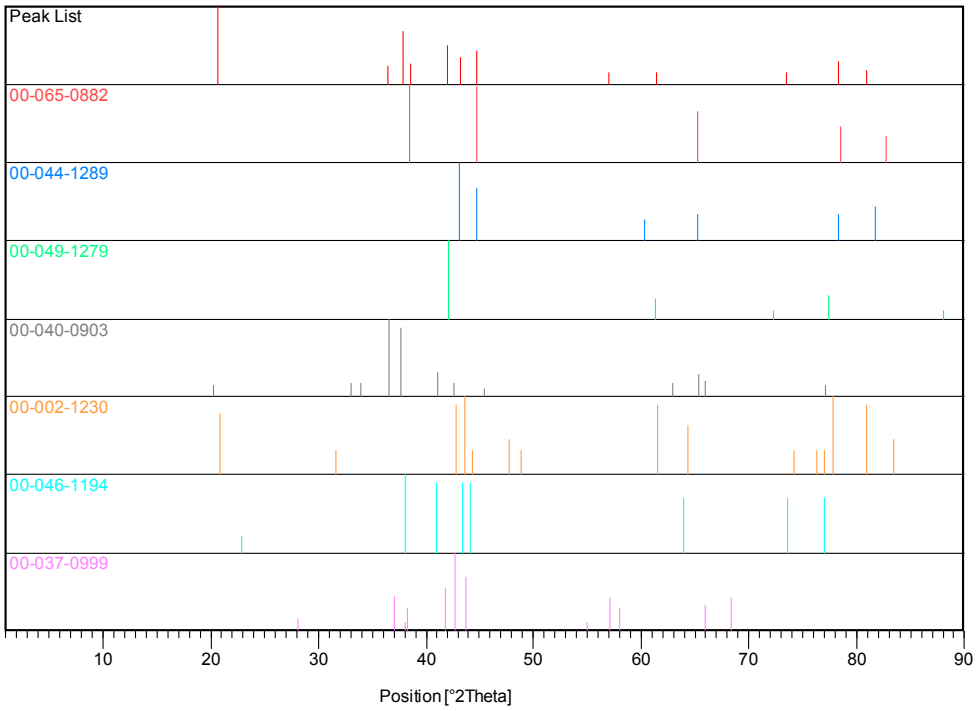
Peak List: (Bookmark 3)

Pos. [°2Th.]	Height [cts]	FWHM [°2Th.]	d-spacing [Å]	Rel. Int. [%]	Tip width [°2Th.]	Matched by
20.6552	2199.45	0.1279	4.30025	100.00	0.1300	00-002-1230
36.4220	121.06	0.5117	2.46684	5.50	0.5200	00-040-0903
37.8599	988.22	0.1791	2.37640	44.93	0.1820	00-040-0903; 00-046-1194; 00-037-0999
38.4967	143.99	0.2303	2.33854	6.55	0.2340	00-065-0882; 00-037-0999
42.0373	545.30	0.1535	2.14940	24.79	0.1560	00-049-1279; 00-037-0999
43.2326	260.01	0.3582	2.09271	11.82	0.3640	00-044-1289; 00-046-1194
44.7711	383.25	0.2047	2.02431	17.42	0.2080	00-065-0882; 00-044-1289
57.0606	50.71	0.4093	1.61410	2.31	0.4160	00-037-0999
61.4010	46.56	0.6140	1.51000	2.12	0.6240	00-049-1279; 00-002-1230
73.4667	49.42	0.6140	1.28899	2.25	0.6240	00-046-1194
78.2714	174.35	0.2814	1.22145	7.93	0.2860	00-065-0882; 00-044-1289
80.9654	67.66	0.4992	1.18650	3.08	0.4160	00-002-1230

Identified Patterns List: (Bookmark4)

Visible	Ref. Code	Score	Compound Name	Displacement [°2Th.]	Scale Factor	Chemical Formula
*	00-065-0882	51	Chromium Carbide	-0.208	0.116	Cr C
*	00-044-1289	49	martensite	-0.263	0.170	C0.14 Fe1.86
*	00-049-1279	47	Aluminum Manganese	-0.380	0.220	Al8 Mn5
*	00-040-0903	36	Aluminum Magnesium	0.199	0.057	Mg2 Al3
*	00-002-1230	30	Aluminum Chromium	0.215	0.034	Al2 Cr3
*	00-046-1194	25	Aluminum Chromium Magnesium	0.219	0.052	Mg3 Cr2 Al18
*	00-037-0999	24	Iron Carbide	0.025	0.054	Fe2 C

Plot of Identified Phases: (Bookmark 5)



Document History: (Bookmark 6)

Insert Measurement:

- Scan name = "PBE-ver2.raw"
- Modification time = "2012/01/11 11:50:58 AM"
- Modification editor = "Anthony"

Interpolate Step Size:

- Step Size = "Derived"
- Modification time = "2012/01/11 11:50:58 AM"
- Modification editor = "Anthony"

Smooth:

- Type of smoothing = "Polynomial"
- Polynomial type = "Cubic"
- Convolution range = "9"
- Modification time = "2012/01/11 11:55:33 AM"
- Modification editor = "Anthony"

Search Peaks:

- Minimum significance = "1.50"
- Minimum tip width = "0.01"
- Maximum tip width = "1.00"
- Peak base width = "2.00"
- Method = "Minimum 2nd derivative"
- Modification time = "2012/01/11 11:55:37 AM"
- Modification editor = "Anthony"

Search-Match:

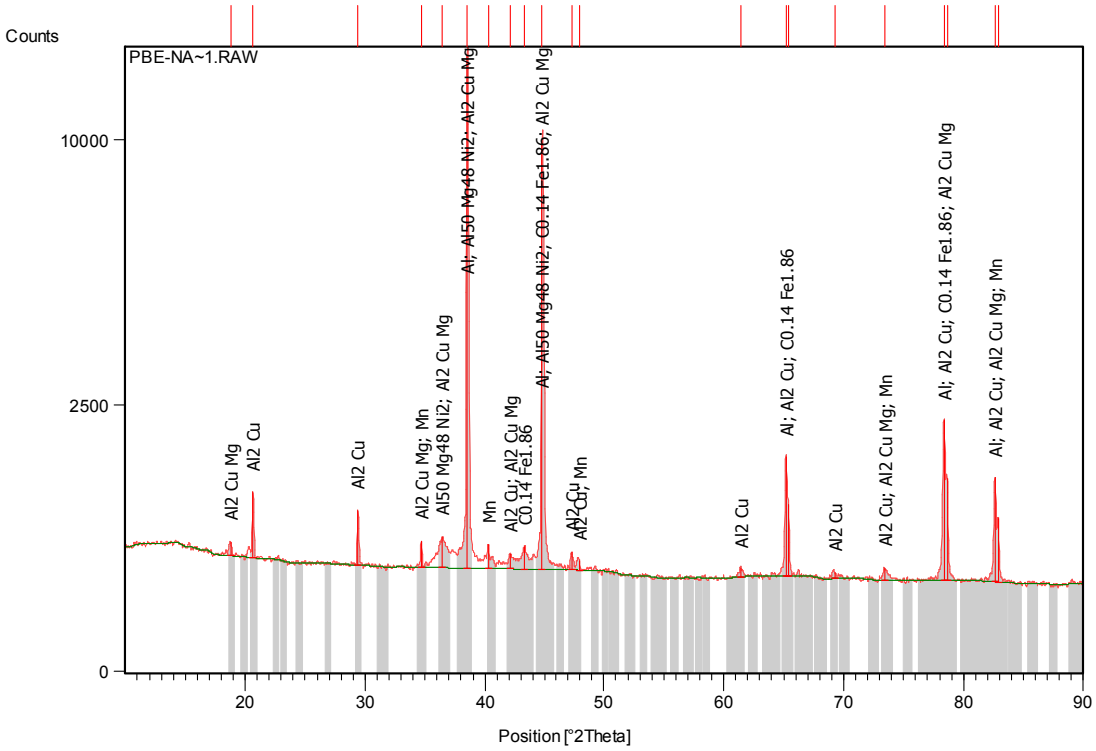
- Data source = "Profile and peak list"
- Restriction = "Restriction set"
- Description = "Default - All ref. patterns possible"
- All of: elements = ""
- At least one of: elements = "C, Na, Mg, Al, Cr, Mn, Fe, Ni, Cu"

- None of: elements = "H, He, Li, Be, B, N, O, F, Ne, Si, P, S, Cl, Ar, K, Ca, Sc, Ti, V, Co, Zn, Ga, Ge, As, Se, Br, Kr, Rb, Sr, Y, Zr, Nb, Mo, Tc, Ru, Rh, Pd, Ag, Cd, In, Sn, Sb, Te, I, Xe, Cs, Ba, La, Ce, Pr, Nd, Pm, Sm, Eu, Gd, Tb, Dy, Ho, Er, Tm, Yb, Lu, Hf, Ta, W, Re, Os, Ir, Pt, Au, Hg, Tl, Pb, Bi, Po, At, Rn, Fr, Ra, Ac, Th, Pa, U, Np, Pu, Am, Cm, Bk, Cf, Es, Fm, Md, No, Lr, D, T"
- Maximum no. of elements = "9"
- Skip marked as deleted by ICDD = "No"
- Skip marked as deleted by a user = "No"
- Quality marks set = ""
- Subfiles = ""
- Scoring schema = "Multi phase"
- Auto residue = "Yes"
- Match intensity = "Yes"
- Demote unmatched strong = "Yes"
- Allow pattern shift = "Yes"
- Two theta shift = "0"
- Identify = "Yes"
- Max. no. of accepted patterns = "20"
- Minimum score = "50"
- Search depth = "10"
- Min. new lines / total lines = "100"
- Minimum new lines = "5"
- Minimum scale factor = "0.1"
- Modification time = "2012/01/11 11:55:46 AM"
- Modification editor = "Anthony"

Anchor Scan Parameters: (Bookmark1)

Sample Identification	**Sample exposed to PBE+Boehmite Nanoparticles**
Measurement Date / Time	01/10/12 13:02:56
Raw Data Origin	BRUKER-binary V3 (.RAW)
Scan Axis	Gonio
Start Position [°2Th.]	10.0020
End Position [°2Th.]	90.0040
Step Size [°2Th.]	0.0260
Scan Step Time [s]	37.0000
Scan Type	CONTINUOUS
Offset [°2Th.]	0.0000
Divergence Slit Type	Fixed
Divergence Slit Size [°]	1.0000
Specimen Length [mm]	10.00
Receiving Slit Size [mm]	0.1000
Measurement Temperature [°C]	25.00
Anode Material	Cu
Generator Settings	30 kV, 10 mA
Diffractometer Type	Unknown
Goniometer Radius [mm]	141.00
Dist. Focus-Diverg. Slit [mm]	91.00
Incident Beam Monochromator	No
Spinning	No

Graphics: (Bookmark2)



Peak List: (Bookmark 3)

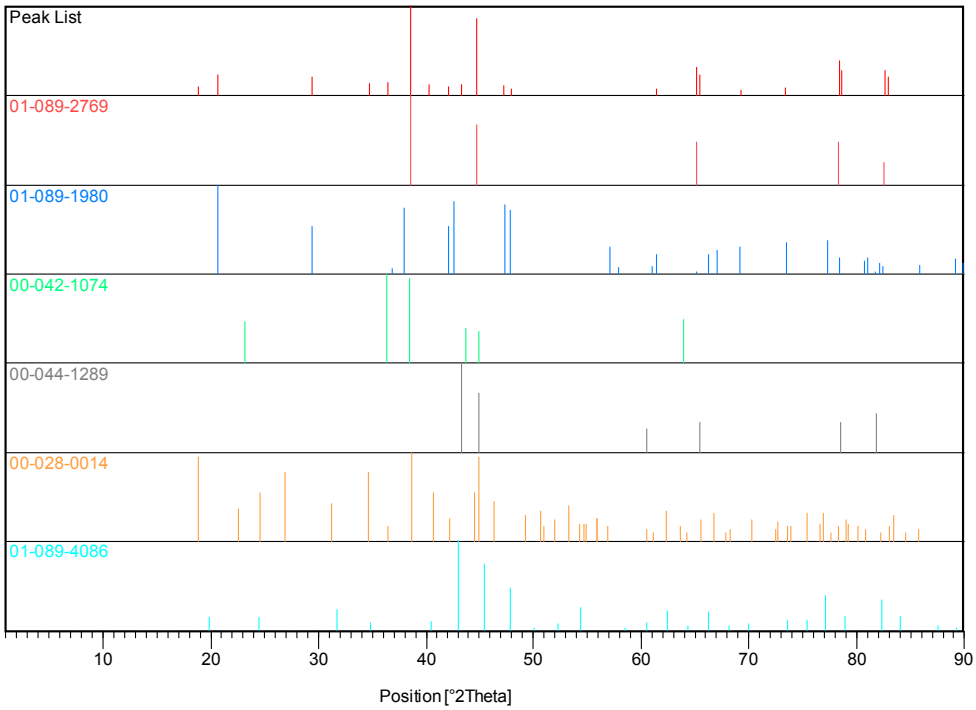
Pos. [°2Th.]	Height [cts]	FWHM [°2Th.]	d-spacing [Å]	Rel. Int. [%]	Tip width [°2Th.]	Matched by
18.7948	116.52	0.2303	4.72151	0.90	0.2340	00-028-0014
20.6531	679.69	0.1279	4.30069	5.22	0.1300	01-089-1980
29.4096	516.49	0.1279	3.03709	3.97	0.1300	01-089-1980
34.6801	213.52	0.1023	2.58665	1.64	0.1040	00-028-0014; 01-089-4086
36.4482	257.42	0.3582	2.46513	1.98	0.3640	00-042-1074; 00-028-0014
38.5237	13017.55	0.1791	2.33696	100.00	0.1820	01-089-2769; 00-042-1074; 00-028-0014
40.2613	195.27	0.1279	2.24002	1.50	0.1300	01-089-4086
42.1307	111.92	0.3070	2.14486	0.86	0.3120	01-089-1980; 00-028-0014
43.3026	177.24	0.3070	2.08949	1.36	0.3120	00-044-1289
44.7689	9586.38	0.1791	2.02440	73.64	0.1820	01-089-2769; 00-042-1074; 00-044-1289; 00-028-0014
47.3145	135.93	0.2047	1.92126	1.04	0.2080	01-089-1980
47.9517	67.53	0.2814	1.89720	0.52	0.2860	01-089-1980; 01-089-4086
61.4281	59.21	0.3070	1.50940	0.45	0.3120	01-089-1980
65.1843	1304.75	0.1560	1.43004	10.02	0.1300	01-089-2769; 01-

						089-1980; 00-044-1289
65.4029	656.79	0.1248	1.42930	5.05	0.1040	
69.2885	41.52	0.7488	1.35502	0.32	0.6240	01-089-1980
73.4008	82.32	0.3744	1.28892	0.63	0.3120	01-089-1980; 00-028-0014; 01-089-4086
78.3657	1933.24	0.1872	1.21922	14.85	0.1560	01-089-2769; 01-089-1980; 00-044-1289; 00-028-0014
78.6319	1012.34	0.1248	1.21875	7.78	0.1040	
82.6181	1041.32	0.1560	1.16691	8.00	0.1300	01-089-2769; 01-089-1980; 00-028-0014; 01-089-4086
82.8890	545.30	0.1560	1.16664	4.19	0.1300	

Identified Patterns List: (Bookmark4)

Visible	Ref. Code	Score	Compound Name	Displacement [°2Th.]	Scale Factor	Chemical Formula
*	01-089-2769	52	Aluminum	0.046	1.056	Al
*	01-089-1980	48	Khatyrkite - synthetic	0.004	0.025	Al2 Cu
*	00-042-1074	26	Aluminum Magnesium Nickel	0.346	0.084	Al50 Mg48 Ni2
*	00-044-1289	25	martensite	-0.099	0.036	C0.14 Fe1.86
*	00-028-0014	20	Aluminum Copper Magnesium	-0.357	0.297	Al2 Cu Mg
*	01-089-4086	23	Manganese	-0.026	0.007	Mn

Plot of Identified Phases: (Bookmark 5)



Document History: (Bookmark 6)

Insert Measurement:

- Scan name = "PBE-NA~1.RAW"
- Modification time = "2012/01/11 11:36:44 AM"
- Modification editor = "Anthony"

Interpolate Step Size:

- Step Size = "Derived"
- Modification time = "2012/01/11 11:36:44 AM"
- Modification editor = "Anthony"

Smooth:

- Type of smoothing = "Polynomial"
- Polynomial type = "Cubic"
- Convolution range = "9"
- Modification time = "2012/01/11 11:47:02 AM"
- Modification editor = "Anthony"

Search Peaks:

- Minimum significance = "1.50"
- Minimum tip width = "0.01"
- Maximum tip width = "1.00"
- Peak base width = "2.00"
- Method = "Minimum 2nd derivative"
- Modification time = "2012/01/11 11:47:09 AM"
- Modification editor = "Anthony"

Search-Match:

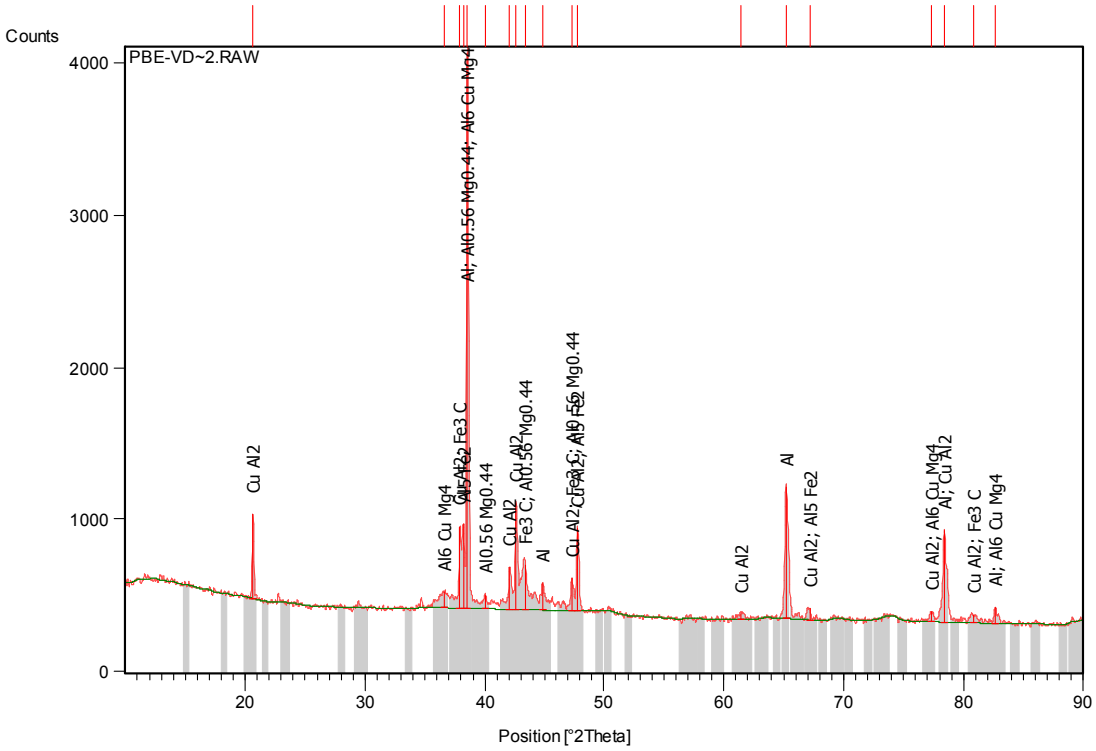
- Data source = "Profile and peak list"
- Restriction = "Restriction set"
- Description = "Default - All ref. patterns possible"
- All of: elements = ""
- At least one of: elements = "C, Na, Mg, Al, Cr, Mn, Fe, Ni, Cu"

- None of: elements = "H, He, Li, Be, B, N, O, F, Ne, Si, P, S, Cl, Ar, K, Ca, Sc, Ti, V, Co, Zn, Ga, Ge, As, Se, Br, Kr, Rb, Sr, Y, Zr, Nb, Mo, Tc, Ru, Rh, Pd, Ag, Cd, In, Sn, Sb, Te, I, Xe, Cs, Ba, La, Ce, Pr, Nd, Pm, Sm, Eu, Gd, Tb, Dy, Ho, Er, Tm, Yb, Lu, Hf, Ta, W, Re, Os, Ir, Pt, Au, Hg, Tl, Pb, Bi, Po, At, Rn, Fr, Ra, Ac, Th, Pa, U, Np, Pu, Am, Cm, Bk, Cf, Es, Fm, Md, No, Lr, D, T"
- Maximum no. of elements = "9"
- Skip marked as deleted by ICDD = "No"
- Skip marked as deleted by a user = "No"
- Quality marks set = ""
- Subfiles = ""
- Scoring schema = "Multi phase"
- Auto residue = "Yes"
- Match intensity = "Yes"
- Demote unmatched strong = "Yes"
- Allow pattern shift = "Yes"
- Two theta shift = "0"
- Identify = "Yes"
- Max. no. of accepted patterns = "20"
- Minimum score = "50"
- Search depth = "10"
- Min. new lines / total lines = "100"
- Minimum new lines = "5"
- Minimum scale factor = "0.1"
- Modification time = "2012/01/11 11:47:15 AM"
- Modification editor = "Anthony"

Anchor Scan Parameters: (Bookmark1)

Sample Identification	**Sample exposed to PBE+VDE**
Measurement Date / Time	01/10/12 14:25:26
Raw Data Origin	BRUKER-binary V3 (.RAW)
Scan Axis	Gonio
Start Position [°2Th.]	10.0020
End Position [°2Th.]	90.0040
Step Size [°2Th.]	0.0260
Scan Step Time [s]	37.0000
Scan Type	CONTINUOUS
Offset [°2Th.]	0.0000
Divergence Slit Type	Fixed
Divergence Slit Size [°]	1.0000
Specimen Length [mm]	10.00
Receiving Slit Size [mm]	0.1000
Measurement Temperature [°C]	25.00
Anode Material	Cu
Generator Settings	30 kV, 10 mA
Diffractometer Type	Unknown
Goniometer Radius [mm]	141.00
Dist. Focus-Diverg. Slit [mm]	91.00
Incident Beam Monochromator	No
Spinning	No

Graphics: (Bookmark2)



Peak List: (Bookmark 3)

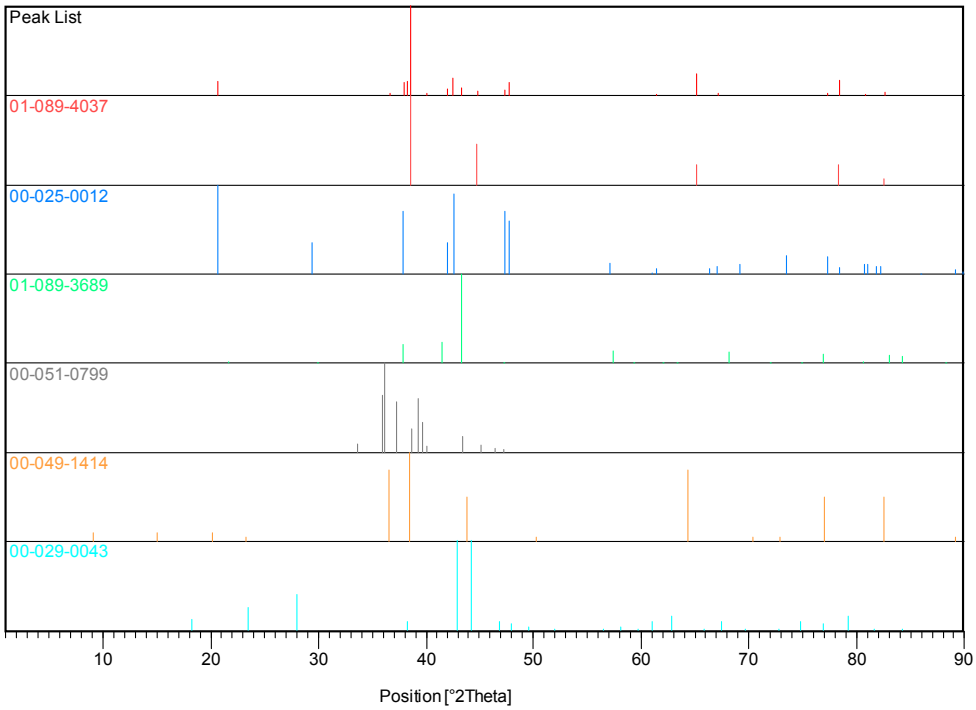
Pos. [°2Th.]	Height [cts]	FWHM [°2Th.]	d-spacing [Å]	Rel. Int. [%]	Tip width [°2Th.]	Matched by
20.6574	553.19	0.1279	4.29979	15.14	0.1300	00-025-0012
36.5860	104.31	0.8187	2.45616	2.85	0.8320	00-049-1414
37.8973	531.04	0.1023	2.37414	14.53	0.1040	00-025-0012; 01-089-3689
38.1868	553.50	0.1535	2.35680	15.14	0.1560	00-029-0043
38.5326	3654.74	0.1791	2.33644	100.00	0.1820	01-089-4037; 00-051-0799; 00-049-1414
39.9882	89.90	0.3070	2.25469	2.46	0.3120	00-051-0799
42.0639	279.65	0.1279	2.14811	7.65	0.1300	00-025-0012
42.5830	696.89	0.1791	2.12312	19.07	0.1820	00-025-0012
43.3869	295.16	0.2814	2.08562	8.08	0.2860	01-089-3689; 00-051-0799
44.8239	177.16	0.1535	2.02204	4.85	0.1560	01-089-4037
47.3428	212.39	0.1535	1.92017	5.81	0.1560	00-025-0012; 01-089-3689; 00-051-0799
47.7761	543.65	0.1535	1.90377	14.88	0.1560	00-025-0012; 00-029-0043
61.4025	40.00	0.6140	1.50997	1.09	0.6240	00-025-0012
65.1872	860.85	0.1791	1.43116	23.55	0.1820	01-089-4037
67.1849	73.41	0.3582	1.39338	2.01	0.3640	00-025-

						0012; 00-029-0043
77.3350	64.42	0.3070	1.23389	1.76	0.3120	00-025-0012; 00-049-1414
78.3995	602.28	0.1791	1.21978	16.48	0.1820	01-089-4037; 00-025-0012
80.8564	52.28	0.6140	1.18880	1.43	0.6240	00-025-0012; 01-089-3689
82.6638	107.89	0.2184	1.16638	2.95	0.1820	01-089-4037; 00-049-1414

Identified Patterns List: (Bookmark4)

Visible	Ref. Code	Score	Compound Name	Displacement [°2Th.]	Scale Factor	Chemical Formula
*	01-089-4037	53	Aluminum	0.045	0.827	Al
*	00-025-0012	63	Khatyrkite, syn	0.007	0.159	Cu Al2
*	01-089-3689	34	Iron Carbide	0.109	0.072	Fe3 C
*	00-051-0799	22	Aluminum Magnesium	0.272	0.050	Al0.56 Mg0.44
*	00-049-1414	7	Aluminum Copper Magnesium	0.207	0.310	Al6 Cu Mg4
*	00-029-0043	19	Aluminum Iron	0.121	0.035	Al5 Fe2

Plot of Identified Phases: (Bookmark 5)



Document History: (Bookmark 6)

Insert Measurement:

- Scan name = "PBE-VD~2.RAW"
- Modification time = "2012/01/11 11:36:51 AM"
- Modification editor = "Anthony"

Interpolate Step Size:

- Step Size = "Derived"
- Modification time = "2012/01/11 11:36:51 AM"
- Modification editor = "Anthony"

Smooth:

- Type of smoothing = "Polynomial"
- Polynomial type = "Cubic"
- Convolution range = "9"
- Modification time = "2012/01/11 11:38:17 AM"
- Modification editor = "Anthony"

Search Peaks:

- Minimum significance = "1.50"
- Minimum tip width = "0.01"
- Maximum tip width = "1.00"
- Peak base width = "2.00"
- Method = "Minimum 2nd derivative"
- Modification time = "2012/01/11 11:38:23 AM"
- Modification editor = "Anthony"

Search-Match:

- Data source = "Profile and peak list"
- Restriction = "Restriction set"
- Description = "Default - All ref. patterns possible"
- All of: elements = ""
- At least one of: elements = "C, Na, Mg, Al, Cr, Mn, Fe, Ni, Cu"

- None of: elements = "H, He, Li, Be, B, N, O, F, Ne, Si, P, S, Cl, Ar, K, Ca, Sc, Ti, V, Co, Zn, Ga, Ge, As, Se, Br, Kr, Rb, Sr, Y, Zr, Nb, Mo, Tc, Ru, Rh, Pd, Ag, Cd, In, Sn, Sb, Te, I, Xe, Cs, Ba, La, Ce, Pr, Nd, Pm, Sm, Eu, Gd, Tb, Dy, Ho, Er, Tm, Yb, Lu, Hf, Ta, W, Re, Os, Ir, Pt, Au, Hg, Tl, Pb, Bi, Po, At, Rn, Fr, Ra, Ac, Th, Pa, U, Np, Pu, Am, Cm, Bk, Cf, Es, Fm, Md, No, Lr, D, T"

- Maximum no. of elements = "9"

- Skip marked as deleted by ICDD = "No"

- Skip marked as deleted by a user = "No"

- Quality marks set = ""

- Subfiles = ""

- Scoring schema = "Multi phase"

- Auto residue = "Yes"

- Match intensity = "Yes"

- Demote unmatched strong = "Yes"

- Allow pattern shift = "Yes"

- Two theta shift = "0"

- Identify = "Yes"

- Max. no. of accepted patterns = "20"

- Minimum score = "50"

- Search depth = "10"

- Min. new lines / total lines = "100"

- Minimum new lines = "5"

- Minimum scale factor = "0.1"

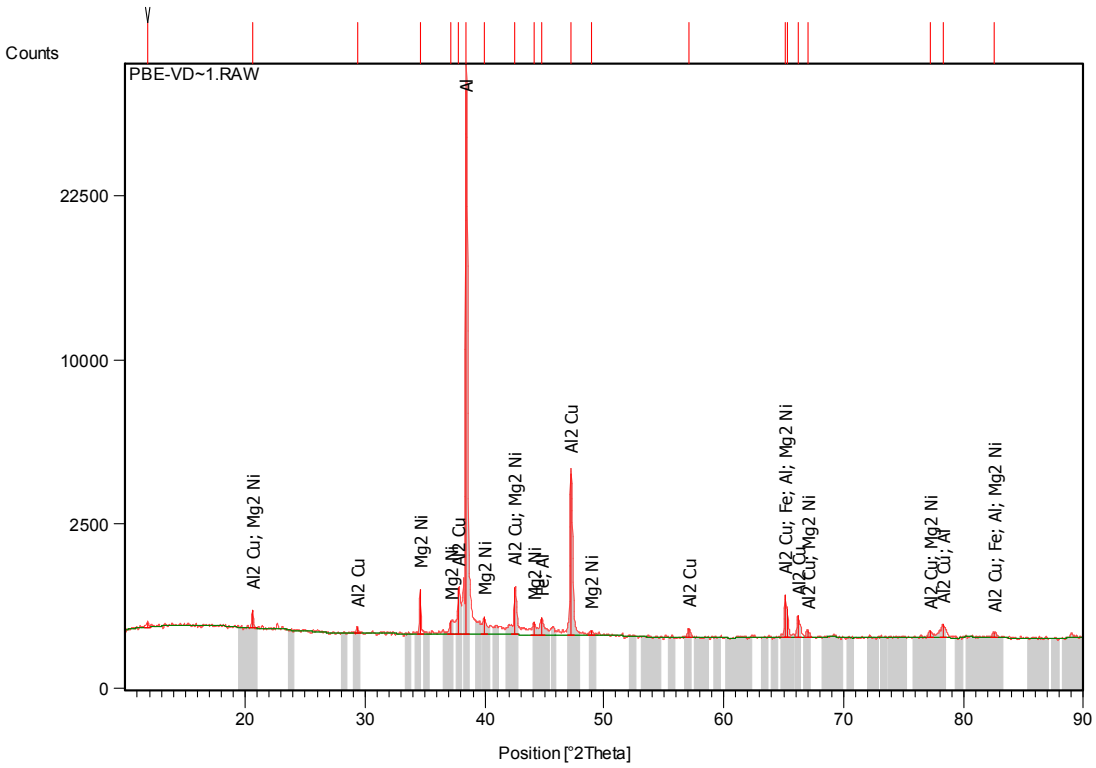
- Modification time = "2012/01/11 11:38:44 AM"

- Modification editor = "Anthony"

Anchor Scan Parameters: (Bookmark1)

Sample Identification	**PDE+VDE+Boehmite Nanoparticle**
Measurement Date / Time	01/10/12 14:00:02
Raw Data Origin	BRUKER-binary V3 (.RAW)
Scan Axis	Gonio
Start Position [°2Th.]	10.0020
End Position [°2Th.]	90.0040
Step Size [°2Th.]	0.0260
Scan Step Time [s]	37.0000
Scan Type	CONTINUOUS
Offset [°2Th.]	0.0000
Divergence Slit Type	Fixed
Divergence Slit Size [°]	1.0000
Specimen Length [mm]	10.00
Receiving Slit Size [mm]	0.1000
Measurement Temperature [°C]	25.00
Anode Material	Cu
Generator Settings	30 kV, 10 mA
Diffractometer Type	Unknown
Goniometer Radius [mm]	141.00
Dist. Focus-Diverg. Slit [mm]	91.00
Incident Beam Monochromator	No
Spinning	No

Graphics: (Bookmark2)



Peak List: (Bookmark 3)

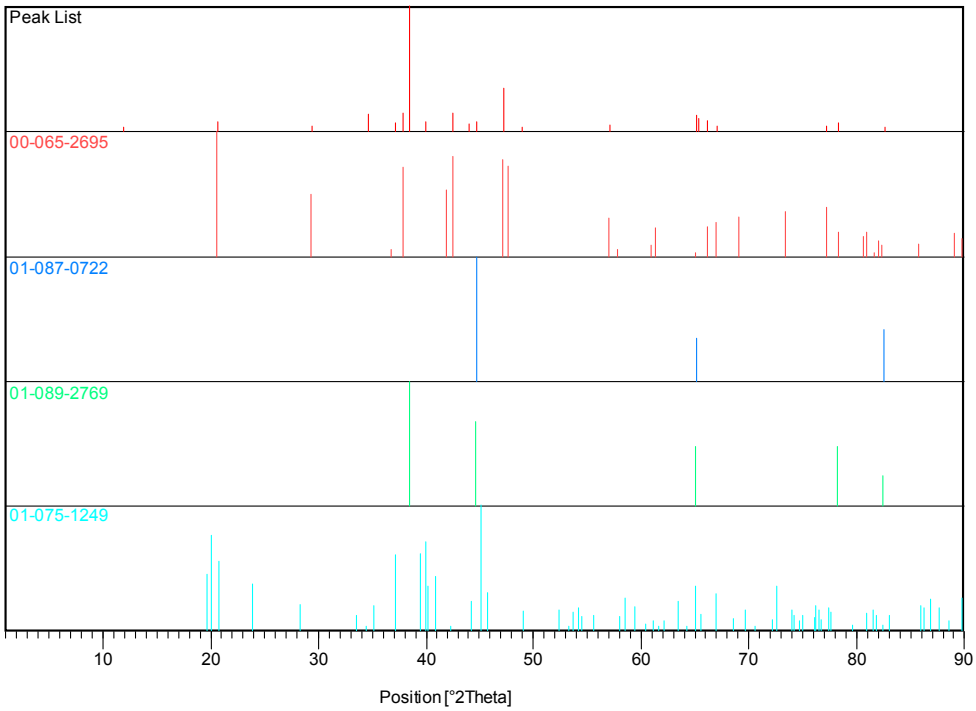
Pos. [°2Th.]	Height [cts]	FWHM [°2Th.]	d-spacing [Å]	Rel. Int. [%]	Tip width [°2Th.]	Matched by
11.8758	40.26	0.8187	7.45215	0.12	0.8320	
20.6087	219.26	0.1023	4.30985	0.66	0.1040	00-065-2695; 01-075-1249
29.3707	62.39	0.3070	3.04102	0.19	0.3120	00-065-2695
34.5869	626.48	0.1279	2.59341	1.89	0.1300	01-075-1249
37.1423	145.78	0.2558	2.42064	0.44	0.2600	01-075-1249
37.8191	677.44	0.1279	2.37887	2.04	0.1300	00-065-2695
38.4163	33180.71	0.2047	2.34325	100.00	0.2080	01-089-2769
39.9195	198.63	0.1791	2.25841	0.60	0.1820	01-075-1249
42.5144	680.07	0.1791	2.12638	2.05	0.1820	00-065-2695; 01-075-1249
44.0827	134.68	0.1535	2.05431	0.41	0.1560	01-075-1249
44.7201	191.53	0.2047	2.02650	0.58	0.2080	01-087-0722; 01-089-2769
47.2366	3994.92	0.1791	1.92424	12.04	0.1820	00-065-2695
48.9817	47.71	0.3070	1.85969	0.14	0.3120	01-075-1249
57.0909	89.89	0.2047	1.61332	0.27	0.2080	00-065-2695
65.1189	555.68	0.1248	1.43132	1.67	0.1040	00-065-2695; 01-087-0722; 01-089-2769; 01-075-1249
65.3162	344.35	0.0936	1.43098	1.04	0.0780	

66.1833	241.49	0.1560	1.41086	0.73	0.1300	00-065-2695
67.0268	65.08	0.3744	1.39514	0.20	0.3120	00-065-2695; 01-075-1249
77.2018	63.27	0.3744	1.23467	0.19	0.3120	00-065-2695; 01-075-1249
78.2840	145.30	0.3120	1.22029	0.44	0.2600	00-065-2695; 01-089-2769
82.5970	47.62	0.4992	1.16715	0.14	0.4160	00-065-2695; 01-087-0722; 01-089-2769; 01-075-1249

Identified Patterns List: (Bookmark4)

Visible	Ref. Code	Score	Compound Name	Displacement [°2Th.]	Scale Factor	Chemical Formula
*	00-065-2695	49	Aluminum Copper	-0.136	0.025	Al2 Cu
*	01-087-0722	48	Iron	-0.051	0.006	Fe
*	01-089-2769	34	Aluminum	-0.030	0.764	Al
*	01-075-1249	18	Magnesium Nickel	-0.015	0.004	Mg2 Ni

Plot of Identified Phases: (Bookmark 5)



Document History: (Bookmark 6)

Insert Measurement:

- Scan name = "PBE-VD~1.RAW"
- Modification time = "2012/01/11 11:36:47 AM"
- Modification editor = "Anthony"

Interpolate Step Size:

- Step Size = "Derived"
- Modification time = "2012/01/11 11:36:47 AM"
- Modification editor = "Anthony"

Smooth:

- Type of smoothing = "Polynomial"
- Polynomial type = "Cubic"
- Convolution range = "9"
- Modification time = "2012/01/11 11:44:06 AM"
- Modification editor = "Anthony"

Search Peaks:

- Minimum significance = "1.50"
- Minimum tip width = "0.01"
- Maximum tip width = "1.00"
- Peak base width = "2.00"
- Method = "Minimum 2nd derivative"
- Modification time = "2012/01/11 11:44:10 AM"
- Modification editor = "Anthony"

Search-Match:

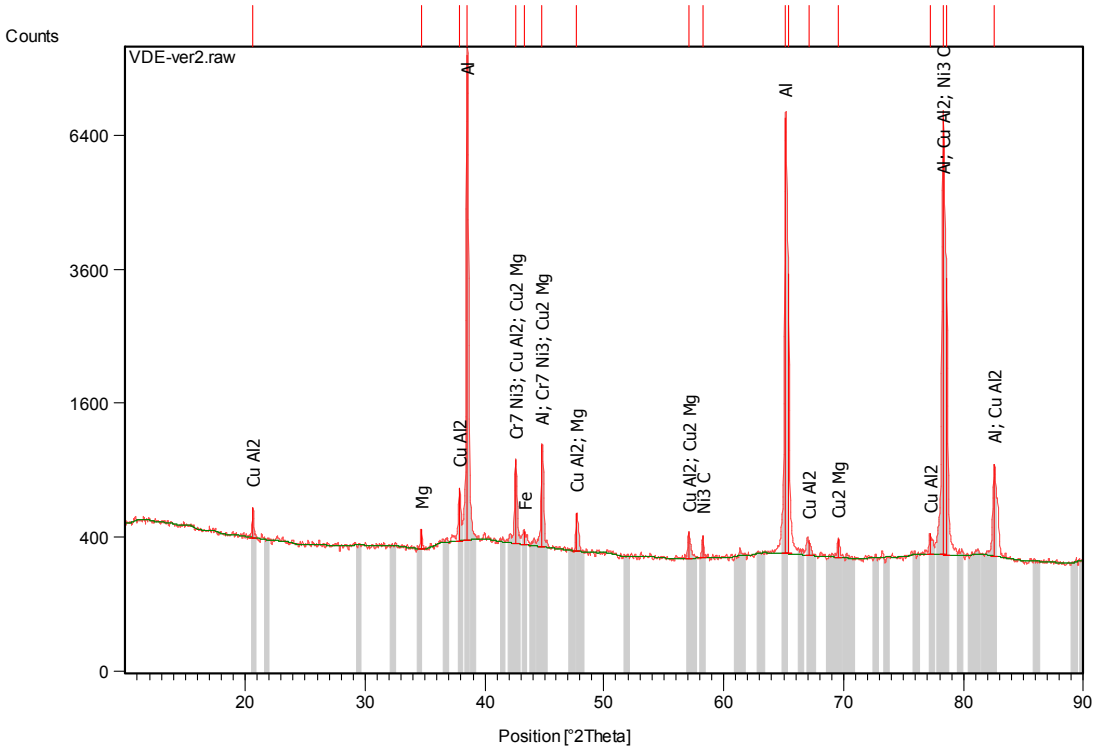
- Data source = "Profile and peak list"
- Restriction = "Restriction set"
- Description = "Default - All ref. patterns possible"
- All of: elements = ""
- At least one of: elements = "C, Na, Mg, Al, Cr, Mn, Fe, Ni, Cu"

- None of: elements = "H, He, Li, Be, B, N, O, F, Ne, Si, P, S, Cl, Ar, K, Ca, Sc, Ti, V, Co, Zn, Ga, Ge, As, Se, Br, Kr, Rb, Sr, Y, Zr, Nb, Mo, Tc, Ru, Rh, Pd, Ag, Cd, In, Sn, Sb, Te, I, Xe, Cs, Ba, La, Ce, Pr, Nd, Pm, Sm, Eu, Gd, Tb, Dy, Ho, Er, Tm, Yb, Lu, Hf, Ta, W, Re, Os, Ir, Pt, Au, Hg, Tl, Pb, Bi, Po, At, Rn, Fr, Ra, Ac, Th, Pa, U, Np, Pu, Am, Cm, Bk, Cf, Es, Fm, Md, No, Lr, D, T"
- Maximum no. of elements = "9"
- Skip marked as deleted by ICDD = "No"
- Skip marked as deleted by a user = "No"
- Quality marks set = ""
- Subfiles = ""
- Scoring schema = "Multi phase"
- Auto residue = "Yes"
- Match intensity = "Yes"
- Demote unmatched strong = "Yes"
- Allow pattern shift = "Yes"
- Two theta shift = "0"
- Identify = "Yes"
- Max. no. of accepted patterns = "20"
- Minimum score = "50"
- Search depth = "10"
- Min. new lines / total lines = "100"
- Minimum new lines = "5"
- Minimum scale factor = "0.1"
- Modification time = "2012/01/11 11:44:26 AM"
- Modification editor = "Anthony"

Anchor Scan Parameters: (Bookmark1)

Sample Identification	**Sample exposed to VDE**
Measurement Date / Time	01/10/12 14:37:22
Raw Data Origin	BRUKER-binary V3 (.RAW)
Scan Axis	Gonio
Start Position [°2Th.]	10.0020
End Position [°2Th.]	90.0040
Step Size [°2Th.]	0.0260
Scan Step Time [s]	37.0000
Scan Type	CONTINUOUS
Offset [°2Th.]	0.0000
Divergence Slit Type	Fixed
Divergence Slit Size [°]	1.0000
Specimen Length [mm]	10.00
Receiving Slit Size [mm]	0.1000
Measurement Temperature [°C]	25.00
Anode Material	Cu
Generator Settings	30 kV, 10 mA
Diffractometer Type	Unknown
Goniometer Radius [mm]	141.00
Dist. Focus-Diverg. Slit [mm]	91.00
Incident Beam Monochromator	No
Spinning	No

Graphics: (Bookmark2)



Peak List: (Bookmark 3)

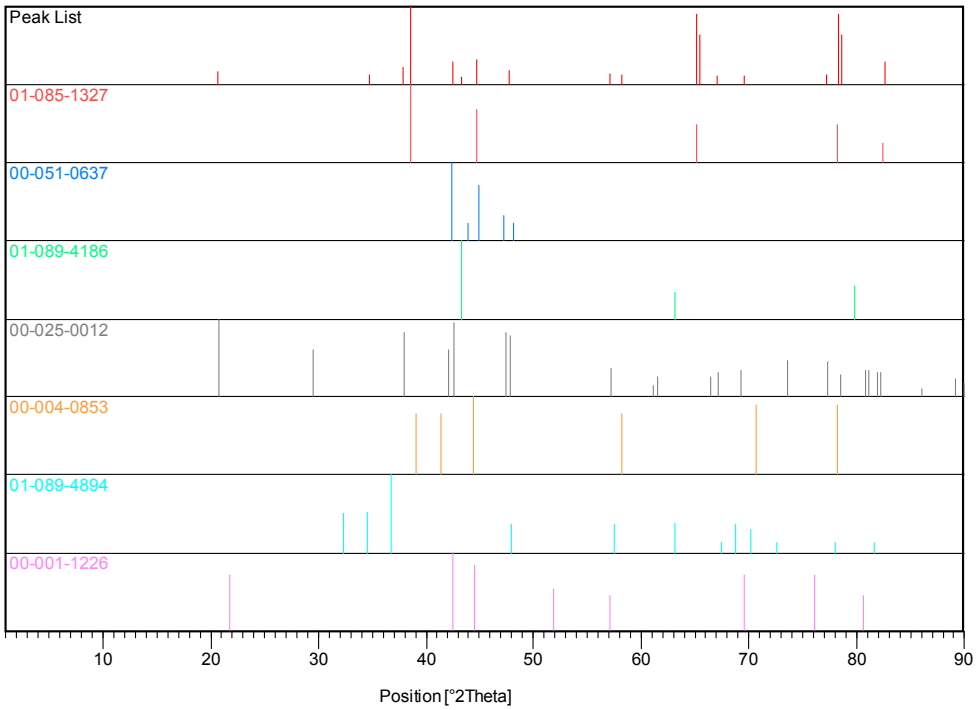
Pos. [°2Th.]	Height [cts]	FWHM [°2Th.]	d-spacing [Å]	Rel. Int. [%]	Tip width [°2Th.]	Matched by
20.6556	196.64	0.1279	4.30016	2.44	0.1300	00-025-0012
34.6716	111.16	0.1535	2.58727	1.38	0.1560	01-089-4894
37.8605	363.35	0.1535	2.37636	4.50	0.1560	00-025-0012
38.5089	8069.07	0.2047	2.33783	100.00	0.2080	01-085-1327
42.5466	627.54	0.2047	2.12485	7.78	0.2080	00-051-0637; 00-025-0012; 00-001-1226
43.3198	76.04	0.3070	2.08870	0.94	0.3120	01-089-4186
44.7570	790.54	0.2047	2.02491	9.80	0.2080	01-085-1327; 00-051-0637; 00-001-1226
47.7389	230.56	0.1791	1.90516	2.86	0.1820	00-025-0012; 01-089-4894
57.0934	141.85	0.2047	1.61325	1.76	0.2080	00-025-0012; 00-001-1226
58.2503	117.83	0.1279	1.58394	1.46	0.1300	00-004-0853
65.1664	6499.64	0.1872	1.43039	80.55	0.1560	01-085-1327
65.3994	3211.01	0.1248	1.42937	39.79	0.1040	
67.0775	80.90	0.3744	1.39421	1.00	0.3120	00-025-0012
69.5532	98.83	0.2496	1.35051	1.22	0.2080	00-001-1226
77.2032	121.12	0.1872	1.23465	1.50	0.1560	00-025-0012
78.3063	6522.83	0.2184	1.22000	80.84	0.1820	01-085-

						1327; 00-025-0012; 00-004-0853
78.5950	3140.30	0.1560	1.21923	38.92	0.1300	
82.5818	657.52	0.2184	1.16733	8.15	0.1820	01-085-1327; 00-025-0012

Identified Patterns List: (Bookmark4)

Visible	Ref. Code	Score	Compound Name	Displacement [°2Th.]	Scale Factor	Chemical Formula
*	01-085-1327	52	Aluminum	0.017	1.027	Al
*	00-051-0637	36	Chromium Nickel	-0.370	0.026	Cr7 Ni3
*	01-089-4186	43	Iron	-0.318	0.009	Fe
*	00-025-0012	31	Khatyrkite, syn	0.090	0.018	Cu Al2
*	00-004-0853	13	Nickel Carbide	-0.111	0.047	Ni3 C
*	01-089-4894	13	Magnesium	0.118	0.003	Mg
*	00-001-1226	24	Copper Magnesium	-0.019	0.046	Cu2 Mg

Plot of Identified Phases: (Bookmark 5)



Document History: (Bookmark 6)

Insert Measurement:

- Scan name = "VDE-ver2.raw"
- Modification time = "2012/01/11 11:51:04 AM"
- Modification editor = "Anthony"

Interpolate Step Size:

- Step Size = "Derived"
- Modification time = "2012/01/11 11:51:04 AM"
- Modification editor = "Anthony"

Smooth:

- Type of smoothing = "Polynomial"
- Polynomial type = "Cubic"
- Convolution range = "9"
- Modification time = "2012/01/11 11:51:11 AM"
- Modification editor = "Anthony"

Search Peaks:

- Minimum significance = "1.50"
- Minimum tip width = "0.01"
- Maximum tip width = "1.00"
- Peak base width = "2.00"
- Method = "Minimum 2nd derivative"
- Modification time = "2012/01/11 11:51:16 AM"
- Modification editor = "Anthony"

Search-Match:

- Data source = "Profile and peak list"
- Restriction = "Restriction set"
- Description = "Default - All ref. patterns possible"
- All of: elements = ""
- At least one of: elements = "C, Na, Mg, Al, Cr, Mn, Fe, Ni, Cu"

- None of: elements = "H, He, Li, Be, B, N, O, F, Ne, Si, P, S, Cl, Ar, K, Ca, Sc, Ti, V, Co, Zn, Ga, Ge, As, Se, Br, Kr, Rb, Sr, Y, Zr, Nb, Mo, Tc, Ru, Rh, Pd, Ag, Cd, In, Sn, Sb, Te, I, Xe, Cs, Ba, La, Ce, Pr, Nd, Pm, Sm, Eu, Gd, Tb, Dy, Ho, Er, Tm, Yb, Lu, Hf, Ta, W, Re, Os, Ir, Pt, Au, Hg, Tl, Pb, Bi, Po, At, Rn, Fr, Ra, Ac, Th, Pa, U, Np, Pu, Am, Cm, Bk, Cf, Es, Fm, Md, No, Lr, D, T"

- Maximum no. of elements = "9"

- Skip marked as deleted by ICDD = "No"

- Skip marked as deleted by a user = "No"

- Quality marks set = ""

- Subfiles = ""

- Scoring schema = "Multi phase"

- Auto residue = "Yes"

- Match intensity = "Yes"

- Demote unmatched strong = "Yes"

- Allow pattern shift = "Yes"

- Two theta shift = "0"

- Identify = "Yes"

- Max. no. of accepted patterns = "20"

- Minimum score = "50"

- Search depth = "10"

- Min. new lines / total lines = "100"

- Minimum new lines = "5"

- Minimum scale factor = "0.1"

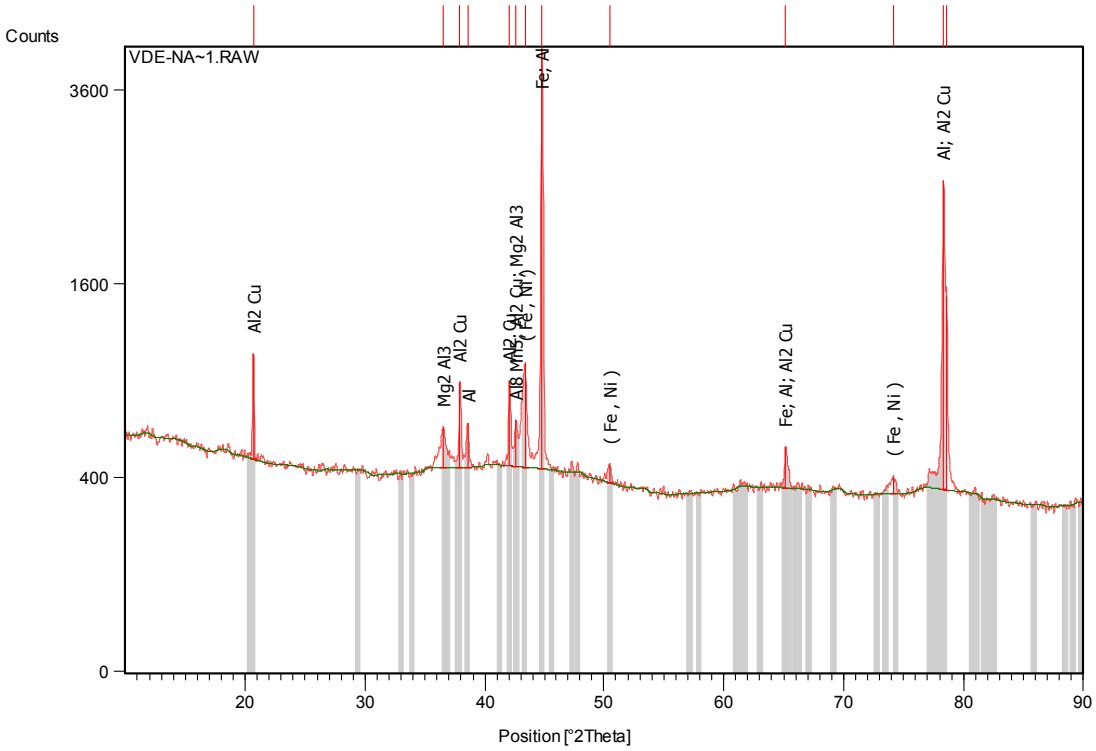
- Modification time = "2012/01/11 11:51:24 AM"

- Modification editor = "Anthony"

Anchor Scan Parameters: (Bookmark1)

Sample Identification	**Sample exposed to VDE+Boehmite Nanoparticle**
Measurement Date / Time	01/10/12 12:50:53
Raw Data Origin	BRUKER-binary V3 (.RAW)
Scan Axis	Gonio
Start Position [°2Th.]	10.0020
End Position [°2Th.]	90.0040
Step Size [°2Th.]	0.0260
Scan Step Time [s]	37.0000
Scan Type	CONTINUOUS
Offset [°2Th.]	0.0000
Divergence Slit Type	Fixed
Divergence Slit Size [°]	1.0000
Specimen Length [mm]	10.00
Receiving Slit Size [mm]	0.1000
Measurement Temperature [°C]	25.00
Anode Material	Cu
Generator Settings	30 kV, 10 mA
Diffractometer Type	Unknown
Goniometer Radius [mm]	141.00
Dist. Focus-Diverg. Slit [mm]	91.00
Incident Beam Monochromator	No
Spinning	No

Graphics: (Bookmark2)



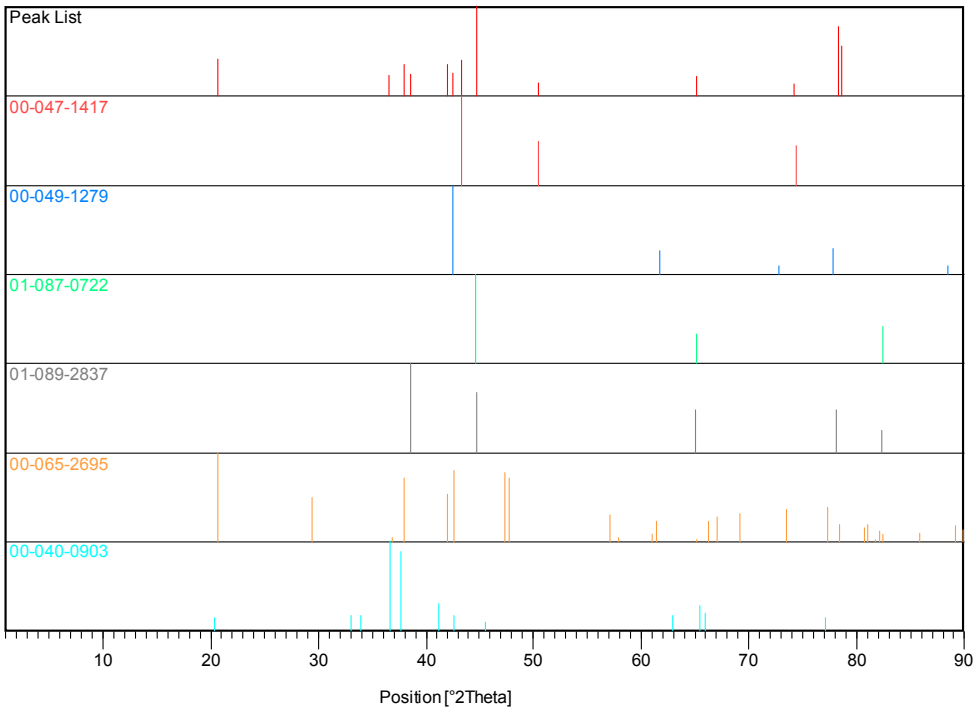
Peak List: (Bookmark 3)

Pos. [°2Th.]	Height [cts]	FWHM [°2Th.]	d-spacing [Å]	Rel. Int. [%]	Tip width [°2Th.]	Matched by
20.6690	598.38	0.1279	4.29741	16.34	0.1300	00-065-2695
36.5344	191.59	0.2303	2.45951	5.23	0.2340	00-040-0903
37.8988	442.07	0.1279	2.37405	12.07	0.1300	00-065-2695
38.5563	213.33	0.1535	2.33506	5.82	0.1560	01-089-2837
42.0304	445.19	0.1535	2.14975	12.15	0.1560	00-065-2695
42.5702	223.60	0.1791	2.12373	6.10	0.1820	00-049-1279; 00-065-2695; 00-040-0903
43.3718	567.20	0.2047	2.08631	15.49	0.2080	00-047-1417
44.7287	3662.78	0.2047	2.02613	100.00	0.2080	01-087-0722; 01-089-2837
50.4793	73.29	0.3070	1.80798	2.00	0.3120	00-047-1417
65.1712	174.05	0.1535	1.43147	4.75	0.1560	01-087-0722; 01-089-2837; 00-065-2695
74.1892	62.80	0.4093	1.27821	1.71	0.4160	00-047-1417
78.3449	2210.45	0.1535	1.22049	60.35	0.1560	01-089-2837; 00-065-2695
78.5985	1147.42	0.1560	1.21918	31.33	0.1300	

Identified Patterns List: (Bookmark4)

Visible	Ref. Code	Score	Compound Name	Displacement [°2Th.]	Scale Factor	Chemical Formula
*	00-047-1417	53	Taenite, syn	-0.180	0.115	(Fe , Ni)
*	00-049-1279	51	Aluminum Manganese	0.064	0.055	Al8 Mn5
*	01-087-0722	42	Iron	-0.061	0.753	Fe
*	01-089-2837	36	Aluminum	0.138	0.412	Al
*	00-065-2695	37	Aluminum Copper	-0.032	0.119	Al2 Cu
*	00-040-0903	31	Aluminum Magnesium	0.229	0.030	Mg2 Al3

Plot of Identified Phases: (Bookmark 5)



Document History: (Bookmark 6)

Insert Measurement:

- Scan name = "VDE-NA~1.RAW"
- Modification time = "2012/01/11 11:51:01 AM"
- Modification editor = "Anthony"

Interpolate Step Size:

- Step Size = "Derived"
- Modification time = "2012/01/11 11:51:01 AM"
- Modification editor = "Anthony"

Smooth:

- Type of smoothing = "Polynomial"
- Polynomial type = "Cubic"
- Convolution range = "9"
- Modification time = "2012/01/11 11:54:01 AM"
- Modification editor = "Anthony"

Search Peaks:

- Minimum significance = "1.50"
- Minimum tip width = "0.01"
- Maximum tip width = "1.00"
- Peak base width = "2.00"
- Method = "Minimum 2nd derivative"
- Modification time = "2012/01/11 11:54:04 AM"
- Modification editor = "Anthony"

Search-Match:

- Data source = "Profile and peak list"
- Restriction = "Restriction set"
- Description = "Default - All ref. patterns possible"
- All of: elements = ""
- At least one of: elements = "C, Na, Mg, Al, Cr, Mn, Fe, Ni, Cu"

- None of: elements = "H, He, Li, Be, B, N, O, F, Ne, Si, P, S, Cl, Ar, K, Ca, Sc, Ti, V, Co, Zn, Ga, Ge, As, Se, Br, Kr, Rb, Sr, Y, Zr, Nb, Mo, Tc, Ru, Rh, Pd, Ag, Cd, In, Sn, Sb, Te, I, Xe, Cs, Ba, La, Ce, Pr, Nd, Pm, Sm, Eu, Gd, Tb, Dy, Ho, Er, Tm, Yb, Lu, Hf, Ta, W, Re, Os, Ir, Pt, Au, Hg, Tl, Pb, Bi, Po, At, Rn, Fr, Ra, Ac, Th, Pa, U, Np, Pu, Am, Cm, Bk, Cf, Es, Fm, Md, No, Lr, D, T"
- Maximum no. of elements = "9"
- Skip marked as deleted by ICDD = "No"
- Skip marked as deleted by a user = "No"
- Quality marks set = ""
- Subfiles = ""
- Scoring schema = "Multi phase"
- Auto residue = "Yes"
- Match intensity = "Yes"
- Demote unmatched strong = "Yes"
- Allow pattern shift = "Yes"
- Two theta shift = "0"
- Identify = "Yes"
- Max. no. of accepted patterns = "20"
- Minimum score = "50"
- Search depth = "10"
- Min. new lines / total lines = "100"
- Minimum new lines = "5"
- Minimum scale factor = "0.1"
- Modification time = "2012/01/11 11:54:12 AM"
- Modification editor = "Anthony"